Additive Manufacturing of High-Performance Engineering and Piezoelectric Polymers through Precipitation Printing

by

Ruowen Tu

A dissertation submitted in partial fulfillment
of the requirements for the degree of
Doctor of Philosophy
(Aerospace Engineering)
in the University of Michigan
2024

Doctoral Committee:

Professor Henry A. Sodano, Chair
Professor Daniel J. Inman
Assistant Professor Abdon Pena-Francesch
Professor Anthony M. Waas

Ruowen Tu

turuowen@umich.edu

ORCID iD: 0000-0003-2681-8030

Dedication

This dissertation is dedicated to my parents; without all their love and support, this would not have been possible.

Acknowledgements

I would like to first acknowledge my advisor, Professor Henry Sodano, for giving me the opportunity to join his research group when I was an undergraduate student. The one-year undergraduate research experience in his group helped me discover my interest and led me in this path of pursuing a doctoral degree. His support, guidance and advice on my research, especially during my senior undergraduate year and the first two years of my Ph.D. journey, were substantial for me to build a solid background and become an independent researcher in the later three years. Under his mentorship, I explored multiple disciplines related to smart materials and functional devices, and pushed the boundaries of state-of-the-art additive manufacturing technologies. I am also sincerely grateful to my dissertation committee members: Prof. Daniel Inman, Prof. Anthony Waas and Prof. Abdon Pena-Francesch, for providing me with generous support and feedback.

I would also like to thank my former group members, Dr. Ethan Sprague, Dr. Jiajun Lin, Dr. Jalal Nasser and Dr. Hyun Chan Kim, for providing me mentorship and giving me constructive feedback on my research. I want to acknowledge all other past and current group members, Dr. Alireza Nafari, Dr. Lisha Zhang, Dr. LoriAnne Groo, Dr. Kelsey Steinke, Dr. Jaehyun Jung, Tianyu Yuan, Bokai Zhang, Tianqi Liu, Steven Mamolo and Boyang Chen, for their valuable support and friendship during my Ph.D. journey. In addition, I would like to express my sincere gratitude to the University of Montana collaborators, Prof. Bret Tobalske and Rémy Delplanche, and the University of Michigan collaborator on the feather transducer project, Dr. Lawren Gamble, without whom the project would not have been successful.

I wholeheartedly show my gratitude to my parents, whose unconditional love supported and helped me gain my confidence when pursuing my academic and research goals. And I would like to gratefully thank my partner, Ziyou Wu, who not only enlightened me as my best interdisciplinary peer mentor but more importantly, accompanied me throughout my Ph.D. She gave me all the emotional support and joy so that we had this happy and unforgettable Ph.D. journey together. Finally, I want to thank all my friends for all their support and our fun together throughout this five-year experience.

Table of Contents

List of Tables

List of Figures

Abstract

Additive manufacturing (AM), or 3D printing of lightweight engineering polymers has become a crucial part in the industrial manufacturing process in the past two decades, which allows for scalable fabrication of complex geometries with cost and material efficiency. However, difficulties have arisen for the AM of high-performance (high-temperature) polymers and multifunctional piezoelectric polymers used in aerospace, automotive and electronic industries. Existing thermal energy-based AM processes such as material extrusion and powder bed fusion have limitations in the quality of produced high-performance polymers due to the huge thermal gradient and stress, and they cannot fabricate common piezoelectric polymers with thermodynamically unfavorable polar crystalline structures. Therefore, new AM processes can be developed to overcome these challenges in high-performance and piezoelectric polymers.

In this dissertation, a novel solvent-based AM process, termed precipitation printing, is developed to enable AM of multiple high-performance engineering and piezoelectric polymers with tailorable porosity and mechanical properties. The proposed method utilizes the dissolution of a target polymer in a suitable solvent to form a printing solution, and the computer-controlled deposition of the printing solution in a non-solvent coagulation bath to induce precipitation and solidification of the target polymer and eventually build 3D structures. This precipitation printing process has been successfully applied to fabricate high-performance polymeric 3D structures made of polysulfone and aramid with exceptional thermal and mechanical properties, and highly piezoelectric poly(vinylidene fluoride) as vibration energy harvesters and stress/strain sensors. Finally, precipitation printing also plays an integral role in achieving our 3D printed artificial feathers with embedded aerodynamic sensing. In summary, precipitation printing provides a new concept and a solution to fill a gap in AM of high-performance and multifunctional structures.

Chapter 1 Introduction

1.1 Motivation

Additive manufacturing (AM), also widely known as three-dimensional (3D) printing, is a manufacturing process that produces 3D structures by adding materials in layers directly from computer-aided design (CAD) [1]. Compared to conventional manufacturing processes, additive manufacturing is based on adding materials to form 3D structures instead of subtracting materials from existing material stocks. After being first developed in the 1980s, the concept and function of AM processes have evolved from rapid prototyping to final product fabrication, and the applicable materials have also expanded to polymers, metals, composites, biomaterials, and multifunctional materials [1,2]. In particular, with the rapid development of computer and CAD technologies, AM has gained significant attention and investment, and its market has grown by almost ten times in the last decade (Figure 1.1). Among all types of AM materials, polymers attract the most research interest and become the most commercially successful AM material category due to their excellent processability, their relatively low-cost AM machine setup, and the capability of tailoring final product properties [3]. It has been widely used to produce polymeric structures with complex geometries, user-customized shapes, or decorative details that change the design frequently, including housings for electronics, glasses frames, shoes, customized automotive parts [4], and medical implants [5], where AM can reduce the manufacturing cost for highly complex shapes or low-volume production. Standard AM processes for polymers include melting-based material extrusion, photocuring-based vat photopolymerization and material jetting, liquid binder-based binder jetting, laser-based powder bed fusion, and direct energy deposition. Despite the variety of existing AM technologies for polymers, currently, most AM-produced parts are made of general-purpose grade or some engineering-grade thermoplastics in the polymer pyramid shown in Figure 1.2 or photocurable thermosetting resins with similar properties to the engineering-grade thermoplastics.

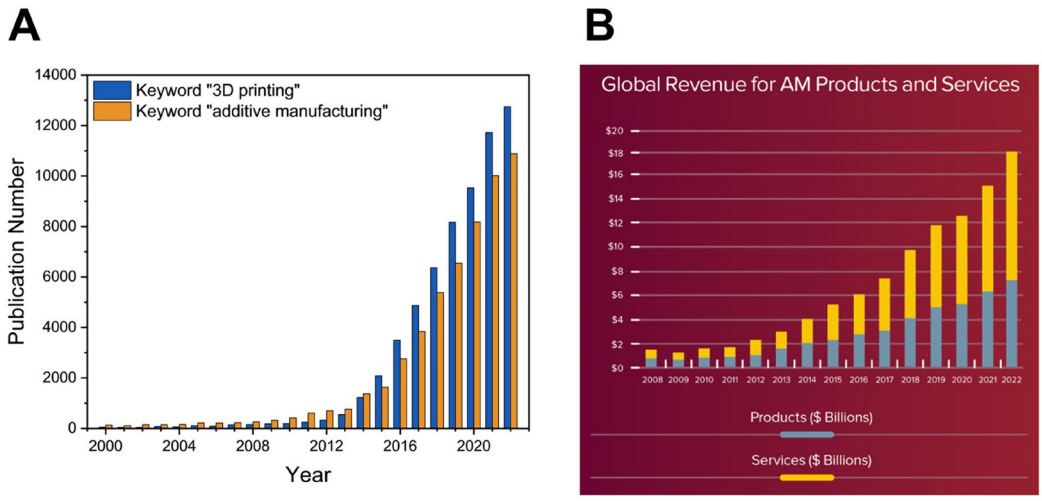

Figure 1.1. A) Publication number with keywords "3D printing" and "additive manufacturing" from the year 2000 to 2022 (data from Web of Science, accessed Dec. 7, 2023). B) Global revenue for additive manufacturing products and services from 2008 to 2022 [6].

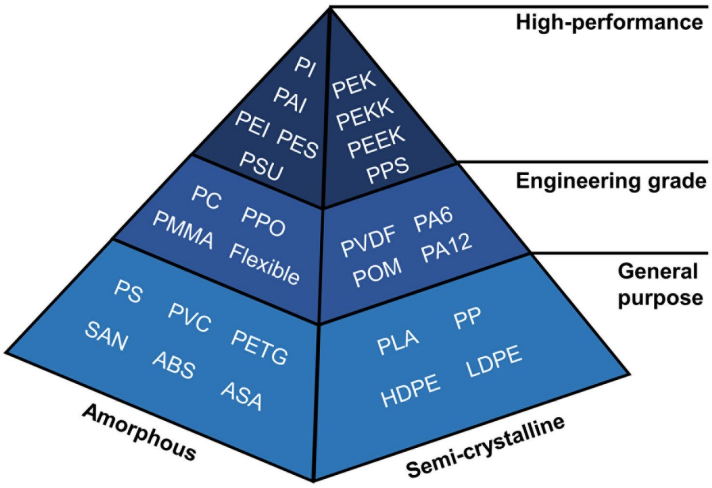

Figure 1.2. Pyramid of different grades of polymers.

Using AM processes like material extrusion and powder bed fusion for the high-performance grade polymers used in structures, electronics, and aerospace industries is still at the research stage. It faces multiple challenges, such as substantial thermal gradients and thermal stress. Recently, solvent-based or rheology-based AM processes have emerged as alternatives to thermal or laser-based processes for polymers, especially high-performance polymers. Solvated thermoplastics, colloidal suspension of polymers, or liquid mixture of polymer precursors can be extruded out of a nozzle to form 3D structures, which utilizes either solvent evaporation (in the case of solvent cast 3D printing) or simply the rheological property of the printing ink (in the case of direct ink writing, DIW) for solidification. Researchers have successfully applied these

processes to common AM polymers like polylactic acid (PLA) [7], engineering polymers like polysulfone [8], and multifunctional polymer composites [9,10]. Although the solvent-based or rheology-based AM processes are currently demonstrated at a laboratory scale and have limitations in final structure height, resolution, and printing ink preparation difficulty, the potential of using these processes to expand the range of applicable polymers and to improve the printed material properties is substantial.

Another type of polymer that attracts substantial research interest in AM is multifunctional polymer, such as piezoelectric polymer. They can be used as sensing components, energy harvesting devices, and actuators in electronics and robotics, and the AM of piezoelectric polymers can substantially reduce the fabrication complexity of piezoelectric devices. However, due to the piezoelectric phase transformation in piezoelectric polymers such as poly(vinylidene fluoride) (PVDF), thermal energy-based AM processes are unsuitable for fabricating piezoelectric polymer devices. Therefore, new methods can be developed to overcome the challenges of piezoelectric polymers in AM.

In this dissertation, a novel solvent-based AM process, termed precipitation printing, is developed to enable AM of multiple engineering and piezoelectric polymers with tailorable porosity and mechanical properties. The proposed method utilizes the precipitation of a solvated polymer, or a colloidal dispersion of a polymer in a non-solvent coagulation bath to form solidified 3D structures based on the non-solvent induced phase separation (NIPS) mechanism [11,12]. As a result, precipitation printing can fabricate 3D structures made of common engineering polymers, high-performance engineering polymers that are difficult to process using existing AM technologies, thermally unstable piezoelectric β phase PVDF, thermosetting rubbers, and polymer blends. In this chapter, a brief introduction of the existing AM processes for polymers with their advantages, limitations, and material selections is provided, which is followed by a literature review of high-performance engineering polymers and piezoelectric polymers, as well as the current progress and challenges in AM of these materials. Finally, some fundamentals of precipitation printing are briefly explained and a dissertation overview is presented.

1.2 Additive manufacturing processes for polymers

1.2.1 Material extrusion

Material extrusion (MEX) is an AM process that uses heat to extrude thermoplastic filaments through a nozzle above the melting point (T_m) for semi-crystalline polymers or the glass transition temperature (T_g) for amorphous polymers and selectively deposits the thermoplastic layer by layer to form 3D structures [13]. It is also known as fused deposition modeling (FDM) or fused filament fabrication (FFF). Due to its simple working mechanism, low cost, and fast fabrication speed, most desktop 3D printers for polymers are based on this AM process. A typical MEX process in Figure 1.3 includes three main steps: thermoplastic filament melting or softening, deposition, and bonding between adjacent paths [14]. First, a thermoplastic filament is fed through rollers and heated around the nozzle above T_m or T_g so that its viscosity drops to a level suitable for extrusion. The extruded thermoplastic is then cooled down and deposited on the printer bed, generally at elevated temperatures, to reduce the first layer of thermal stress. Finally, the deposited thermoplastic bonds to the adjacent paths by thermal joining, using the heat transferred from the nozzle tip to soften the interfaces between paths or layers for interfacial bonding.

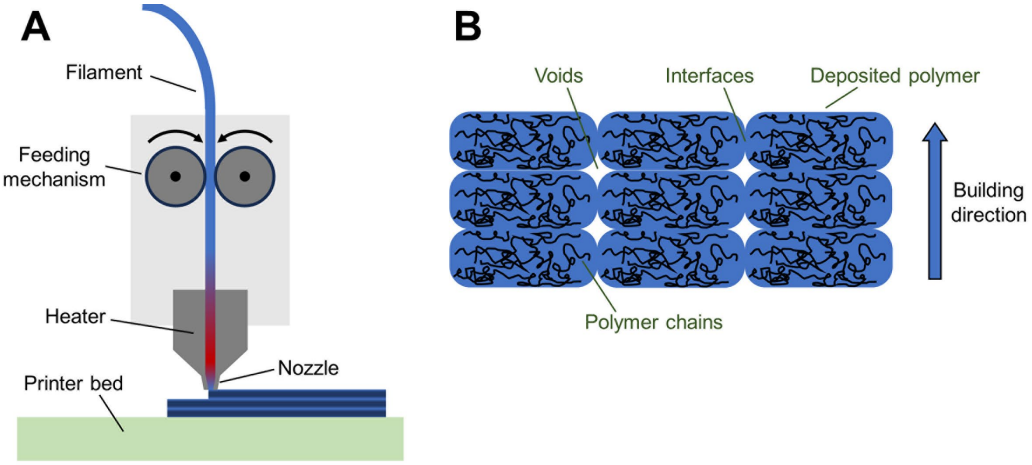

Figure 1.3. A) Material extrusion (MEX) process. B) Illustration of deposited polymer layers and voids formed by MEX.

Despite the previously mentioned advantages, the material selection for MEX is limited to low T_m or T_g thermoplastics with low viscosity during extrusion. Common polymers for this process include acrylonitrile butadiene styrene (ABS), polylactic acid (PLA), polycarbonate (PC), polystyrene (PS), polyamide nylon, and thermoplastic polyurethane (TPU), which have T_m or T_g below 200 °C [15]. MEX has also been applied to thermoplastic-based fiber-reinforced composites

or nanocomposites, like short glass fiber reinforced ABS [16], carbon fiber reinforced ABS [17], carbon/glass/Kevlar fiber reinforced nylon [18], graphene-filled PC-ABS [19], iron/ABS and copper/ABS composites [20], to improve mechanical properties or allow for multifunctionality. Recently, MEX of some high-temperature engineering thermoplastics such as polyetheretherketone (PEEK), polyphenylene sulfide (PPS), and polyetherimide (PEI) has also been attempted using high-power heaters to generate nozzle temperatures up to 400 °C [21–23]. However, the large thermal gradient during printing makes the material extrusion process for high-temperature polymers no longer as robust as the standard material extrusion process for low T_m or T_g thermoplastics. The essential heating process in MEX also restricts it from the application for thermally unstable polymers that decompose below T_m or thermodynamically unfavorable polymer phases (such as the β phase of neat PVDF [24]).

During the MEX process, the thermal gradient between the nozzle and printing bed/previous layer is the leading cause of defects and challenges. First, the thermal gradient causes residual thermal stress in each layer, which can accumulate, eventually leading to warping and detachment from the printing bed [25–27]. This phenomenon can be mitigated by heating the printing bed, but it becomes more severe when using a higher nozzle temperature. Second, the extruded thermoplastic hardens rapidly due to the thermal gradient and cooling rate, which may fail to fill all the free space between adjacent paths and create voids (Figure 1.3B). Third, the fast cooling and hardening of the deposited thermoplastic also results in weaker thermal joining strength as the interfacial bonding mechanism. This is a typical feature of structures produced by MEX, which is the origin of mechanical anisotropy. These structures have higher Young's modulus and strength in the printing path direction and lower properties in the direction perpendicular to the path interfaces [28–30]. The mechanical properties in the vertical building direction are usually the lowest due to the weak interlayer bonding. Therefore, researchers have developed a z-pinning strategy to overcome the anisotropy in parts made by MEX [31,32].

1.2.2 Vat photopolymerization

Vat photopolymerization (VPP) is an AM process that uses light to cure small-thickness photopolymers layer by layer in a vat full of photopolymers, which has the longest history among all AM processes. It has multiple different configurations, including point light source stereolithography (SLA), area light source digital light processing (DLP), micro stereolithography

(μSL), and two-photon polymerization (TPP) [33,34]. Vat photopolymerization generally produces 3D structures with high resolution and good surface finish due to the accuracy of a light source and small layer thickness. Still, the process is slow for point light source SLA, μSL, and TPP. With the development of semiconductors, especially digital micromirror devices (DMD), digitally controlled projectors in the DLP process can project area lights with accurate geometries, which accelerates the printing speed significantly by curing an entire layer of photopolymer simultaneously (Figure 1.4) [35,36]. More recently, modifications like continuous liquid interface production (CLIP) have been developed to remove the discrete layers in the printing process by introducing an oxygen-permeable window to produce a liquid dead zone between the window and the cured structure [37,38]. On the other hand, microscale AM was achieved by μSL and TPP, where the resolution of printing can reach the scale of 100 nm [39–42]. Thus, vat photopolymerization has been developed for decades and has become a versatile AM process with high resolution, fast printing speed, and low final product anisotropy [43].

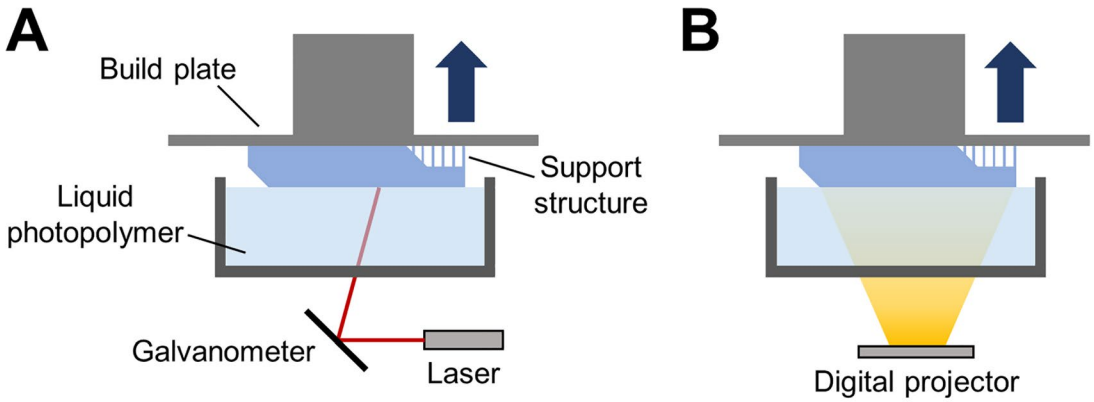

Figure 1.4. Vat photopolymerization processes. A) SLA setup. B) DLP setup.

The material selection for vat photopolymerization is limited to photocurable polymers or hybrid material systems with photocurable components, which usually form crosslinked thermosets after curing. Unlike the thermoplastics used in the MEX processes, the crosslinked final parts produced by VAT photopolymerization are non-recyclable. The most common photocurable polymers are based on acrylates for free-radical polymerization or epoxies for cationic photopolymerization [33,44]. Acrylate-based free-radical polymerization is highly reactive and fast but has high shrinkage after curing. Epoxy-based cationic photopolymerization has low shrinkage, but the reaction is slow, and the cured parts are brittle. Therefore, most commercial photopolymers are a combination of these two types. A photo-sensitive initiator is

also needed to trigger the polymerization. As a result of photocuring chemistry, materials produced from vat photopolymerization usually do not possess high modulus, strength, or T_g compared to engineering plastics produced by conventional manufacturing processes. On the other hand, soft and gel-like materials can be made by vat photopolymerization, which is widely used in the biomedical field [45,46].

1.2.3 Material jetting

Material jetting is an AM process that selectively deposits thin layers of liquid droplets of photopolymers and uses ultraviolet (UV) light for photopolymerization (Figure 1.5) [47,48]. Since liquid material is used in material jetting, any overhang geometry needs gel-like support structures [49], which can be dissolved after the print is complete. Two commercially available material jetting systems are PolyJet by Stratasys and MultiJet Printing (MJP) by 3D Systems. Compared to vat photopolymerization, the material jetting process moves the printheads to deposit photopolymers in different locations instead of moving the light focus. The advantages of material jetting include high printing precision, low surface roughness, easy detachment, and, most importantly, the ability to print multiple materials using multiple printheads.

Like vat photopolymerization, the materials for material jetting are photopolymers, which can be either rigid, semi-rigid, or soft. Moreover, the multi-material feature of material jetting allows for fabricating polymer composites by combining rigid and soft materials based on the specific design [50]. Hierarchical structures like lattices and honeycombs can be designed to have different modulus materials in various locations for balanced stiffness, toughness, and wear resistance [51,52]. However, due to the high complexity and cost of the material jetting machine, materials being used in this process have been mainly commercially available resins designed explicitly for PolyJet or MJP. Research on novel materials for material jetting is not as common as MEX and vat photopolymerization.

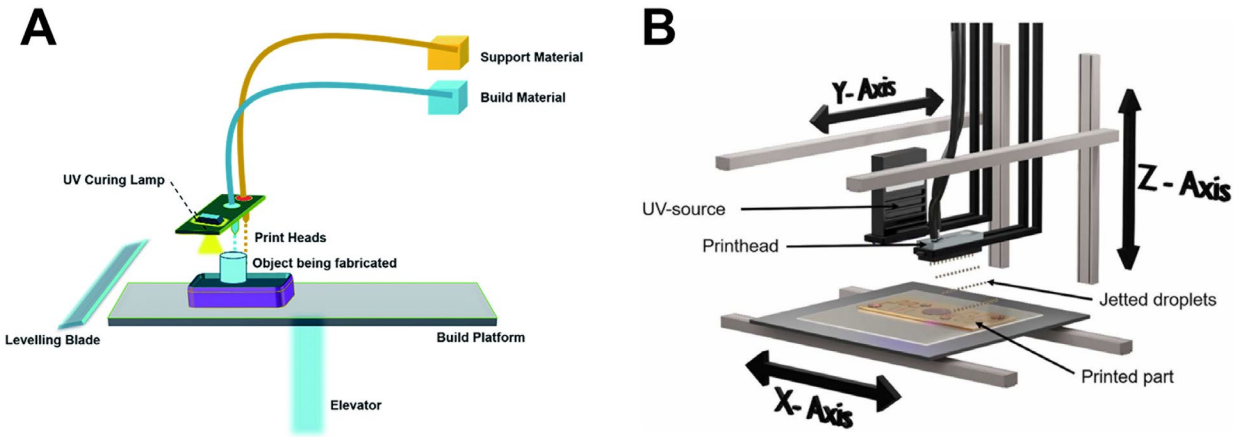

Figure 1.5. Material jetting process. A) Single-build material printhead system [47]. B) Multiple build material printheads system [48].

1.2.4 Binder jetting

Binder jetting is another type of jetting AM process, where only liquid binder material is selectively jetted to a powder bed [53]. For each layer in this process, a thin layer of powder is coated on the bed evenly, and the printhead deposits liquid binder to form the desired 2D shape. Optional heating to evaporate the solvent in the liquid binder can be used after each layer. After all layers are finished, the fragile as-printed part is post-heated for binder curing, and a stronger final part is obtained [54]. Binder jetting is a versatile, low-cost, large-scale AM process that can be adapted to almost any type of powder, including polymers, metals, ceramics, and hybrid powders, which is popular for the AM of high-temperature metals and ceramics in particular. Although binder jetting also has applications in polymer powders, the cured binder material cannot be burned off entirely due to the potential decomposition of the target polymer powder. Therefore, the mechanical properties of binder jetting-produced polymer parts depend on the binder properties and the number of remaining pores, which are typically significantly lower than those of the neat polymer [55–57]. Post-processes such as hot isostatic pressing and infiltration using other liquid materials are adopted by researchers to improve the final part's mechanical properties [56,58,59]. Although binder jetting can theoretically be applied to almost any type of powder, the main limitation of binder jetting is that multiple steps and post-processes are required for producing high-strength final parts.

1.2.5 Powder bed fusion

Laser-based or electron beam-based powder bed fusion (PBF) is an AM process that uses a focused beam to thermally fuse or sinter loose powder to form solid structures [60,61]. Depending on the degree of melting, this process can also be divided into selective laser melting (SLM) or electron beam melting (EBM) using full melting and selective laser sintering (SLS) using partial melting. During this PBF process, a thin layer of loose powder is evenly spread on the building bed for each layer. One or multiple high-energy beams selectively scan the target area for melting or sintering. This is repeated for many layers until the final 3D structure is obtained. Since solid powder is used in this process, overhang structures without needing support design and complicated interlocked structures can be achieved. Using fine powder and small beam spot for PBF, the printing resolution is typically high (at micron level), and the mechanical properties of PBF-produced parts are generally higher than binder jetting or MEX.

PBF can be used on metal, ceramic, or polymer powders like binder jetting. Although PBF has significant advantages and a market for metal AM, it is also widely used on high-melting point polymers [62], such as polyamides (nylon) and polyaryletherketones (PAEKs) [63–65], due to the localized high-temperature generated at the laser focus. However, the limitation of PBF is not only from the cost of expensive PBF machines but also from the challenge of producing and recycling fine powder for high-quality PBF [62]. As a thermal energy-based process, the multidisciplinary physics, including laser irradiation, heat transfer, melting pool characteristics, and material phase change, both computational and experimental, are the challenges researchers face to produce improved-quality PBF parts [63].

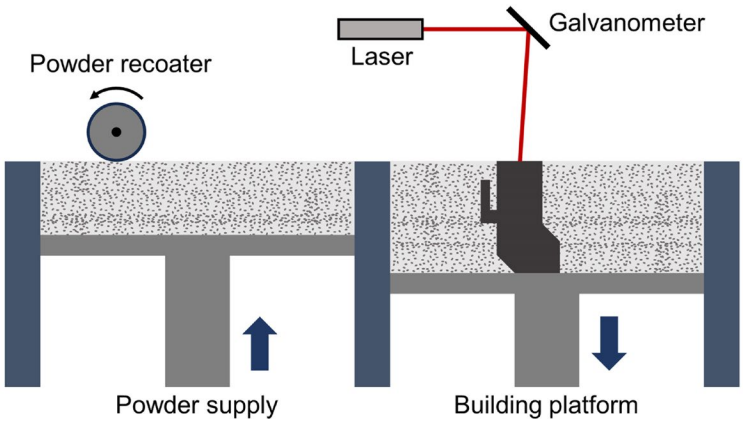

Figure 1.6. Powder bed fusion process and setup.

1.2.6 Other processes

1.2.6.1 Solvent cast 3D printing

Besides the five well-developed AM processes for polymers defined in ISO/ASTM 52900-21, researchers have developed solvent-based processes in the last two decades, which are still in the laboratory development stage before full commercialization. One solvent-based process is solvent cast 3D printing [7,8,64–66]. For each layer, the process starts with dissolving a polymer in a suitable solvent as the printing solution, followed by dispensing the printing solution selectively on a heated building platform. In contrast, the solvent evaporates (Figure 1.7). This process is named solvent cast 3D printing because it shares the exact mechanism as the solvent casting process for thin films but repeats casting for multiple layers to form 3D structures. Almost all thermoplastics that can be dissolved in a solvent apply to this AM process, yet the solvent evaporation rate plays an essential role in the feasibility of 3D structure formation. When using a low boiling point solvent (high vapor pressure at room temperature), like acetone, tetrahydrofuran (THF), or dichloromethane (DCM), solvent evaporation at room temperature is fast enough for each layer to dry out before the deposition of the next layer, making it suitable for building up tall 3D structures. When using a high boiling point solvent (low vapor pressure at room temperature), like water, dimethyl sulfoxide (DMSO), or *N,N*-dimethylformamide (DMF), the building platform must be heated at elevated temperatures to accelerate the evaporation process. This leads to a problem: as the layer number increases, the temperature at the top layer is significantly lower than the building platform due to the polymer's low thermal conductivity, which can cause shape distortion and structure instability from the remaining solvent. Therefore, if the target polymer cannot be dissolved in a low boiling point solvent or a hybrid solvent system, the solvent cast 3D printed structures will be limited in height. Another application of this process is to produce all metal or all ceramic structures by solvent cast 3D printing of a highly loaded polymer solution with metal or ceramic powder, followed by a subsequent sintering and infiltration process [64,67].

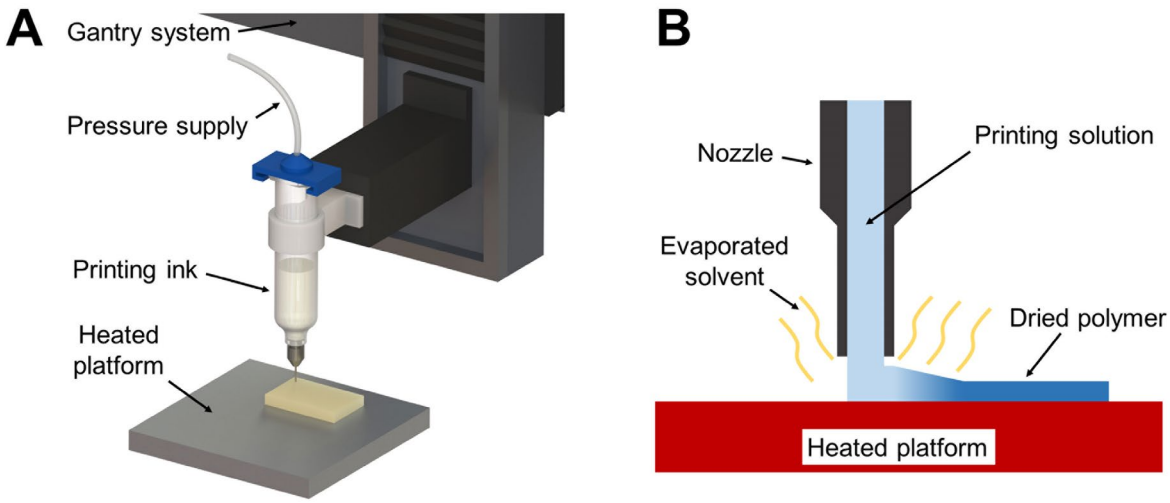

Figure 1.7. Solvent cast 3D printing process. A) Isometric 3D view of the solvent cast 3D printing setup. B) Detailed solvent cast 3D printing process near the nozzle.

1.2.6.2 Direct ink writing

Direct ink writing (DIW) is another new AM process that was developed in the 2000s [9], which uses the rheological behavior of the viscoelastic printing ink to form 3D structures (Figure 1.8A) based on the initial concept of Robocasting [68]. It can be applied to any material as long as a viscoelastic printing ink with proper rheological behaviors can be obtained [69]. In particular, shear thinning behavior as a non-Newtonian fluid is critical for ink rheology. This means the ink has a higher viscosity at rest and a lower viscosity when extruded through a nozzle by shear stress. A typical viscosity range for printing inks at a low shear rate (0.1 s^{-1}) is between 0.1 to 1000 Pa·s [70–72]. During the DIW process, in situ heat or UV-assisted curing can be applied to improve the printed part's stiffness and stability [73–80]. For example, Aw et al. showed a DIW process of a frontally polymerized thermoset using a 100 °C printing bed to trigger the exothermic curing reaction, which can provide heat to the newly deposited ink to continue polymerization [80]. Sarmah et al. developed a multi-walled carbon nanotubes (MWCNTs) loaded epoxy ink for DIW, which enabled thermal curing during the DIW process through radio-frequency heating of the MWCNTs [79]. UV-DIW is a more efficient strategy to harden the printed ink, which has been applied to acrylate/epoxy hybrid ink [74], fiber-reinforced acrylate/epoxy hybrid ink [75], single-walled carbon nanotubes (SWCNTs) filled polyurethane ink [76], and bismaleimide (BMI) ink [77]. Our research group has demonstrated that the UV-DIW of vinyl ester resin thickened by fumed silica using a photo initiator for free-radical polymerization and a subsequent thermal curing process can further improve the crosslink density and mechanical properties [78]. DIW without

heating or UV curing can also be achieved, although more strict rheological properties are required. In this case, the shear storage modulus (G') of the printing ink needs to exceed the shear loss modulus (G'') under low shear stress, indicating an elastic or solid-like state after extrusion [76,77,81]. The shear yield stress (τ_y) is the shear stress where G' starts to decrease significantly, and a higher τ_y of the printing ink leads to a more stable and solid-like printed 3D structure (Figure 1.8B). After DIW, the green parts are usually post-cured for better mechanical performance. The limitation of DIW is the challenging design of the printing ink to match the strict rheology requirements, which typically need special rheological modifiers. In addition, homogeneous printing ink with desired high viscosity is challenging even if a high-power shear mixer is used.

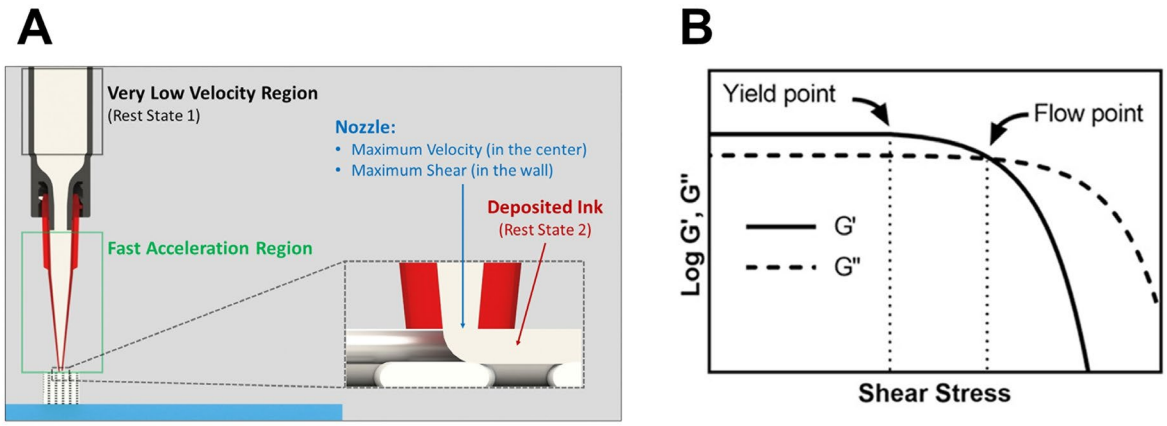

Figure 1.8. A) Direct ink writing (DIW) process [82]. B) Ideal rheology requirement on the DIW printing ink [83].

1.3 High-performance engineering polymers

1.3.1 Types of high-performance engineering polymers

High-performance engineering polymers, or high-temperature polymers, have attracted considerable attention as engineering polymers in the electrical, automotive, aerospace and defense industries [84]. As polymers, their density is usually below 2 g·cm^{-3}, lighter than ceramics, metals, and alloys. Thus, developing these high-performance polymers can potentially replace ceramics and alloys for applications where service temperatures are from 150 to 300 °C and weight reduction is desired. Being distinct from general purpose or common engineering polymers such as ABS, nylon, polymethyl methacrylate (PMMA), and polyethylene terephthalate (PET), high-performance polymers typically have T_g above 150 °C or T_m above 300 °C, making them suitable for continuous service under elevated temperatures. They can be divided into three categories: high T_g amorphous thermoplastics, high T_g amorphous thermosets, and high T_m semi-crystalline

thermoplastics (including high T_m highly crystalline thermoplastics). High T_g amorphous thermoplastics include polysulfone (PSU), polyethersulfone (PES), polyphenylsulfone (PPSU), polyetherimide (PEI), thermoplastic polyimide (TPI) and polyamide-imide (PAI). For high T_g amorphous thermosets, the most widely known group is polyimide (PI), especially Kapton® from DuPoint. High T_m semi-crystalline thermoplastics include polyphenylene sulfide (PPS), PEEK, polyetherketone (PEK), polyetherketoneketone (PEKK), some semi-crystalline TPI, and highly crystalline aromatic polyamide (aramid). Aramid can further be classified into para-aramid (Twaron® from Teijin and Kevlar® from DuPont) and meta-aramid (Nomex® from DuPont). Table 1.1 summarizes the thermal properties of the above-mentioned high-performance polymers. It should be noted that in the cases of para-aramid and meta-aramid, their highly crystalline structure implies the reported T_g is only for the small amorphous portion, and the T_m is usually near or above the decomposition temperature.

1.3.2 Additive manufacturing of high-performance engineering polymers

The AM processes of high-performance engineering polymers are currently limited to MEX, PBF, and customized DIW, which have been successfully applied to the AM of polysulfone family (PSU, PES, PPSU), PAEK family (PEK, PEEK, PEKK), PPS, PEI, TPI, and PI. Due to the lack of inherent photoreactive chemical structures, high-performance polymers generally cannot be adapted to photocuring AM processes, such as vat photopolymerization and material jetting, without significant adjustment of the chemical composition [85].

Table 1.1. Thermal properties of high-performance polymers.

Polymer type	Classification	T_g (°C)	T_m (°C)
PSU [86]	Amorphous thermoplastic	185	/
PES [86]	Amorphous thermoplastic	220	/
PPSU [86]	Amorphous thermoplastic	220	/
PEI [87]	Amorphous thermoplastic	217	/
PAI [88]	Amorphous thermoplastic	277	/
TPI [89]	Amorphous/semi-crystalline thermoplastic	249	388
PI (Kapton®) [90]	Amorphous thermoset	360	/
PPS [91]	Semi-crystalline thermoplastic	85	285
PEEK [21,90]	Semi-crystalline thermoplastic	147	343
PEK [92]	Semi-crystalline thermoplastic	164	372
PEKK [90,92]	Semi-crystalline thermoplastic	163	360
Para-aramid (Twaron®)	Highly crystalline thermoplastic	/	>500
Para-aramid (Kevlar®) [90,93]	Highly crystalline thermoplastic	330	560
Meta-aramid (Nomex®) [90,93]	Highly crystalline thermoplastic	285	375

The polysulfone family has high thermal stability, strength, low thermal expansion, and flame retardancy [86]. The repeating units of the three types of polysulfones, PSU, PES, and PPSU, are shown in Figure 1.9. Since the UV resistance of the polysulfone family is low, they cannot be processed by any UV-assisted AM methods [94]. In addition, the viscosity of polysulfones above T_g is still high, which makes it challenging for MEX and PBF to process polysulfones. The commercially available polysulfone family filaments for MEX, produced by 3DXTECH, have recommended nozzle temperatures of 360–375 °C for PSU, 340–390 °C for PES, and 390–410 °C for PPSU, all at least 150 °C above their T_g. Wu et al. processed PES filaments for MEX from the granular PES pellets and used a nozzle temperature of 360 °C for the MEX process [95]. Although continuous thermal extrusion of polysulfones can be achieved, the high temperature-induced thermal gradient can lead to weak interfacial bonding strength between the paths. As a result, the MEX-produced PSU has a tensile strength of around 52 MPa and a Young's modulus of 2.1 GPa in the printing plane (X-Y plane) according to 3DXTECH, which are significantly lower than injection molded PSU (70 MPa tensile strength and 2.48 GPa Young's modulus according to Udel® PSU). Moreover, the MEX-produced PPSU has a tensile strength of around 55 MPa and Young's modulus of 2.1–2.3 GPa in the X-Y plane according to 3DXTECH and Stratasys, which are also lower than injection molded PPSU (84 MPa tensile strength and 2.65 GPa Young's modulus according to Radel® PPSU). Solvent cast 3D printing has been attempted on PSU and PSU-based composites, but internal pores (pore size ranges from 0.3 to 2.8 μm) existed throughout the printed samples due to the rapid evaporation of solvents, implying unsatisfying mechanical properties [8]. On the other hand, research about processing fine powders for PBF made of polysulfones was done by Mys et al. [96], but to date, no polysulfone family powder has yet been used in the PBF process. It should be noted that the efforts of PBF on sulfur-containing polymers are mainly focused on PPS, a semi-crystalline polymeric sulfide with lower heat resistance to the polysulfone family, but is easier to process [97].

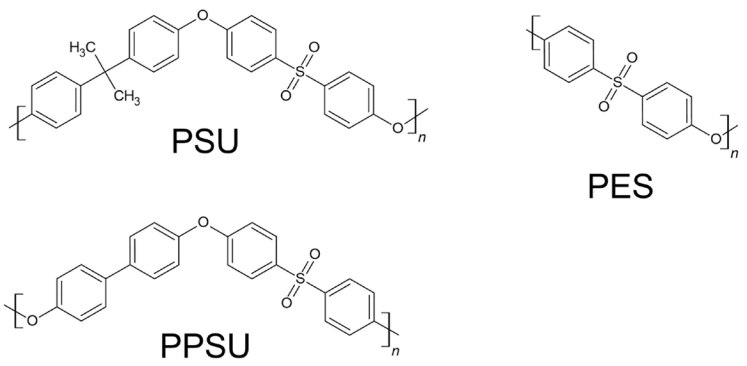

Figure 1.9. Chemical structure repeating units of the polysulfone family.

PAEKs are another important family of high-temperature polymers that attract the most interest in high-performance AM polymers due to their semi-crystallinity and good processability. They are aromatic polymers with alternating ketone and ether groups on their backbone (Figure 1.10). Their tunable crystallinity can lead to tailorable melt rheology and mechanical properties. The crystalline region in PAEKs restricts the polymer chain movements even above T_g, making them suitable for use between T_g and T_m [98]. Unlike the AM of the polysulfone family, which is currently limited to MEX, both MEX and PBF can be applied to PAEKs. MEX filaments based on PAEKs are provided by multiple companies, like 3DXTECH, JUNHUA, and INTAMSYS, among which PEEK is the most popular type. Neat PEEK produced by injection molding has excellent mechanical properties, including 98 MPa tensile strength, 4.0 GPa Young's modulus, and 45% elongation at break, according to the Victrex 450G datasheet. For MEX of PEEK, a nozzle temperature around 380–420 °C is typically required for continuous extrusion of PEEK filament. As for the trials of using MEX to produce PEEK in the literature, Rahman and Reese fabricated PEEK specimens made of Arevo Labs' PEEK, which resulted in 2.6–2.8 GPa Young's modulus and 54–73 MPa tensile strength (varies based on the printing angle), lower than the injection molded PEEK [21]. Yang et al. studied the effect of different thermal processing conditions on the mechanical properties of the MEX-produced PEEK made of Victrex 450G and found that using a 200 °C annealing process could improve the Young's modulus from 3.2 to 3.9 GPa, and the tensile strength from 73 to 82 MPa [99]. Tseng et al. demonstrated screw extrusion-based MEX of PEEK 90G using a 390 °C nozzle temperature and achieved the highest Young's modulus of 4.13 GPa and tensile strength of 94.7 MPa comparable to the injection molded PEEK 90G, but the elongation at break is below 3%, significantly lower than the injection molded specimens (20%) [100]. However, they also showed that the stiffness and brittleness of PEEK

produced by MEX were due to the almost 40% degree of crystallinity, which was much higher than that of the injection molded PEEK (20.8%). Another problem of MEX of semi-crystalline PEEK is the shrinkage during crystallization. The considerable shrinkage can cause significant warping and eventually the detachment of the printed structure from the building platform. Therefore, using MEX to produce PEEK with a stable printing process and comparable mechanical properties of injection-molded PEEK is still challenging.

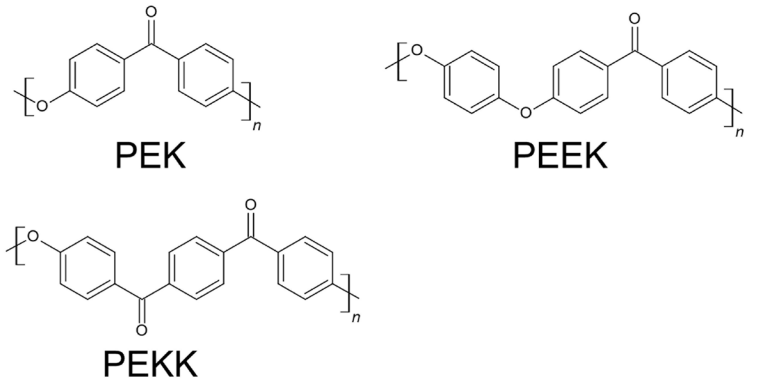

Figure 1.10. Chemical structure repeating units of the PAEK family.

On the other hand, PBF has been widely used to produce 3D PAEK structures since fine PAEK powders are commercially available from EOS (HP3 PEK and PEKK 100) and Victrex (450PF and 150PF). Berretta et al. studied the PBF process for PEK and PEEK and compared their properties to injection-molded PEK [101]. Their results showed that PBF-produced PEK had a tensile strength of 88 MPa and PEEK had a tensile strength of 63 MPa, both lower than the injection molded PEK (98 MPa), but the PBF process increased the crystallinity of PEK and PEEK by more than 15%. Yi et al. prepared new grades of PEEK by modifying the backbone of PEEK and compared their mechanical properties with standard PAEK powders processed through PBF [102]. While specimens made of common PEK (HP3) and PEEK (450PF) showed comparable Young's modulus but decreased tensile strength and elongation at break compared to the injection-molded PEK and PEEK, specimens made of their modified PEEK powder showed significantly improved elongation at break (up to 13.6%) over standard PAEK powders with slight reduction in Young's modulus and tensile strength. PBF-produced PAEKs generally have a higher degree of crystallinity and more brittle mechanical behavior than injection-molded ones due to the incomplete melting of the crystalline region by rapid laser heating and slower cooling for more crystallization in PBF [102]. Future modification of the PAEK composition is needed to develop optimized PAEK powder for the PBF process.

PEI is a high-performance amorphous polymer with a famous trade name, Ultem®, popular in the MEX industry. Chuang et al. tested the mechanical properties of Ultem® 9085 produced by MEX using a 375 °C nozzle, which had a 2.2 GPa Young's modulus and a 72 MPa tensile strength, compared to the injection molded specimens with a 3.4 GPa Young's modulus and an 83 MPa tensile strength [22]. Gardber reported an 89 MPa tensile strength of MEX-fabricated Ultem® 1010, further reinforced by their carbon nanotube yarn (4.7 wt%) to achieve a tensile strength of 112 MPa [103]. Other researchers also performed extensive characterization of MEX-produced Ultem® parts and found up to 80%–85% mechanical properties relative to the injection molded specimens could be realized through MEX [104,105]. Like the amorphous polysulfones, PBF of PEI has not been achieved yet, possibly due to the high viscosity above T_g that restricts particle coalescence.

TPI has the highest heat resistance among all high-performance polymers available in the current AM market (T_g = 249 °C). Depending on the formulation, it can be either amorphous or semi-crystalline. Commercially available amorphous TPI filament for MEX is from 3DXTECH, based on SABIC EXTEM™ TPI, which requires an extremely high nozzle temperature of 445 °C and a chamber temperature of 225 °C. In the literature, Ye et al. used semi-crystalline TPI (AURUM PL450C) for MEX with a nozzle temperature of 388 °C (at T_m), and the resulting TPI specimens had a tensile strength of 66.7 MPa and a flexural strength of 97.9 MPa [106]. However, cross-section images of the TPI specimens showed many voids between infill lines due to the fast cooling of deposited TPI after extrusion. Besides MEX, AM of photocurable TPI for vat photopolymerization was also attempted by researchers. Hegde et al. synthesized soluble poly(amic ester)s with acrylate groups for photocuring in the vat photopolymerization process, followed by a solvent removal and thermal imidization process up to 350 °C [107]. During the imidization process, the initial crosslinks decomposed, resulting in a TPI chemical structure. The imidized final TPI structures had a dimensional contraction of 53%, and they exhibited 2.2 GPa Young's modulus, 80 MPa tensile strength, and around 380 °C T_g. Other research on DIW or UV-DIW of thermosetting PI also proved the feasibility of using the two-step process (AM plus subsequent imidization) to produce 3D PI structures [108,109].

In conclusion, the current challenges in AM of high-performance polymers include strict processing temperature requirements, undesired voids (between printing lines for MEX and between particles for PBF) induced reduction in mechanical properties, thermal gradient-induced

weak interfacial bonding, and heating/cooling rate-related crystallinity change. Moreover, the AM of some high-performance polymers, such as aramid, has not been attempted and studied. Existing AM processes and materials must be modified to overcome these challenges, and novel AM processes can be developed for high-performance polymers.

1.4 Piezoelectric polymers

Piezoelectric materials have an electromechanical coupling effect, in which mechanical stress applied to the material results in the accumulation of electric charge (ΔQ) (direct piezoelectric effect, Figure 1.11). Conversely, using an electric field on the piezoelectric material can generate a mechanical strain as deformation (Figure 1.11). This electromechanical coupling is essential for the electronic industry, where force/strain sensors and energy harvesters are designed based on the direct piezoelectric effect, and actuators used in speakers, laser mirror systems, diesel engines, and atomic force microscopes are manufactured based on the converse piezoelectric effect [110]. For ferroelectric-type piezoelectric materials, electric field poling is the crucial step to align dipoles following the external field direction, leading to apparent piezoelectricity.

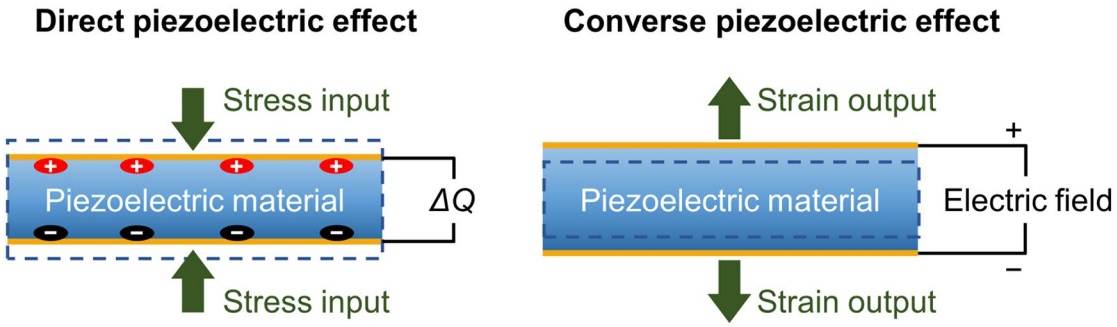

Figure 1.11. Direct and converse piezoelectric effects.

For polymers, piezoelectricity is common in fluoropolymers, polyureas, polyamides, polypeptides, polysaccharides, polyesters, and some biopolymers such as collagen and cellulose [111–113]. However, most piezoelectric polymers only possess piezoelectricity at the molecule level, which commonly results in zero apparent bulk piezoelectricity due to the random orientation of dipoles in bulk materials. Thus, aligning the dipoles in bulk materials is crucial to utilizing the apparent piezoelectricity. Among all piezoelectric polymers, only some fluoropolymers like poly(vinylidene fluoride) and polyamides such as odd-numbered nylons [114–116] display ferroelectricity, which means their dipoles can be aligned by applying external electric fields.

1.4.1 Poly(vinylidene fluoride)

Poly(vinylidene fluoride) (PVDF) is a widely studied and used piezoelectric polymer since its discovery in 1969 because of its outstanding piezoelectric and ferroelectric properties amongst all polymers [117–119]. The strong electronegativity of the fluorine atoms relative to hydrogen and carbon atoms forms a strong electric dipole in each repeating unit within the PVDF monomer chain, which provides the basis of ferroelectricity [120,121]. Compared to piezoelectric ceramics such as lead zirconate titanate (PZT), polymeric PVDF has higher flexibility, higher piezoelectric voltage constants (g_{31} and g_{33}), lower density, and nontoxicity. As a semi-crystalline polymer, PVDF has multiple crystalline phases, α, β, γ, δ, and ε, resulting from the different chain conformations. The typical α phase has a TGTG' conformation (T: trans, G: gauche) that is non-polar, and its polar counterpart δ phase is rarely observed unless induced by high electric fields [122]. The γ phase has a T_3GT_3G' conformation that is polar, while its nonpolar form, ε phase, is again uncommon [123]. The highest polarity phase is the β phase, which has a TTT conformation with all dipoles aligned in the monomer chain, making it the best piezoelectric phase among all other crystalline phases [124]. In summary, the chain conformation of the three typical phases of PVDF is shown in Figure 1.12. Maximizing the β phase content in the PVDF polymer is essential to improve the piezoelectric performance of PVDF. Unfortunately, the β phase with a high permanent dipole moment in the chain is thermodynamically unfavorable, which means typical crystallization of PVDF from melt or solvent evaporation only results in a non-polar α phase or less polar γ phase [125]. Therefore, a great deal of research has been done to promote the β phase content in PVDF through process and chemical modification.

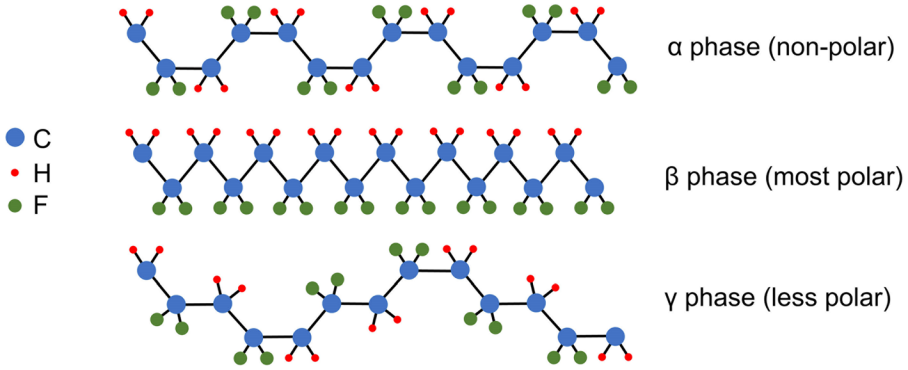

Figure 1.12. Typical crystalline phases in PVDF.

Mechanical drawing or stretching is the most common process to promote the β phase content in PVDF. Matsushige et al. found that at 75 °C, the α to β phase transformation happened

above the necking point during uniaxial drawing [126]. Vijayakumar et al. studied the effect of draw ratio and temperature on the α to β phase transformation, and found that at draw ratio = 4 and 65 °C, the highest β phase fraction obtained was 0.98 [127]. They also observed that the phase transformation was due to the deformation of the spherulitic structure under drawing. Elevated temperature electric poling can also induce α to β phase transformation, shown by Ye et al. [128], using a field strength of 150 $MV \cdot m^{-1}$ at 95 °C. Solvent casting of PVDF solution using polar solvents at low temperatures can lead to the formation of γ phase, and Satapathy et al. showed subsequent annealing at 90 °C for 5 h could transform γ phase to β phase [129]. Phase inversion of PVDF cast solution in a low-temperature water coagulation bath can also result in β phase dominant PVDF [130–132]. In particular, Tao et al. discovered that using a weaker polar solvent (hexamethylphosphoramide, HMPA, in this case) for PVDF in the phase inversion process had better β phase promotion [133]. Regardless of the processing method, the piezoelectric charge coefficient d_{33} for neat β phase PVDF is around $-30\ pC \cdot N^{-1}$ [128,130,134,135], while the highest reported value is $-62\ pC \cdot N^{-1}$ [136].

Chemical modification of PVDF results in several PVDF copolymers with better β phase content during crystallization. Copolymerization of 60–80 mol% vinylidene fluoride (VDF) with trifluoroethylene (TrFE) can produce P(VDF-TrFE), which can spontaneously crystallize into β phase [137]. It exhibits a ferroelectric to paraelectric transition Curie temperature from 60 to 140 °C, depending on the VDF content. The highest reported d_{33} for P(VDF-TrFE) is $-63.5\ pC \cdot N^{-1}$ from a 50 mol% VDF composition [138]. Polymerization of VDF, TrFE, and chlorotrifluoroethylene (CTFE) to form a P(VDF-TrFE-CTFE) terpolymer with more than 7 mol% CTFE can produce a ferroelectric relaxor phase [139]. However, with a low CTFE mol% (below 5 mol%), Han et al. discovered that the P(VDF-TrFE-CTFE) terpolymer had mixed ferroelectric and relaxor phases, which resulted in enhanced piezoelectric charge coefficient (d_{33} of $-55.4\ pC \cdot N^{-1}$) due to the introduced CTFE as a structural defect [140].

1.4.2 Additive manufacturing of poly(vinylidene fluoride)

Although most existing research on piezoelectric PVDF focuses on spin-coated, solvent-cast, or extruded thin films, using MEX, material jetting, or vat photopolymerization-based AM processes to fabricate piezoelectric PVDF devices with complex geometries has received significant interest from researchers. Multi-material AM processes can also produce piezoelectric

devices with conductive electrodes in one step. However, as mentioned before, neat β phase PVDF is not thermodynamically favorable, indicating that PVDF structures produced by MEX are α phase dominant. Thus, researchers developed MEX with in-situ electric field poling to promote β phase and dipole alignment (Figure 1.13A). Lee and Tarbutton [141], Porter et al. [142] and Kim et al. [143] used a similar setup for MEX by applying a high voltage (kV level) between the heated metal nozzle and the metal printing platform, and the metal platform was covered with insulating Kapton® tape to avoid shorting. The printed PVDF with in-situ poling showed improvement of β phase content compared to directly printed PVDF, but the conversion from α phase to β phase was below 60%, and the d_{31} coefficients were measured to be 1.19 $pC \cdot N^{-1}$ and 0.048 $pC \cdot N^{-1}$ by Porter et al. [142] and Kim et al. [143], respectively. More recently, a corona poling-assisted MEX process was developed by Fan et al. [144], which improved the d_{33} coefficient from −0.7 to −1.1 $pC \cdot N^{-1}$. In addition, Bodkhe et al. combined solvent cast 3D printing of PVDF with in-situ poling, and produced piezoelectric PVDF and PVDF/$BaTiO_3$ nanocomposites for pressure sensing (Figure 1.13B) [65,145]. However, they discovered that in-situ poling decreased the β phase content for the solvent cast 3D printing process. Moreover, adding nanoparticles in PVDF to form nanocomposites can produce PVDF with high β phase content, based on the interaction between the PVDF chain and nanoparticles for preferred dipole orientation [146,147]. Pei et al. used a PVDF/tetraphenylphosphonium chloride (TPPC) nanocomposite filament for MEX and promoted the β/γ phase content to 83.8% and a d_{33} coefficient of −1.85 $pC \cdot N^{-1}$ due to the ion-dipole interaction between the positively charged TPPC and PVDF's CH_2-CF_2 dipoles [148]. Similarly, Liu et al. used ionic liquid (1-ethyl-3-methylimidazolium tetrafluoroborate) to assist the formation of more than 93% β phase during MEX and successfully fabricated piezoelectric energy harvesters based on this method [149]. The main drawback of this method is the significantly increased dielectric loss due to the existence of ionic particles or liquids, which has a detrimental effect on the piezoelectric output. On the other hand, AM of P(VDF-TrFE) can result in higher β phase content than neat PVDF due to the more steric effects induced by adding TrFE. Material jetting of P(VDF-TrFE) solution was demonstrated by Haque et al., which had outstanding β phase content up to 92.8% [150]. DIW of P(VDF-TrFE) solution was studied by Spanou et al. [151] and Shepelin et al. [152], and the results also showed significant β phase content of more than 80%. However, P(VDF-TrFE) is a much more expensive material than neat PVDF, limiting its potential

application in the industry. Therefore, using AM to produce neat PVDF with high β phase content is still challenging.

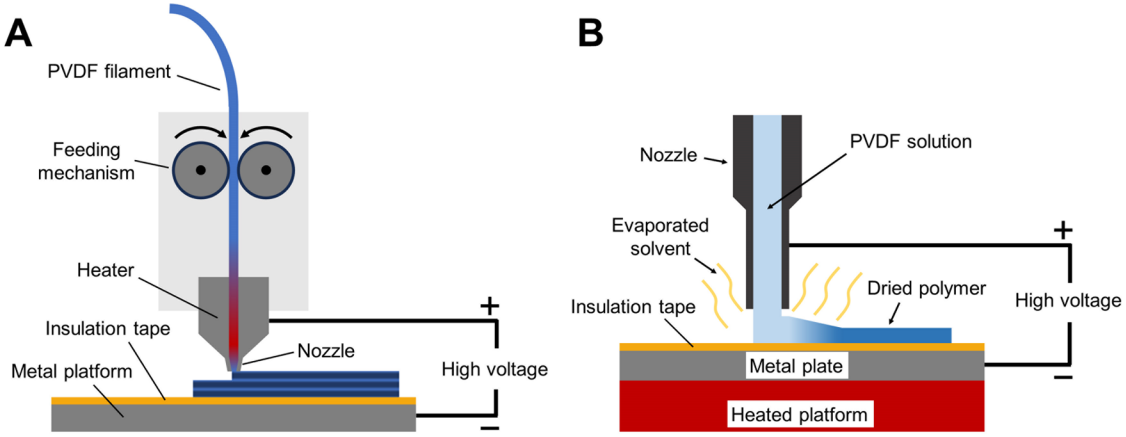

Figure 1.13. AM of PVDF with in-situ poling. A) MEX with in-situ poling. B) Solvent cast 3D printing with in-situ poling.

1.4.3 Piezoelectric polymer composites

Piezoelectric polymer composites are a type of composites consisting of a polymer matrix and piezoelectric fillers, typically piezoceramic particles, to overcome the brittleness of piezoceramics. Many piezoceramics have been produced as micro or nano particles, nanorods or nanowires, such as lead zirconium titanate (PZT), barium titanate ($BaTiO_3$), lead titanate ($PbTiO_3$), $Pb(Mg_{1/3}Nb_{2/3})O_3$-$PbTiO_3$ (PMN-PT) and $(K,Na)NbO_3$ (KNN), to be integrated into polymer matrices to form polymer composites or nanocomposites. Zhou et al. developed a scalable approach to synthesize PZT nanowires, which could be embedded into polydimethylsiloxane (PDMS) to form bending mode energy harvesters with a power density of 2.4 $\mu W \cdot cm^{-3}$ [153]. Lead-free $BaTiO_3$ and KNN nanoparticles and nanowires were integrated into nanocellulose [154], PEI [155], PLA [156], PI [157], and PDMS [158] to form eco-friendly piezoelectric devices. High piezoelectric coefficient piezoceramics like PMN-PT were combined with flexible polymer matrices to fabricate piezoelectric energy harvesters [159–161]. High-temperature energy harvesting was also realized in our group's previous work by using aligned $PbTiO_3$ nanowires distributed in a PAI matrix, which could be used at 200 °C for at least 100 h while producing 20 $\mu W \cdot m^{-2}$ areal power density under random vibration [162]. Compared to PVDF, piezoelectric polymer composites require no stretching and lower electric field for poling, but generally have lower piezoelectric coefficients than PVDF and its copolymers.

1.4.4 Additive manufacturing of piezoelectric polymer composites

AM of piezoceramics is challenging because they are brittle and difficult to process. Current AM processes for piezoceramics are binder jetting, vat photopolymerization, and DIW, all of which use a sacrificial polymer before ceramic sintering [163–165]. However, the AM of piezoelectric polymer composites attracts more research interest due to the better processability and flexibility after adding a polymer matrix. For example, MEX is a popular process to fabricate piezoelectric composites using customized composite filaments. Castles et al. produced 50 wt% $BaTiO_3$/ABS composite filaments for MEX and showed robustness and reproducibility in producing 3D $BaTiO_3$/ABS structures using MEX [166]. Dual material MEX of a TPU/30vol% PZT filament and a conductive TPU/carbon black filament was achieved by Tao et al., which could produce flexible piezoelectric nanocomposites with d_{33} up to 5.52 $pC \cdot N^{-1}$ [167]. DIW is another widely used AM process for functional materials and composite materials. Moreover, our group's previous works demonstrated that shear stress during the DIW process could align high aspect ratio piezoelectric nanowires in the printing direction (Figure 1.14), which could further improve the piezoelectric properties in the preferred direction [156,162]. Dual material DIW of a $BaTiO_3$/PDMS piezoelectric ink and a conductive MWCNTs/PDMS ink were achieved by Renteria et al. to fabricate flexible force sensors, where a d_{33} of 11.5 $pC \cdot N^{-1}$ was obtained by using the 50 wt% $BaTiO_3$/PDMS nanocomposites [168]. Vat photopolymerization enables the fabrication of piezoelectric polymer composites with complex lattice geometries, such as the PZT-based nanocomposite by Yao et al. [169] and $BaTiO_3$/polyethylene glycol diacrylate (PEGDA) nanocomposites by Kim et al. [170]. Even though various processes have enabled AM of piezoelectric polymer composites, improving the piezoelectric properties of printed composites to match these of piezoelectric nanocomposite thin films and commercial PVDF films is still challenging.

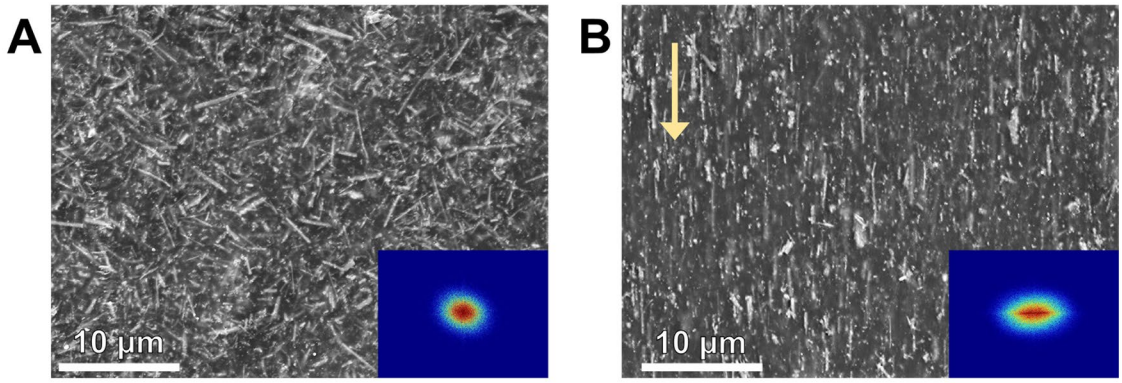

Figure 1.14. A) SEM image and fast Fourier transform (FFT) power spectrum of a cast nanocomposite film. B) SEM image and FFT power spectrum of a DIW nanocomposite film (arrow indicates the DIW direction).

1.4.5 Stretchable piezoelectric polymers and polymer composites for sensing

Stretchable piezoelectric stress/strain sensing materials have gained substantial research interest over the past decade due to the development of wearable electronics for biomedical applications [171,172], biomechanical study [173], motion capture technology, and soft robotics [174]. Compared to piezoresistive materials, piezoelectric materials have excellent sensing linearity, ultralow response time, and no intrinsic power consumption, which are suitable for dynamic sensing applications. However, since most piezoelectric materials are nearly inextensible (elongation<10%), many research studies on stretchable piezoelectric devices focus on pattern design that can improve the device stretchability by using meshes [175], wavy shapes [176,177], serpentine interconnects [178,179] and kirigami designs [180,181]. For example, Duan et al. used DIW of PVDF fiber on pre-stretched PDMS to produce in-plane wavy piezoelectric structures that could measure in-plane deformation up to 110% strain [177]. Ji and Zhang showed a serpentine patterned PVDF sensor with stretchability up to 35%, and a voltage sensitivity of 0.97 $mV \cdot \mu\varepsilon^{-1}$ that could monitor respiratory and heartbeat signals in real-time [179]. Kim et al. developed piezoelectric strain sensors with stretchability up to 320% based on kirigami designs, which were demonstrated on virtual reality haptic gloves for finger motion sensing [180]. Although creative pattern design allows for high device stretchability using inextensible piezoelectric materials, complex geometries also cause limitations such as calibration difficulty, high strain rate dependence, and short fatigue life at the joints.

Developing new piezoelectric materials with intrinsic stretchability is the other approach for stretchable piezoelectric sensors, which can be combined with smart pattern designs to further boost the device's stretchability. The primary type of stretchable piezoelectric materials are

nanocomposites that consist of piezoelectric nanofillers and an elastomer matrix [167,168,182–185]. Chou et al. mixed 65 vol% PZT particles into silicone rubber and showed that the nanocomposite had a high open-circuit voltage output of 20 V and up to 200% stretchability, allowing it to be used for energy harvesters or stretchable load sensors [186]. Similarly, Quinsaat et al. developed elastic piezoelectric nanocomposites of 38 vol% PZT in a PDMS matrix with d_{33} = 3.6 pC·N^{-1}, d_{31} = −30 pC·N^{-1} and a strain at break of 254%, which was used as a compression detection sensor [187]. Although nanocomposites with piezoelectric ceramic fillers generally have high voltage outputs, poor sensing performance under high strain (>50%) can be expected due to the significant difference in modulus between the matrix and filler, which results in low stress transfer efficiency, slip and interfacial failure. Another type of stretchable piezoelectric material is sandwich composites, which contain a piezoelectric center layer sandwiched by two elastomer shell layers. Electrospun PVDF and its copolymer P(VDF-TrFE) are popular piezoelectric layer materials for the sandwich composite due to their convenient self-polarized electrospinning process [188]. Thus, researchers have developed flexible sandwich composites of electrospun P(VDF-TrFE) embedded in PDMS for high-resolution pressure sensing applications [189,190]. However, most PVDF-based sandwich composites have limited stretchability (~30%) and cannot be used in applications that require large extension (strain>50%).

Besides nanocomposites, polymer blends containing the polar β phase PVDF have been widely studied as piezoelectric films and nanofibers, such as PVDF/PMMA [191–193], PVDF/polyvinyl alcohol (PVA) [194], PVDF/TPU [195] and PVDF/photopolymers [196]. Polymer blending β phase PVDF and another elastomer can be an alternative approach to produce novel intrinsically stretchable piezoelectric materials. A polar elastomer, such as polar acrylonitrile butadiene rubber (NBR), has been shown to form a compatible polymer blend with PVDF, while vulcanization of the NBR phase can further stabilize blend morphology and improve interfacial bonding between phases [197,198]. The NBR rich PVDF/NBR blends exhibit outstanding elongation at break of more than 300% [198]. Therefore, the potential of using PVDF/NBR polymer blend as a highly stretchable (strain>50%) piezoelectric material for dynamic sensing should be explored.

1.5 Fundamentals of precipitation printing

In this dissertation, precipitation printing is developed as a novel solvent-based AM process for the above-mentioned high-performance engineering and piezoelectric polymers with tailorable microstructure and porosity. In this section, the fundamental concepts used in the proposed presentation printing process are briefly explained.

1.5.1 Hansen solubility parameters

As a solvent-based AM process, solvent selection for the target polymer is the first step of precipitation printing. Hansen solubility parameters are widely used in industries as a guide to predict material solubility in solvents [199]. According to the theory of Hansen solubility sphere, three parameters, dispersion solubility parameter δ_d, polar solubility parameter δ_p, and hydrogen bonding solubility parameter δ_h form a three-dimensional space to determine the solubility of a polymer in different solvents [199,200]. The distance (R_a) between the polymer coordinates (δ_{d1}, δ_{p1}, δ_{h1}) and the solvent coordinates (δ_{d2}, δ_{p2}, δ_{h2}) is given by Equation 1.1.

$$R_a^2 = 4(\delta_{d2} - \delta_{d1})^2 + \left(\delta_{p2} - \delta_{p1}\right)^2 + (\delta_{h2} - \delta_{h1})^2 \quad (1.1)$$

For each polymer, it has an experimentally determined solubility radius, R_0. A relative energy difference (RED) is defined as the ratio R_a/R_0. By convention, solvents with RED less than one can likely dissolve the polymer, and a lower RED indicates better solubility. On the other hand, solvents with RED more than one are generally considered non-solvents for the target polymer.

1.5.2 Non-solvent induced phase separation

During the precipitation printing process, the mutual diffusion between the solvent and non-solvent can lead to a phenomenon called non-solvent induced phase separation (NIPS), or phase inversion. This mechanism has been studied in the porous polymeric membrane fabrication process, where a cast polymer solution on a substrate is immersed in a non-solvent bath to form a thin membrane [11,12,133,201,202]. Polymer/solvent/non-solvent ternary phase diagrams can be used to illustrate the NIPS process, and Figure 1.15 presents a typical ternary phase diagram. In Figure 1.15, a binodal curve is the limit where phase separation is thermodynamically favorable, and a spinodal curve is the limit for unstable phase separation (spinodal decomposition). The region on the left side of the binodal curve is a single-phase stable region, where the polymer is either in the form of a solid or a homogenous solution. The region between the binodal and spinodal

curves is the metastable region, where liquid-liquid demixing occurs and results in the separation of polymer-lean and polymer-rich phases. On the right side of the spinodal curve is the unstable region, where the polymer precipitates out as a separate phase. It should be noted that the positions of the binodal and spinodal curves can be experimentally determined (cloud points), but in this dissertation no direct cloud point measurements were performed. All ternary phase diagrams used in this dissertation are illustrations to explain the printing solution phase separation progress based on the observed microstructure in SEM images. Three dashed arrows indicate the three possible evolution paths of a printing solution during the wet spinning or precipitation printing process. They start on the polymer-solvent edge as a homogeneous solution and evolve towards the right. The direction of the evolution path depends on the diffusion rate between the solvent and non-solvent. A faster diffusion of the solvent into non-solvent than the diffusion of the non-solvent into non-solvent leads to an upward evolution path to the right. Therefore, the red evolution path means a rapid spinodal decomposition, the blue evolution path indicates a metastable liquid-liquid demixing process, and the green evolution path presents a single-phase gelation process.

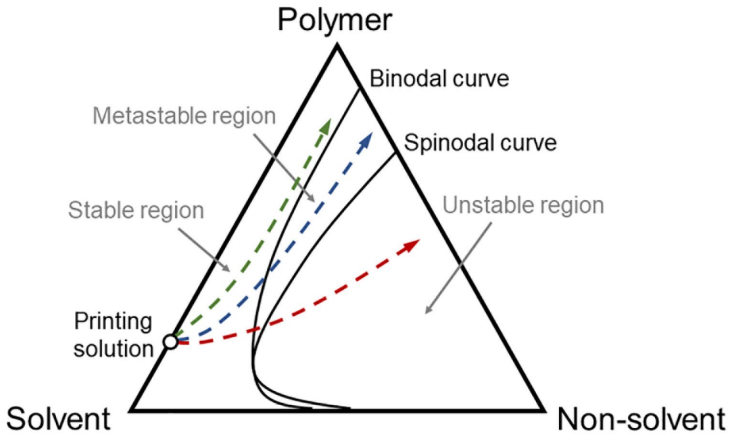

Figure 1.15. A typical ternary phase diagram. Different possible evolution paths are as follows. Red: spinodal decomposition. Blue: Metastable liquid-liquid demixing process. Green: single-phase gelation process.

1.5.3 Solvent welding

In a solvent-based AM process, solvent welding, or solvent cementing, is the main mechanism for interlayer bonding. In a solvent welding process, the solvent softens the surface of a thermoplastic part, allowing an increased mobility of polymer chains. When two thermoplastic parts softened by the solvent are pressed together, polymer chain diffusion between the parts results in a single piece of welded thermoplastic after the complete evaporation of the solvent [203,204]. The quality of solvent welding depends on the solvent power to dissolve the

thermoplastic and the rate of solvent evaporation. During precipitation printing when the solvent is used in a non-solvent bath, instead of solvent evaporation, the solvent diffuses into the non-solvent bath. Thus, the quality of solvent welding in a non-solvent bath depends on the solvent power to dissolve the thermoplastic and the rate of solvent diffusion into the non-solvent.

1.6 Dissertation overview

In this section, an overview description of the research in each of the upcoming chapters is provided as follows.

Chapter 2 introduces the concept of precipitation printing, a novel solvent-based AM process for polymers, polymer blends, and polymer nanocomposites, and provides a detailed setup of the precipitation printing process. Like other solvent-based AM processes, thermoplastics or nanocomposites are dissolved or dispersed in a suitable solvent to form a printing solution or colloid for precipitation printing. After dispensing the printing solution in a non-solvent coagulation bath, the solidification process in precipitation printing is based on the mutual diffusion between the solvent and non-solvent and, eventually, the precipitation of the solute polymer in the non-solvent bath. Once printing is completed, the printed structures can be post-processed by drying to evaporate the residual solvent and non-solvent. In addition, with this novel mechanism for AM of polymers, the microstructure and porosity of the printed final structures can be tailored by controlling the printing conditions. Thus, in the later part of Chapter 2, the effect of solvent/non-solvent pairs, the effect of printing solution concentration, and the effect of non-solvent bath temperature on the microstructure and porosity tailoring using precipitation printing are studied based on two polymers: PMMA and PVDF.

Chapter 3 develops the application of precipitation printing in high-performance polymers. Specifically, amorphous thermoplastic PSU and highly crystalline para-aramid (Kevlar®) are used as two representatives for precipitation printing to demonstrate the capability of using this process to produce 3D structures made of high-performance polymers. In the case of PSU, by selecting different solvent/non-solvent pairs and using different PSU solution concentrations, the microstructure and porosity of the precipitation printed PSU can be tailored to be either highly porous or fully dense. Furthermore, the mechanical and thermal properties of the printed dense and porous PSU are characterized. In the second half of this chapter, additive manufacturing of all-aramid 3D structures is achieved for the first time through simultaneous precipitation printing

and protonation of an aramid nanofiber (ANF) colloid (printing ink). The ANF printing ink is prepared through a deprotonation and dissolution process of Kevlar® fabric using a potassium hydroxide (KOH)/dimethyl sulfoxide (DMSO)/water system. By precipitation printing the ANF printing ink in a propylene glycol (PG) bath, wet ANF structures can be obtained, which can be further washed and dried to induce ANF self-assembly and form all-aramid structures. Moreover, the dimensional contraction, mechanical and thermal properties of the resulting all-aramid structures are studied.

Chapter 4 focuses on the application of precipitation printing in piezoelectric PVDF. By dissolving PVDF in *N,N*-dimethylformamide (DMF), and precipitation printed in a water bath, porous PVDF with dominant β phase is obtained. The mechanism for β phase formation in this process is based on the hydrogen bonding between PVDF and water during precipitation printing. The phase composition of the resulting PVDF is characterized by multiple characterization techniques, including Fourier-transform infrared spectroscopy (FTIR), X-ray diffraction (XRD), and differential scanning calorimetry (DSC). The directly printed porous PVDF can be subsequently hot pressed for densification. After electric poling, the piezoelectric properties of the precipitation printed PVDF with and without hot pressing are measured. Finally, the applications of precipitation printed piezoelectric PVDF as energy harvesters and strain sensors are demonstrated.

Chapter 5 develops the last application of precipitation printing in producing stretchable PVDF-based piezoelectric sensors. Specifically, polymer blends of PVDF and acrylonitrile butadiene rubber (NBR) are formed using precipitation printing, where a solution of both PVDF and unvulcanized NBR dissolved in DMF is precipitated inside a water bath and solidified as a polymer blend that can be vulcanized by subsequent hot pressing. The PVDF phase in the resulting PVDF/NBR blends is still β phase dominant after phase characterization. In addition, the rapid liquid-solid phase separation at room temperature can produce a unique blend morphology, where the PVDF and NBR phases have submicron-level phase separation. After measuring the piezoelectric properties of the PVDF/NBR blends, they are used to fabricate stretching mode and compression mode piezoelectric sensors, which exhibit excellent dynamic strain/stress sensing performance under large strains, without strain/loading rate and pre-stretch dependence.

The final chapter of this dissertation starts with a brief overview of the detailed findings and achievements discussed throughout the dissertation. This overview is followed by the

contributions of this dissertation and their possible influence on future research in the field of additive manufacturing of high-performance and multifunctional polymers. Finally, a discussion of the potential future work to improve and expand the precipitation printing process is provided.

Chapter 2 Development and Study of Precipitation Printing

2.1 Chapter introduction

This chapter focuses on the development of precipitation printing and a systematic study of the parameters in the precipitation printing process [205]. The motivation of developing precipitation printing technique is to provide an additive manufacturing approach for polymers that are thermally unstable for the existing material extrusion method or require extremely high temperature for melting. Instead of using heat to melt thermoplastics to form processable liquid-state printing materials, the solvent-based precipitation printing technique utilizes solvent power to dissolve thermoplastics and form printing solutions. Unlike other solvent-based additive manufacturing methods such as solvent cast 3D printing [7,206] that require heat for solidification as the solvent evaporates, the solidification process in precipitation printing is based on the mutual diffusion between the solvent and non-solvent after dispensing the printing solution in a non-solvent coagulation bath, and eventually the precipitation of the polymer in the non-solvent bath. Thus, in this chapter, the mechanism of the precipitation printing process is proposed and explained in detail. In addition, with this novel mechanism for additive manufacturing, the microstructure and porosity of the printed final structures can be tailored by controlling the printing conditions. Both microporous foam-like structures and fully dense structures can be achieved using precipitation printing.

In the following section of this chapter, the setup of the precipitation printing process and the proposed printing mechanism are explained. Various polymeric materials are printed using this technique to demonstrate its capability of expanding the applicable polymers for additive manufacturing. In the last three sections of this chapter, the microstructure and porosity tailoring using precipitation printing is studied. In particular, the effect of solvent/non-solvent pairs, the effect of printing solution concentration and the effect of non-solvent bath temperature are investigated based on two polymers: poly(methyl methacrylate) (PMMA) and poly(vinylidene fluoride) (PVDF). Understanding the effects of precipitation printing conditions on the

microstructure and porosity is crucial to predict and control the properties of the prints in future applications.

2.2 Precipitation printing process and mechanism

2.2.1 Precipitation printing process and setup

Printing solution is a key component of the precipitation printing process. It is a homogeneous solution or a colloid consisting of a polymer dissolved in a solvent, or with additional fillers that are uniformly dispersed. To prepare the printing solution for a target material, a suitable solvent for the polymer is used to dissolve the polymer and disperse the filler in the case of polymer nanocomposites. The choice of solvent will therefore be dependent on the material to be printed, but common solvents such as acetone, *N,N*-dimethylformamide (DMF), dimethyl sulfoxide (DMSO), tetrahydrofuran (THF) and *N*-methyl-2-pyrrolidoneare (NMP) are generally used. The polymer is first dissolved in the solvent through a combination of shear mixing (FlackTek SpeedMixer) and bath sonication (Branson 2800) until a uniform solution is obtained. Any additional reinforcement or multifunctional fillers are added to the obtained solution by its weight ratio and uniformly dispersed using an ultrasonic homogenizer (Model 500, Fisher Scientific). The printing solution is then loaded into a 10 mL syringe (Nordson EFD) with a stainless-steel nozzle (inner diameter varies based on the desired printing resolution). The syringe is connected to a high-precision dispensing system (Ultimus V, Nordson EFD) so that the printing solution dispensing pressure is controlled during the precipitation printing process. The syringe is also fixed onto a gantry system (AGS1500, Aerotech) which controls the printing movement by G-code (Figure 2.1).

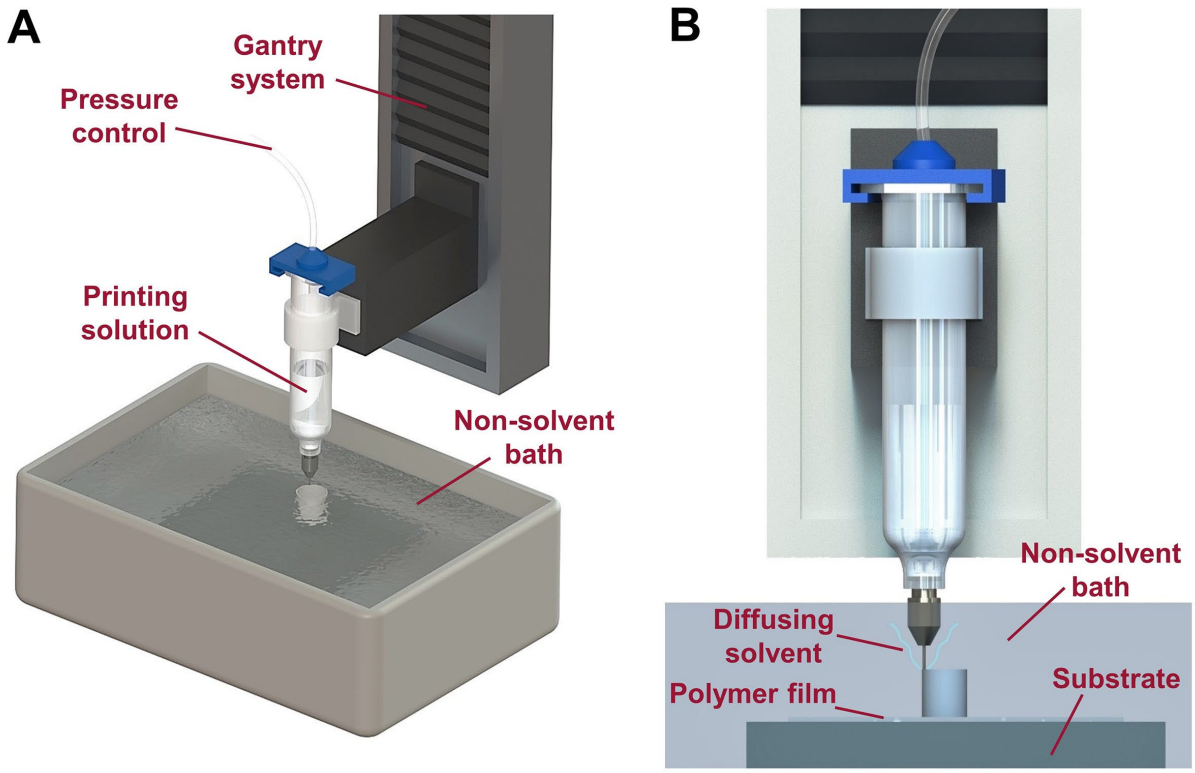

Figure 2.1. A) 3D view of the precipitation printing setup. B) 2D side view of the precipitation printing process.

A non-solvent for the precipitation printing process is selected such that the solvent in the printing solution is miscible and the polymer to be printed has limited or no solubility in it. A glass pan containing the non-solvent serves as the coagulation bath for precipitation printing. Due to the relatively large amount of non-solvent used in this process, low-cost and non-toxic liquids such as water and propylene glycol (PG) are generally used, although other liquids like isopropanol (IPA) and 1-butanol can also be used for particular materials. For one target polymer to be printed, multiple solvent/non-solvent pairs can be selected to produce structures with different microstructure, and the effect of solvent/non-solvent pairs will be studied in Chapter 2.3.

The printing substrate consists of a glass plate and a surface film layer of the polymer to be printed (Figure 2.1). The thin polymer film layer is prepared by doctor-blade casting of the printing solution and subsequent drying on a hot plate to evaporate the solvent. By using this thin polymer layer, precipitation printed structures have strong adhesion to the printing substrate by solvent welding. To prevent the printed structure from sticking irreversibly to the initial film layer, the first two layers of all prints are printed as low infill percentage raft layers. Once precipitation printing is complete, prints are left in the non-solvent bath for an hour to allow any left solvent to diffuse out of the polymer. Finally, printed structures are taken out of the bath with their raft layers

removed and dried overnight (Figure 2.2). The specific drying temperatures for different materials are listed in the following sections.

The precipitation printing process is unique compared to other additive manufacturing processes for polymers. Unlike the most common material extrusion method (also known as fused deposition modeling, FDM) that requires a nozzle temperature higher than the polymer melting point, the solvent-based precipitation printing process can be achieved at room temperature, or at slightly elevated temperatures (typically below 50 °C) for a faster diffusion rate. The post-processing temperature for precipitation printed structures is typically 80–120 °C, with some exceptions up to 250 °C for high-temperature materials such as para-aramid. When compared to solvent-cast 3D printing which has thermal stress and solvent evaporation-induced contraction during printing [7], precipitation printing allows for better dimensional stability and less warping during the printing process. In addition, when compared to direct ink writing (DIW) [9,69,71], which has strict rheological requirements on the printing solution such as shear thinning and storage modulus higher than loss modulus at low shear rates, precipitation printing does not have such requirements since the non-solvent induced gelation can provide the structural stability of precipitation printed polymers.

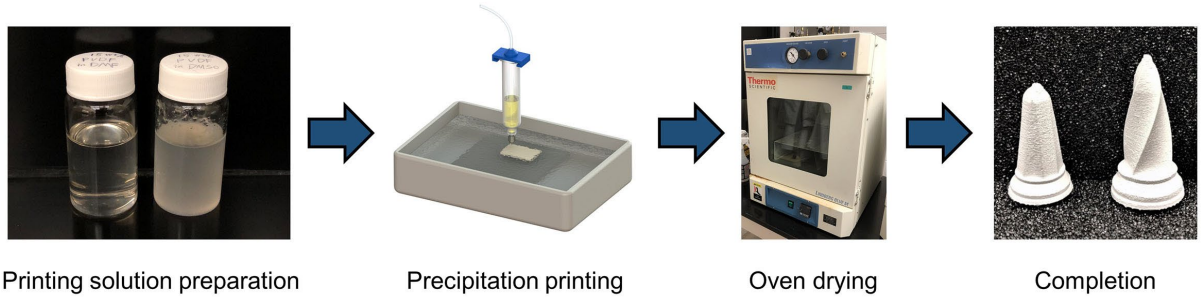

Figure 2.2. Steps of the precipitation printing process to obtain final structures.

2.2.2 Precipitation printing mechanism

The mechanism of precipitation printing is based on the different solubility of the polymer or polymer composites in two mutually miscible solvents. When the polymer solution is dispensed in a non-solvent bath, the mutual diffusion between the solvent and non-solvent leads to a rapid increase of the polymer solution concentration and a reduction of the polymer solubility, which results in phase separation and precipitation of the polymer. This mechanism has been previously studied in the literature as the non-solvent induced phase separation (NIPS) for membrane formation [11,12,201,207]. Depending on the solvent and non-solvent types and precipitation

printing conditions such as temperature, the NIPS process can take different paths including single-phase gelation, liquid-liquid demixing and spinodal decomposition (solid precipitation) [11], which controls the final microstructure and porosity of precipitation printed materials. Polymer/solvent/non-solvent ternary phase diagrams will be used to explain the microstructure formation in the following sections [208].

Interfacial bonding between infill paths and interlayer bonding in the precipitation printing process is based on the solvent welding mechanism for thermoplastics [204,209,210]. The solvent in the printing solution can partially dissolve and swell the adjacent infill path and the layer beneath, providing a local region with fast polymer diffusion to mix the newly deposited polymer solution and the previously printed paths or layers for joining. Since the solvent welding process takes place at the same time as the solvent diffuses into the non-solvent, the solvent welding rate must be faster than the solvent diffusion rate into the non-solvent to ensure a sufficient interfacial bonding strength.

The post-processing step of precipitation printed structures is a thermal-induced drying process to evaporate trapped non-solvent and residual solvent. If there is residual solvent inside a printed structure, solvent evaporation will typically result in a dimensional contraction of the structure after complete drying.

In the following three sections of this chapter, the microstructure and porosity tailoring of precipitation printed structures are studied on two thermoplastic polymers: PMMA and PVDF. PMMA represents an amorphous thermoplastic that has a glass transition temperature (T_g) of 100 °C (according to the storage modulus curve from dynamic mechanical analysis), which is in the glassy state at room temperature. PVDF represents a semi-crystalline thermoplastic that has a T_g of −41 °C and a crystalline melting temperature between 160–170 °C [211]. The effect of solvent/non-solvent pairs, printing solution concentration and non-solvent bath temperature are investigated for the precipitation printing of PMMA and PVDF.

2.2.3 Precipitation printed representative materials

Precipitation printing can be applied to various thermoplastic materials such as acrylonitrile butadiene styrene (ABS), polylactic acid (PLA), polystyrene (PS), acrylonitrile styrene acrylate (ASA), polyethylene (PE) and polycaprolactone (PCL), which has been demonstrated by Karyappa et al. [212]. In this section, more thermoplastics, thermosets and polymer nanocomposites of

different properties are printed to expand the range of precipitation printable materials. Figure 2.3A shows precipitation printed rigid PMMA in the form of a wrench and chess samples, with printing parameters tabulated in Table 2.1. In this case, the slightly porous microstructure of the printed PMMA using a low concentration PMMA printing solution causes the reduction in final structure transparency. Figure 2.3B contains two printed highly porous PVDF chesses to highlight the dimensional stability and accuracy of precipitation printed structures over the build height. Microscale high resolution printing can also be achieved using a small diameter (0.15 mm) 30-gauge nozzle. In Figure 2.3C and D, a PVDF micro lattice of size 4 mm × 4 mm × 3 mm with a printing line width of 100 μm measured by scanning electron microscopy (SEM) imaging is presented. The printing resolution is limited by the internal diameter of the nozzle and therefore a finer nozzle will further enhance the printing resolution.

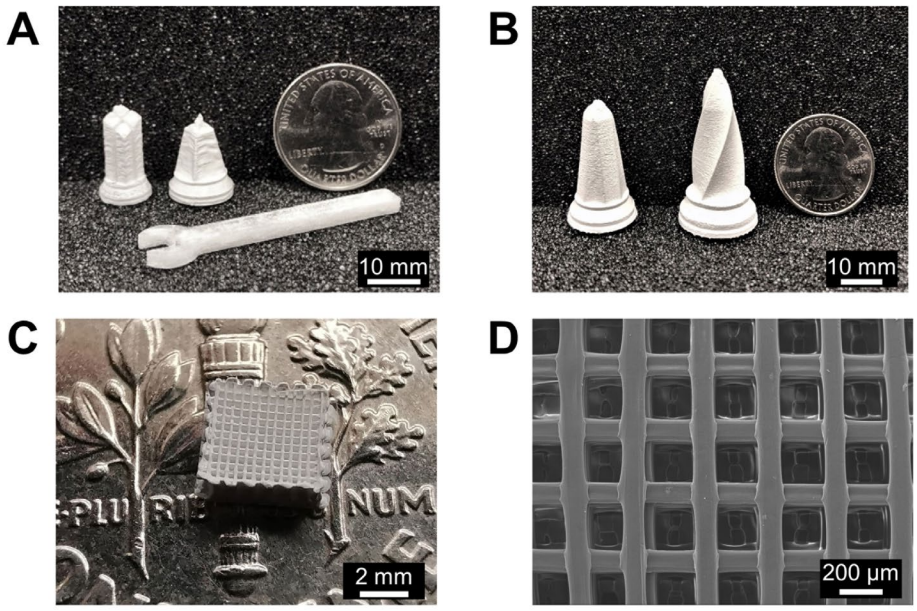

Figure 2.3. A) Precipitation printed PMMA chesses and wrench. B) Precipitation printed PVDF chesses. C) PVDF micro lattice structure on a dime coin. D) SEM image of the micro lattice.

Table 2.1. Printing parameters for various materials for 3D structure demonstration.

	PMMA	PVDF	MWCNTs/PVDF	NBR
Solvent	acetone	DMF	DMF	DMF
Non-solvent	water	water	water	water
Solution concentration (wt%)	25	15	15	25
Layer height (mm)	0.05	0.05	0.05	0.05
Nozzle diameter (mm)	0.25	0.25	0.30	0.25
Printing speed ($mm \cdot s^{-1}$)	7	7	7	8
Line width (mm)	0.40	0.20	0.20	0.20
Pressure (psi)	2.0	2.5	1.4	30

Additive manufacturing of polymer nanocomposites as multifunctional materials can be conveniently integrated to precipitation printing. To demonstrate the utility of the precipitation printing process for the realization of functional nanocomposites, electrically conductive structures have been printed using multiwalled carbon nanotubes (MWCNTs) dispersed in a PVDF matrix. Figure 2.4A shows two precipitation printed MWCNTs/PVDF nanocomposite thin-walled tubes demonstrating the high aspect ratio and dimensional stability of the printing process. The nanocomposite tube can have a wall thickness of only 0.25 mm. Figure 2.4B shows an SEM image of the surface of a MWCNTs/PVDF nanocomposite sample and as can be seen in Figure 2.4B, MWCNTs are randomly dispersed in PVDF as indicated by the yellow arrows, allowing the printing of electrically conductive structures. The electrical conductivity of MWCNTs/PVDF nanocomposites with respect to the weight fraction of MWCNTs in PVDF is shown in Figure 2.4C. As can be seen in the plot, there is a rapid increase in nanocomposite electrical conductivity when MWCNTs are increased from 2 wt% to 4 wt%. While the MWCNTs/PVDF nanocomposite's electrical conductivity keeps rising as the MWCNTs weight fraction goes up, the printing solution becomes very viscous and prone to clogging of the nozzle when the weight fraction of MWCNTs is higher than 6 wt%. After considering the electrical conductivity and printability, nanocomposites with 6 wt% of MWCNTs were selected as the optimum for precipitation printing. Figure 2.4D shows two small 3D printed MWCNTs/PVDF nanocomposite tower structures with a total resistance of 16 kΩ on a neat PVDF base, which serve as the electrodes for a lighted LED. In addition, this structure showcases the capability of printing conductive PVDF nanocomposites onto an existing PVDF structure, which can be used as a 3D electrode printing process for piezoelectric PVDF devices in the future. Polymer nanocomposites containing MWCNTs have also been shown to act as piezoresistive sensors to measure strain [213]. The piezoresistivity of the precipitation printed MWCNTs/PVDF nanocomposite was measured by printing a strain gauge with a fine parallel-grid pattern to increase the accuracy of strain measurement. Figure 2.4E shows the printed strain gauge on a polyimide strip that was coated with a thin layer of PVDF applied using a doctor blade. To assess the piezoresistivity, the electrical resistance of the printed strain gauge was measured under varying levels of strain from 0 to 3.0 % applied to the sample by an Instron universal testing systems (model 5982). The electrical resistance-strain relationship is shown in Figure 2.4F, with a linear region from 0.8 % to 2.7 % strain ($R^2 = 0.996$). The plot also shows two nonlinear regions, one at very low strains where MWCNTs inside PVDF matrix are

still coiled or curled in the polymer followed by their extension and orientation and the other at larger strains followed by their slipping inside the polymer.

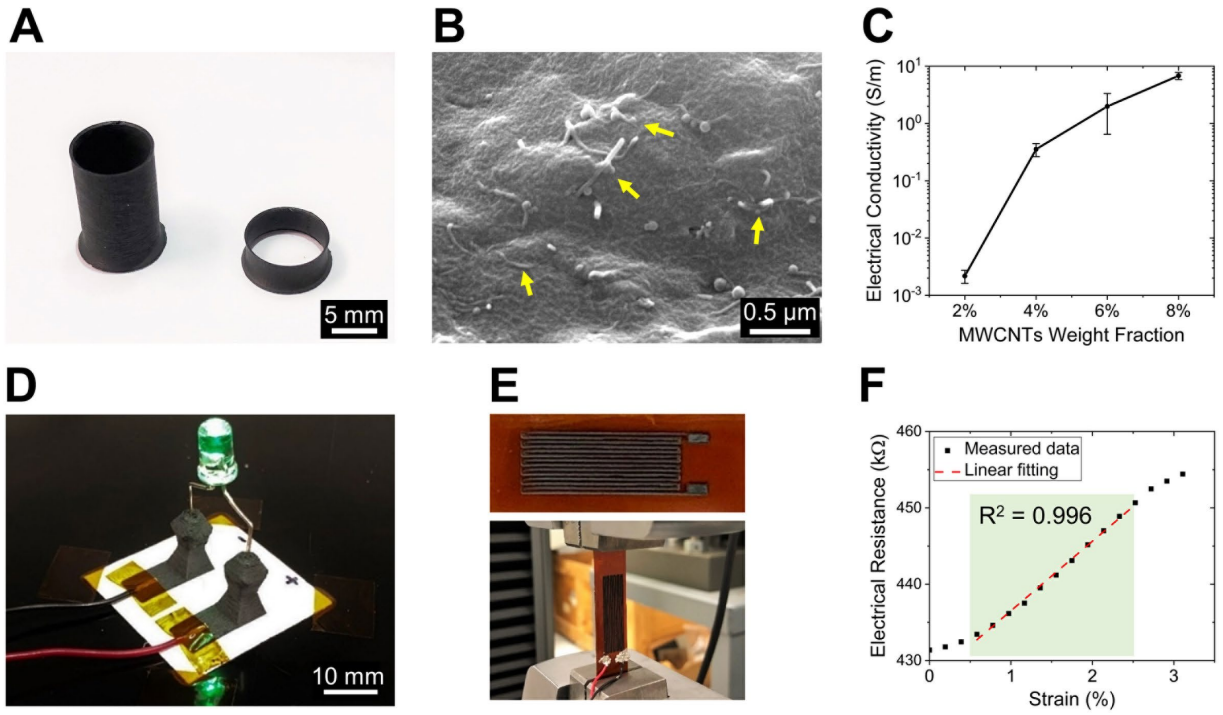

Figure 2.4. A) Precipitation printed MWCNTs/PVDF nanocomposite thin-walled structures. B) SEM image of the surface of printed MWCNTs/PVDF sample (6 wt% MWCNTs). C) Electrical conductivity of the printed MWCNTs/PVDF nanocomposite increases as the weight fraction of MWCNTs increases. D) Printed MWCNTs/PVDF nanocomposite tower structures serve as two electrodes of a lighted LED. E) Precipitation printed MWCNTs/PVDF strain gauge during tensile testing. F) Tested electrical resistance-strain relationship of the strain gauge.

In addition to thermoplastics, thermosetting polymers can also be printed through this method and have been demonstrated through the printing of acrylonitrile butadiene rubber (NBR) and subsequent vulcanization through radical polymerization. Figure 2.5A shows a printed block M which was first printed as a mixture of NBR and a latent peroxide catalyst (tert-butyl peroxybenzoate) at room temperature and then dried in a vacuum chamber. The color of NBR before vulcanization was cream and turned to brown after the vulcanization process at 125 °C in an oven for 20 min to allow the tert-butyl peroxybenzoate to form radicals beyond its self-accelerating decomposition temperature (SADT) of 65.8 °C [214], as shown in Figure 2.5B. The precipitation printing method allowed uniform mixing of the liquid catalyst (*e.g.*, peroxide) with soluble unvulcanized rubber enabling a uniform cross-linked structure after curing. However, although the precipitation printing technique provided high precision 3D printing for an accurately finished part, it is difficult to maintain the dimensional stability during the elevated temperature

vulcanization process due to contraction. Moreover, NBR is used for the demonstration of a heart valve shaped 3D printed check valve. Figure 2.5C–E present the 3D printed check valve's closed and open state. The size of this 3D printed check valve is 15 mm in diameter and 4 mm in height. This valve allows flow to pass in one direction when the applied pressure opens the gap automatically and blocks flow in the other direction when the gap is sealed by the applied pressure. The flow rates in two directions (direction 1: flow comes from the top side, direction 2: bottom side of the check valve) at different pressures were measured to verify the effectiveness of this check valve. Figure 2.5F shows the flow rate test setup with flow direction from the top side, and the experiment result in Figure 2.5G indicates the check valve can restrict the flow rate to a low level (about 1 mL/s) from the top of the valve and it allows flow rate to increase as the pressure rises in the other direction.

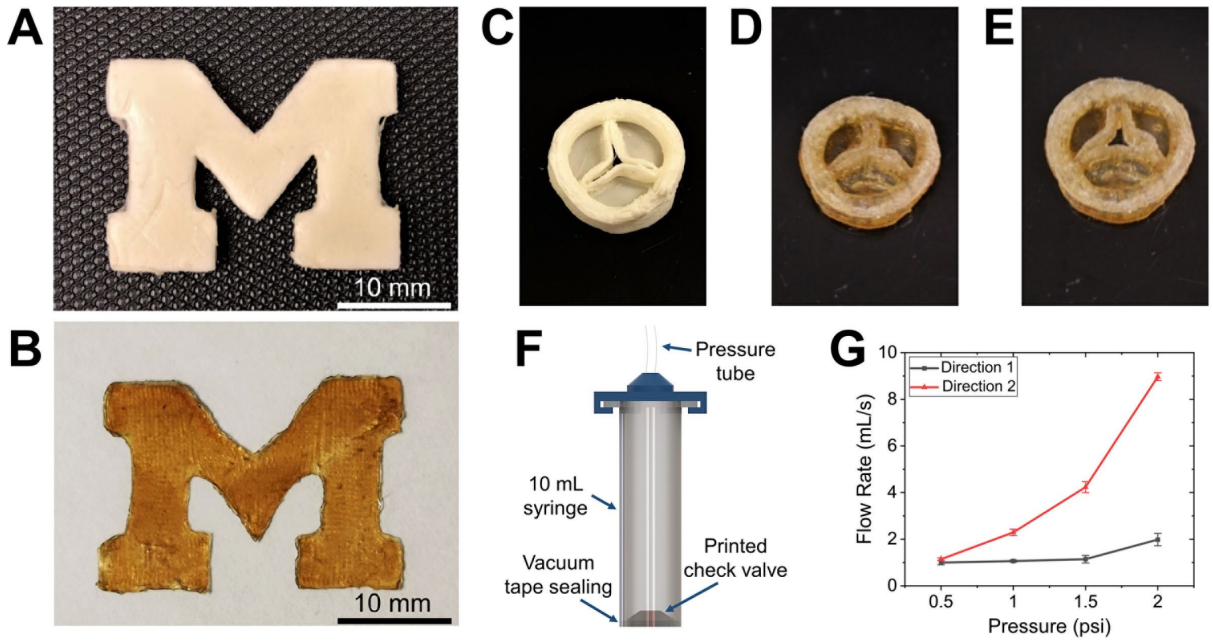

Figure 2.5. A) Precipitation printed NBR block M before curing. B) The NBR block M after curing. C) Precipitation printed NBR check valve before curing, top view. D) The NBR check valve after curing, closed state. E) The NBR check valve after curing, open state. F) Flow rate test setup (flow comes from the top side). G) Flow rate-pressure relationship for two different flow directions.

2.3 Effect of solvent/non-solvent pairs

2.3.1 Wet spinning of poly(methyl methacrylate) fibers

During the precipitation printing process, mutual diffusion takes place between the solvent in the printing solution and the non-solvent, resulting in the previously mentioned NIPS phenomenon. To select a solvent to form the printing solution of a target polymer, Hansen

solubility parameter as a widely used method to predict material solubility is used [199]. In the case of PMMA, its Hansen solubility parameters and the relative energy difference (RED) of some common solvents relative to PMMA are shown in Table 2.2 [200]. As a result, DMF and acetone were selected as two solvents for PMMA printing solutions.

Table 2.2. Hansen solubility parameters of PMMA (R_0 = 11 $MPa^{0.5}$) and common solvents.

	δ_d ($MPa^{0.5}$)	δ_p ($MPa^{0.5}$)	δ_h ($MPa^{0.5}$)	RED
PMMA	17.9	10.1	5.4	/
N,N-dimethylformamide (DMF)	17.4	13.7	11.3	0.63
Acetone	15.5	10.4	7.0	0.46
Ethanol	15.8	8.8	19.4	1.33
Propylene glycol (PG)	16.8	9.4	23.3	1.64
Water	15.6	16	42.3	3.42

Previous works on membranes formed by NIPS have shown that the phase separation rate (or precipitation rate) and the membrane cross-section morphology depend on not only the solubility of the polymer in the solvent and non-solvent, but also the diffusion rate between the solvent and non-solvent. The diffusion rate depends on the diffusivity, which is related to the viscosity of the liquid based on the Stokes-Einstein relation. Therefore, two non-solvents with highly different dynamic viscosity (μ), water (μ = 1 mPa·s at 20 °C) and propylene glycol (PG, μ = 56 mPa·s at 20 °C), were studied for the NIPS process of PMMA. To investigate the effect of solvent/non-solvent pairs on the microstructure morphology of precipitation printed PMMA, wet spinning tests of two types of PMMA printing solutions in two types of non-solvent baths were performed. It should be noted that wet spinning was selected as the preliminary test method to study the effect of solvent/non-solvent pairs because it is simple and shares the same NIPS mechanism with precipitation printing. PMMA (Sigma-Aldrich, average molecular weight ~120,000) was dissolved in acetone (ACS reagent, Sigma-Aldrich) and DMF (certified ACS, Fisher Chemical) to form 35 wt% PMMA/acetone and PMMA/DMF solutions, respectively. For each wet spinning test, the printing solution was loaded in a 10 mL syringe with a 26-gauge (0.25 mm inner diameter) nozzle, and wet spun into the corresponding non-solvent bath using 25 psi pressure (Figure 2.6). After collecting the wet spun fibers, they were dried in a vacuum oven (25 in. -Hg) at 80 °C for 12 h to evaporate the non-solvent and residual solvent. The cross-sections of the wet spun fibers were then examined by a scanning electron microscope (SEM, JEOL JSM-7800FLV).

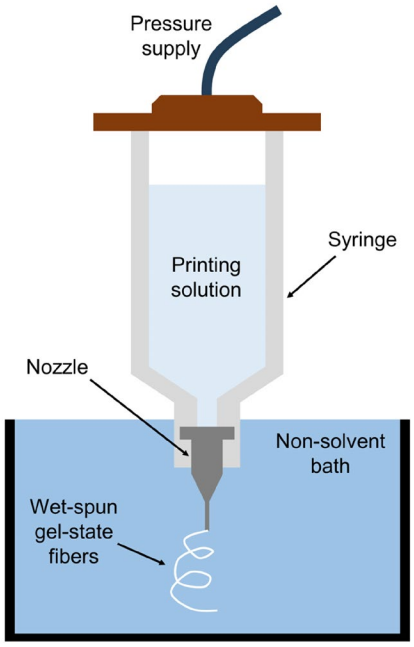

Figure 2.6. Wet spinning process setup.

Figure 2.7 shows the cross-section SEM images of the wet spun PMMA fibers using different solvent/non-solvent pairs. In the case of PMMA/acetone/water (Figure 2.7A), the fiber has an overall dense cross-section with a non-circular shape, with some small voids of sizes below 1 μm. This means after being dispensed out of a circular nozzle, the PMMA/acetone solution does not precipitate (or solid-liquid phase separate) immediately, which allows sufficient time for gel-state fiber shape change. The gradual increase of the PMMA concentration before solid-liquid phase separation by the mutual diffusion between acetone and water leads to the dense microstructure in this case. In the case of PMMA/DMF/water (Figure 2.7B), the fiber has a circular cross-section with pores larger than 10 μm, which indicates a faster PMMA precipitation rate on the fiber surface than the PMMA/acetone/water case. The fixed circular outer surface of the fiber restricts the volume contraction of the gel-state fiber, causing the formation of large pores after the drying of trapped water. On the other hand, when using the high viscosity PG with a lower RED to PMMA as the non-solvent, both PMMA/acetone/PG and PMMA/DMF/PG cases result in fully dense and non-circular fibers (Figure 2.7C and D). These dense microstructures indicate the PMMA solutions possibly underwent a single-phase gelation path before being removed from the bath, where the solution concentration increased up to gelation but never reached the solid-liquid phase separation limit [215,216].

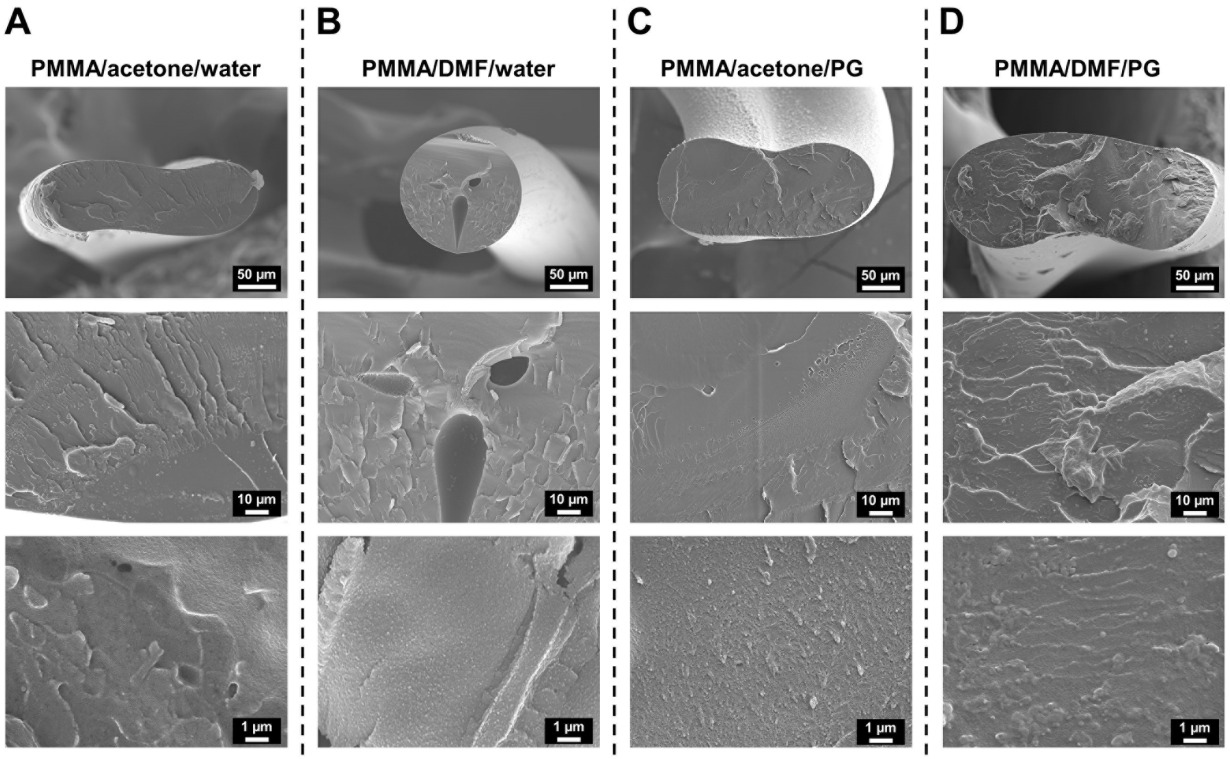

Figure 2.7. Cross-section SEM images of the wet spun PMMA fibers using the following solvent/non-solvent pairs: A) acetone/water, B) DMF/water, C) acetone/PG, D) DMF/PG.

2.3.2 Tensile testing of precipitation printed poly(methyl methacrylate)

After the wet spinning tests, two representative solvent/non-solvent pairs, PMMA/acetone/water (slightly porous) and PMMA/DMF/PG (fully dense) were used for precipitation printing of ASTM D638 type V specimens with printing parameters listed in Table 2.3. It should be noted that due to the anisotropy of 3D printed parts, three infill configurations, all 0°, all 90°, and 0°/90° alternating patterns relative to the loading direction were printed. After drying all PMMA specimens at 80 °C for 12 h under vacuum (25 in. -Hg), tensile tests were performed according to ASTM D638 with a testing speed of 1 $mm \cdot s^{-1}$. Reference specimens were solution cast PMMA films with the laser cut D638 type V shape. Figure 2.8 shows the tensile test results from the PMMA/acetone/water system. The Young's modulus of printed PMMA using this system is slightly lower than the reference PMMA films, especially for the 90° specimens (14% reduction). However, the tensile strength and tensile toughness (defined as the absorbed strain energy before failure) of the printed PMMA in this case are significantly lower than the PMMA films due to the low elongation at break originated from the stress concentration at internal voids.

It is worth mentioning that defects (voids) in precipitation printed parts generally originate from the following three aspects. First, rapid solvent/non-solvent exchange during the precipitation process can lead to the formation of a highly porous microstructure through spinodal decomposition (will be discussed in Section 2.3.3). Second, bubbles in the printing solution can result in big pores in the printed structure due to insufficient infill. However, bubbles can be eliminated completely by proper degassing of the printing solution. Third, defects (voids) occur at the interfaces between layers or adjacent printing lines due to insufficient solvent welding, which is the main source of defects in the case of PMMA precipitation printing. Among all infill configurations of printed PMMA, 0°/90° alternating specimens have the best tensile properties because they have the fewest interfacial defects between infill lines by using the alternating pattern. The alternating pattern provides a self-repairing chance for the upper layer printing solution to cover and fill the voids between the printing lines of the lower layer. The tensile fracture surfaces of the printed PMMA were examined by SEM imaging in Figure 2.9. Although the PMMA cross-sections have an overall dense microstructure, macroscale voids caused by insufficient infill between paths can be seen, especially in all 0° and all 90° specimens. The voids induced stress concentration is considered the main source of low elongation at break and low tensile toughness.

Table 2.3. Printing parameters for PMMA using different solvent/non-solvent pairs.

	PMMA/acetone/water	PMMA/DMF/PG
Solution concentration (wt%)	35	35
Layer height (mm)	0.04	0.06
Nozzle diameter (mm)	0.30	0.41
Printing speed ($mm \cdot s^{-1}$)	5	7
Line width (mm)	0.40	0.40
Pressure (psi)	5	6

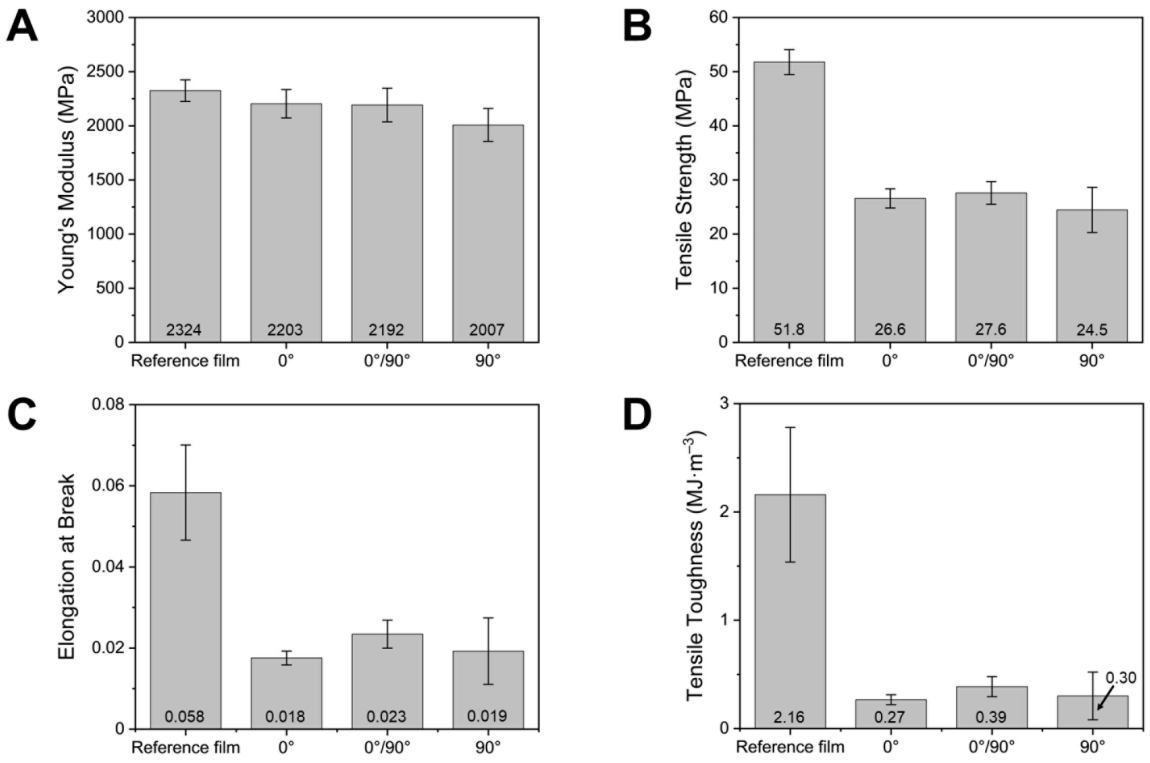

Figure 2.8. Tensile test results of PMMA printed from the PMMA/acetone/water system: A) Young's modulus, B) tensile strength, C) elongation at break, D) tensile toughness.

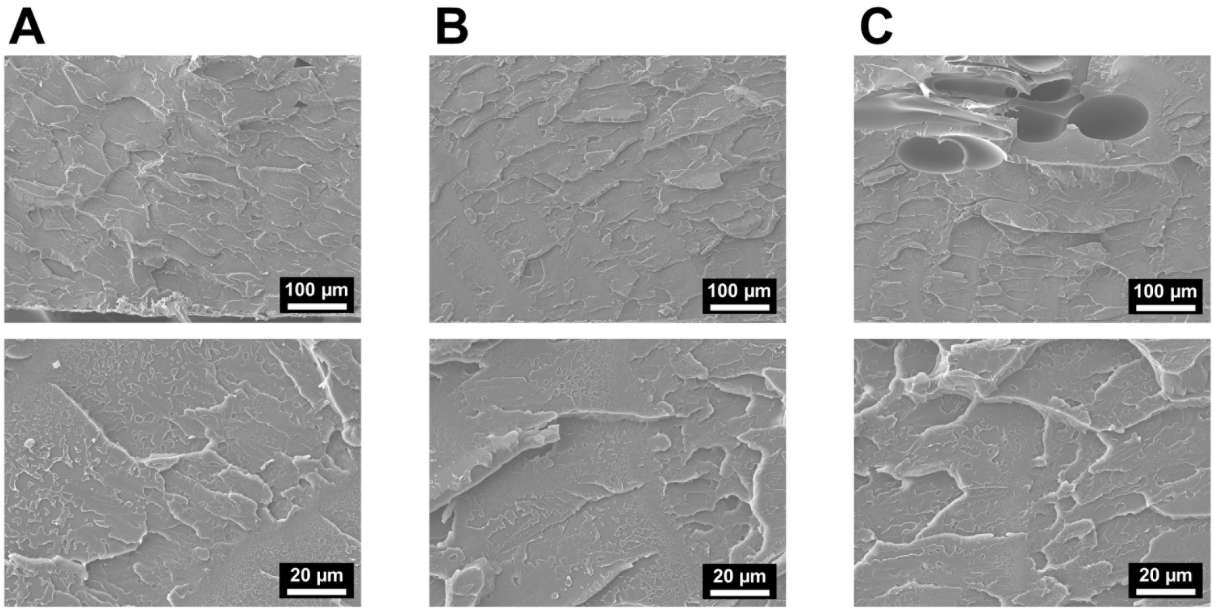

Figure 2.9. SEM images of the tensile fracture surfaces of PMMA printed from the PMMA/acetone/water system. A) 0° specimen. B) 0°/90° alternating specimen. C) 90° specimen.

Figure 2.10 contains the tensile test results of the precipitation printed PMMA from the PMMA/DMF/PG system. In this case, the Young's moduli of precipitation printed PMMA specimens have negligible difference compared to the PMMA films (one-way ANOVA $p = 0.69$),

while the tensile strengths are 80–90% of the PMMA films. Elongation at break and tensile toughness of the printed PMMA are comparable or even higher than the PMMA films. Compared to the PMMA/acetone/water case, the improved tensile properties in the PMMA/DMF/PG case are attributed to the slow precipitation rate and dense microstructure of the printed PMMA. Among the three infill configurations, since defects are significantly reduced in all specimens, 0° specimens exhibit the highest elongation and tensile toughness due to the higher ductility in the printing direction. The lower tensile strength but higher elongation at break of printed PMMA relative to the PMMA films can be explained by the residual high-boiling point PG (188 °C) even after 80 °C vacuum drying. The SEM images in Figure 2.11, which are the tensile fracture cross-sections of the printed PMMA using the PMMA/DMF/PG system, exhibit fully dense and rough surfaces without any printing paths for all printing configurations, indicating a low anisotropy.

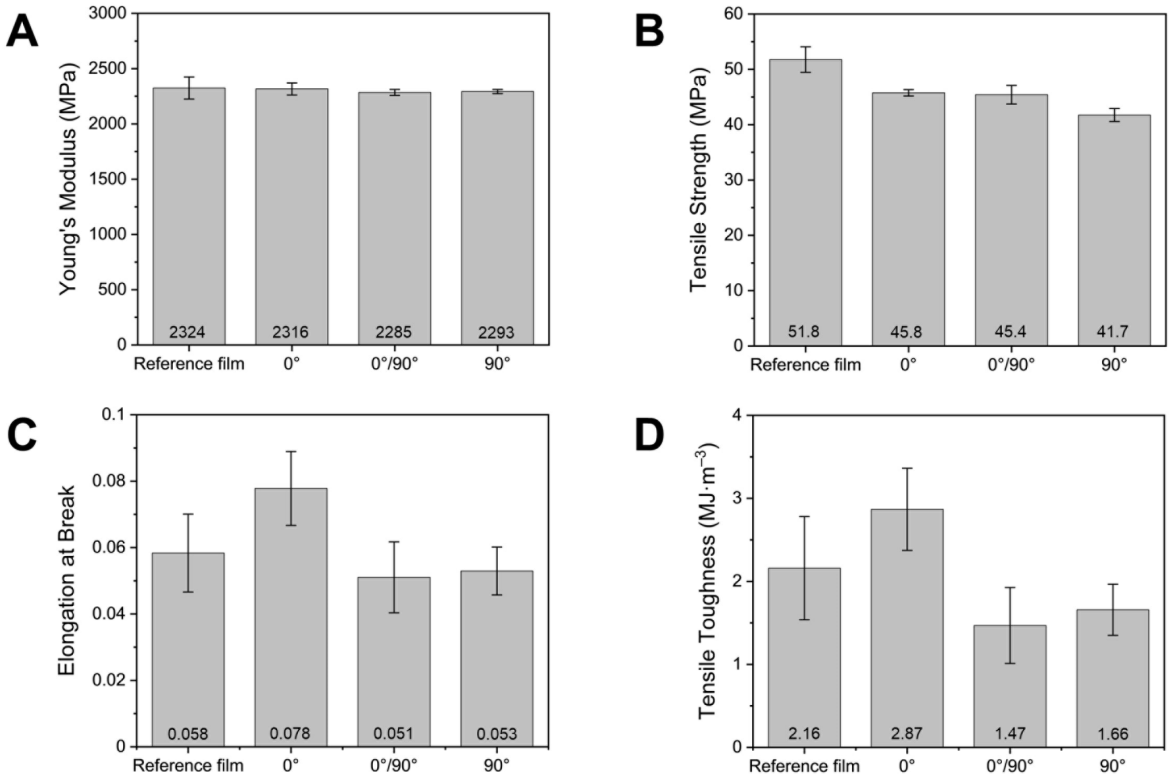

Figure 2.10. Tensile test results of PMMA printed from the PMMA/DMF/PG system: A) Young's modulus, B) tensile strength, C) elongation at break, D) tensile toughness.

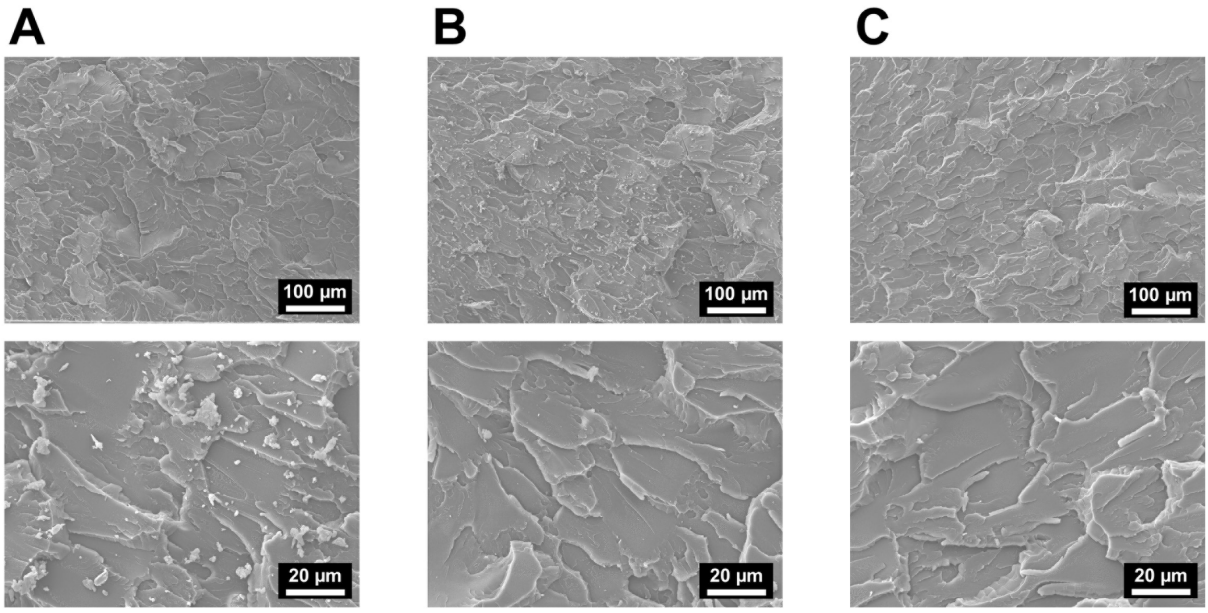

Figure 2.11. SEM images of the tensile fracture surfaces of PMMA printed from the PMMA/DMF/PG system. A) 0° specimen. B) 0°/90° alternating specimen. C) 90° specimen.

2.3.3 Wet spinning of poly(vinylidene fluoride) fibers

The other thermoplastic polymer used in this study is PVDF, which is semi-crystalline and highly hydrophobic. The Hansen solubility parameters and the RED of some common solvents relative to PVDF are shown in Table 2.4 [200]. As a result, DMF, NMP and *N,N*-Dimethylacetamide (DMAc) are considered good solvents for preparing PVDF printing solutions, and water and PG are two non-solvents. For wet spinning tests, PVDF powder (Kynar 301F) was first dissolved in DMF (certified ACS, Fisher Chemical), NMP (99+%, Thermo Scientific) and DMAc (certified ACS, Fisher Chemical) to form 20 wt% PVDF/DMF, PVDF/NMP and PVDF/DMAc solutions, respectively. The three printing solutions were again loaded in a 10 mL syringe with a 26-gauge (0.25 mm inner diameter) nozzle, and wet spun into the corresponding non-solvent bath using 40 psi pressure. The drying process was 120 °C vacuum (25 in. -Hg) drying for 12 h.

Figure 2.12 shows the cross-section SEM images of the wet spun PVDF fibers using three different solvents and water as the non-solvent. The PVDF fiber cross-sections are non-circular when using DMAc and DMF as the solvent, and the one using NMP as the solvent is circular. This can be explained that DMAc and DMF are better solvents (lower RED) for PVDF than NMP, which leads to delayed fiber surface phase separation and allows shape change and contraction. All three fibers in Figure 2.12 are porous, with a relatively less porous surface layer, large finger-

shapes pores in the radial direction, and a microporous core. This unique microstructure has been discovered in asymmetric membrane formation via NIPS in the literature [12,217,218]. In these three cases, the solvent and non-solvent are highly miscible with low viscosity, causing the rapid formation of a precipitated microporous surface layer. The internal solvent from the polymer solution then has the tendency to diffuse towards the outer surface of the gel-state fiber quickly, which causes the formation of finger-shapes pores in the radial direction [219,220]. As the amount of internal solvent decreases due to diffusion, the polymer concentration and viscosity of the core increases, resulting in a slower phase separation rate and a sponge-like microporous core.

Table 2.4. Hansen solubility parameters of PVDF (R_0 = 4.1 $MPa^{0.5}$) and common solvents.

	δ_d ($MPa^{0.5}$)	δ_p ($MPa^{0.5}$)	δ_h ($MPa^{0.5}$)	RED
PVDF	17.0	12.1	10.2	/
N,N-dimethylformamide (DMF)	17.4	13.7	11.3	0.51
Dimethyl sulfoxide (DMSO)	18.4	16.4	10.2	1.25
N,N-dimethylacetamide (DMAc)	16.8	11.5	9.4	0.26
N-methyl-2-pyrrolidoneare (NMP)	18	12.3	7.2	0.88
Propylene glycol (PG)	16.8	9.4	23.3	3.26
Water	15.6	16	42.3	7.92

Polymer/solvent/non-solvent ternary phase diagrams can used to describe the NIPS process and its mechanism. It should be noted that all ternary phase diagrams used in this dissertation are illustrations to explain the printing solution phase separation progress based on the observed microstructure in SEM images. Figure 2.13A explains the NIPS mechanism that forms the PVDF microstructure in Figure 2.12, where similar mutual diffusion rate between the solvent (DMAc, DMF or NMP) and water causes a relatively flat evolution path, which results in fast crossing of the spinodal curve and spinodal decomposition of both the fiber surface and core. In addition, the evolution path end point for the fiber core usually does not reach the right edge of the ternary phase diagram, since the mutual diffusion between the solvent and non-solvent eventually turns into a steady-state solvent/non-solvent mixture.

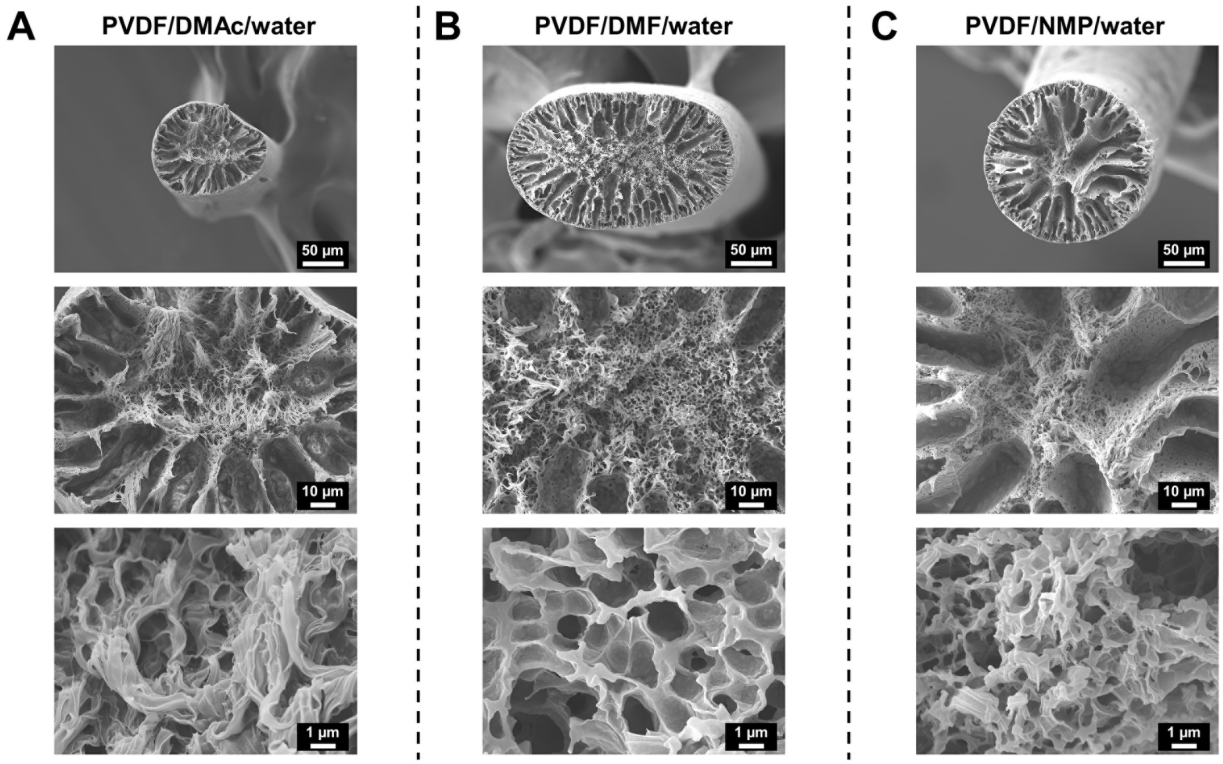

Figure 2.12. Cross-section SEM images of the wet spun PVDF fibers using the following solvent/non-solvent pairs: A) DMAc/water, B) DMF/water, C) NMP/water.

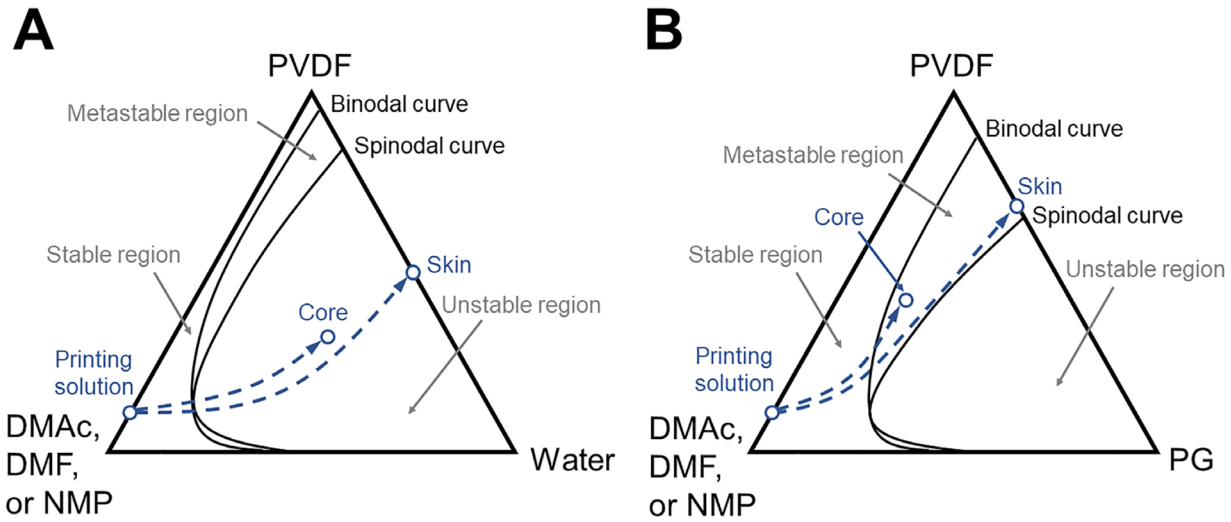

Figure 2.13. Ternary phase diagrams of PVDF/solvent/non-solvent systems. A) DMAc, DMF or NMP as the solvent, water as the non-solvent. B) DMAc, DMF or NMP as the solvent, PG as the non-solvent.

On the other hand, when using PG as the non-solvent, the high viscosity of PG hinders the mutual diffusion between the solvent and non-solvent. All wet spun fiber cross-sections in Figure 2.14 have a uniformly porous microstructure with porous broccoli-shaped spherulites (about 1–10 µm diameter). The outer surface of the PVDF/DMAc/PG and PVDF/DMF/PG fibers are non-circular, while the PVDF/NMP/PG fiber has a circular shell due to a faster precipitation of the

surface layer. The diameter and porosity of the broccoli-shaped spherulites increase as the solvent RED to PVDF increases (NMP > DMF > DMAc). This microstructure originates from the liquid-liquid demixing of PVDF-rich and PVDF-lean phases in the metastable region, where nuclei of PVDF-rich phase forms and slowly grows into the porous broccoli-shaped spherulites [221,222]. The evolution paths in the ternary phase diagram are indicated in Figure 2.13B. Since high viscosity PG diffuses slowly into the PVDF gel-state fiber, both the fiber skin and core experience steep evolution paths that stay in the metastable region, and no spinodal decomposition happens in these three cases in Figure 2.14.

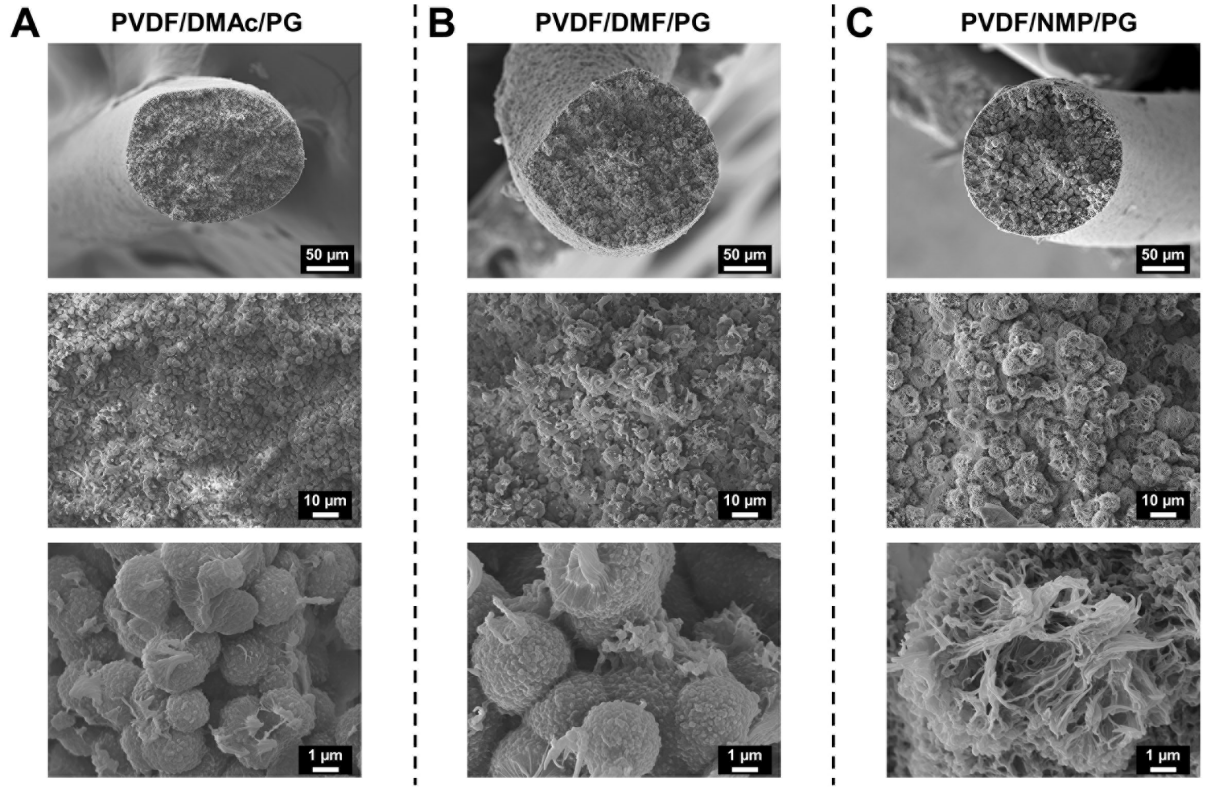

Figure 2.14. Cross-section SEM images of the wet spun PVDF fibers using the following solvent/non-solvent pairs: A) DMAc/PG, B) DMF/PG, C) NMP/PG.

2.3.4 Tensile testing of precipitation printed poly(vinylidene fluoride)

Two representative solvent/non-solvent pairs, PVDF/DMF/water (high porosity) and PVDF/DMAc/PG (low porosity) were used for precipitation printing of ASTM D638 type V specimens with printing parameters listed in Table 2.5. Drying of PVDF specimens was at 120 °C vacuum (25 in. -Hg) for 12 h. Prior to tensile testing, the density of the PVDF prepared from this system was measured to be 0.746 g·cm^{-3}, 42% of fully dense PVDF (1.78 g·cm^{-3}). The tensile test procedure was following ASTM D638, the same as the previous PMMA case. Figure 2.15 shows

the tensile test results from the PVDF/DMF/water system. Due to the high porosity, the Young's modulus and tensile strength of the precipitation printed PVDF in this case are lower than 40% of the corresponding ones of the PVDF films. However, the elongation at break of the printed PVDF is comparable or even higher than dense PVDF films, which can be explained by the microstructure with interconnected PVDF networks surrounding the finger-shape pores and the pore shape change under tension. Among the three configurations, 0° specimens have the highest Young's modulus and tensile strength, while 90° specimens have the lowest tensile properties. The anisotropic tensile properties indicate that this porous material is stronger in the longitudinal continuous printing direction than the transverse direction.

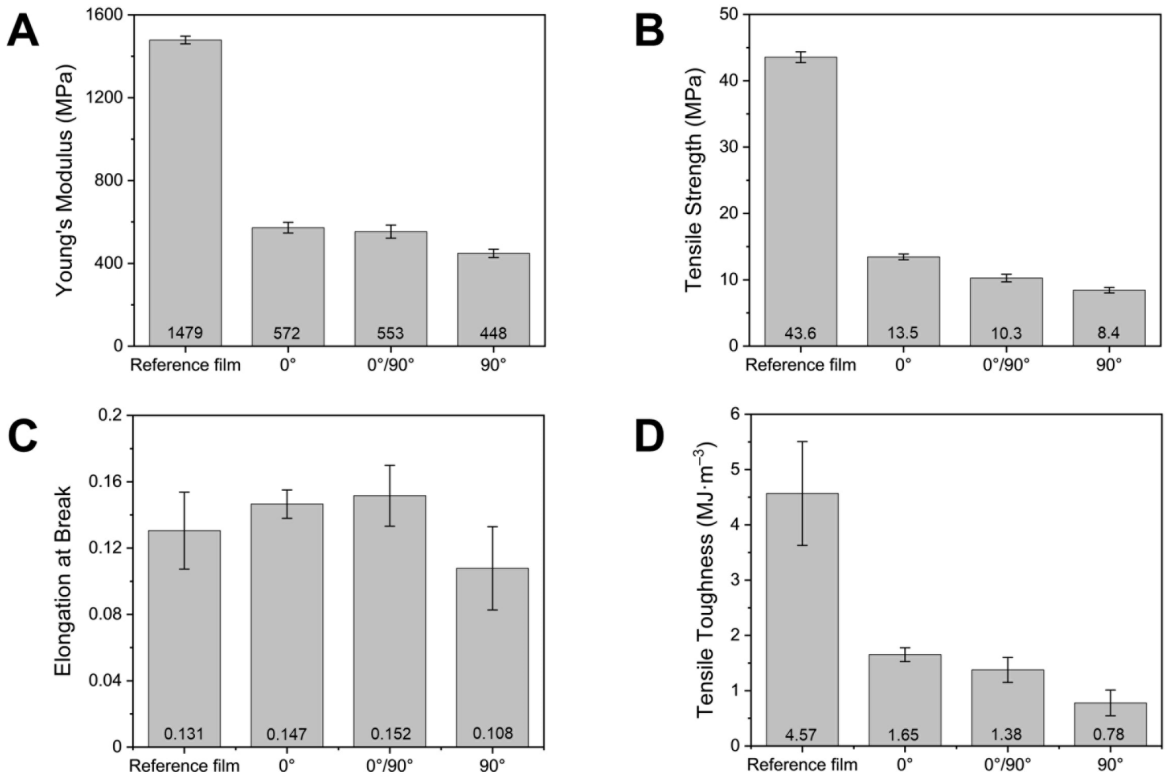

Figure 2.15. Tensile test results of PVDF printed from the PVDF/DMF/water system: A) Young's modulus, B) tensile strength, C) elongation at break, D) tensile toughness.

Table 2.5. Printing parameters for PVDF using different solvent/non-solvent pairs.

	PVDF/DMF/water	PVDF/DMAc/PG
Solution concentration (wt%)	20	20
Layer height (mm)	0.04	0.04
Nozzle diameter (mm)	0.25	0.30
Printing speed (mm·s^{-1})	7	7
Line width (mm)	0.20	0.40
Pressure (psi)	9.5	8.0

The tensile fracture surface SEM images in Figure 2.16A and B show that printed PVDF specimens have substantial pull-outs in the 0° layers as the continuous printing direction, but have weak interfaces between 90° infill lines (Figure 2.16C). In addition, layer stratification can be observed in all specimens, in particular the 0°/90° alternating specimens and all 90° specimens, confirming the highly anisotropic microstructure of printed PVDF using the PVDF/DMF/water system. The weak interface between infill lines and layers is caused by the insufficient solvent welding power, because the solubility of PVDF in DMF is readily reduced with the presence of water.

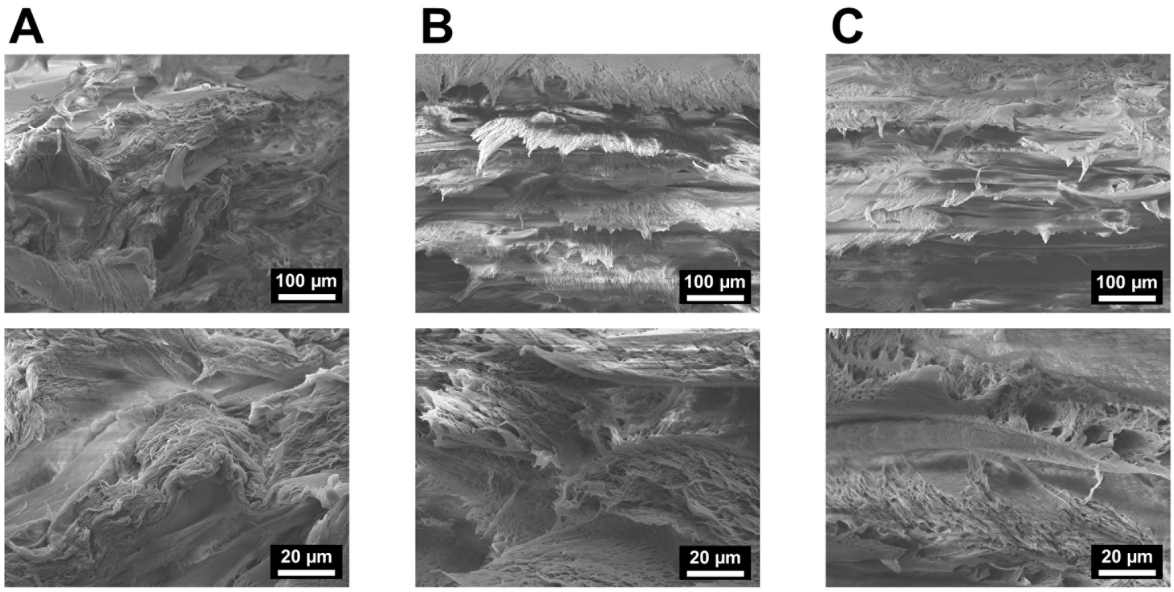

Figure 2.16. SEM images of the tensile fracture surfaces of PVDF printed from the PVDF/DMF/water system. A) 0° specimen. B) 0°/90° alternating specimen. C) 90° specimen.

The PVDF precipitation printed from the PVDF/DMAc/PG system has a higher density of 1.21 $g \cdot cm^{-3}$, 68% of fully dense PVDF. In this case, a higher degree of anisotropy can be seen in the tensile test results in Figure 2.17. The Young's modulus and tensile strength of 0° specimens is 55% and 79% higher than those of the 90° specimens, respectively, while the 0°/90° alternating specimens have intermediate tensile properties. Although the overall Young's moduli in this case are improved compared to the previous PVDF/DMF/water case due to the lower porosity, the elongations at break are decreased more than 50%. This can be explained by the PVDF microstructure printed from the PVDF/DMAc/PG system, where internal porous spherical cells (or sponge-shape pores) have weak interconnection with each other and allow easy fracture between cells. Like wet spinning, the outer surface of each printing line has the lowest porosity, resulting in highest strength along the continuous printing line direction. SEM images of the tensile

fracture surfaces in Figure 2.18 show less significant layer stratification than the PVDF/DMF/water case, but the interface between infill lines is still weak due to the poor solvent welding effectiveness onto the weakly connected PVDF spherulites, which can be seen as some relatively smooth adhesive failure sites in the 90° specimen (Figure 2.18C).

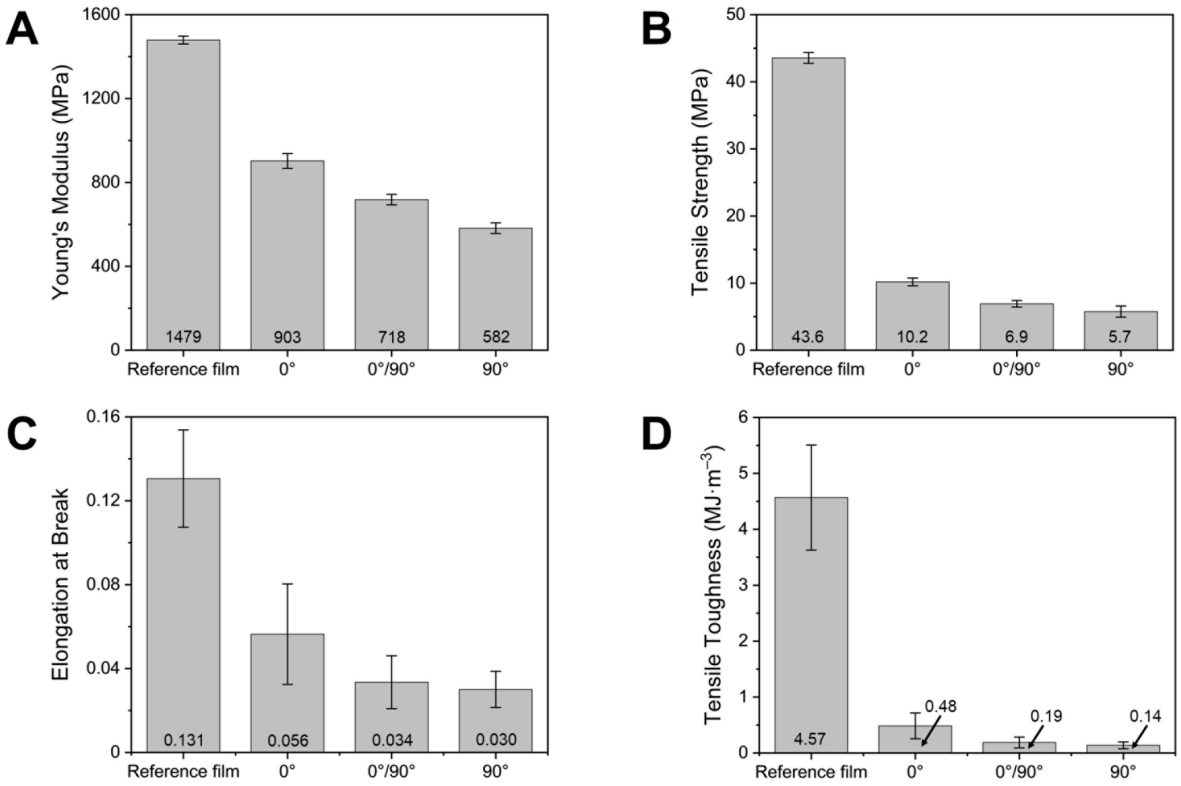

Figure 2.17. Tensile test results of PVDF printed from the PVDF/DMAc/PG system: A) Young's modulus, B) tensile strength, C) elongation at break, D) tensile toughness.

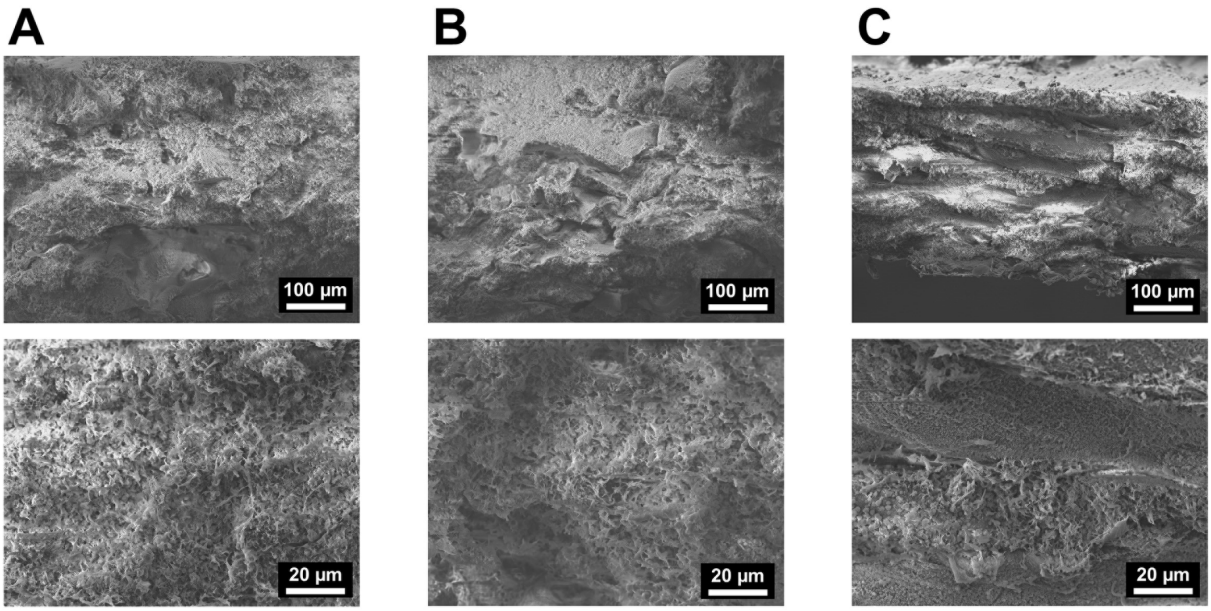

Figure 2.18. SEM images of the tensile fracture surfaces of PVDF printed from the PVDF/DMAc/PG system. A) 0° specimen. B) 0°/90° alternating specimen. C) 90° specimen.

Combining the SEM images, density measurements and tensile test results, we can see that the solvent/non-solvent pair used for the precipitation printing plays a significant role in the microstructure and mechanical properties of a printed target polymer. In general, a good solvent with low RED to the target polymer and a weak non-solvent with high viscosity can avoid spinodal decomposition and produce structures with a dense microstructure and high mechanical properties, while a strong non-solvent with low viscosity can be used to prepare porous and lightweight structures. However, depending on the phase separation type, such as liquid-liquid demixing and spinodal decomposition, different porous microstructures can lead to large variations in mechanical properties. Therefore, precipitation printing allows microstructure and mechanical property tailoring of the prints, but preliminary studies (like wet spinning) of different solvent/non-solvent pairs need to be applied to a wider range of thermoplastic polymers as a guide for future applications.

2.4 Effect of printing solution concentration

2.4.1 Poly(methyl methacrylate)

The effect of printing solution concentration on the precipitation printed PMMA was investigated using the PMMA/acetone/water system. The PMMA/acetone printing solution concentration varied from 25 to 40 wt%, and the printing parameters are listed in Table 2.6. It

should be noted that the pressure used for printing different concentration solutions was adjusted for the maximum infill, considering the viscosity difference among the solutions. After precipitation printing of five 14 mm × 8 mm × 1 mm rectangular bars for each concentration, the same drying process at 80 °C for 12 h under vacuum was applied to all PMMA specimens. The final dimensions of the PMMA specimens were measured using calipers and micrometers and used to calculate the dimensional contraction relative to the design value. Due to the removal of the raft layers that caused inaccurate specimen thickness measurement, average dimensional contraction was calculated using the in-plane contractions in *x* and *y*-directions. The mass of each PMMA specimen was also weighed on an analytical scale (Mettler Toledo) to calculate the final density.

Figure 2.19 contains the average dimensional contraction and final density of PMMA printed from different concentration solutions. When the PMMA solution concentration increases from 25 to 40 wt%, the average dimensional contraction is within 3.7%–4.9% with no statistically significant change (ANOVA $p = 0.17$), but the final density increases from 0.89 to 1.08 $g \cdot cm^{-3}$. Since the PMMA has a density of 1.18 $g \cdot cm^{-3}$, precipitation printed PMMA using all tested concentrations still contain voids or remaining solvents after drying.

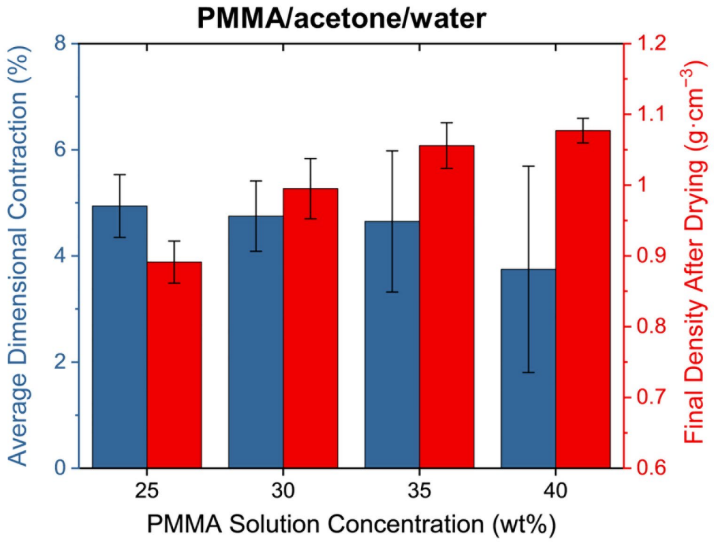

Figure 2.19. Dimensional contraction and final density of PMMA printed from different concentration PMMA/acetone solutions in a water bath.

Table 2.6. Printing parameters for different concentration PMMA/acetone solutions in a water bath.

Parameters	Values			
PMMA solution concentration (wt%)	25	30	35	40
Layer height (mm)	0.04	0.04	0.04	0.04
Nozzle diameter (mm)	0.30	0.30	0.30	0.30
Printing speed (mm·s^{-1})	5	5	5	5
Line width (mm)	0.40	0.40	0.40	0.40
Pressure (psi)	0.4	1.6	5.0	22

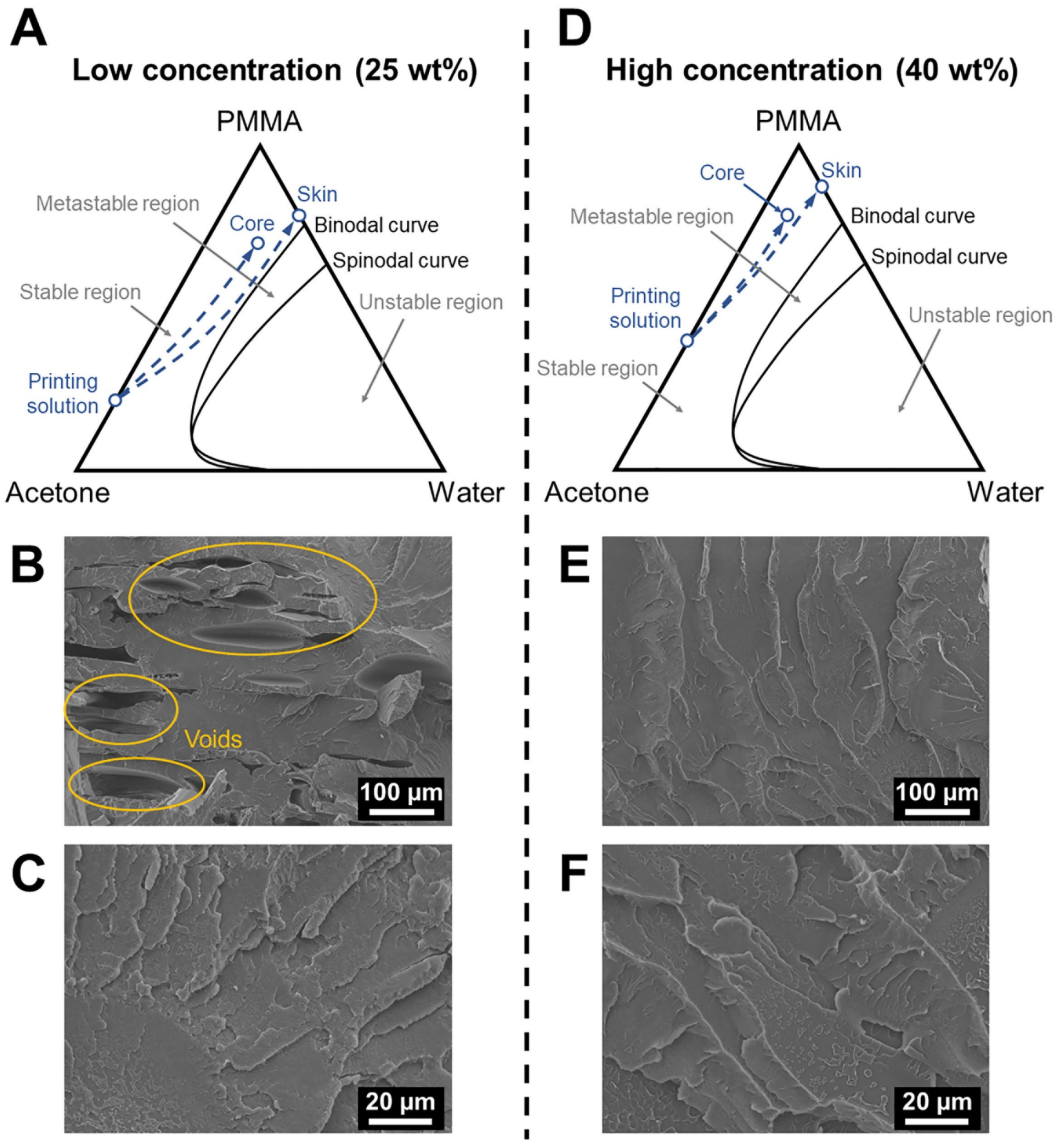

Figure 2.20. Ternary phase diagrams and cross-section SEM images of PMMA printed from low and high concentration solutions. A–C) PMMA printed from a low concentration (25 wt%) solution. D–F) PMMA printed from a high concentration (40 wt%) solution.

To explain the concentration effect, ternary phase diagrams and SEM images of the PMMA cross-sections are presented in Figure 2.20. In Figure 2.20A, when using a low concentration (25

wt%) solution, although the starting point on the PMMA-acetone edge is low, the evolution paths stay in the single phase stable region as mostly dense microstructures in Figure 2.20B and C are observed. The macroscale voids in Figure 2.20B are found mainly on the layer interfaces or gaps between infill lines, which are caused by the insufficient polymer infill between printing lines using low concentration solutions. Specifically, when using a low concentration solution, more acetone and water are trapped inside the printed wet structure, and they tend to form internal voids after drying in this case because the low boiling point acetone and water on the structure outer surface evaporate immediately after removing from the bath and form a dense PMMA shell that has low mobility for contraction (also explained in Chapter 2.5.1). In Figure 2.20D, when using a high concentration (40 wt%) solution, the evolution paths again end in the stable region before crossing the binodal curve, resulting in a dense microstructure. SEM images in Figure 2.20E and F also confirm the fully dense microstructure of PMMA without visible voids, due to a sufficient polymer infill between printing lines. Therefore, in the case of a ternary system where a dense microstructure is usually formed during the NIPS process, like this PMMA/acetone/water system, higher printing solution concentration reduces the defects between printing lines and improves the density of printed polymer. However, as a dense PMMA shell usually immediately forms on the structure outer surface after removing from the bath due to the fast evaporation of surface acetone and water, the dimensional contraction is quickly defined at the same time, which is not influenced by the printing solution concentration.

2.4.2 Poly(vinylidene fluoride)

The effect of printing solution concentration on the precipitation printed PVDF was studied using the PVDF/DMF/water system. The PVDF/DMF printing solution concentration varied from 10 to 25 wt%, and the printing parameters are listed in Table 2.7. After precipitation printing of the same size rectangular specimens as the previous PMMA section, all PVDF specimens were dried at 120 °C for 12 h under vacuum. Figure 2.21 shows the average dimensional contraction and final density of PVDF printed from different concentration solutions. When the PVDF solution concentration increases from 10 to 25 wt%, the average dimensional contraction increases from 10.8% to 16.5%, and the final density also increases from 0.478 to 0.978 $g \cdot cm^{-3}$. Considering the density of neat PVDF that is 1.78 $g \cdot cm^{-3}$, the density percentage of printed PVDF specimens ranges from 27% to 55%.

Table 2.7. Printing parameters for different concentration PVDF/DMF solutions in a water bath.

Parameters	Values			
PVDF solution concentration (wt%)	10	15	20	25
Layer height (mm)	0.04	0.04	0.04	0.04
Nozzle diameter (mm)	0.25	0.25	0.25	0.25
Printing speed (mm·s−1)	7	7	7	7
Line width (mm)	0.20	0.20	0.20	0.20
Pressure (psi)	1.0	2.5	9.5	28

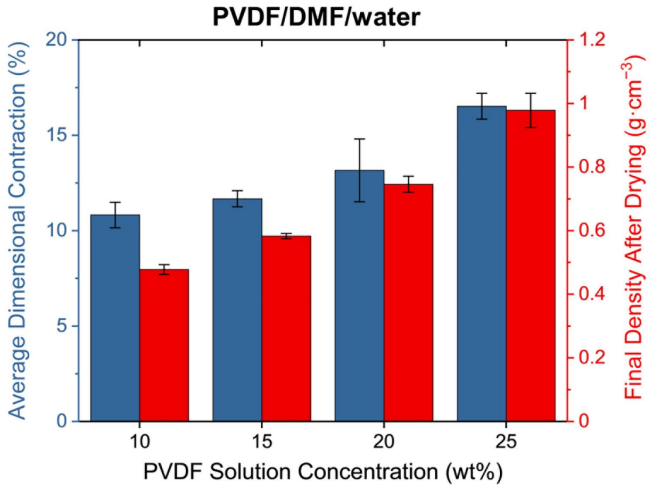

Figure 2.21. Dimensional contraction and final density of PVDF printed from different concentration PVDF/DMF solutions in a water bath.

The dimensional contraction and density trends with respect to the PVDF printing solution concentration can be explained using the ternary phase diagrams in Figure 2.22. In the case of a low concentration (10 wt%) solution, the evolution paths start from the lower end of the PVDF-DMF edge, quickly undergo spinodal decomposition and end in the unstable region with a high fraction of water and DMF (Figure 2.22A). The cross-section SEM images of PVDF printed from this low concentration solution in Figure 2.22B and C exhibit a highly porous microstructure with randomly distributed pores, which verifies the spinodal decomposition mechanism. On the other hand, when using a high concentration (25 wt%) solution, the evolution paths start from a higher point on the PVDF-DMF edge, but still undergo spinodal decomposition (Figure 2.22D). Compared to the low concentration case, the high concentration printing solution has a high viscosity that hinders DMF/water diffusion, which results in higher residual DMF content after precipitation printing. The evaporation of high residual DMF content in a porous PVDF structure during the drying process causes PVDF contraction and densification by capillary forces. This explanation is supported by the cross-section SEM images of PVDF printed from the high

concentration solution in Figure 2.22E and F, where the porous PVDF microstructure produced by spinodal decomposition becomes more compact after contraction compared to the low concentration case in Figure 2.22B and C. Thus, for a ternary system where a highly porous microstructure is formed by spinodal decomposition, such as this PVDF/DMF/water system, higher printing solution concentration increases the dimensional contraction after drying, but also increases the final structure density.

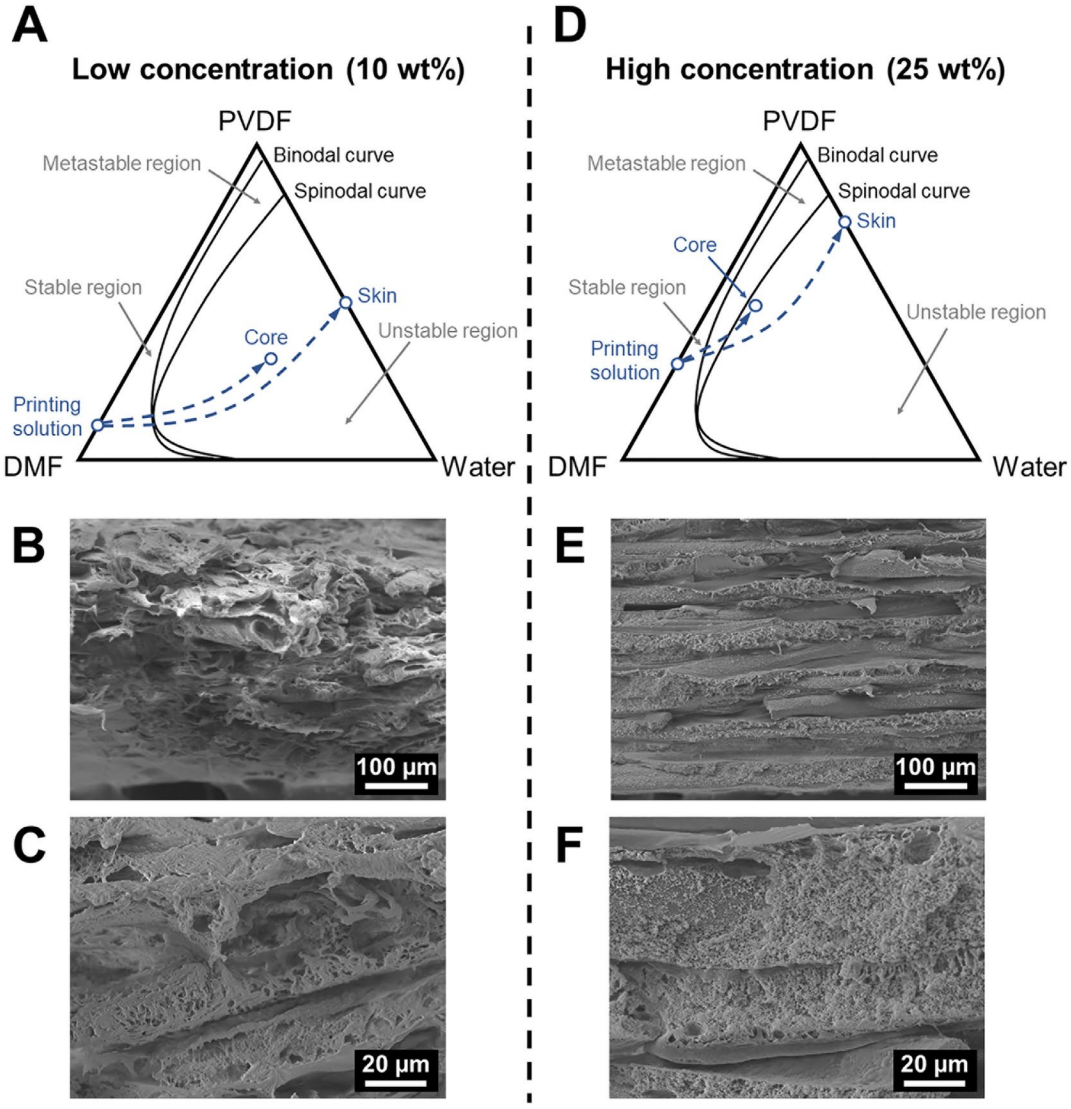

Figure 2.22. Ternary phase diagrams and cross-section SEM images of PVDF printed from low and high concentration solutions. A–C) PVDF printed from a low concentration (10 wt%) solution. D–F) PVDF printed from a high concentration (25 wt%) solution.

2.5 Effect of non-solvent bath temperature

Non-solvent bath temperature is one important environment condition of the precipitation printing process, or specifically the NIPS process. Since the NIPS process is based on mass diffusion, the non-solvent bath temperature affects the kinetics, in particular the diffusivity according to the Stokes-Einstein relation, following the Equation 2.2:

$$\frac{D_{T_1}}{D_{T_2}} = \frac{T_1}{T_2}\frac{\mu_{T_2}}{\mu_{T_1}} \tag{2.2}$$

where D is the diffusivity, T_1 and T_2 are the corresponding temperature in Kelvin, and μ is the dynamic viscosity. As the temperature increases, the dynamic viscosity of the solvent and non-solvent decreases, which further increases the diffusivity in Equation 2.2. In general, higher non-solvent bath temperature can lead to faster solvent/non-solvent exchange and phase separation during the precipitation printing process.

2.5.1 Poly(methyl methacrylate)

To study the non-solvent bath temperature effect on the precipitation printing of PMMA, the PMMA/DMF/PG system was used instead of using acetone as the solvent in the previous section due to the limited temperature range that can be used on acetone (boiling point 56 °C). The testing temperature was controlled by a hot plate under the non-solvent bath and a thermocouple immersed in the non-solvent bath, and four different temperatures (20, 30, 40 and 50 °C) were tested. The printing parameters in Table 2.8 for different temperatures were kept the same. Five 14 mm×8 mm×1 mm rectangular bars were printed for each temperature case, and the corresponding dimensional contraction and final density after 120 °C vacuum drying for 12 h were measured.

Table 2.8. Printing parameters for the PMMA/DMF/PG system with different temperatures.

Parameters	Values
Non-solvent bath temperature (°C)	20, 30, 40 and 50
Solution concentration (wt%)	30
Layer height (mm)	0.06
Nozzle diameter (mm)	0.41
Printing speed (mm·s^{-1})	7
Line width (mm)	0.40
Pressure (psi)	2.5

The results in Figure 2.23 show that as the temperature increases from 20 to 50 °C, the dimensional contraction of printed PMMA reduces significantly from 18.9% to 3.4%, while the final density after drying increases from 0.95 to 1.09 g·cm^{-3}, which is from 80% to 92% of the density of neat PMMA. The mechanism behind these trends is explained using the ternary phase diagrams in Figure 2.24. According to the wet spinning results in Section 2.3.1, since PG is a weak non-solvent for PMMA with a relatively low RED value, the binodal and spinodal curves in Figure 2.24A are far from the PMMA-DMF edge, indicating a large single-phase stable region on the left. In the case of a low non-solvent bath temperature (20 °C), the cross-section SEM images in Figure 2.24B and C exhibit an overall dense PMMA microstructure with few voids. This means the evolution paths in Figure 2.24A end in the single-phase stable region without crossing the binodal curve. The few voids can be caused by insufficient infill between printing lines due to the higher viscosity of the printing solution at low temperatures. Moreover, the low temperature of the NIPS process hinders the core of the printed PMMA from completing DMF/PG exchange, which results in an evolution end point with a large amount of residual DMF. The high dimensional contraction in the low temperature case is also attributed to the evaporation of DMF during the drying process.

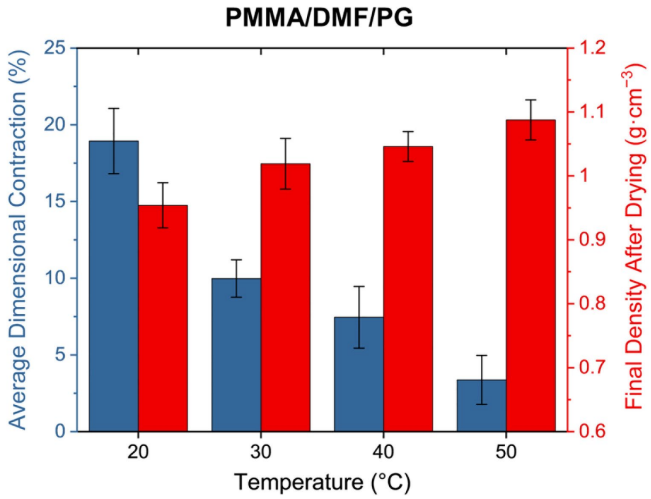

Figure 2.23. Dimensional contraction and final density of PMMA printed from the PMMA/DMF/PG system with different temperatures.

On the other hand, when using a high temperature (50 °C), the binodal and spinodal curves in Figure 2.24D move further away from the PMMA-DMF edge, due to the higher solubility of polymers in both the solvent and non-solvent under a higher temperature [223,224]. In this larger single-phase stable region, the PMMA solution undergoes a single-phase gelation process without phase separation, which again results in the dense and compact microstructure in Figure 2.24E and

F. The PMMA printing solution has lower viscosity at higher temperatures, which ensures better infill quality between printing lines and explains the density improvement. Because of the higher diffusivity at this temperature, the end point of the evolution path for the printed PMMA core region has less DMF than the low temperature case, and the dimensional contraction decreases.

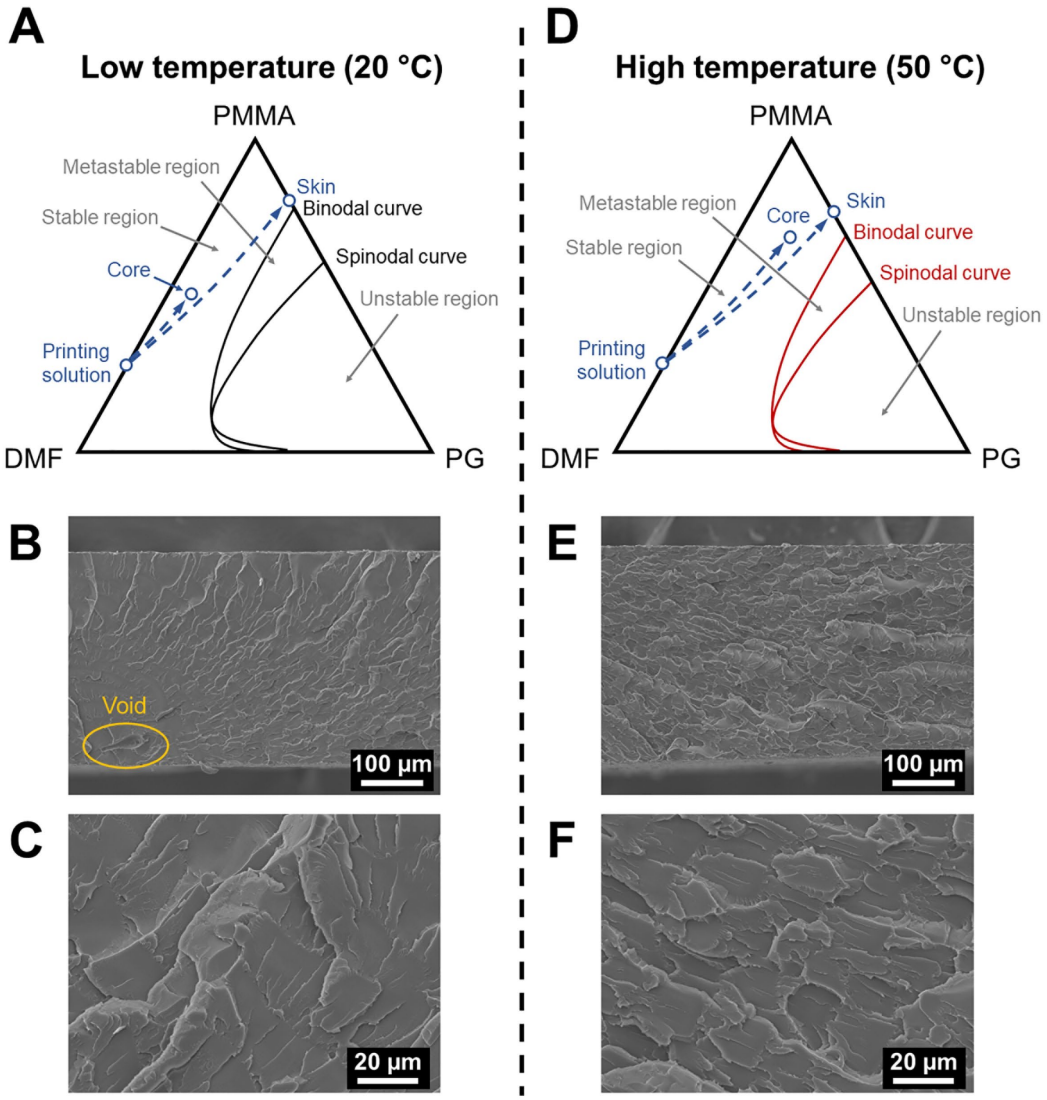

Figure 2.24. Ternary phase diagrams and cross-section SEM images of PMMA printed at low and high temperatures. A–C) PMMA printed at a low temperature (20 °C). D–F) PMMA printed at a high temperature (50 °C).

It is worth mentioning that for the PMMA/DMF/PG system, the residual DMF trapped inside the printed PMMA can cause significant contraction, which is different from the generally low level of contraction (below 5%) in the PMMA/acetone/water system (Section 2.4.1). This is because both DMF and PG have high boiling points and low vapor pressures. When using a 120 °C vacuum oven for drying, the PMMA molecules have a high mobility above its T_g (100 °C), while trapped DMF and PG can move towards the surface of the structure and evaporate slowly.

This slow but relatively uniform drying process is the cause of contraction and densification (Figure 2.25). However, as explained in Section 2.4.1, in the case of the PMMA/acetone/water system, acetone and water have low boiling points and high vapor pressures. After being removed from the water bath, the printed PMMA outer surface dries out quickly even at room temperature, which forms a dense PMMA shell on the outer surface that defines the dimensional contraction. When using an 80 °C vacuum oven for drying, the evaporation of the internally trapped acetone and water then leads to the formation of internal voids.

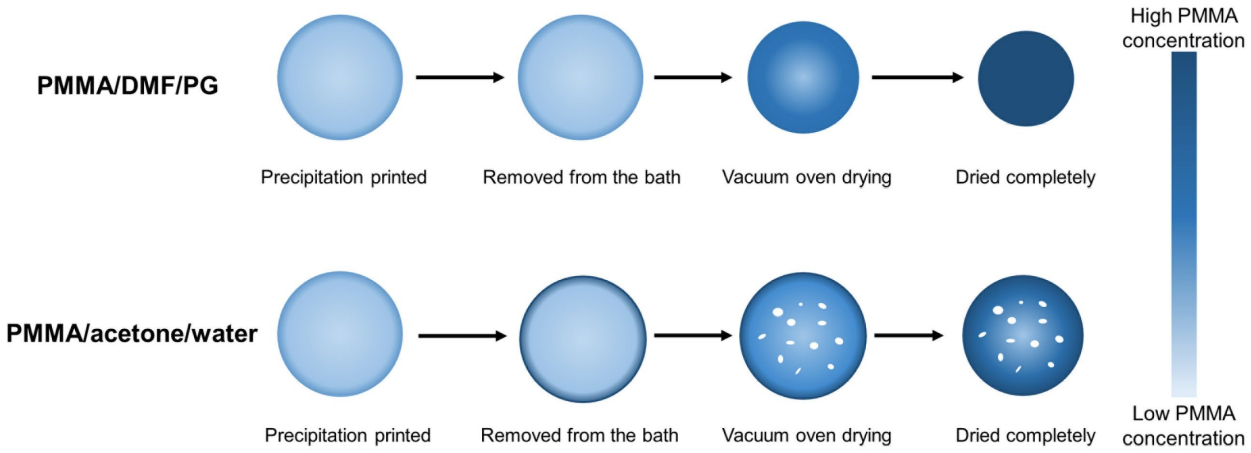

Figure 2.25. Explanation of the different PMMA contraction after drying using the PMMA/DMF/PG system and the PMMA/acetone/water system.

2.5.2 Poly(vinylidene fluoride)

The non-solvent bath temperature effect on the precipitation printing of PVDF was studied using the PVDF/DMF/water system, and the printing parameters are tabulated in Table 2.9. It should be noted that two sets of printing pressure were tested, one is constant pressure for all temperatures, the other is different pressures for different temperatures to maximize infill. Rectangular specimens were printed for each temperature case, and the corresponding dimensional contraction and final density after 120 °C vacuum drying for 12 h were calculated.

Table 2.9. Printing parameters for the PVDF/DMF/water system with different temperatures.

Parameters	Values
Non-solvent bath temperature (°C)	20, 30, 40 and 50
Solution concentration (wt%)	20
Layer height (mm)	0.04
Nozzle diameter (mm)	0.30
Printing speed (mm·s−1)	7
Line width (mm)	0.20
Pressure (psi)	Indicated in Figure 2.26

In Figure 2.26A, if using a constant 3.0 psi pressure for PVDF printing, the dimensional contraction reduces from 15.4% to 11.7% when the temperature increases from 20 to 50 °C. However, the final density of PVDF does not have a significant change around 0.7 $g \cdot cm^{-3}$ with respect to temperature (ANOVA $p = 0.15$). This is mainly caused by the fast phase separation (spinodal decomposition) of the PVDF/DMF/water system which usually produces a highly porous microstructure according to the wet spinning results in Section 2.3.3. When at a low temperature (20 °C) in Figure 2.27A, the binodal and spinodal curves are very close to the PVDF-DMF edge since water is an extremely strong non-solvent with a high RED value to PVDF. Inevitable spinodal decomposition makes both the printed PVDF core and skin porous (Figure 2.27B and C), but low diffusivity at this temperature causes a high remaining DMF content in the core. When at a high temperature (50 °C), although the binodal and spinodal curves shift away from the PVDF-DMF edge (Figure 2.27D), cross-section SEM images in Figure 2.27E and F suggest that the evolution paths of PVDF still undergo the spinodal decomposition, no matter the core or the skin. The higher temperature's effect on the PVDF evolution path is the extended end point for the core towards the PVDF-water edge, due to a more complete DMF/water exchange. The evaporation of lower residual DMF content in a porous PVDF structure during the drying process causes the lower PVDF contraction at higher temperatures. However, since the deposited amount of PVDF in each rectangular specimen also increases slightly at higher temperatures as a constant pressure is applied to the printing solution with reduced viscosity, the final density after considering contraction does not change much.

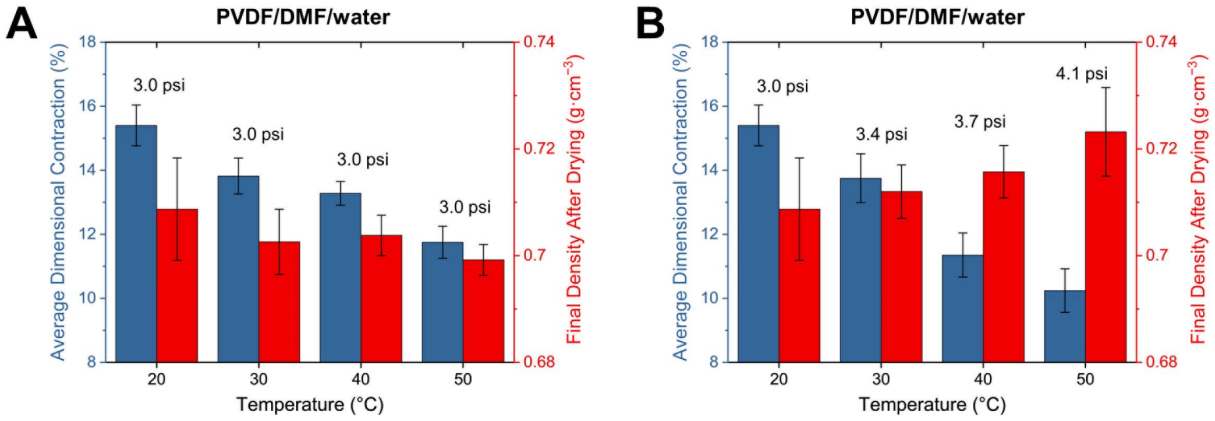

Figure 2.26. Dimensional contraction and final density of PVDF printed from the PVDF/DMF/water system with different temperatures. A) Using a constant pressure of 3.0 psi for different temperatures. B) Using different pressures (3.0–4.1 psi) for different temperatures to maximize infill.

In addition to the constant pressure printing, the other set of tests was performed by adjusting the pressure for maximum infill at different temperatures. Having a highly porous microstructure allows additional infill to reduce the porosity of a previous layer by filling its pores with the higher-pressure printing solution and the solvent welding process. Figure 2.26B shows the dimensional contraction and final density of PVDF printed using increased pressure (from 3.0 to 4.1 psi) when the non-solvent bath temperature increases. Because the solvent/non-solvent exchange is faster at higher temperatures, pores are formed more completely during the same period (here is the time to print each layer) and can be filled again with the higher-pressure printing solution. Moreover, at each temperature, the solvent welding performance also improves as the pressure increases, but the pressure is limited by avoiding printing solution overflow to the surrounding area. Therefore, the results in Figure 2.26B show that after adjusting the pressure, the dimensional contraction reduces from 15.4% to 10.2% when the temperature rises from 20 to 50 °C, and the final density of printed PVDF increases from 0.709 to 0.723 $g \cdot cm^{-3}$ (ANOVA $p = 0.03$).

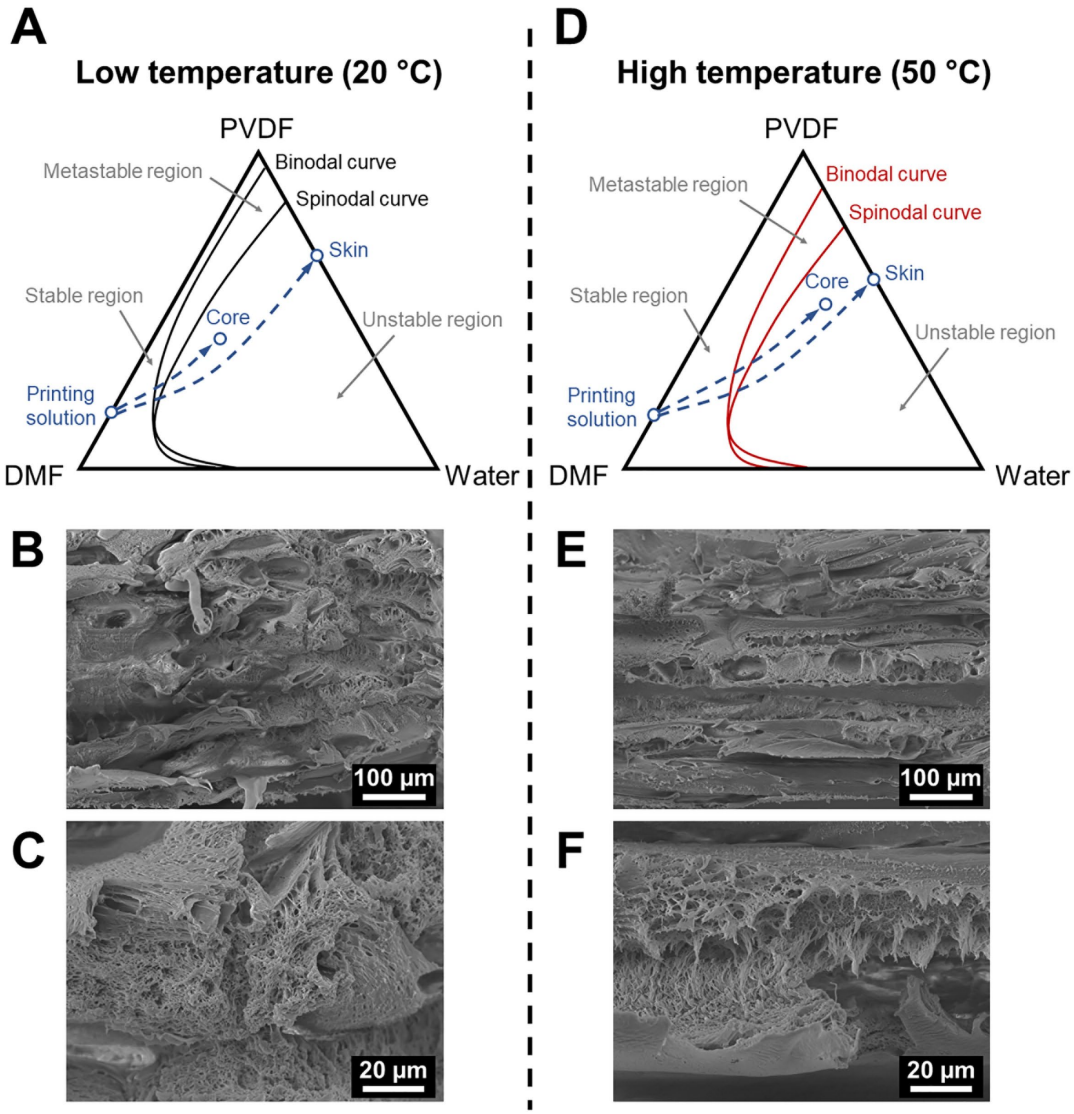

Figure 2.27. Ternary phase diagrams and cross-section SEM images of PVDF printed at low and high temperatures. A–C) PVDF printed at a low temperature (20 °C) with a 3.0 psi pressure. D–F) PVDF printed at a high temperature (50 °C) with a 3.0 psi pressure.

2.6 Chapter summary

In this chapter, the concept and mechanism of precipitation printing were formally presented and explained. Precipitation printing is a solvent-based additive manufacturing method that utilizes the precipitation, or phase separation of solvated polymer in a non-solvent coagulation bath for solidification. The printing solution is dispensed in the non-solvent bath with computer-designed printing paths controlled by a programmed gantry system, and the layer-by-layer fabrication of 3D structures is enabled through solvent welding as the joining mechanism. The detailed laboratory setup for the precipitation printing process, the selection of solvents and non-solvents for a target polymer were discussed in this chapter. The effects of multiple precipitation

printing conditions on the microstructure, density and mechanical properties of two representative thermoplastics, PMMA and PVDF, were investigated comprehensively and explained using ternary phase diagrams. As a result, a stronger solvent with lower RED to the polymer based on the Hansen solubility parameters is preferred for stronger interfacial bonding and less porous microstructure. A strong non-solvent with a high RED value and high diffusivity usually leads to porous microstructures of printed polymer due to spinodal decomposition or metastable liquid-liquid demixing, while a weak non-solvent with a low RED value and low diffusivity can produce dense microstructures via the single-phase gelation process. Moreover, the density of the printed structure generally increases as the printing solution concentration increases, but the trend of dimensional contraction with respect to the concentration depends on the evaporation rate and boiling point of the solvent and non-solvent pair. Finally, the dimensional contraction of the printed polymer after drying reduces as the non-solvent bath temperature increases during the precipitation printing process. The development of precipitation printing provides a new approach to additively manufacture thermoplastic polymers at relatively low temperatures (typically 20–50 °C), especially for those thermally unstable or high melting point polymers. The study of the effects of various printing conditions offers a guide to design and tailor the microstructure, porosity and mechanical properties of precipitation printed materials for specific applications.

Chapter 3 Precipitation Printing of High-Performance Engineering Polymers

3.1 Chapter introduction

In Chapter 3, precipitation printing is applied to high-performance engineering thermoplastics. As a solvent-based additive manufacturing process, solvent power is used to dissolve high-performance thermoplastics in the precipitation printing process instead of using thermal energy to melt thermoplastics in material extrusion and powder bed fusion processes. Thus, precipitation printing can be performed at room temperature, while the temperature required to subsequently evaporate solvent and non-solvent is significantly lower than the melt processing temperature. In the first half of Chapter 3, precipitation printing is performed on polysulfone (PSU), a high-performance amorphous thermoplastic. By selecting different solvent/non-solvent pairs and using different PSU solution concentrations, the microstructure and porosity of the precipitation printed PSU can be tailored to be either highly porous or fully dense. In particular, the mechanical properties of precipitation printed fully dense PSU are comparable to the solvent cast PSU films from the same source, and the anisotropy of printed PSU specimens in different directions is much lower than high-performance polymers produced by material extrusion. Furthermore, the glass transition temperature and thermal stability of the printed PSU samples are measured to show that they can be used in high-temperature environments.

In the second half of Chapter 3, additive manufacturing of all-aramid 3D structures is achieved for the first time through simultaneous precipitation printing and protonation of aramid nanofiber (ANF) solution (printing ink). The ANF printing ink is prepared through a deprotonation and dissolution process of Kevlar® fabric using a potassium hydroxide (KOH)/dimethyl sulfoxide (DMSO)/water system [225–227]. When printing the prepared high concentration ANF printing inks in propylene glycol (as a weak non-solvent and a proton donor), the ANFs can precipitate and protonate simultaneously to form 3D wet ANF structures. Followed by subsequent washing in water and drying, wet ANFs can assemble into solid all-aramid 3D structures through capillary

force, hydrogen bonding and π-π stacking induced self-assembly. To the author's knowledge, this work is the first demonstration of additive manufacturing of all-aramid 3D structures through ANF self-assembly, which possess unprecedented thermal and mechanical properties compared to all existing unfilled polymeric materials fabricated by additive manufacturing. Therefore, precipitation printing provides a unique additive manufacturing approach to fabricate high-performance polymeric structures for specific applications in extreme environments.

3.2 Precipitation printing of polysulfone

3.2.1 Ternary system selection

In the precipitation printing process, the polymer/solvent/non-solvent ternary system selection dictates the solution evolution path during the non-solvent induced phase separation (NIPS) and the microstructure formation of printed polymer, which has been explained in Chapter 2. In this section, the target high-performance thermoplastic is polysulfone (PSU), and the raw material is in the form of PSU pellets (Udel® P-3500, Solvay). As presented in Chapter 2, Hansen solubility parameter is a widely used method to predict the solubility of polymers in solvents. To select the compatible solvents for PSU, a table of Hansen solubility parameters and relative energy difference (RED) of some common solvents relative to PSU is shown below (Table 3.1) [200]. According to the convention that solvents with RED less than one can likely dissolve PSU, *N,N*-dimethylformamide (DMF), 1-methyl-2-pyrrolidinone (NMP) and tetrahydrofuran (THF) were selected and then successfully tested as the three solvents in this work. Moreover, solvent welding is the bonding mechanism between adjacent infill paths and layers during precipitation printing [204,209,210]. A solvent with lower RED value usually indicates faster PSU dissolution and higher PSU solubility, which can result in a stronger solvent welding strength. Thus, Hansen solubility parameters in Table 3.1 are further used to explain the printability and interfacial bonding of PSU printed with different solvents later in this section.

Table 3.1. Hansen solubility parameters and RED of common solvents relative to PSU.

	δ_d ($MPa^{0.5}$)	δ_p ($MPa^{0.5}$)	δ_h ($MPa^{0.5}$)	RED relative to PSU
PSU	19.7	8.3	8.3	/
N,N-dimethylformamide	17.4	13.7	11.3	0.96
Dimethyl sulfoxide	18.4	16.4	10.2	1.09
N-methyl-2-pyrrolidinone	18.0	12.3	7.2	0.67
Tetrahydrofuran	16.8	5.7	8.0	0.80
Acetone	15.5	10.4	7.0	1.09

3.2.1.1 Casting solution phase inversion time study

For the non-solvent, two nontoxic liquids, water and propylene glycol (PG) were used as the coagulation bath. The NIPS behavior of PSU solutions from three different solvents in the two non-solvent baths were first investigated through casting solution phase inversion time study. Three 25 wt% solutions were prepared by dissolving the PSU pellets in DMF (certified ACS, Fisher Chemical), NMP (99+%, Thermo Scientific) and THF (certified ACS, Fisher Chemical), respectively, through bath sonication (Branson 2800) for 5–8 h. After complete dissolution, the three solutions were cast on individual glass slides using a doctor-blade method (constant solution thickness of 50 μm) and immersed in two baths, water (deionized) and PG (99.9%, SK picglobal), then the time for PSU phase inversion was recorded. As a result, in Figure 3.1, all cast solutions have a transparent color on the glass slides before immersion in the non-solvent (recording time t = 0 s). When immersed in a water bath, PSU/DMF (here PSU/solvent represents a solution) has a sudden change of color to bright white in as little as 1 second, while PSU/NMP has a color change to light grey first at t = 1 s and slowly to white until t = 5 s. PSU/THF has a slow color change after water immersion, forming a translucent film after 30 seconds. Since a more white and opaque color of the film indicates a higher film porosity due to a faster precipitation or phase separation rate, the precipitation rate of the PSU/DMF/water (meaning PSU/solvent/non-solvent) system is faster than the PSU/NMP/water system and much faster than the PSU/THF/water system. On the other hand, when a weaker and more viscous non-solvent PG is in the coagulation bath, all three PSU solutions show slower color change than in the water baths. PSU/DMF can stay transparent for 1 second, and PSU/NMP can keep transparent for 5 seconds in PG, while PSU/THF does not have color change in 30 seconds. The phase inversion time results can provide a basic idea of how solvent/non-solvent pair affects the PSU precipitation rate and guidance to find the suitable pair for precipitation printing.

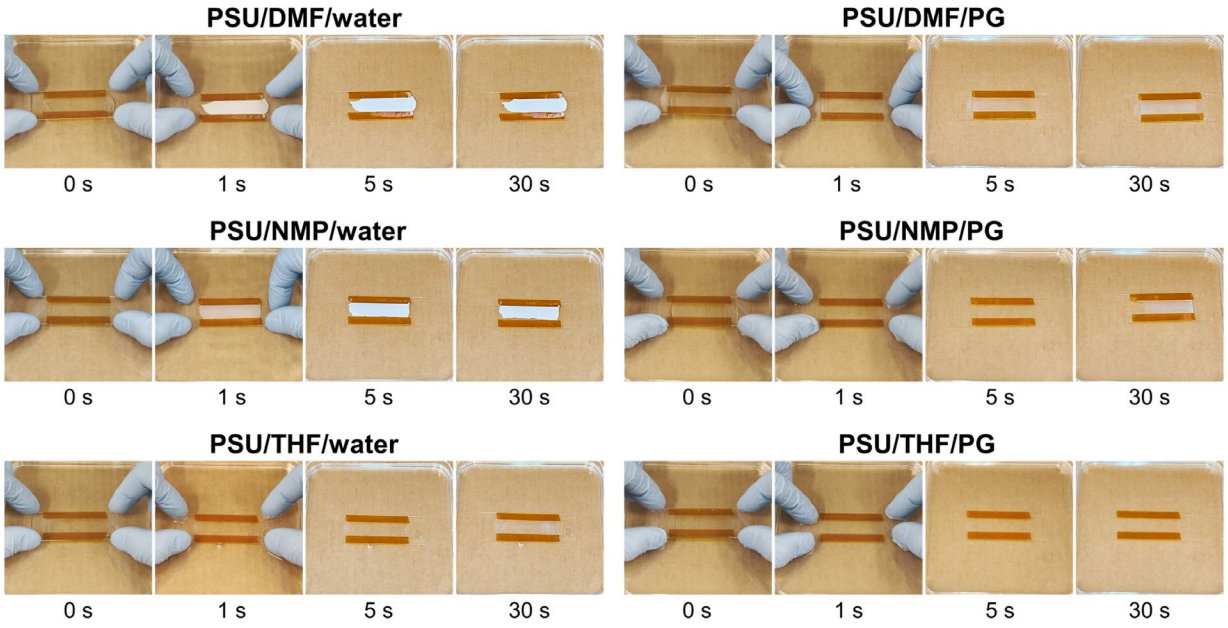

Figure 3.1. Phase inversion time of cast PSU solutions from three types of solvents in two types of non-solvent baths.

3.2.1.2 Wet spinning study

After the phase inversion time study, wet spinning of the three PSU solutions in water and PG was performed to investigate the solvent/non-solvent effect on PSU microstructures. The three solutions were loaded in 10 mL syringes with 26-gauge nozzles (0.254 mm inner diameter) for PSU fiber wet spinning in 500 mL beakers filled with water or PG, using a pressure of 40 psi (276 kPa). Figure 3.2 shows the wet spinning process of the six PSU/solvent/non-solvent systems and the length of gel-state fiber before complete precipitation or solidification. A long gel-state fiber implies slower precipitation or phase separation rate. Here, the gel-state fiber length agrees with the phase inversion time study, where gel-state fibers are longer in PG than in water for all three types of solutions.

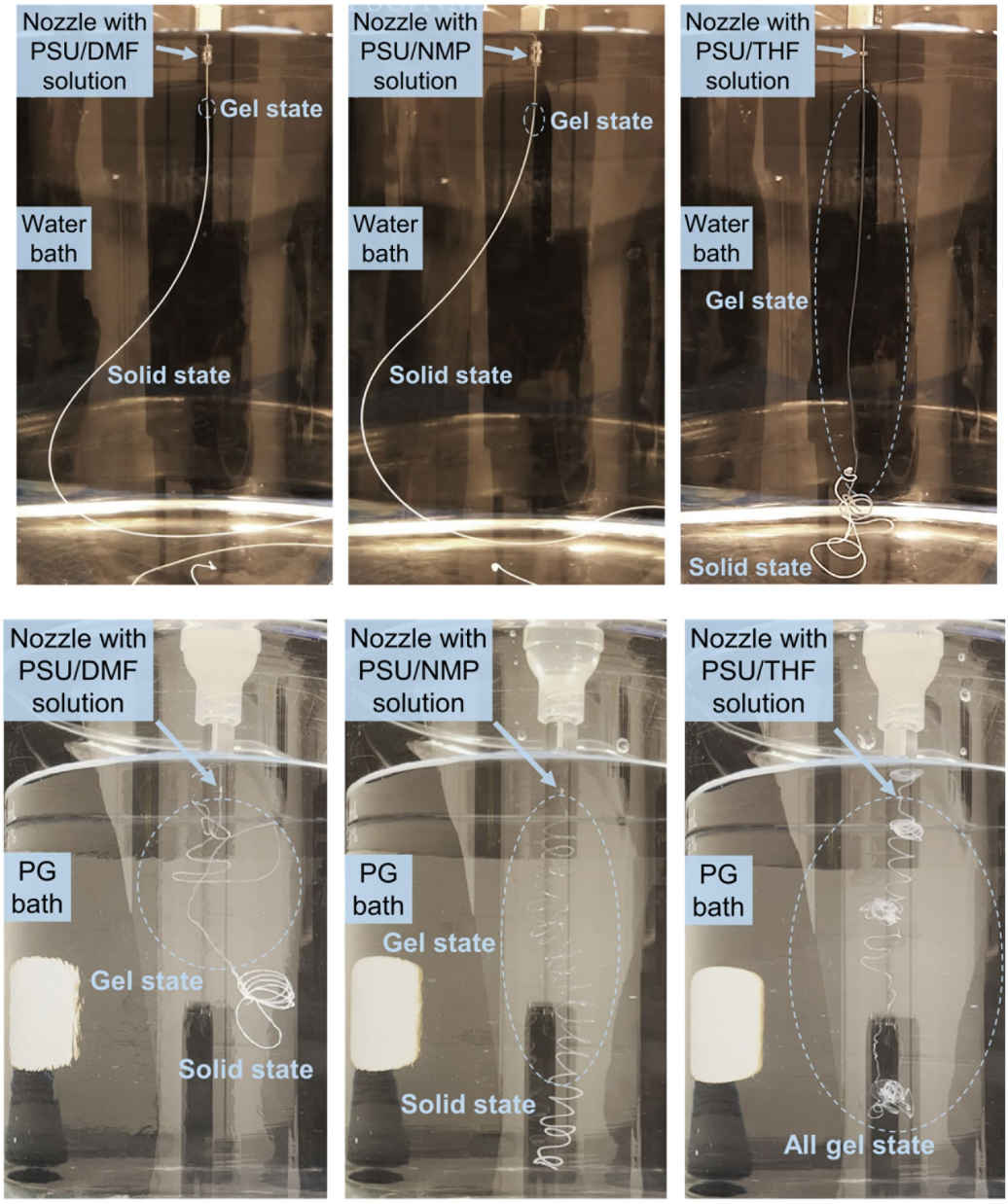

Figure 3.2. Wet spinning process of different PSU solutions in water and PG baths. The dashed circles are the gel-state fibers before complete precipitation or solidification.

The wet spun PSU fibers were collected and dried at 160 °C overnight, and their tensile fracture cross-sections were examined by a scanning electron microscope (SEM, JEOL JSM-7800FLV). The resulting cross-section microstructures are displayed in Figure 3.3. In the cases of fibers from the PSU/DMF/water and PSU/NMP/water systems, the cross-section shape remains circular (same as the nozzle shape) due to the fast precipitation rate, especially on the fiber surface. The ternary phase diagram in Figure 3.4A can be used to explain the porous microstructure formation in these two cases. Low viscosity and high miscibility of DMF, NMP and water allow

rapid mutual diffusion between the solvent and non-solvent at the fiber surface, and the PSU solution quickly undergoes a spinodal decomposition and forms a slightly porous skin layer with micropores. The internal solvent in the wet fiber has the tendency to diffuse towards the fiber skin, which leads to the formation of large finger-shaped pores from the fiber center [217]. The evolution path of the wet fiber core in the ternary phase diagram usually stops at a point before reaching the right edge, since the mutual diffusion between the solvent and non-solvent eventually turns into a steady state. In contrast to the PSU/DMF/water and PSU/NMP/water systems, fibers from the other four solvent/non-solvent pairs have noncircular and less porous cross-sections due to a slower mutual diffusion process between THF and water, or between all three solvents and PG, which makes the evolution paths bypass spinodal decomposition (Figure 3.4B–E). In particular, fibers from the PSU/NMP/PG, PSU/THF/water and PSU/THF/PG systems have fully dense microstructures, which are potentially suitable for dense PSU structure printing.

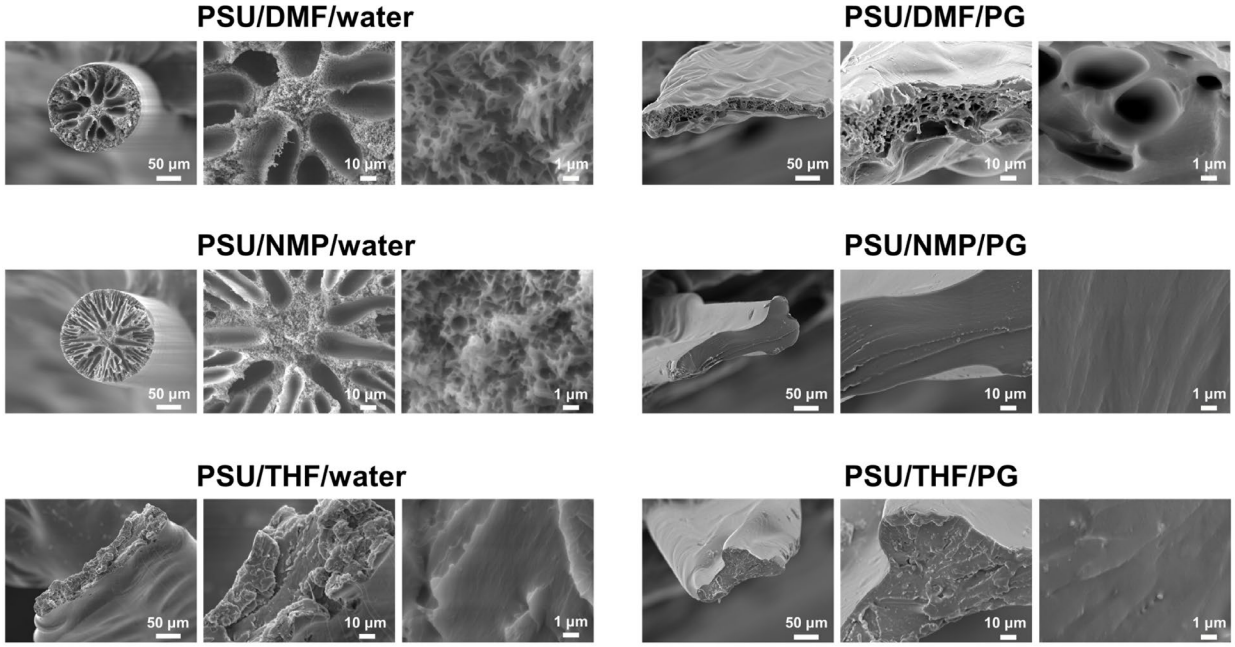

Figure 3.3. SEM images of the cross-sections of PSU fibers obtained from wet spinning of three PSU solutions in two types of non-solvent baths.

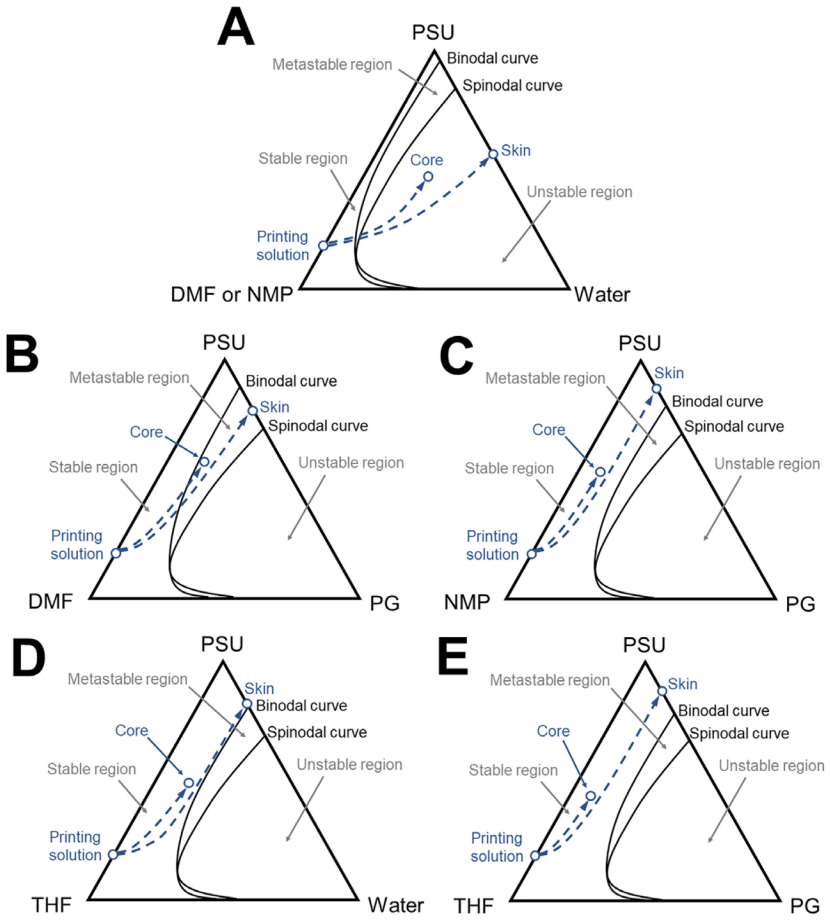

Figure 3.4. Ternary phase diagrams to explain the microstructure formation. A) Highly porous microstructure from the PSU/DMF/water or PSU/NMP/water system. B) Less porous microstructure from the PSU/DMF/PG system. C) Dense microstructure from the PSU/NMP/PG system. D) Dense microstructure from the PSU/THF/water system. E) Dense microstructure from the PSU/THF/PG system.

However, preliminary precipitation printing tests using the PSU/THF solution showed that PSU structures printed from both the PSU/THF/water and PSU/THF/PG systems formed a highly solidified nonporous surface layer due to the fast evaporation of surface THF, which acts as a shell and prevents the internal solvent and non-solvent from moving outside the structure (a printed cube as an example in Figure 3.5A and mechanism explanation in Figure 3.5C). During the drying process, the residual solvent and non-solvent were trapped inside the samples and formed internal bubbles when evaporated, resulting in damaged samples (Figure 3.5B). In contrast, no bubble formation was observed during the drying process of the PSU structures printed from the PSU/NMP/PG system, due to slower and more uniform drying attributed to the high boiling point and low vapor pressure of NMP and PG (Figure 3.5C). Therefore, only the PSU/NMP/PG system was selected for the dense PSU structure printing.

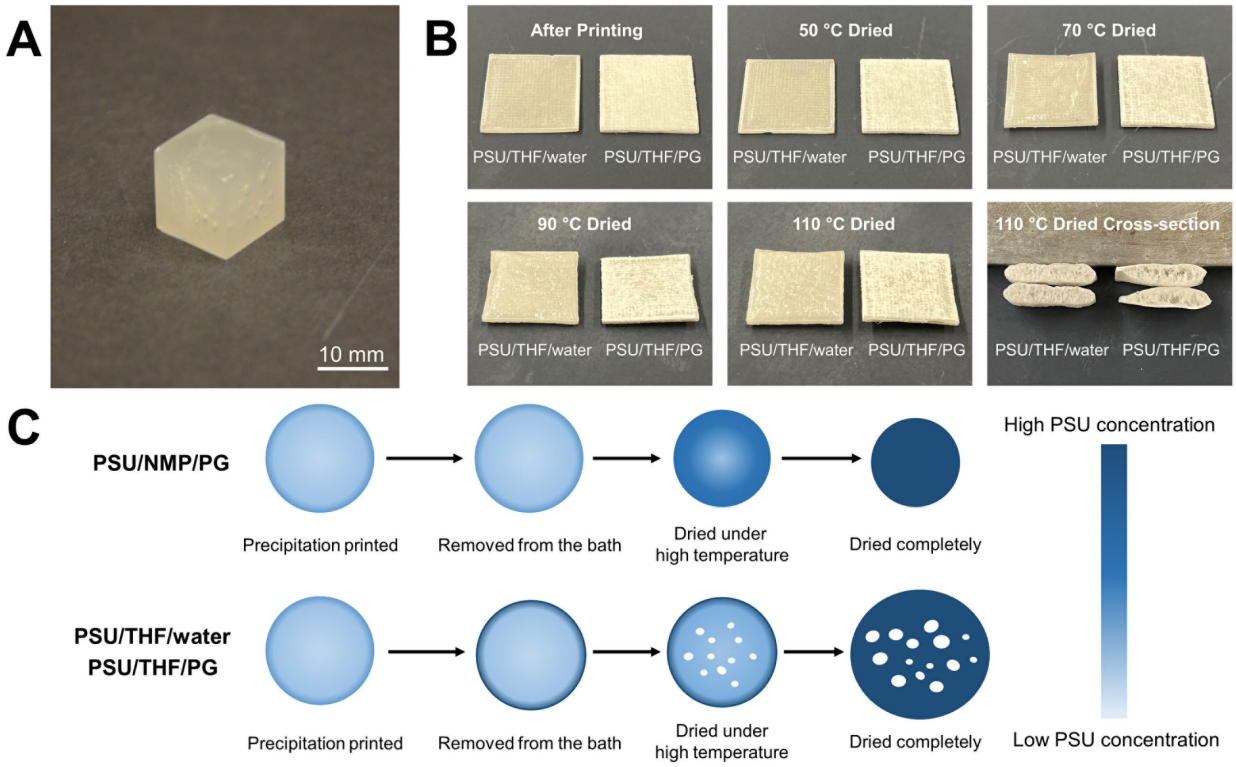

Figure 3.5. A) A cube printed from the PSU/THF/water system. B) Printed square PSU samples from the PSU/THF/water and PSU/THF/PG systems show internal bubble forming during the drying cycle. C) Drying path explanation of precipitation printed structures from the PSU/NMP/PG and PSU/THF/water or PG systems.

3.2.1.3 Solvent selection for porous structure printing

For porous PSU structure printing, a fast precipitation system such as PSU/DMF/water can be adopted. However, unlike the phase inversion and wet spinning studies where single layer or single fiber PSU samples are formed, the 3D printability of porous PSU structures also depends on the effectiveness of interfacial bonding between the adjacent infill paths and layers through the solvent welding mechanism [204,209,210]. Due to the high RED value of DMF in Table 3.1 and a fast DMF diffusion rate into water, solvent welding using DMF during the precipitation printing process does not provide sufficient interfacial bonding strength for continuous printing. In Figure 3.6, when using pure DMF as the solvent, the precipitated PSU does not bond to the doctor-bladed PSU film substrate and disintegrates since the diffusion of DMF into the water is too fast for enough solvent welding. Thus, for more stable porous PSU structure printing in a water bath, THF (lower RED than DMF and slower diffusion into water) was mixed with DMF to form a hybrid solvent for PSU and improve the effectiveness of solvent welding. Four different mixing ratios (DMF wt%:THF wt% = 20:80, 40:60, 60:40 and 80:20) were tested for printability, and the results show that more than 40 wt% THF is needed for sufficient interlayer bonding (Figure 3.6). Since

more THF in the hybrid solvent can also result in less porosity of printed PSU according to the wet spinning study, 60DMF40THF (DMF wt%:THF wt% = 60:40) was finally selected as the solvent for porous PSU printing in a water bath, considering both the porosity and printability.

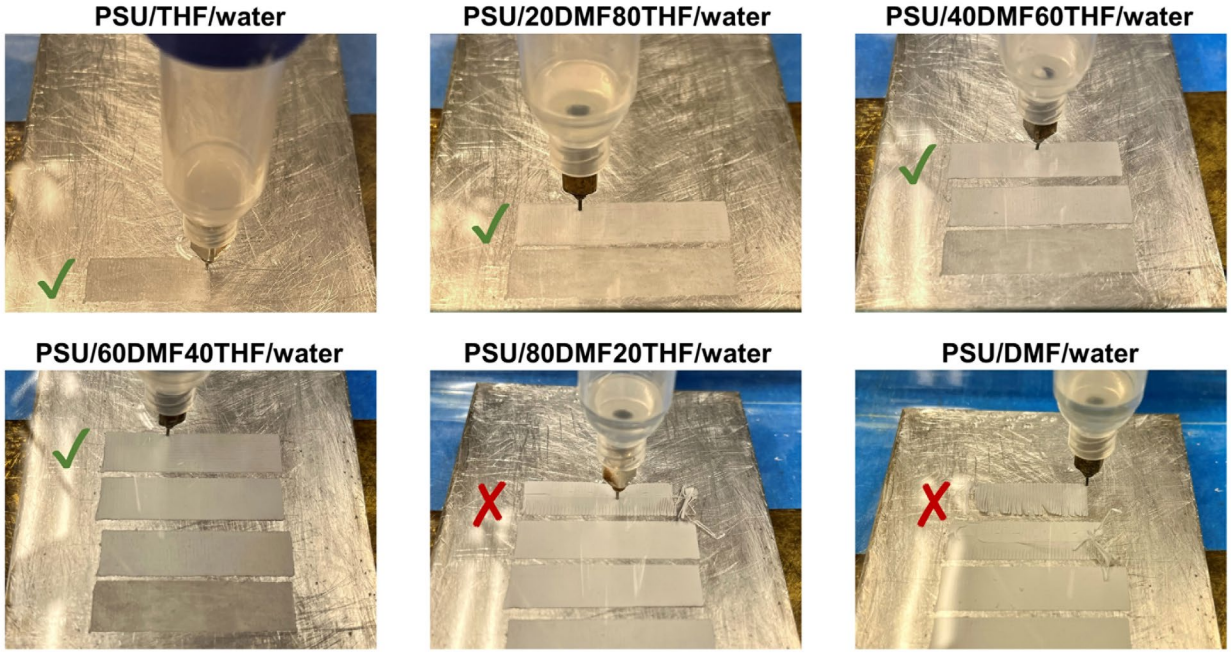

Figure 3.6. Printability tests of PSU dissolved in 6 different solvents: pure THF, 20DMF80THF, 40DMF60THF, 60DMF40THF, 80DMF20THF and pure DMF. Water is the coagulation bath.

3.2.2 Precipitation printing and post-processing conditions

Based on the ternary system selection, two types of PSU/solvent/non-solvent systems were prepared for the precipitation printing of dense and porous PSU structures. A 35 wt% PSU/NMP solution paired with PG as the coagulation bath was selected for dense PSU printing, and a 20 wt% PSU/60DMF40THF solution paired with water was used for porous PSU printing. The prepared PSU solutions were loaded in a 10 mL syringe with a 22-gauge nozzle (0.40 mm inner diameter), which was attached to a gantry system (AGS1500, Aerotech) and a high-precision dispenser (Ultimus V, Nordson EFD). A metal plate with a thin layer of doctor-bladed PSU film was immersed in the coagulation bath (water or PG) as the printing substrate (Figure 3.7A and B). Two sacrificial raft layers were used for all prints to improve the printing substrate adhesion. The detailed printing parameters for different solvent/non-solvent pairs are listed in Table 3.2. After precipitation printing, the printed samples were cut from the metal plate and dried following the drying cycles in Figure 3.7C, which has a maximum temperature of 190 °C for dense PSU and 160 °C for porous PSU.

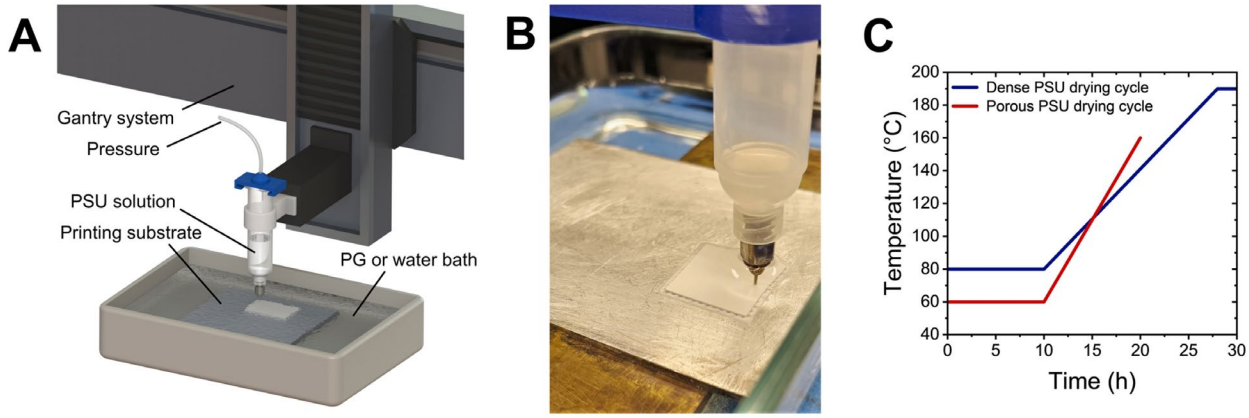

Figure 3.7. A) Precipitation printing setup for PSU. B) A photo showing the printing process of a square PSU sample. C) Drying cycles of the dense and porous PSU.

Table 3.2. Precipitation printing parameters for both dense and porous PSU samples.

Dense PSU							
Solvent	Non-solvent	Weight fraction (wt%)	Nozzle gauge	Layer height (μm)	speed ($mm \cdot s^{-1}$)	Line width (mm)	Pressure (psi)
NMP	PG	20	22	25	7	0.4	1
NMP	PG	25	22	25	7	0.4	3
NMP	PG	30	22	25	7	0.4	10
NMP	PG	35	22	25	7	0.4	30
NMP	PG	35	24	20	5	0.35	85
NMP	PG	35	30	20	3	0.15	80
Porous PSU							
60DMF40THF	water	20	22	30	6	0.4	0.6
60DMF40THF	water	25	22	30	6	0.4	1.6
60DMF40THF	water	30	22	30	6	0.4	3
60DMF40THF	water	35	22	30	6	0.4	8
60DMF40THF	water	20	24	30	6	0.4	1.3
60DMF40THF	water	20	30	20	4	0.15	6
60DMF40THF	water	20	30	20	8	0.1	6

3.2.3 Dimensional contraction and density of printed polysulfone

As a solvent-based printing method, precipitation printed PSU samples have unavoidable dimensional contraction after the removal of solvents, especially for dense PSU samples. During the precipitation printing of PSU/NMP in a PG bath, a slow diffusion rate causes some NMP to remain inside the printed PSU structure after being removed from the PG bath. In the subsequent drying process, the residual NMP moves out of the PSU structure gradually and uniformly due to its low vapor pressure, resulting in a dense PSU structure with uniform dimensional contraction (Figure 3.5C). The dimensional contraction was measured by taking the average of the contractions in three different dimensions. The effect of solute weight fraction on the dense structure

contraction was tested by printing 20, 25, 30, and 35 wt% PSU/NMP solutions in a PG bath. It should be noted that solutions with PSU content lower than 20 wt% are not considered since the viscosity is too low for dispensing pressure control, and solutions with PSU content higher than 35 wt% cannot be obtained in a lab scale mixing equipment. In Figure 3.8A, the average dimensional contraction of printed PSU after the drying cycle reduces from 24% to 11% when the PSU weight fraction is increased from 20 wt% to 35 wt%. This finding indicates that with a higher PSU weight fraction, less NMP needs to diffuse into PG or evaporate during the drying cycle, resulting in a lower contraction. Thus, 35 wt% PSU/NMP is used in this work for dense PSU printing with minimal contraction. The measured density of the printed and dried dense PSU is 1.22±0.11 $g \cdot cm^{-3}$, within a 5% difference compared to the density of the PSU pellets (1.24 $g \cdot cm^{-3}$).

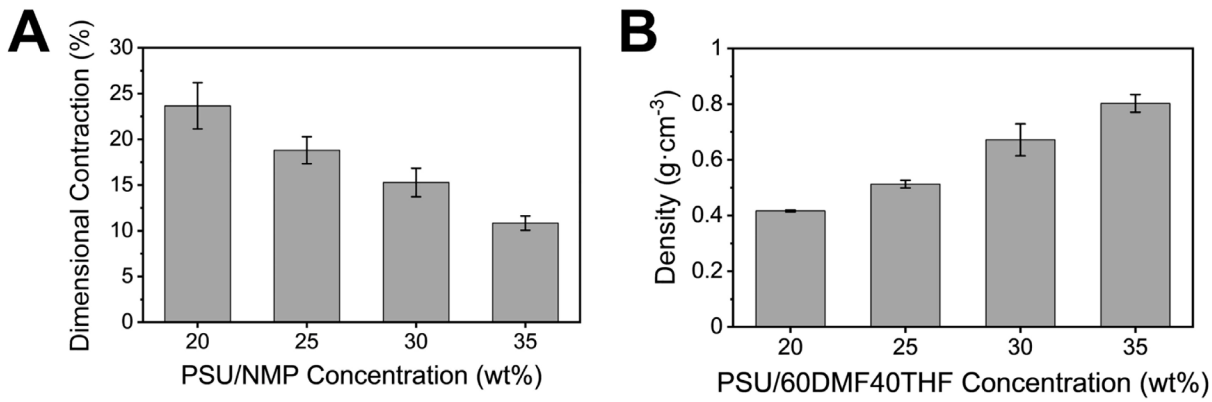

Figure 3.8. A) Dimensional contraction of dense PSU printed from PSU/NMP solutions with different solute weight fractions in a PG bath. B) Density of porous PSU printed from PSU/60DMF40THF solutions with different solute weight fractions in a water bath.

Nevertheless, when using the PSU/60DMF40THF/water system to print porous PSU structures, dimensional contraction is not significant (all within 6%) due to the fast diffusion of solvents into water that completes the precipitation. Instead, the solute weight fraction influences the final structure density and porosity. The density of printed 100%-infilled porous PSU samples using 20, 25, 30, and 35 wt% PSU/60DMF40THF solutions in a water bath is shown in Figure 3.8B. As the solute weight fraction increases, the density of the porous sample increases, which agrees with the results in Chapter 2 and also from Karyappa et al. using other polymer/solvent/non-solvent systems [212]. This trend can be explained that a lower solute weight fraction solution has a lower viscosity, which promotes the solvent/non-solvent diffusion rate and the PSU precipitation rate. Moreover, a lower solute content means more solvent must diffuse into the non-solvent, resulting in more empty space for pore formation. SEM images in Figure 3.9 also confirm that the

PSU printed from a lower solute content solution has a higher porosity. Therefore, 20 wt% PSU/60DMF40THF is selected for porous PSU printing, which has a 66% porosity (based on density measurement) when the structure is printed with 100% infill factor.

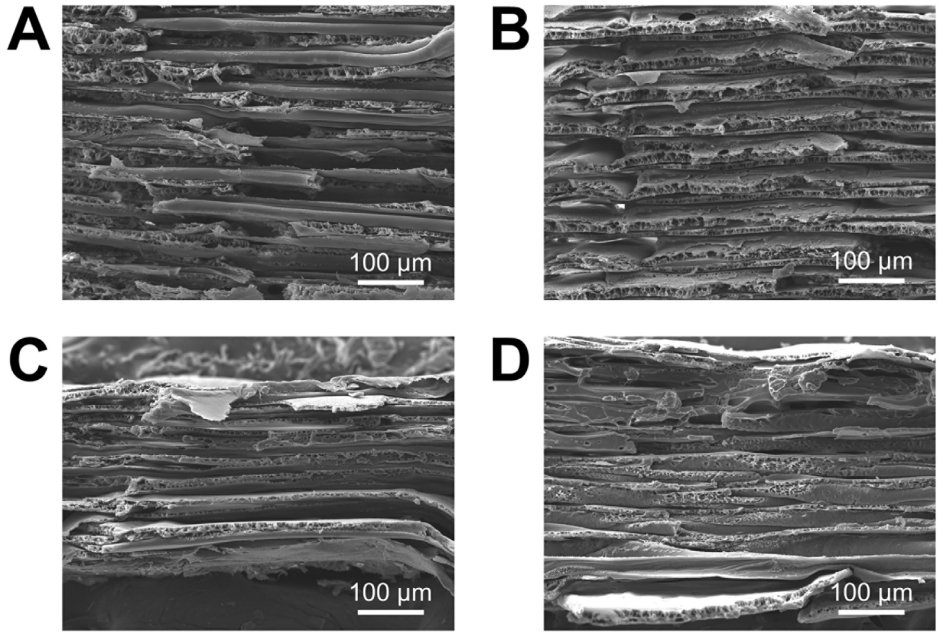

Figure 3.9. SEM images of the cross-sections of porous PSU printed from different weight fraction PSU/60DMF40THF solutions. A) 20 wt%. B) 25 wt%. C) 30 wt%. D) 35 wt%.

3.2.4 Mechanical properties of printed polysulfone

The mechanical properties of the printed PSU were measured using a universal testing system (Model 5982, Instron). More specifically, tensile tests were performed on the PSU samples with three configurations (Figure 3.10A), 0°/90° infill in the *x*-*y* plane (denoted as 0°/90°), −45°/45° infill in the *x*-*y* plane (denoted as ±45°) and *z*-direction (denoted as vertical), following ASTM D638. The tensile specimens were printed in the type V shape, and an extension rate of 1 $mm \cdot min^{-1}$ was applied during tensile testing. The tensile fracture surfaces were examined by SEM. Single-edge notched bending (SENB) tests were performed on the PSU samples with three configurations (Figure 3.10B) to measure the critical stress intensity factor (K_{IC}) and fracture toughness (G_{IC}), following ASTM D5045-99. A crosshead speed of 10 $mm \cdot min^{-1}$ was applied during SENB testing.

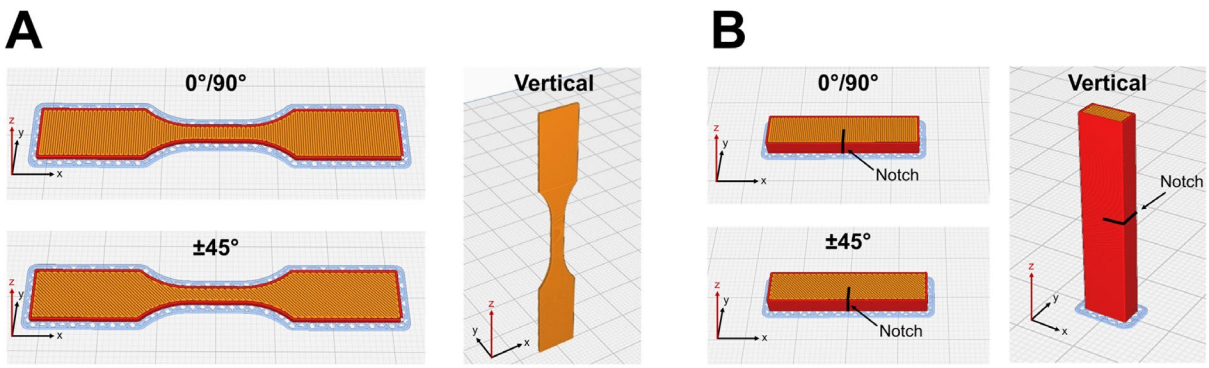

Figure 3.10. A) Three different printing configurations of tensile test specimens. B) Three different printing configurations of SENB specimens.

The tensile properties of printed dense PSU samples are compared with PSU thin films made by solvent casting and laser cutting. In Figure 3.11A and B, the Young's modulus and tensile strength of the dense PSU samples show no dependence on printing configurations, and they are comparable to the values of PSU films (ANOVA $p = 0.643$ and $p = 0.750$, respectively). The average Young's modulus and tensile strength of dense PSU with all printing configurations are 2,469 MPa and 70.58 MPa, respectively, which agree with the properties of the raw material (2,480 MPa and 70.3 MPa, respectively, according to Udel® P-3500 data sheet). The elongation at break of the 0°/90° and ±45° samples are comparable to the PSU film (Figure 3.11C), yet the values are relatively low for a ductile thermoplastic like PSU. This low elongation at break can be explained by the stress concentration induced by the defects on the edges of laser-cut PSU films and the small voids between the infill paths of printed PSU samples. However, the elongation at break of the vertical samples is about 25% higher than the 0°/90° and ±45° samples, indicating fewer defects formed during the vertical stacking of layers. The SENB fracture results in Figure 3.11D and E show that both K_{IC} and G_{IC} are lowest in the 0°/90° configuration and highest in the vertical configuration, which means the interface between adjacent infill paths is weaker than the interface between vertically stacked layers. This unique property of strong interlayer strength can be attributed to the applied pressure toward the previous layer during printing that further improves the solvent welding performance. Compared to common thermoplastics and high-temperature thermoplastics fabricated by material extrusion which usually have only 30%–50% [228,229] or 20%–30% [104,230] tensile strength in the layer stacking direction relative to the raw material tensile strength, respectively, precipitation printing can outperform material extrusion due to the high mechanical properties in the layer stacking direction.

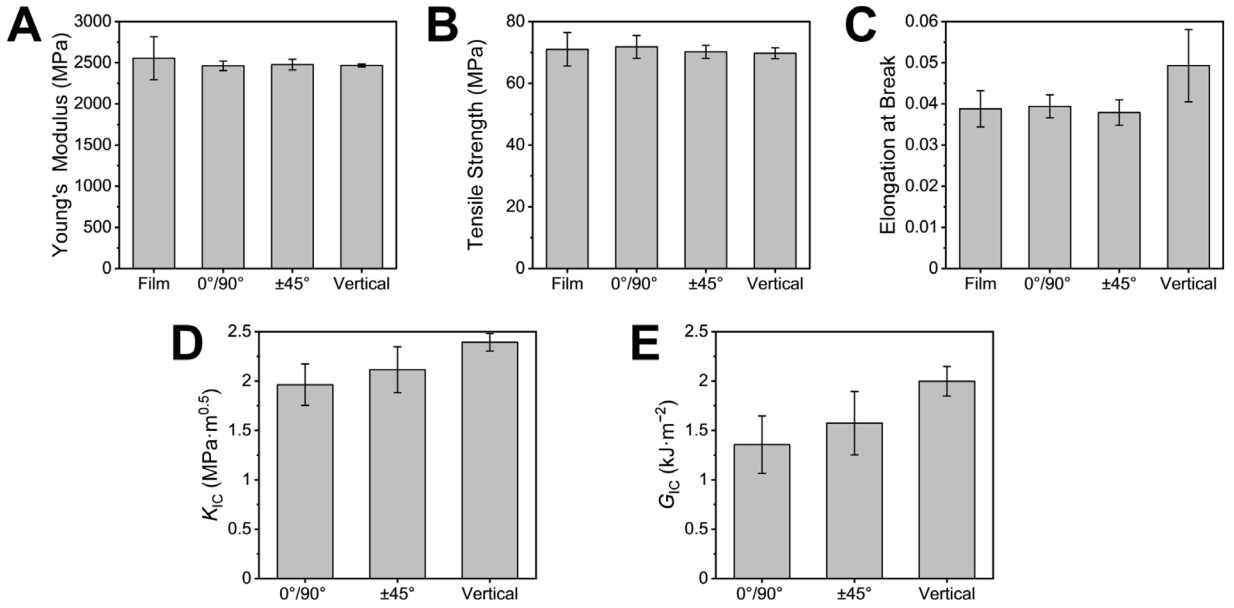

Figure 3.11. Tensile properties of printed dense PSU: A) Young's modulus; B) tensile strength; C) elongation at break. Fracture toughness of printed dense PSU: D) K_{IC}; E) G_{IC}.

Figure 3.12 contains SEM images of the tensile fracture surfaces of printed dense PSU samples with different configurations. In general, all samples with different configurations have dense and rough fracture surfaces, where no layer stratification or infill pattern can be observed. The cross-section images and the mechanical properties indicate that by using NMP (lowest RED for PSU) as the solvent for strong solvent welding and using PG for slow precipitation rate, the printed dense PSU samples have a uniform microstructure and a low degree of anisotropy. When comparing different printing configurations, 0°/90° samples in Figure 3.12A have the most voids with diameters below 10 μm, ±45° samples in Figure 3.12B have fewer and smaller voids, yet vertical samples in Figure 3.12C have the roughest ductile fracture surface with the fewest micron-level voids. Therefore, small voids tend to form on the interface between adjacent infill lines instead of the interface between layers, which explains the slight anisotropy in mechanical properties. The stronger layer interfaces with fewer defects can be explained by the applied pressure to the extruded PSU solution onto the previous layer, which helps the new layer fill interlayer voids and squeeze out bubbles. It should also be noted that these small voids in the SEM images do not significantly influence the tensile properties but make the PSU samples less resistant to crack propagation.

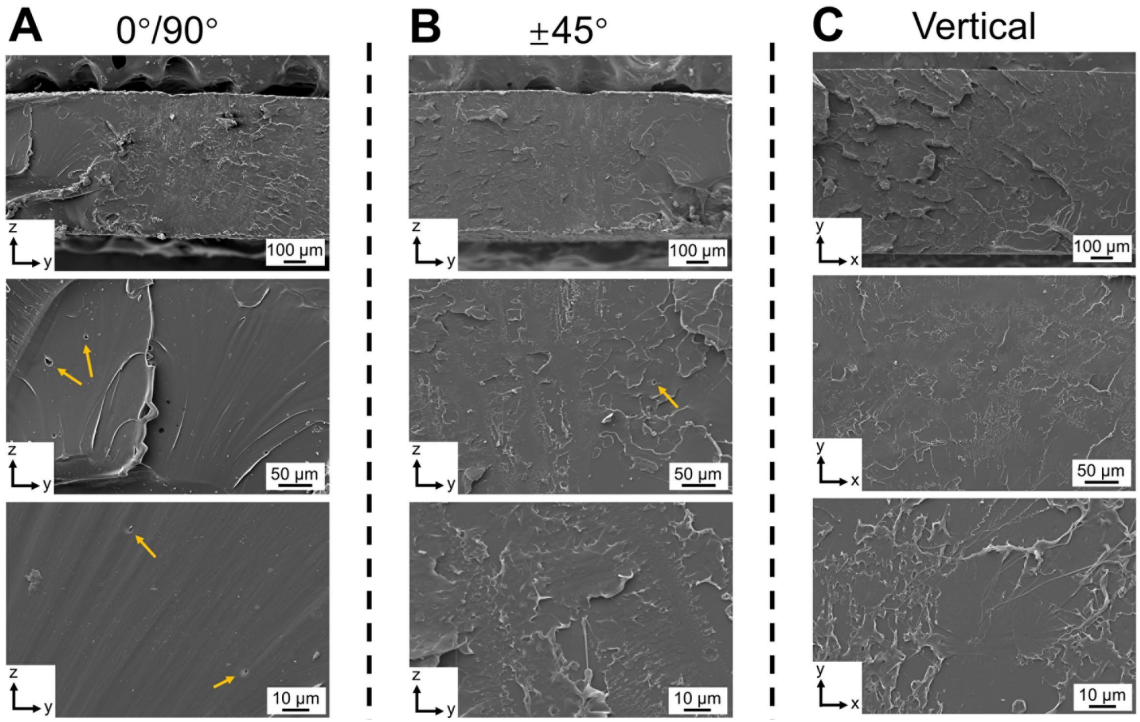

Figure 3.12. SEM images of the cross-sections of printed dense PSU after tensile failure: A) 0°/90° samples; B) ±45° samples; C) vertical samples. Yellow arrows indicate the voids.

On the other hand, printed porous PSU behaves differently compared to printed dense PSU. With only 34% density relative to the raw PSU pellets, porous PSU samples exhibit significantly weaker mechanical properties than dense PSU samples. The Young's modulus of 0°/90° and ±45° configurations are about 470 MPa, while that of the vertical configuration is only 147 MPa (Figure 3.13A). The tensile strength of the ±45° configuration is the highest (9.3 MPa) among the three, yet that of the vertical configuration is the lowest (1.6 MPa, Figure 3.13B). Similarly, the ±45° configuration has the highest elongation at break, and the vertical configuration is the lowest (Figure 3.13C). These results indicate that the printed porous PSU samples are highly anisotropic, which are strong in the infill direction but weak on the infill interfaces. The 0°/90° samples have half number of layers that have infill interfaces perpendicular to the loading direction, which are susceptible to failure at low strains. The ±45° samples have shear stress on both the infill direction and interfaces, which are less vulnerable during tensile testing. In addition, the interfaces between vertical layers are found to be the weakest spot in porous PSU samples, similar to the printed structures by extrusion-based methods reported in the literature [13,28–30]. The SENB test results also show that ±45° samples have higher K_{IC} and G_{IC} values and stronger resistance to crack propagation than 0°/90° samples, while the vertical samples have a significantly lower resistance to cracks propagating between layer interfaces (Figure 3.13D and E).

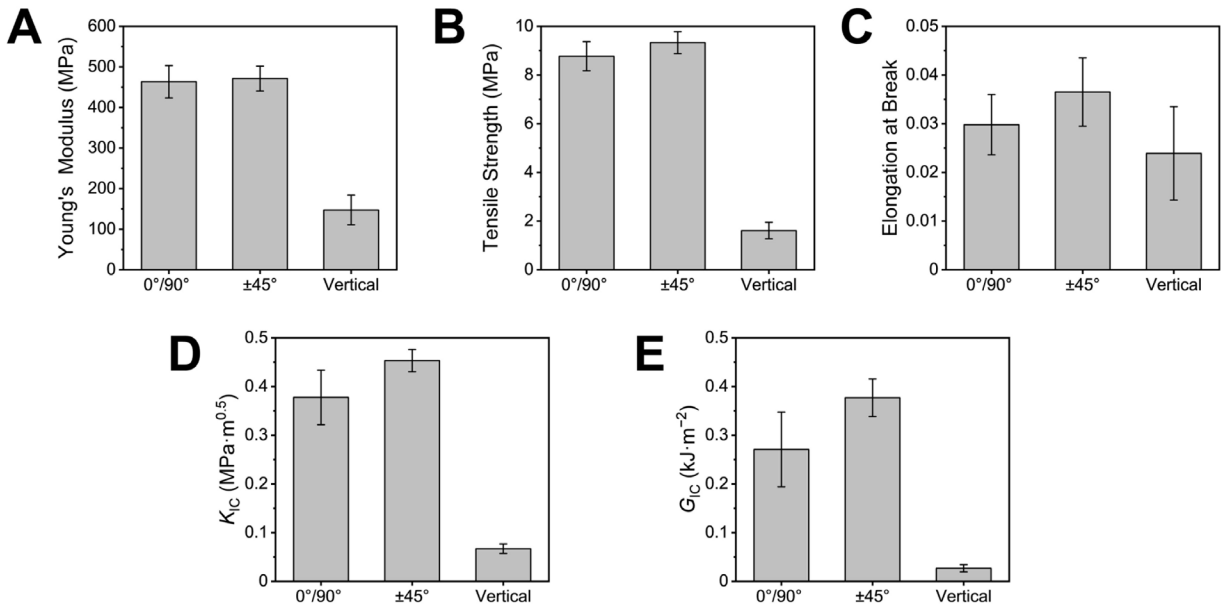

Figure 3.13. Tensile properties of printed porous PSU: A) Young's modulus; B) tensile strength; C) elongation at break. Fracture toughness of printed porous PSU: D) K_{IC}; E) G_{IC}.

The SEM images of the tensile fracture surfaces of printed porous PSU samples can explain the failure mechanism mentioned above. In Figure 3.14A, the fracture surfaces of 0°/90° samples are generally flat, with alternating 0° layers (the more porous layers) and 90° layers (the less porous layers). As seen in the cross-sections of wet spun porous PSU fibers in Figure 3.3 (the PSU/DMF/water case, for example), each printed infill path has a similar cross-section with a less porous skin and a more porous core. Due to the fast solvent/non-solvent diffusion process at the outer surface of each infill path, the solvent welding mechanism cannot provide sufficient bonding between adjacent infill lines, making the interface between infill lines weaker than the strength of the individual infill path itself. This explanation is supported by the SEM images of 0°/90° samples, where the 90° layers (loading direction perpendicular to the infill lines) break at the interfaces and show the less porous skins of infill paths. Unlike the 0°/90° samples, ±45° samples have teeth-like fracture surfaces due to the anisotropic nature of the infill lines (Figure 3.14B), but layer stratification can be clearly observed in both 0°/90° and ±45° samples. In addition, the top and bottom surfaces of each layer are smooth, with only a low degree of porosity in Figure 3.14B. In Figure 3.14C, the fracture surfaces of vertical samples have a low porosity morphology similar to the top and bottom surfaces of each layer, indicating the fracture is a complete layer separation that occurs at the layer interface. The relatively low mechanical properties of the vertical samples also show that the solvent welding-induced interfacial bonding between layers is weaker than the interfacial bonding between adjacent infill paths. Therefore, when using a weak solvent

(60DMF40THF in this case has a relatively high RED for PSU) and a non-solvent bath with fast precipitation rate, insufficient interfacial solvent welding makes printed porous PSU highly anisotropic, most robust in the infill path direction, and weakest in the layer stacking direction. These mechanical testing results and cross-section SEM images show that precipitation printing enables microstructure and mechanical property tailoring of PSU by controlling the solvent/non-solvent pairs and printing parameters.

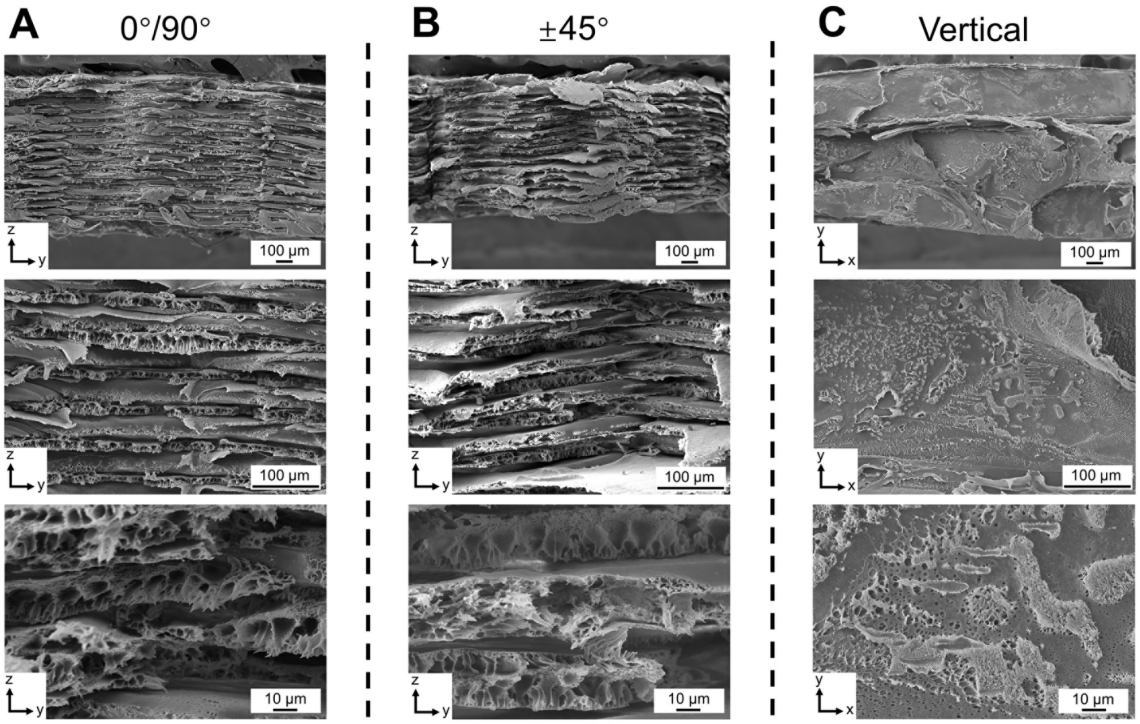

Figure 3.14. SEM images of the cross-sections of printed porous PSU after tensile failure: A) 0°/90° samples; B) ±45° samples; C) vertical samples.

3.2.5 Thermal properties of printed polysulfone

As a high-temperature engineering thermoplastic, the thermomechanical properties and thermal stability of printed PSU are crucial when PSU is used in extreme environments. It should be noted that the highest drying temperatures for the dense and porous PSU are 190 °C and 160 °C, respectively, to remove excessive solvents and non-solvents that may degrade the thermal properties. The glass transition temperature (T_g) of the printed PSU was measured using a dynamic mechanical analyzer (DMA, Q800, TA Instruments), with a 1 Hz frequency and a temperature ramp rate of 5 °C·min^{-1}. Figure 3.15A shows the storage modulus and tan δ of the printed dense and porous PSU. The T_g based on the tan δ peak of the dense PSU is 207 °C, and that of the porous PSU is 210 °C. Alternatively, when calculating based on the storage modulus curve, the T_g of the

dense PSU is 195 °C, and that of the porous PSU is 201 °C. The slightly higher T_g of the porous PSU can be caused by its low thermal conductivity, which reduces the sample internal temperature. However, the DMA results confirm that both printed dense and porous PSU are suitable for high-temperature applications up to about 200 °C. Thermogravimetric analysis (TGA) was performed on printed PSU samples to investigate its thermal stability using a thermal analyzer (Q600, TA Instruments), with a temperature ramp rate of 10 °C·min^{-1}. As a result, Figure 3.15B shows the thermal stability of printed dense and porous PSU. In the temperature range below 300 °C, the weight loss of both dense and porous PSU is lower than 0.5%, indicating that the remaining solvent trapped inside the samples is negligible after drying. The decomposition temperature (T_d), defined at 5% weight loss, is 506 °C for dense PSU and 503 °C for porous PSU. Both the high T_g and T_d values prove that the printed PSU samples with the designed drying process have excellent thermal stability and can be used in extreme environments.

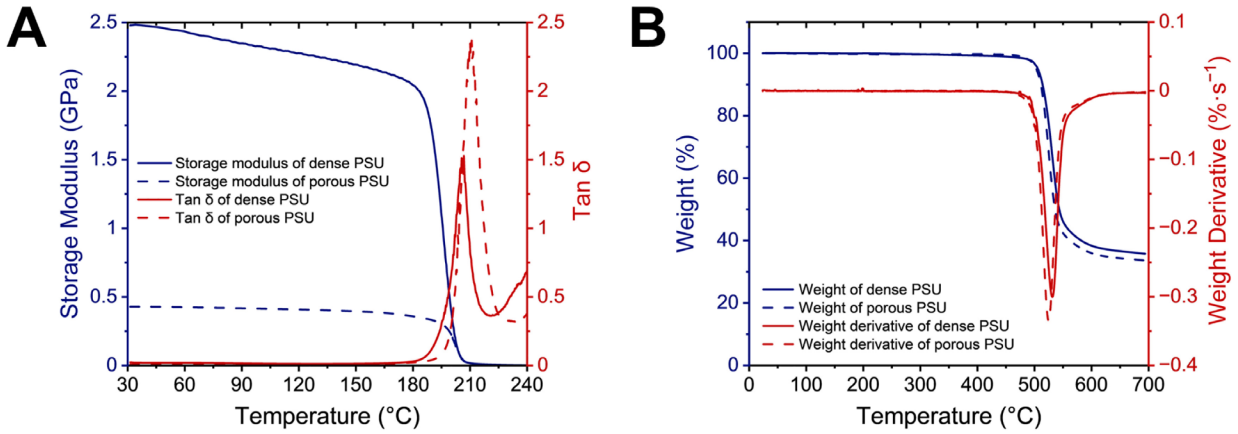

Figure 3.15. A) Storage modulus and tan δ of printed dense and porous PSU samples showing T_g. B) Weight change of the printed dense and porous PSU samples with respect to temperature in a nitrogen environment.

3.2.6 Demonstration of printed polysulfone structures

As an additive manufacturing method, precipitation printing can fabricate complex PSU 3D structures. Figure 3.16A–C are three printed dense PSU structures. In Figure 3.16A, a printed dense block M is shown after being polished on both sides demonstrating high transparency, which indicates the dense internal structure of this sample. Figure 3.16B shows a thin-wall duct that was vertically printed without any support materials. This structure shows the possibility of additively manufacturing high-temperature PSU ducts with complex shapes, which can be used for hot gas exhausts. It should be noted that due to the small cross-section area and thus short printing time for each layer, insufficient solvent diffusion and incomplete PSU precipitation caused nozzle

dragging of the gel-state previous layer, which resulted in a rough sample without high transparency. A larger duct structure can potentially resolve this problem and have a smoother surface finish. Figure 3.16C presents a tiny escalator model placed on top of a coin to show the high-resolution printing capability of a dense PSU and a support-free 45° overhang angle.

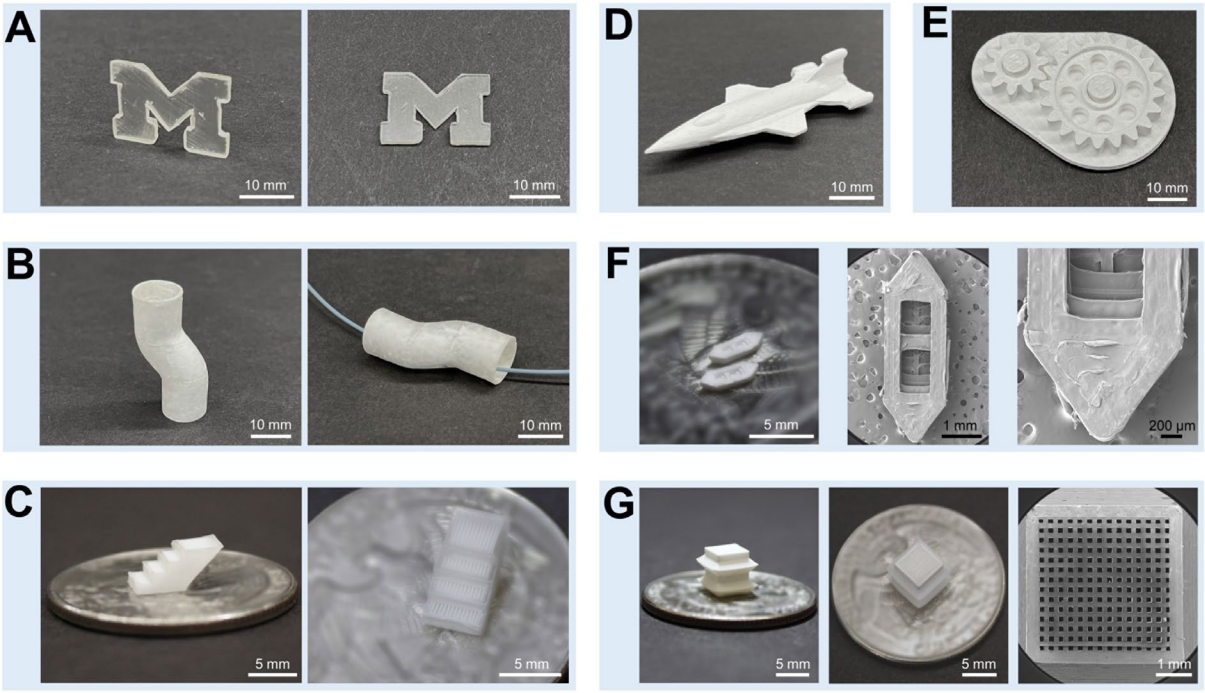

Figure 3.16. Printed dense PSU structures: A) a block M; B) a thin-wall duct; C) a tiny escalator model. Printed porous PSU structures: D) an aircraft model; E) a gearbox set; F) two tiny boats with the SEM image showing details; G) a pagoda model with a micro-lattice internal structure showing high printing resolution.

Additionally, Figure 3.16D–G show various printed porous PSU structures. Due to the rapid precipitation rate, porous PSU precipitation printing has better scalability and geometry control than dense PSU, which allows for more complex structures. For example, Figure 3.16D shows a printed aircraft model, and Figure 3.16E shows a printed three-component gearbox set with accurate shapes of the gear teeth. Porous PSU precipitation printing is also a promising high-resolution printing method for small-scale structures. In Figure 3.16F, two tiny boats similar to the size of rice grains are printed, with the printed details shown in the SEM images. In Figure 3.16G, a pagoda model is designed to have sharp overhangs on the outside and a micro-lattice internal pattern. As shown in the SEM image, the printed line width of the micro-lattice can reach down to 100 µm. These demonstrations prove that precipitation printing can fabricate complex PSU structures with an overhang tolerance similar to common material extrusion methods, yet keeping a high printing resolution.

3.3 Precipitation printing of self-assembled all-aramid 3D structures

The additive manufacturing process for all-aramid 3D structures is designed based on the extensively studied aramid fiber deprotonation and dissolution process to form ANFs [225–227], and the simultaneous wet spinning and protonation process to produce tough ANF-assembled filaments previously developed by our group [231]. The key concept is to adapt the simultaneous wet spinning and protonation of ANF wet filaments into a computer-controlled precipitation printing process, where the wet spun ANF filaments can be deposited layer-by-layer following the designed printing paths. Figure 3.17 displays the whole process for the additive manufacturing of all-aramid 3D structures. Like the wet spinning of ANF-assembled filaments, printed ANF wet structures need to be washed in deionized (DI) water and dried to allow ANF self-assembly into solid and dense structures.

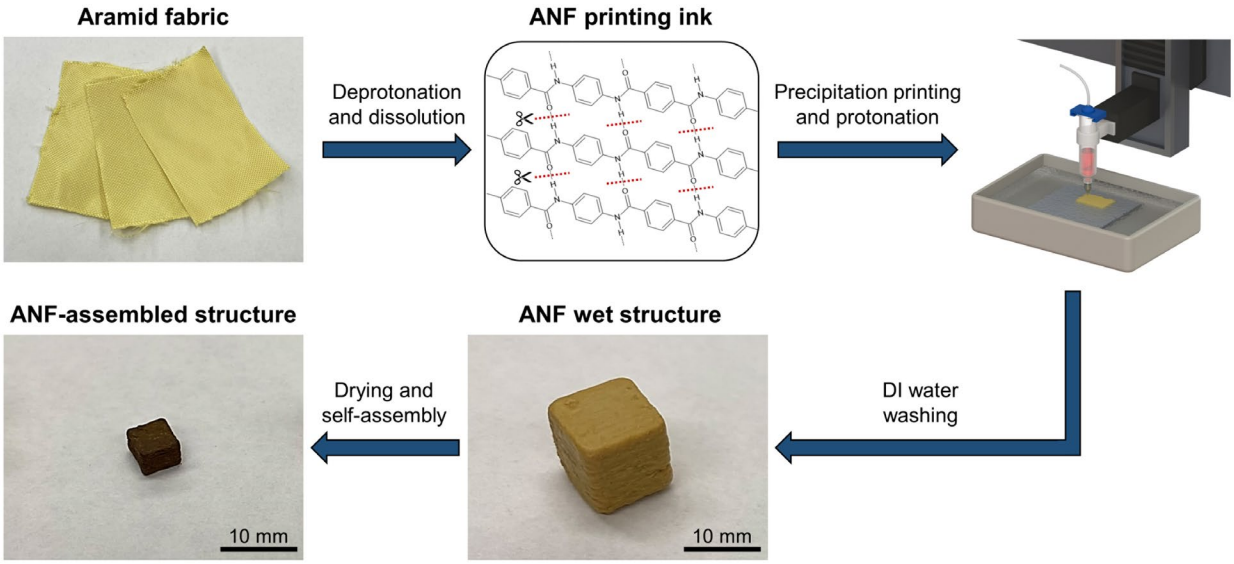

Figure 3.17. Additive manufacturing process for all-aramid 3D structures using an ANF self-assembly approach.

3.3.1 Aramid nanofiber printing ink preparation

To prepare the ANF printing inks, aramid fabrics (Kevlar® KM2+, style 790, CS-800) were cut into small pieces and weighed inside a 250 mL glass bottle to obtain the corresponding amount in Table 3.3. The amount of KOH (Fisher Chemical) was weighed in a small beaker and DI water was then added to the beaker to dissolve KOH, according to Table 3.3. The resulting high concentration KOH aqueous solution was poured into the bottle with already weighed fabrics, followed by adding the designed amount of DMSO (certified ACS, Sigma Aldrich) to the same bottle. It should be noted that instead of using the original KOH/DMSO system to disassemble

aramid fabric [227], the addition of DI water in this system is to increase the solubility of KOH in the solution [226], which allows for the preparation of high concentration ANF printing inks. In addition, for all ANF printing inks, the amount of DI water is kept as 4 wt% of DMSO for the fastest dissolution, following the results by Yang et al. [226]. The resulting aramid/KOH/DMSO/water mixtures were poured into a 500 mL PTFE liner installed on a pressure reactor (Parr 4560 series) with a mechanical stirrer (turbine type impeller), heated at 60 °C and stirred at 200 RPM (Figure 3.18A). Typically, after one day of mechanical stirring, most of the aramid fabrics could be disassembled into a dark red color and highly viscous ANF colloid (printing ink). ANF printing inks were obtained by picking out the undissolved aramid fabric chunks, and the actual concentration of the ANF printing inks was measured by protonating, washing and drying a sample amount of the ANF printing ink and comparing the weight of the dried aramid and the initial ink. As a result, ANF printing inks with concentration ranges from 4.5 wt% to 9.7 wt% are obtained by this preparation method (Figure 3.18B), which provide better feasibility for the additive manufacturing of aramid 3D structures than the lower than 2 wt% ANF colloids used in other literature works [232–234]. Moreover, since KOH is the deprotonation agent for aramids, the KOH/aramid ratio can affect the degree of deprotonation and the diameter of obtained ANFs. In this work, the KOH/aramid ratio in the prepared inks ranges from 32% to 50%, whose influence on the viscosity of printing inks and mechanical properties of assembled ANF structures are studied. In Figure 3.18C, the viscosity of the 6 printing inks with different concentrations and different KOH/aramid ratios is measured under shear rate between 0.075 to 15 s^{-1}, using a cone-plate viscometer (DVNext, AMETEK Brookfield) at room temperature. All printing inks exhibit a shear thinning behavior, which is ideal for the precipitation printing process. Both ANF printing ink concentration and KOH/aramid ratio have an influence on the ink viscosity at a low shear rate (0.075 s^{-1}), where a higher concentration or a higher KOH/aramid ratio leads to a higher the ink viscosity. The shear thinning behavior is stronger in the case of a low concentration ANF printing ink with a high KOH/aramid ratio (Ink 1 for example), and it is weaker in the case of a high concentration ANF printing ink with a low KOH/aramid ratio (Ink 6 for example). It should be noted that viscoelastic properties of the printing inks are not measured since precipitation printed ANF printing ink can have simultaneous protonation and gelation in the coagulation bath, unlike a direct ink writing (DIW) process where the stability of the printed parts depends on the viscoelastic behavior of the ink.

Table 3.3. Composition of the six ANF printing inks used in this study.

ANF printing ink	Ink 1	Ink 2	Ink 3	Ink 4	Ink 5	Ink 6
Aramid fabric (g)	7.5	12	12.5	12.5	14	16.1
KOH (g)	3.75	5.3	4	4.63	5.6	6
DMSO (g)	150	200	150	150	150	150
DI water (g)	6	8	6	6	6	6
KOH/aramid ratio	50%	44%	32%	37%	40%	37%
Measured concentration (wt%)	4.5	6.3	7.2	7.2	8.8	9.7

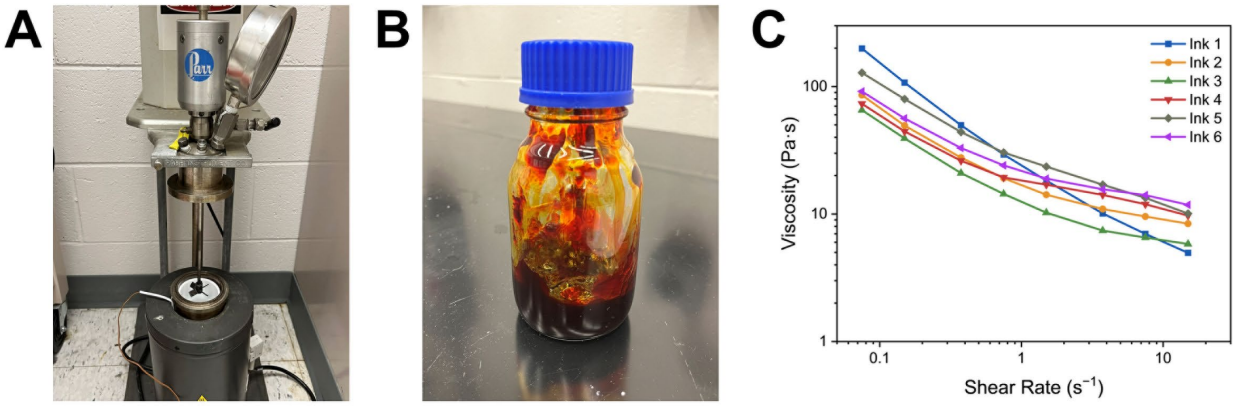

Figure 3.18. A) Mechanical stirrer for aramid fabric dissolution process. B) 6.3 wt% ANF printing ink (Ink 2). C) Shear thinning behavior of the six different ANF printing inks.

The ANFs protonated and isolated from different prepared ANF printing inks were examined using atomic force microscope (AFM) imaging (XE-70, Park Systems), and the measured ANF diameter distributions are presented in Figure 3.19. Both the ANF printing ink concentration and KOH/aramid ratio have influence on the degree of deprotonation and the resulting ANF diameter. The KOH/aramid ratio has a more significant impact on the ANF mean diameter, which increases as the KOH/aramid ratio decreases. When comparing ANFs isolated from two printing inks with the same KOH/aramid ratio (Ink 4 and Ink 6), the ANF mean diameter and standard deviation from the higher concentration Ink 6 are both higher than the ones from Ink 4. Among the ANFs isolated from the 6 printing inks, the largest ANF mean diameter is from Ink 3 (94.4 nm) and the smallest ANF mean diameter is from Ink 1 (55.6 nm).

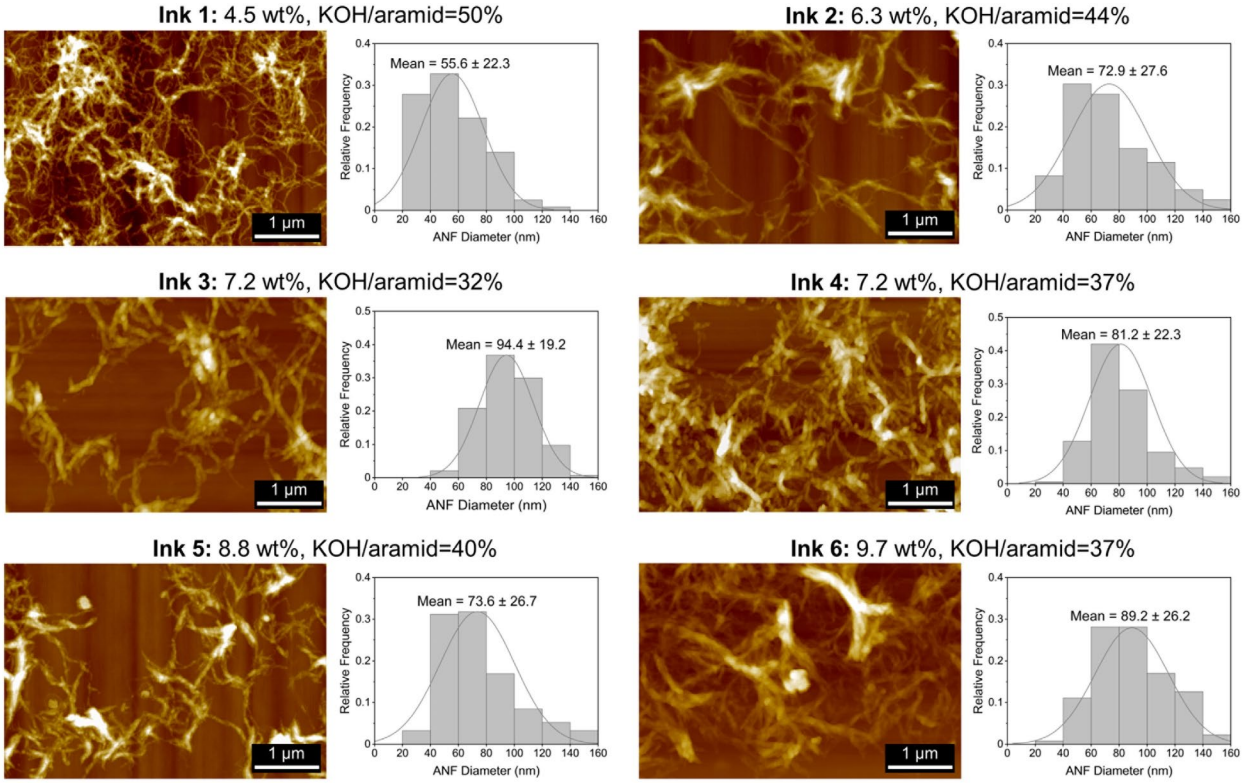

Figure 3.19. AFM images of the isolated ANFs from the six different ANF printing inks and the distributions of the ANF diameter.

3.3.2 Precipitation printing setup and post-processing steps

The precipitation printing setup for ANF printing inks is similar to the setup for PSU. ANF printing inks were loaded in a 10 mL syringe, and an 1/4 inch long 18-gauge nozzle (0.84 mm inner diameter) was used for all inks (Figure 3.20A). For all prints, the printing speed was 14 $mm \cdot s^{-1}$, and the printing width was 0.84 mm. Propylene glycol (PG, 99.9%, SK picglobal) was selected as a weak non-solvent and protonation agent for ANFs in the coagulation bath, which could delay the protonation time for better inter-path bonding than using a strong proton donor like water. The main difference in ANF precipitation printing setup compared to the setups for all other thermoplastics is the printing substrate. Instead of using a doctor-bladed thermoplastic film for substrate adhesion, a piece of 120 grit sandpaper with adhesive backing was attached to a metal plate to act as the printing substrate for ANF printing inks. During the precipitation printing process for ANF printing inks, after the ANF printing ink is extruded out of the nozzle, slow solvent exchange between DMSO and PG takes place, and the increasing content of PG in the deposited ANF mixture gradually caused the protonation and precipitation of ANFs (Figure 3.20B). The deposited ANFs change from a deprotonated dark red color liquid into a protonated orange color

hydrogel with sufficient stiffness to support stable 3D structures during printing. Figure 3.20C demonstrates a precipitation printing and protonation process of a 3D gear part, which indicates the slow color change rate as protonation takes place. This simultaneous precipitation and protonation process allows each individual ANF layer to be protonated as a semi-rigid hydrogel layer during the vertical building process, providing exceptional structural stability relative to the DIW process of high concentration deprotonated ANF printing inks.

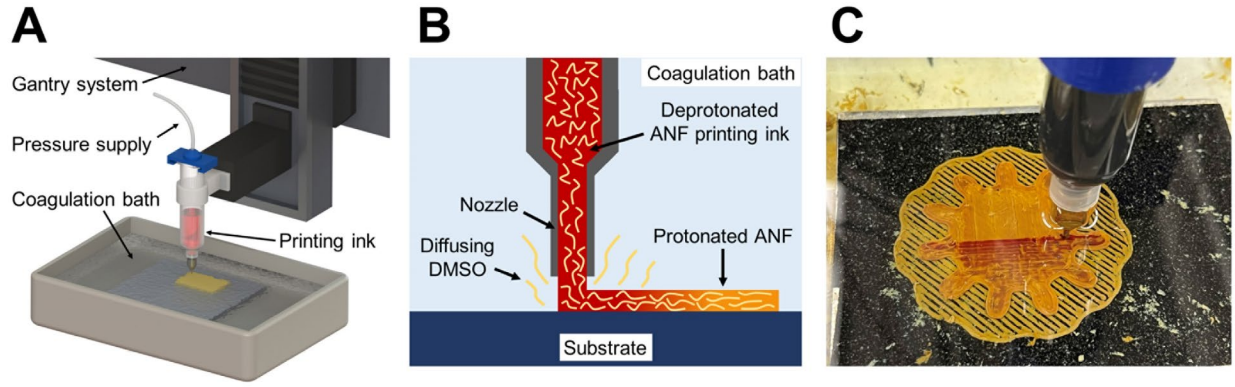

Figure 3.20. A) Precipitation printing setup for ANF printing inks. B) Simultaneous precipitation and protonation of ANFs in a PG bath. C) An example of simultaneous precipitation printing and protonation of an ANF gear part on top of one raft layer.

After precipitation printing of 3D ANF wet structures in the form of PG filled ANF hydrogels, the ANF wet structures were removed from the sandpaper substrate and immersed in a DI water bath to wash away the residual DMSO, PG and KOH. To accelerate the solvent exchange rate, the DI water bath was heated at 50 °C. Three times of DI water washing with a 2–3 h duration for each washing step and fresh DI water replacement between each washing step were performed to ensure the removal of all residues. After this, water based ANF wet structures could be obtained. It should be noted that the ANF wet structures typically have the same shape and dimension as the designed structures, since both the simultaneous precipitation printing and protonation process and the washing step have negligible shrinkage effect on the printed structures. However, the subsequent drying process of the ANF wet structures could induce a significant amount of dimensional contraction. The ANF wet structures were first placed in a 50 °C convection oven for 12 h to evaporate water, during which capillary force from water evaporation could pull ANFs together. As the ANFs were hierarchically assembled by the capillary force, hydrogen bonding and aromatic π-π stacking between the ANFs could further order and pack ANFs in a way similar to the aramid fibers. Additional heat treatment at 300 °C for 2 h was applied to all dried ANF

samples to ensure the removal of high boiling point PG and DMSO. After this heat treatment, dense and strong self-assembled all-aramid 3D structures were finally completed.

3.3.3 Density and dimensional contraction of self-assembled all-aramid structures

The density of self-assembled all-aramid samples from different ANF printing ink concentrations was measured to investigate the compactness of ANF 3D structures. In Figure 3.21A, the measured density of self-assembled ANF samples ranges from 1.26 to 1.28 $g \cdot cm^{-3}$, corresponding to 87.5% to 88.9% of the density of the precursor aramid fiber (1.44 $g \cdot cm^{-3}$). The density results indicate that although ANFs are self-assembled into 3D structures, the compactness of assembled macroscale structures is lower than that of the stretched and aligned aramid fiber, possibly due to the lower aramid chain alignment, compactness, and the degree of hydrogen bonding between assembled ANFs. However, the density of the assembled ANF structures has no significant dependence on the ANF printing ink concentration ranging from 4.5 wt% to 9.7 wt% (ANOVA p = 0.184), implying the compactness of the assembled ANF structures is not affected by the initial ANF weight fraction in the wet structures. Therefore, solid self-assembled all-aramid structures (or ANF structures) with slightly lower than 90% theoretical density can be produced by the proposed printing process from a wide range of ANF printing ink concentrations.

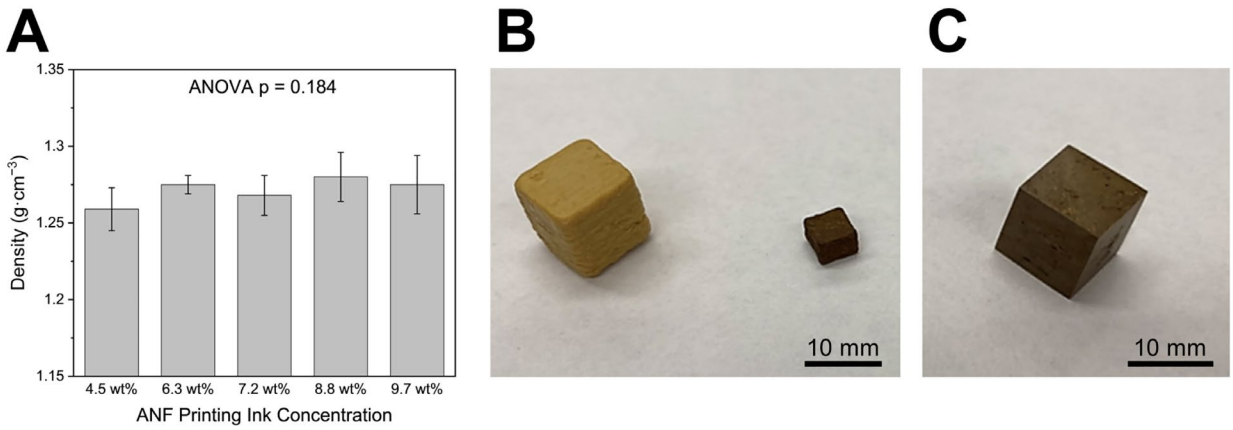

Figure 3.21. A) Density of self-assembled all-aramid structures from different ANF printing ink concentrations. B) Wet and dried all-aramid cubes with the same initial side length of 10 mm. C) Modified design based on the measured contraction to reproduce a dried all-aramid cube with a side length of 10 mm (surface polished).

On the other hand, since the ANF weight fraction in the wet structures is dictated by the printing ink concentration, the dimensional contraction during the drying and self-assembly process also depends on the printing ink concentration. Specifically, higher ANF printing ink concentration leads to lower dimensional contraction when producing self-assembled all-aramid

structures with similar densities. Thus, the dimensional contraction of cubic structures printed from the two highest concentration inks using a 0°/90° alternating infill pattern was measured and shown in Table 3.4, where the X-Y plane is the printing plane and Z direction is the layer stacking direction. By using a 0°/90° alternating infill pattern, the contractions in X and Y directions are almost identical (within 1% difference), but the Z direction contraction is significantly more than the in-plane contractions, due to the lower packing density between layers. The all-aramid cube produced from the 9.7 wt% ink has reduced contraction in all dimensions relative to the cube produced from the 8.8 wt% ink, confirming that higher ANF printing ink concentration can lead to lower dimensional contraction. Although 9.7 wt% is already the highest concentration ANF printing ink that has been prepared in this work, the in-plane dimensional contraction is still about 50% and the Z direction contraction is about 62%, which can be clearly seen in Figure 3.21B when comparing the wet and dry all-aramid structures. Interestingly, shape distortion except the different contraction ratio between in-plane and out-of-plane directions is not observed, which is attributed to the standard atmosphere drying process and the structural stability of the wet ANF structures. Thus, by designing the initial wet structure larger than the target structure based on the measured contraction ratios, additive manufacturing of self-assembled all-aramid 3D structure can be practically realized. As an example, the dried and surface polished all-aramid cube with a side length of 10 mm in Figure 3.21C shows a successful geometry reproduction test, which was designed and printed to be 19.6 mm×19.8 mm×26.4 mm initially using the 9.7 wt% ink.

Table 3.4. Dimensional contraction of all-aramid cubic structures printed from the two highest concentration inks using a 0°/90° alternating infill pattern.

Self-assembled all-aramid structures	X direction contraction	Y direction contraction	Z direction contraction
From 8.8 wt% ANF printing ink	54.7%	55.3%	70.0%
From 9.7 wt% ANF printing ink	49.1%	49.4%	62.1%

3.3.4 Crystallinity of self-assembled all-aramid structures

The crystallinity of the all-aramid structures produced through the deprotonation-printing-protonation-drying process was investigated through X-ray diffraction using a Rigaku Ultima IV X-ray diffractometer with CuKα radiation (λ = 0.154 nm). Specifically, a printed and self-assembled ANF structure using the 7.2 wt% printing ink (Ink 3, KOH/aramid = 32%) was selected as the representative sample for XRD analysis and compared with the original aramid fabric. In

Figure 3.22A, the XRD pattern of the ANF structure exhibit all three crystalline peaks of the aramid fabric at 2θ = 20.5° (110), 23° (200) and 28.4° (004), while the peaks of ANF structure are broader than the ones of aramid fabric. After applying curve deconvolution of the XRD patterns using pseudo-Voigt profiles (50% Gaussian 50% Lorentzian) in Figure 3.22B and C, the degree of crystallinity (χ_c) of the self-assembled ANF structure was calculated to be 59.5%, lower than that of the highly aligned aramid fabric (87.5%). In particular, the (200) peak intensity in the self-assembled ANF structure is lower than the aramid fabric, but the (004) peak intensity in the self-assembled ANF structure is higher. The mean size of crystalline domains can be calculated using the Scherrer equation based on the (110) peak:

$$D = \frac{K\lambda}{\beta cos\theta} \tag{3.1}$$

where D is the mean size of crystalline domains, K is the shape factor (0.9 is used here), λ is the X-ray wavelength, β is the line broadening at half the maximum intensity (FWHM) in radians, and θ is the Bragg angle. As a result, the mean crystalline domain size of the self-assembled ANF structure is 3.5 nm, which is 28% lower than the mean crystalline domain size of the aramid fabric (4.9 nm).

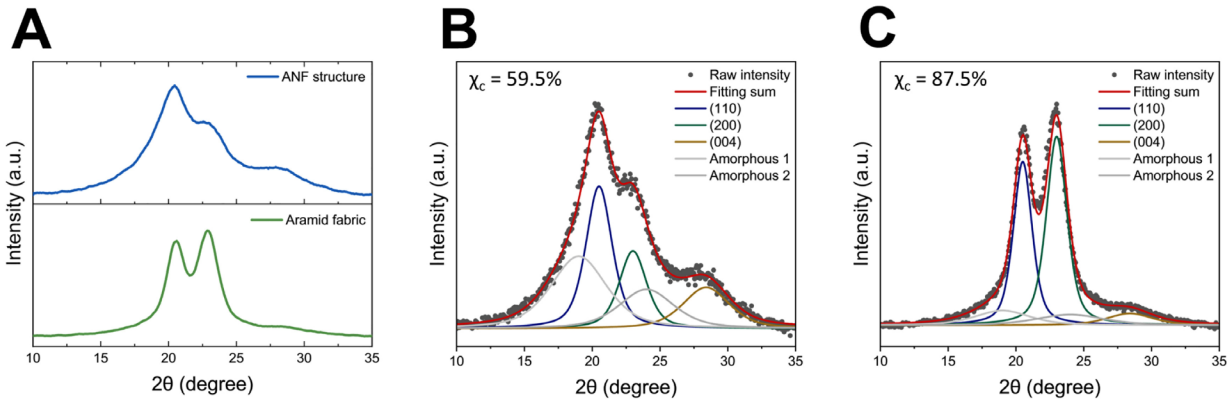

Figure 3.22. A) XRD patterns of self-assembled ANF structure and original aramid fabric. B) XRD deconvolution of crystalline peaks in self-assembled ANF structure. C) XRD deconvolution of crystalline peaks in aramid fabric.

3.3.5 Mechanical properties of self-assembled all-aramid structures

The mechanical properties of self-assembled all-aramid structures were characterized through tensile testing. All-aramid tensile specimens were designed to have an ASTM D638 type V specimen shape after drying by considering the contraction ratio. All tensile tests were performed on an Instron E3000 testing frame with an extension rate of 1 mm·min^{-1}. First, the tensile properties of printed 0° infilled all-aramid samples produced from five different ANF

printing inks (Ink 1–5) were studied. In Figure 3.23, the all-aramid specimens produced from Ink 3 have the highest Young's modulus, tensile strength and elongation at break, and the specimens produced from Ink 1 have the lowest tensile properties.

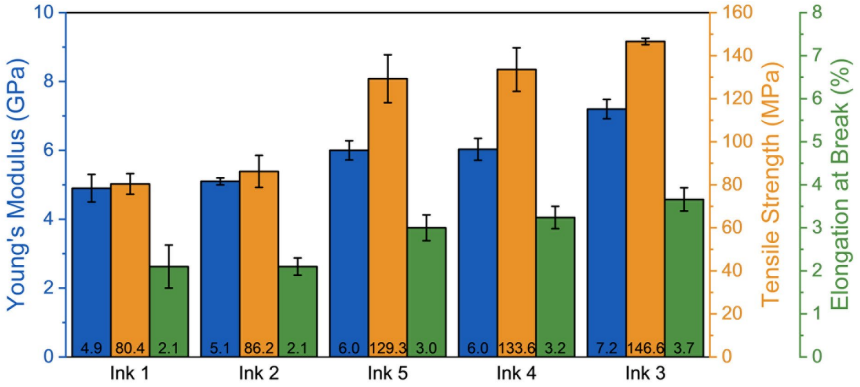

Figure 3.23. Tensile properties of printing 0° infilled all-aramid samples from five different ANF printing inks.

To investigate the relationship between the tensile properties of the printed all-aramid specimens and the composition of ANF printing inks, we compared the Young's modulus, tensile strength with respect to the ANF printing ink concentration and KOH/aramid ratio. In Figure 3.24A, neither the Young's modulus nor tensile strength has a clear relationship with respect to the ANF printing ink, but in Figure 3.24B, both the Young's modulus and tensile strength have a decreasing trend as the KOH/aramid ratio increases. This trend can be explained that the KOH/aramid ratio in the ANF printing ink affects the degree of deprotonation and ANF diameter, where a higher KOH/aramid ratio leads to more complete deprotonation and smaller ANF diameters in Figure 3.24C and also Figure 3.19 in Chapter 3.3.1. Since the original aramid fabric has high alignment, compactness and high degree of hydrogen bonding, as the degree of deprotonation reduces and the ANF diameter increases, more properties of the original aramid fabric can be preserved. In addition, the reassembly process of ANFs into all-aramid structures usually cannot recover the nanoscale compactness and degree of hydrogen bonding of the original aramid fabric, larger diameter ANFs from lower KOH/aramid ratios that preserve more original aramid properties can result in better mechanical properties of the reassembled all-aramid structures. In particular, the 0° infilled all-aramid specimens produced from Ink 3 (KOH/aramid ratio = 32%) exhibit outstanding Young's modulus of 7.2 GPa, tensile strength of 146.6 MPa and elongation at break of 3.7%. The tensile fracture surface of a 0° infilled all-aramid sample produced from Ink 3 was examined by SEM imaging. In Figure 3.25, the large area SEM image shows that the self-assembled all-aramid structure has a compact interior at macroscale without

any visible layer stratification and infill paths. The higher magnification SEM images can provide more insight on the microstructure of the assembled ANFs, where a rough microstructure morphology formed by aggregated and entangled ANFs can be seen. The SEM images confirm that the compactness of self-assembled ANFs is low at microscale and nanoscale, which can explain the density difference between the self-assembled ANF structures and the original aramid fabrics. It should also be noted that for future work, ANFs can be aligned by shear stress during the precipitation printing process by using a long nozzle, a faster printing speed and a higher pressure, to further improve the self-assembly compactness and mechanical properties.

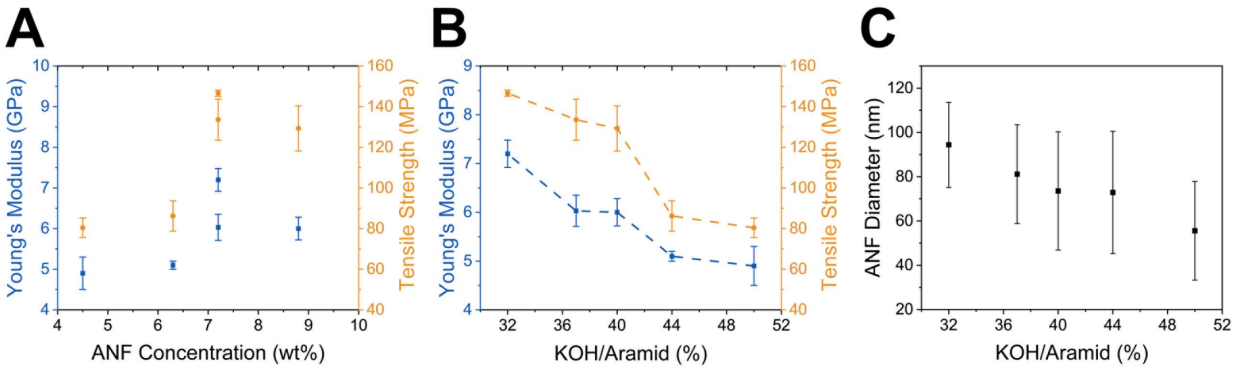

Figure 3.24. A) Tensile properties with respect to the ANF printing ink concentration. B) Teneile properties with respect to the KOH/aramid ratio in ANF printing inks. C) ANF diameter with respect to the KOH/aramid ratio in ANF printing inks.

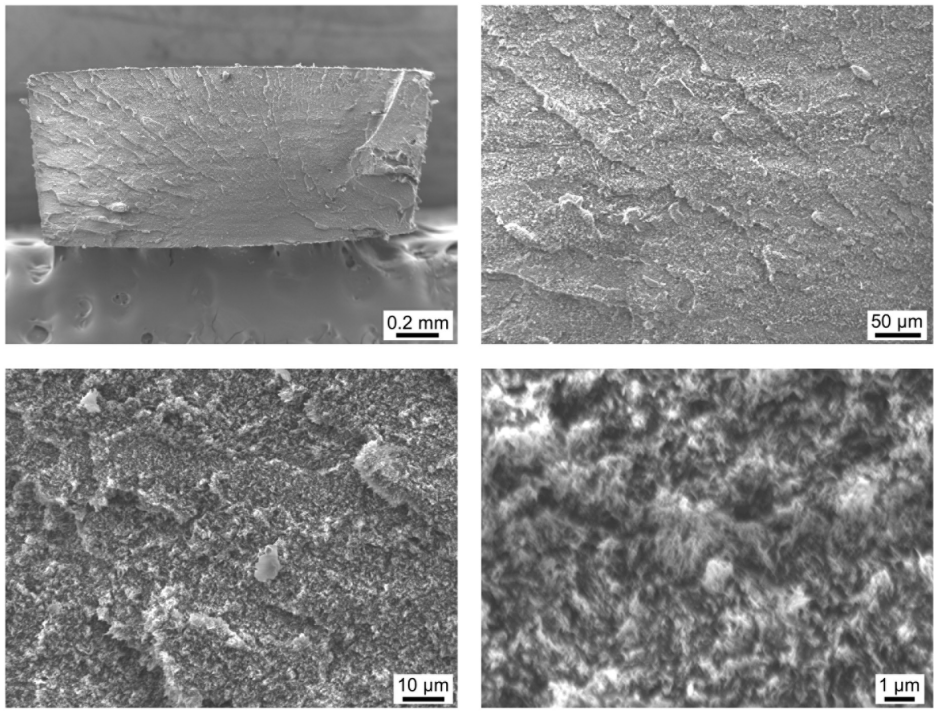

Figure 3.25. SEM images of the tensile fracture surface of a 0° infilled all-aramid sample.

The effect of printing infill direction on the tensile properties was then investigated using Ink 3. In Figure 3.26, all 0° infilled all-aramid samples have the highest tensile properties, while all 90° infilled all-aramid samples have the lowest tensile properties. This can be explained by the anisotropic properties of the high aspect ratio ANFs, which are strong and stiff in the aramid backbone direction and weak in the transverse direction and the interfaces between ANFs. When using 0°/90° alternating infill patterns, the resulting all-aramid samples have tensile properties between the ones of all 0° and all 90° samples. As a high-performance polymer, the high-temperature tensile properties of 0° infilled all-aramid samples were measured and displayed in Figure 3.27. When tested at 100 °C, 200 °C and 300 °C, the Young's modulus of the 0° infilled all-aramid samples drops to 6.0 GPa, 4.5 GPa and 3.6 GPa, respectively. Similarly, the all-aramid samples' tensile strength reduces as the temperature increases, but they still possess a considerable tensile strength of 75 MPa even at 300 °C. On the contrary, the elongation at break increases as the temperature increases, indicating the all-aramid samples become more ductile at high temperatures. These tensile properties confirm that the precipitation printed and self-assembled all-aramid structures can be used as advanced structures in extreme environments with a service temperature up to at least 300 °C.

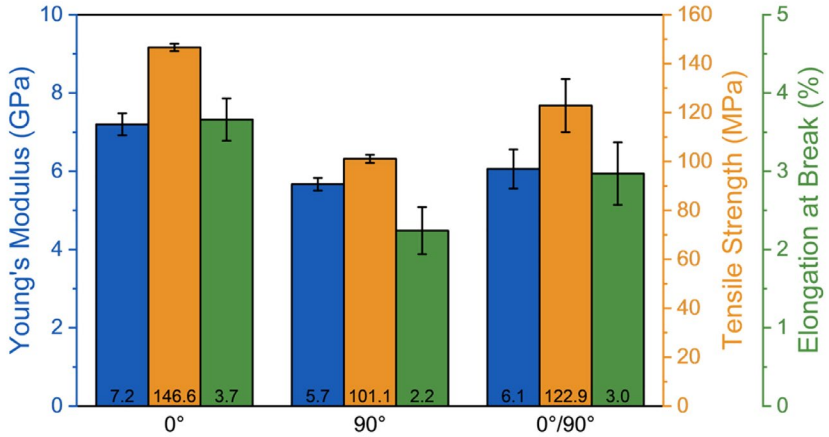

Figure 3.26. Tensile properties of printing all-aramid samples with different infill patterns from ANF printing inks with a 32% KOH/aramid ratio.

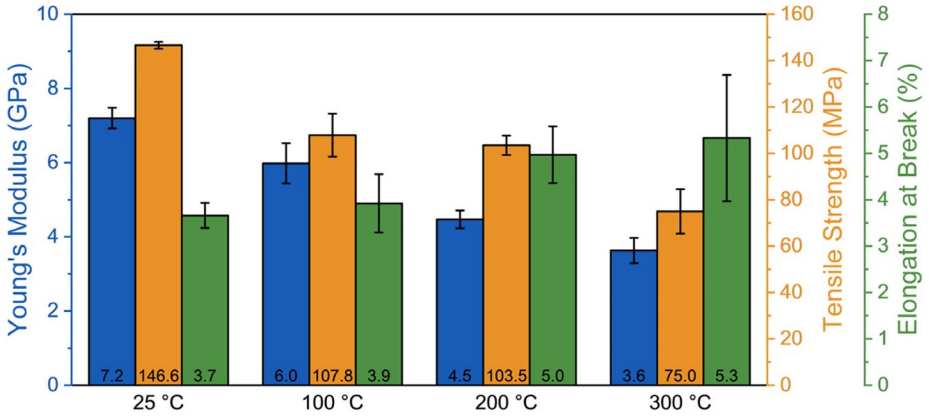

Figure 3.27. Temperature dependent tensile properties of printing 0° infilled all-aramid samples from ANF printing inks with a 32% KOH/aramid ratio.

3.3.6 Thermal properties and flame resistance of self-assembled all-aramid structures

DMA (Q800, TA Instruments) was performed on a self-assembled all-aramid structure (or ANF structure) with a temperature ramp rate of 5 °C ·min^{-1} from 30 °C to 500 °C in air. In Figure 3.28A, the storage modulus drops to 3.35 GPa at 330 °C, half of the storage modulus at 30 °C, and remains stable in the range from 360 °C to 420 °C. The second drop of storage modulus above 420 °C is possibly related to the initial thermal decomposition of self-assembled ANF structure in air. Although some small tan δ peaks can be seen in the testing temperature range, no significant glass transition behavior is observed due to the high degree of crystallinity. The thermal stability of self-assembled ANF structures was then investigated through TGA and DTG (Q600, TA Instruments) with a temperature ramp rate of 10 °C ·min^{-1} from 30 °C to 1000 °C in nitrogen. In Figure 3.28B, the self-assembled ANF structure has a T_d (5% weight loss) of 517 °C, 33 °C lower than the T_d of the original aramid fabric (550 °C). Similarly, the DTG peak of ANF structure is at lower temperature than the aramid fabric. This implies the deprotonation-printing-protonation-drying process to produce all-aramid 3D structures has some damage to the overall chemical structure stability, such as the compactness, the degree of hydrogen bonding and π-π stacking interaction between aramid backbones. Nonetheless, self-assembled all-aramid structures inherit most of the high thermal stability of the precursor aramid fabric. In Figure 3.28C, the flame resistance of a printed all-aramid rectangular bar is demonstrated. After the first and second ignition by a butane torch, the printed all-aramid rectangular bar stopped burning only 0.3 s and 0.7 s after the flame was removed, respectively. After the third time ignition at the same tip location, the sample stopped burning 2.6 s after the removal of flame. This test shows the outstanding flame resistance of the

self-assembled all-aramid structure, which can be repeatably used to stop flame without any compromise of its structural integrity.

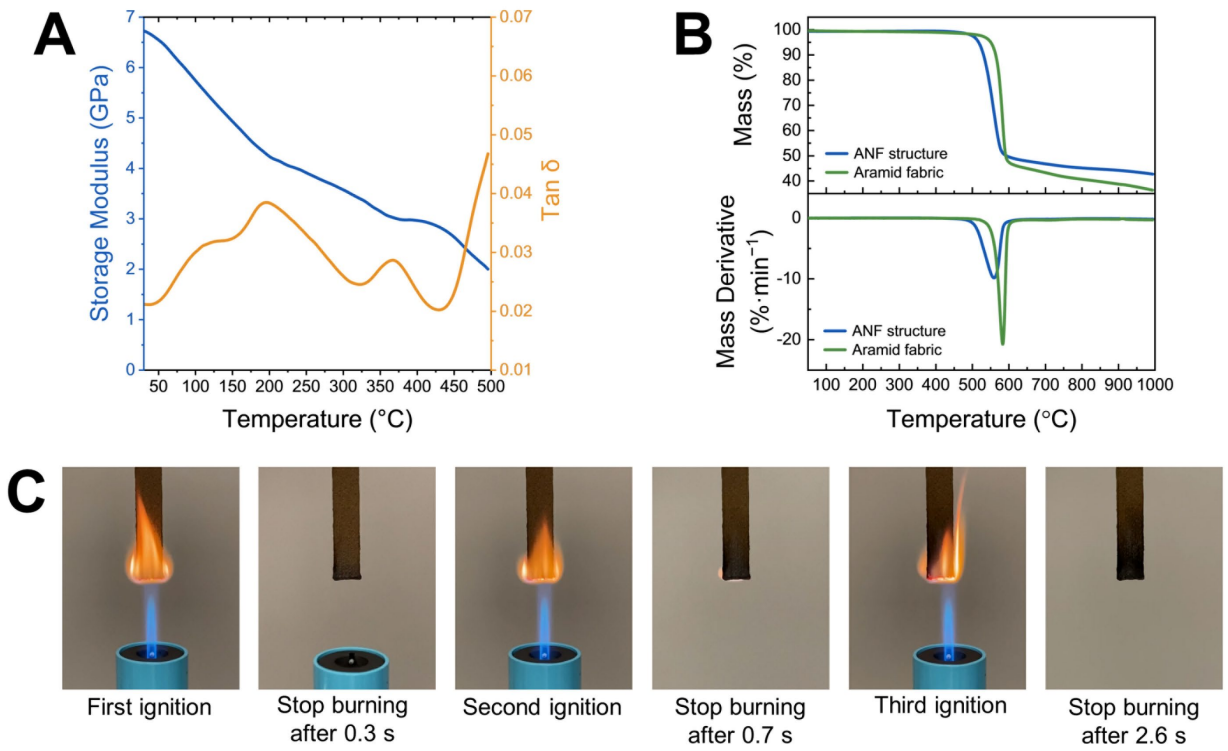

Figure 3.28. A) Storage modulus and tan δ of a self-assembled ANF structure. B) TGA and DTG curves of self-assembled ANF structure and original aramid fabric in a nitrogen environment. C) Flame resistance test of a self-assembled ANF structure.

Combining the outstanding mechanical properties and thermal stability, the precipitation printed then self-assembled all-aramid material in this work becomes an unprecedented high-performance polymer that can be processed through additive manufacturing. In Figure 3.29, when compared to other high-performance unfilled polymers fabricated by additive manufacturing processes such as material extrusion, powder bed fusion and DIW [21,22,99,101,102,107,235], the all-aramid material significantly outperforms all others in terms of Young's modulus, tensile strength and T_g. It should be noted that since the T_g of the DIW polyimide (PI) by Hegde et al. [107] and our all-aramid material is difficult to define, the temperature when the storage modulus drops to half of its room temperature value is used as a conservative estimation for T_g in this comparison.

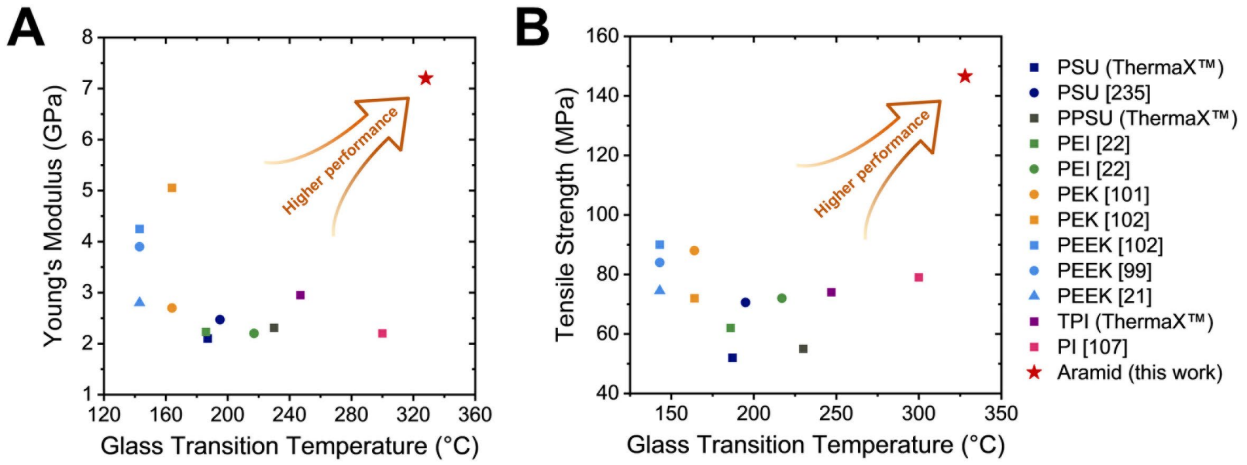

Figure 3.29. Comparison of the precipitation printed then self-assembled all-aramid material to other additively manufactured unfilled high-performance polymers in terms of Young's modulus, tensile strength and glass transition temperature.

3.3.7 Demonstration of self-assembled all-aramid 3D structures

After understanding the ratio of dimensional contraction, complex geometry all-aramid structures can be designed, printed and self-assembled through the proposed process. Figure 3.30A shows a printed all-aramid gear set, whose gear teeth details are preserved without distortion after drying. After drilling holes at their centers and inserting metal shafts, a high strength, high heat resistance and lightweight gear set is produced, which can potentially be used in high-temperature engines and gas turbines to replace metal gears. Figure 3.30B displays a printed all-aramid propeller with a diameter of about 100 mm, similar the size of a quad drone propeller. The all-aramid propeller is fixed on the shaft of a DC motor, which can spin in a hot air environment created by a heat gun. Thermal imaging using a FLIR ONE® PRO thermal camera shows that the propeller hub has a temperature of 227 °C and its blade has a temperature of 128 °C under heating. However, the all-aramid propeller has no shape distortion and shows no softening effect under this hot environment. Combining its excellent flame resistance shown in Section 3.3.6, precipitation printed then self-assembled all-aramid materials can have potential applications in extreme environment exploration robots and fire rescue drones, where high-performance and lightweight parts can be additively manufactured to replace traditionally machined metal parts.

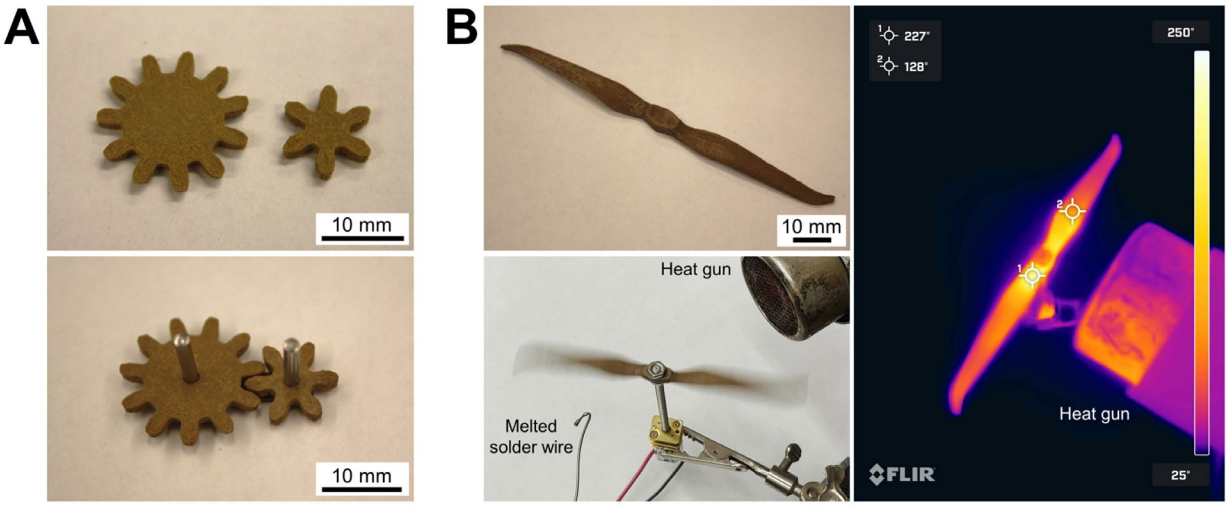

Figure 3.30. A) A printed all-aramid gear set. B) A printed all-aramid propeller that can be used in a high-temperature environment.

3.4 Chapter summary

In this chapter, precipitation printing was applied to two representative high-performance polymers, PSU and para-aramid. In the case of PSU, phase inversion time study, wet spinning study and solvent welding performance study were used to determine the ternary systems for both dense and porous PSU precipitation printing. As a result, the printed dense PSU samples exhibit excellent mechanical properties (2.47 GPa Young's modulus and 70.6 MPa tensile strength) comparable to reference PSU thin films, while the mechanical properties in the vertical build direction are the highest due to the strong interlayer bonding. On the other hand, the printed porous PSU samples have only 34% density relative to the dense PSU, and their mechanical properties are highly anisotropic due to the fast precipitation rate and weak interlayer bonding. However, the precipitation rate also affects the dimensional stability, which leads to about 10% dimensional contraction for dense PSU and outstanding dimensional accuracy with negligible contraction for porous PSU. Both printed dense and porous PSU samples exhibit a T_g around 200 °C and a T_d about 500 °C in nitrogen, showing their potential application in high-temperature environments.

Moreover, additive manufacturing of all-aramid 3D structures was achieved for the first time through simultaneous precipitation printing and protonation of high concentration ANF printing inks followed by self-assembly of ANFs. The self-assembled all-aramid structures have significant dimensional contractions of more than 50%, but these predictable contractions can provide guidance for producing dry structures with expected dimensions by designing larger wet ANF structures. The printed and self-assembled all-aramid material has outstanding mechanical

and thermal properties, which outperforms all existing unfilled high-performance polymers produced by additive manufacturing. The demonstration of the printed 3D all-aramid gears and propeller shows the potential application of printed all-aramid structures as lightweight replacement parts for metals in extreme environments.

Chapter 4 Precipitation Printing of Piezoelectric Poly(vinylidene fluoride)

4.1 Chapter introduction

In Chapter 4, precipitation printing is used as an additive manufacturing method for piezoelectric poly(vinylidene fluoride) (PVDF), to promote its most polar β phase [236]. PVDF is first dissolved in *N,N*-dimethylformamide (DMF) or dimethyl sulfoxide (DMSO) to form a printing solution, then precipitation printed in a water bath to produce a porous 3D structure. The mechanism for β phase promotion in this process is based on the hydrogen bonding between PVDF's highly electronegative fluorine atoms and water molecule's hydrogen atoms during non-solvent induced phase separation (NIPS), which orients the PVDF dipoles with a TTT conformation. Multiple characterization techniques are used to study the phase composition of the precipitation printed PVDF, and the effects of solvent type, printing direction and post-processing conditions on the phase composition are studied. In addition, the dielectric, ferroelectric and piezoelectric properties of the printed PVDF are measured, and the results confirm that a high β phase content PVDF with excellent piezoelectricity can be produced by precipitation printing with subsequent electric poling. This process is then applied to fabricate PVDF-based piezoelectric energy harvesters, including a stretching mode (d_{31}) energy harvester and a compression mode (d_{33}) shoe insole energy harvester. Finally, piezoelectric PVDF sensors produced by the proposed process are used in another project about 3D printed dove feathers with embedded aerodynamic sensing, where the PVDF sensors are integrated into the 3D printed feather rachis for in flight vibration sensing. Therefore, the work in Chapter 4 presents an effective additive manufacturing process to produce piezoelectric PVDF, which provides a scalable approach to fabricate piezoelectric PVDF-based energy harvesters and sensors.

4.2 Precipitation printing process for poly(vinylidene fluoride)

Solutions for precipitation printing were prepared by dissolving 15 wt% PVDF powder (Kynar 301F) in DMF (certified ACS, Fisher Chemical). To inspect the effect of solvent choice on PVDF β phase, 15 wt% PVDF was also dissolved in dimethyl sulfoxide (DMSO) (certified

ACS, Fisher Chemical). These clear PVDF solutions were obtained via a combination of mixing through centrifugal shear mixing (FlackTek SpeedMixer) and ultra-sonication (Branson 2800). For precipitation printing, the PVDF solution was loaded into a 10 mL syringe with a 26-gauge (254 µm inner diameter) stainless-steel dispensing needle which was pneumatically controlled by a high precision dispenser (Ultimus V, Nordson EFD), and installed on a Cartesian gantry system (AGS1500, Aerotech) for vertical and translational movements (Figure 4.1A).

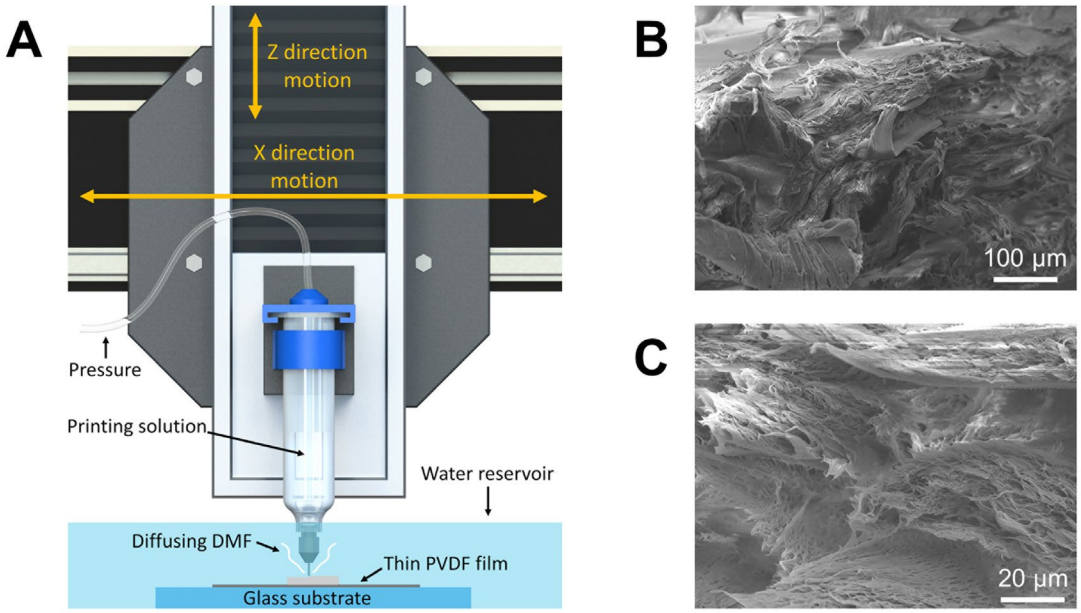

Figure 4.1. A) Precipitation printing of PVDF. B) and C) SEM images of the porous PVDF microstructure produced from precipitation printing.

A glass plate with a thin doctor-blade cast PVDF film adhered on the top surface was immersed in a water bath to act as the printing substrate. It should be noted that the cast thin PVDF film can improve adhesion between the printed structure and the substrate. During the precipitation printing process, the pressure, layer height, printing speed and printing line width were set to be 2.5 psi (17.2 kPa), 50 µm, 7 mm·s^{-1} and 150 µm, respectively. Both parallel (all 0°) and alternating (0° and 90° alternating layer by layer) printing infill patterns were tested to study the effect of infill direction on the PVDF phase composition. After the printing process was completed, the PVDF samples were left in the water for 1 hour to allow for complete DMF diffusion into the water, then the samples were removed from the water bath and dried under vacuum (25 in. -Hg) overnight. As studied in Chapter 2, precipitation printed PVDF using the PVDF/DMF/water system produces highly porous microstructures (Figure 4.1B and C).

4.3 Phase characterization

4.3.1 Fourier-transform infrared spectroscopy

Fourier-transform infrared spectroscopy (FTIR) was performed on precipitation printed PVDF samples from both DMF solution and DMSO solution using a Nicolet iS50 FTIR spectrometer with a Smart iTR Attenuated Total Reflectance (ATR) accessory, while solvent cast PVDF films from DMF solution (dried at 180 °C) were used as references. As a result, in Figure 4.2A, unlike the solvent cast PVDF films which have a strong α phase absorption peak around 763 cm^{-1}, precipitation printed PVDF samples from both DMF and DMSO solutions show an evident β phase peak at 1275 cm^{-1}, but no clear 763 cm^{-1} α phase peak. A small shoulder around 1234 cm^{-1} indicates the existence of γ phase in both solvent cast and precipitation printed PVDF samples. While historically the absorption peak around 830–840 cm^{-1} was assigned to β phase [125], recently it was found to be a combination of the electroactive (EA, β + γ) phases (β phase at 840 cm^{-1} and γ phase at 831 cm^{-1}) [237,238]. Precipitation printed PVDF using parallel or alternating infill patterns does not have a significant influence on the crystalline phase formation according to FTIR.

Quantitative crystalline phase fraction calculation based on FTIR can be performed based on the theories developed by Gregorio et al. [125], Benz and Euler [239], using the characteristic absorbance peaks of α phase at 763 cm^{-1}, β phase at 1275 cm^{-1}, γ phase at 1234 cm^{-1} and EA phases at 830–840 cm^{-1}. Equation 4.1 by Gregorio et al. can be used to calculate the fraction of α phase and EA phases based on Beer-Lambert law and the absorption peaks at 763 cm^{-1} and 840 cm^{-1} (or the maximum in 830–840 cm^{-1}):

$$F_{EA} = \frac{I_{840}}{\left(\frac{K_{840}}{K_{763}}\right) I_{763} + I_{840}} \tag{4.1}$$

where F_{EA} is the fraction of the EA phases (β+γ), I_{763} and I_{840} are the absorbances at 763 cm^{-1} and the maximum in 830–840 cm^{-1}, respectively, while K_{840}/K_{763} is the ratio of absorption coefficients at these respective wavenumbers, which is 1.26 [125]. However, the fractions of β phase and γ phase cannot be decoupled using this equation.

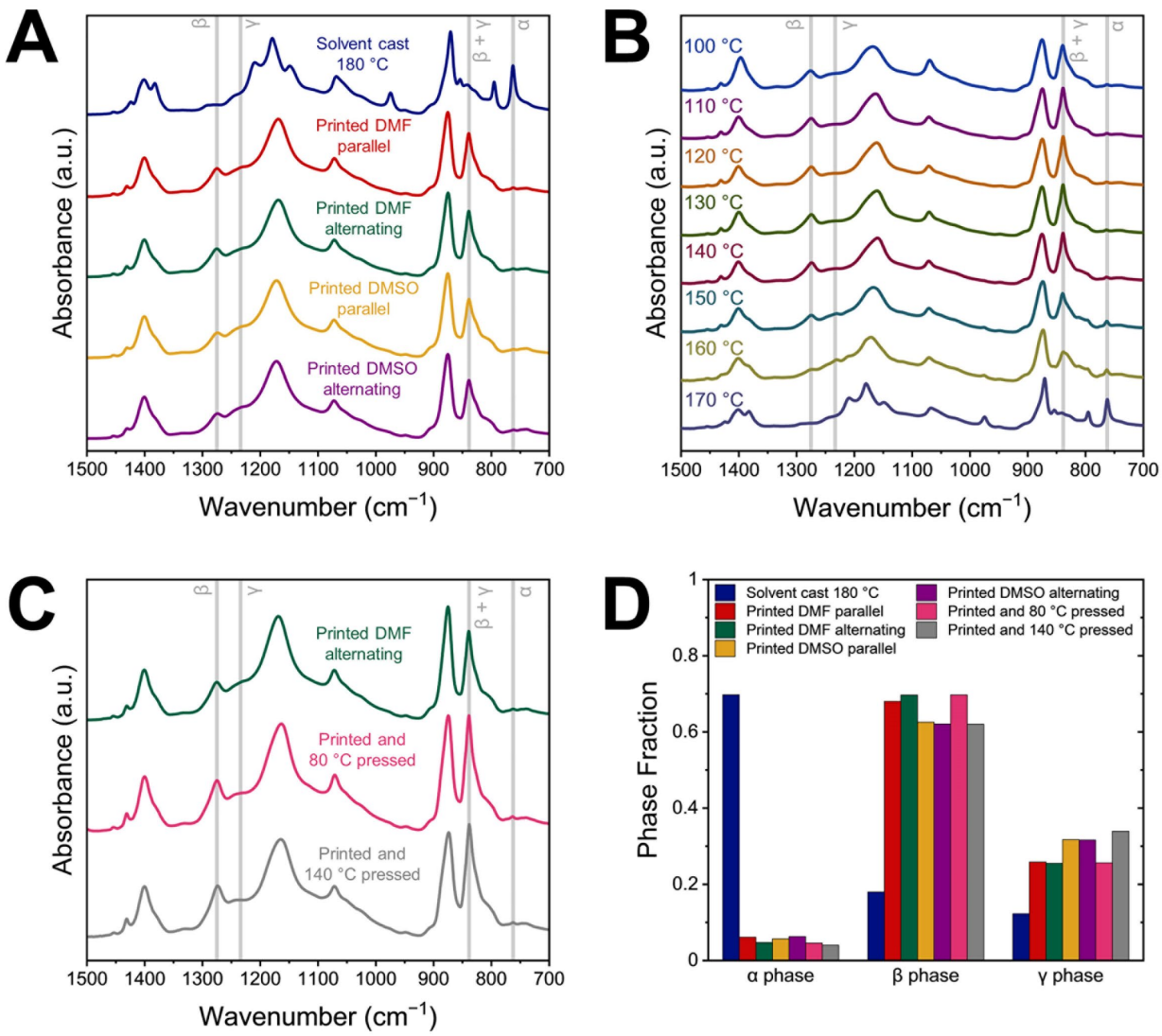

Figure 4.2. A) FTIR spectra of precipitation printed PVDF using DMF and DMSO as the solvent and two different infill patterns, compared to solvent cast PVDF at 180 °C. B) FTIR spectra of precipitation printed PVDF post-heated at different temperatures. C) FTIR spectra of precipitation printed PVDF hot pressed at different temperatures. D) Crystalline phase fraction results of all PVDF samples in this study, based on FTIR.

On the other hand, Benz and Euler [239] derived equations to calculate the fractions of individual α, β and γ phases based on the absorption peaks at 763 cm^{-1}, 835 (or 830–840) cm^{-1} and 1275 cm^{-1}, respectively:

$$I_{763} = K_{\alpha}^{763} X_{\alpha} t \tag{4.2}$$

$$I_{1275} = K_{\beta}^{1275} X_{\beta} t \tag{4.3}$$

$$I_{835} = \left(K_{\beta}^{835} X_{\beta} + K_{\gamma}^{835} X_{\gamma} + K_{am}^{835} \left(1 - X_{\alpha} - X_{\beta} - X_{\gamma}\right) \right) t \tag{4.4}$$

where I_{763}, I_{835}, I_{1275} are the baseline-corrected absorbances at 763 cm^{-1}, 835 (or 830–840) cm^{-1} and 1275 cm^{-1} respectively, and K_{α}^{763}, K_{β}^{1275}, K_{β}^{835}, K_{γ}^{835} and K_{am}^{835} are the absorption coefficients

for each phase, including amorphous (am), at corresponding absorption peaks, respectively. Furthermore, X_α, X_β and X_γ are the mole fractions of each phase, and t is the thickness of the sample in μm. According to this theory, the total thickness of the sample was determined by the experimentally calibrated thickness-absorbance relation at 1070 cm^{-1} peak, $I_{1070}=0.095t+0.07$, where t is in the unit of μm, using sample thickness ranging from 0 to 10 μm [240]. However, using this thickness-absorbance relation gave an unreasonable calculation result for thick precipitation printed PVDF samples (about 100 μm thick), which indicates that directly using this theory to calculate the individual phase fraction is not applicable. Therefore, a combination of these phase fraction calculation theories was developed in this research. Based on Equation 4.1, the fraction of individual β and γ phases can be further determined by the curve deconvolution of the 830–840 cm^{-1} EA phases absorption peak, while neglecting the contribution from the amorphous phase due to the relatively negligible absorption coefficient of the amorphous phase at this peak [239]. The curve deconvolution was performed using Voigt profiles [241,242], and a sample deconvolution result is shown in Figure 4.3. The equation to calculate the individual β phase is as follows:

$$F(\beta)=\frac{F_{EA}I_\beta^{840}}{\left(\frac{K_\beta^{840}}{K_\gamma^{831}}\right)I_\gamma^{831}+I_\beta^{840}}=\frac{I_{840}}{\left(\frac{K_{840}}{K_{763}}\right)I_{763}+I_{840}}\times\frac{I_\beta^{840}}{\left(\frac{K_\beta^{840}}{K_\gamma^{831}}\right)I_\gamma^{831}+I_\beta^{840}} \tag{4.5}$$

where I_γ^{831} and I_β^{840} are the absorbances of individual γ and β phases at the corresponding wavenumber after the curve deconvolution. $K_\beta^{840}/K_\gamma^{831}$ is the ratio of absorption coefficients of γ and β phases at the corresponding wavenumbers, which is approximately 0.88, estimated by using the experimentally measured absorption coefficients of γ and β phases at 835 cm^{-1} [239]. The γ phase fraction can be obtained by simply subtracting the β phase fraction from the F_{EA}, and the α phase fraction is $F_\alpha=1-F_{EA}$. The calculated results in Figure 4.2D show that precipitation printed PVDF samples all have more than 90% EA phases including more than 60% β phase, which are substantially higher than the solvent cast PVDF with 30% EA phases including 18% β phase. Printed PVDF from a DMF solution has approximately 6% higher β phase fraction than printed PVDF from a DMSO solution, yet the infill patterns show no significant influence on the phase composition. Therefore, considering the β phase fraction and final sample isotropy, PVDF printed from the DMF solution using the alternating pattern is selected as the fabrication process for the entire research.

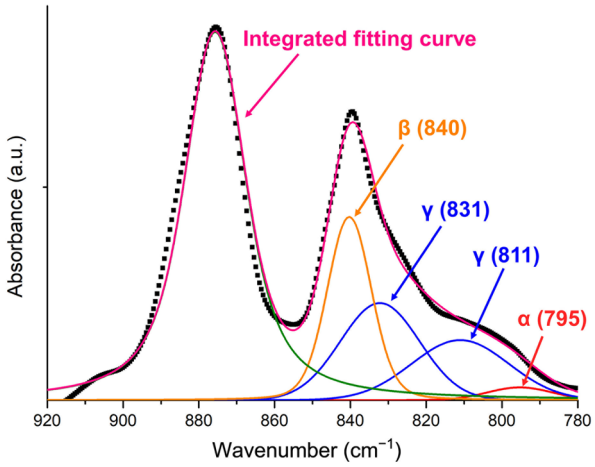

Figure 4.3. Sample curve deconvolution of PVDF FTIR spectrum between 780 and 920 cm^{-1}.

Moreover, the thermal stability of the precipitation printed PVDF was tested by varying the post-heating temperature. In Figure 4.2B, the α phase absorption peak at 763 cm^{-1} remains negligible when the temperature is below 150 °C, while the β phase peak at 1275 cm^{-1} is an intense peak. When the temperature is above 150 °C, the α phase peak becomes more distinguishable and the β phase peak intensity reduces. This means the β phase in the printed PVDF is stable below 150 °C, and the β to α transformation takes place at a temperature higher than 150 °C. Since precipitation printed PVDF is highly porous, hot pressing can be applied to densify the PVDF. Based on the β phase thermal stability, two hot pressing temperatures, 80 °C and 140 °C were tested using FTIR study, while keeping the pressure around 60 MPa. From Figure 4.2C and D, hot pressing at both temperatures does not induce the transformation into α phase, but hot pressing at 80 °C has higher β phase content then hot pressing at 140 °C. In the following two characterization sections, 80 °C hot pressing is chosen based on the higher β phase content.

4.3.2 X-ray diffraction

To verify the crystalline phase composition in solvent cast and precipitation printed PVDF, X-ray diffraction (XRD) was performed on PVDF samples using a Rigaku Ultima IV X-ray diffractometer with CuKα radiation (λ = 0.154 nm). Figure 4.4A shows the XRD patterns of solvent cast PVDF, precipitation printed PVDF and precipitation printed then hot pressed PVDF, and Figure 4.4B is the zoomed-in view in the 2θ range from 16° to 24°. Solvent cast PVDF exhibits α phase characteristic diffraction peaks at 17.6° (100), 18.4° (020) and 19.9° (021) [243]. On the contrary, precipitation printed PVDF shows a γ phase peak at 18.5° (020), and a broad peak that combines a γ phase peak at 20.1°–20.3° (110/101) and a β phase peak at 20.7°–20.8° (110/200)

[237,243]. The precipitation printed then hot pressed PVDF has a weaker γ phase peak at 18.5° and a more pronounce β phase peak at 20.7°–20.8° than the directly precipitation printed PVDF, indicating that 80 °C hot pressing promotes the β phase formation and possibly also the total degree of crystallinity, which will be studied in the next section.

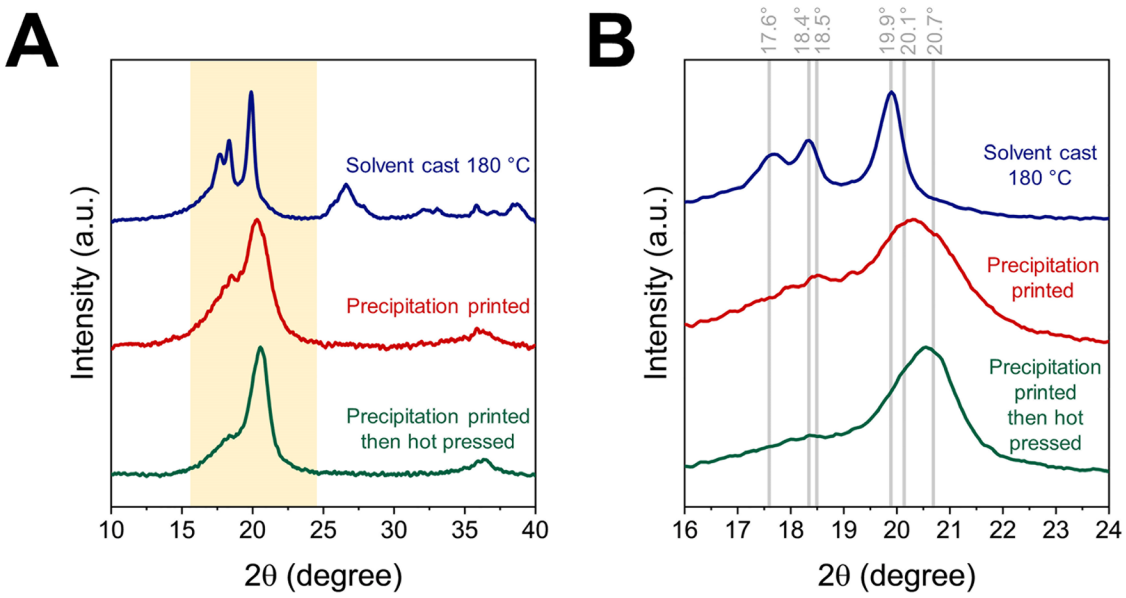

Figure 4.4. A) XRD patterns of solvent cast PVDF at 180 °C, precipitation printed PVDF and precipitation printed then hot pressed PVDF. B) Zoomed-in view of the XRD patterns in the 2θ range from 16° to 24°.

4.3.3 Differential scanning calorimetry

The melting behavior and total degree of crystallinity of the three types of PVDF samples were investigated through differential scanning calorimetry (DSC), using a differential scanning calorimeter (Q2000, TA Instruments) with a temperature ramp from 30 °C to 200 °C at 5 °C·min^{-1} rate. In Figure 4.5, the solvent cast PVDF shows a sharp and narrow α phase dominant melting, which has an onset melting temperature (T_m) of 156 °C. The precipitation printed PVDF and precipitation printed then hot pressed PVDF have a broad β phase dominant melting, which has a lower onset T_m of 150 °C. A small γ phase melting shoulder in 168–172 °C range can also be observed in these two PVDF samples. The β phase onset T_m agrees with the thermal stability test in Figure 4.2B, implying the β phase transformation to α phase takes place when the β phase melts.

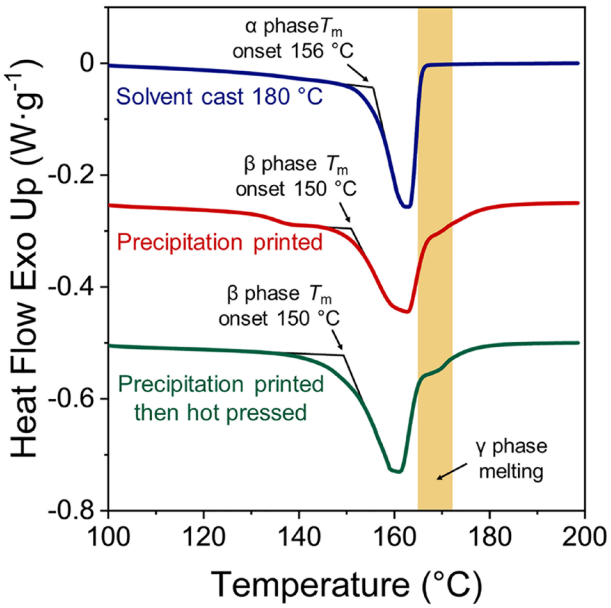

Figure 4.5. DSC melting curves of solvent cast PVDF at 180 °C, precipitation printed PVDF and precipitation printed then hot pressed PVDF.

The total degree of crystallinity (χ_c) can be calculated by the ratio of the melting enthalpy of the sample (ΔH_m) and the melting enthalpy of totally crystalline material ($\Delta H_0 = 104.50$ J·g^{-1} [244]):

$$\chi_c = \frac{\Delta H_m}{\Delta H_0} \tag{4.6}$$

where the melting enthalpy (ΔH_m) of the sample is the area integral of the melting peak in heat flow-time DSC curve. Table 4.1 contains the calculated χ_c and its breakdown into three crystalline phases based on the FTIR phase fraction results in Figure 4.2D. The precipitation printed PVDF has significantly improved χ_c (about 10%) than the solvent cast PVDF, and hot pressing can further improve the χ_c and the total amount of β phase ($\chi_c(\beta)$). Combining FTIR, XRD and DSC analysis, it can be concluded that precipitation printed PVDF exhibits higher χ_c with dominant β phase, some γ phase and negligible α phase that outperforms solvent cast PVDF films, and the β phase content can be enhanced by hot pressing.

Table 4.1. Degree of crystallinity (χ_c) of the three types of PVDF samples.

PVDF Sample	χ_c	$\chi_c(\alpha)$	$\chi_c(\beta)$	$\chi_c(\gamma)$
Solvent cast at 180 °C	34.2%	23.9%	6.1%	4.2%
Precipitation printed	43.5%	2.1%	30.3%	11.1%
Precipitation printed then hot pressed	46.2%	2.1%	32.3%	11.9%

4.4 Mechanism of β phase formation

The mechanism through which precipitation printing induces high β phase PVDF is explained by the interaction between PVDF and water, where the hydroxyl group (O-H) of the water molecules can form hydrogen bonds (H-bonds) with the electronegative fluorine atoms of the PVDF molecules to promote all-trans chain conformation (TTT) [132,245], as illustrated in Figure 4.6. It has been observed that during the phase inversion of cast PVDF solution in a water bath, the surface of the solution has rapid mass exchange between the solvent and water, which increases the polymer concentration at the interfacial region, and preferably leads to better oriented CH_2-CF_2 packing (*e.g.* all-trans) due to conformation entropy [246]. During the precipitation printing process, the PVDF solution is dispensed inside the water bath, which continuously creates a local interfacial region between the PVDF solution and water around the dispensing nozzle. Due to the layer-by-layer additive manufacturing characteristics, this interfacial region becomes dominant throughout a printed sample, and thus promotes the formation of the polar β phase and γ phase in the entire PVDF structure.

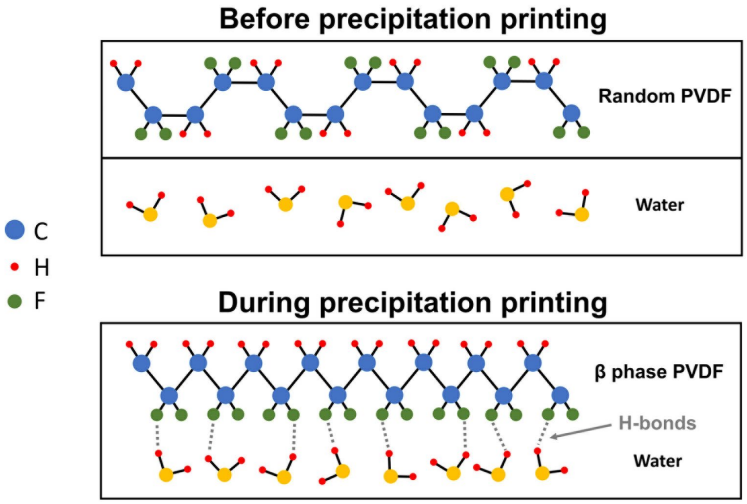

Figure 4.6. Mechanism of β phase formation during precipitation printing.

4.5 Ferroelectric and dielectric properties

The ferroelectric property of the PVDF samples was determined by measuring the ferroelectric hysteresis loop (*D*-*E* loop) through a Sawyer-Tower circuit (Figure 4.7A). Two PVDF samples, one being the solvent cast PVDF at 180 °C, the other being the precipitation printed then 80 °C hot pressed PVDF, were immersed in an oil bath at room temperature to avoid breakdown under the high external electric field. A function generator (33210A, Keysight Technologies) was

used to provide a 1 Hz sinusoidal voltage signal and was amplified (×1000) using a voltage amplifier (Model 10/10B, TREK). The electric field across the sample, E, and the polarization or electric displacement of the sample, D, were determined by the following equations:

$$E = \frac{V_s - V_{ref}}{t} \tag{4.7}$$

$$D = \frac{C_{ref} V_{ref}}{A} \tag{4.8}$$

where V_s is the amplified source voltage, V_{ref} is the voltage measured across the reference capacitor, C_{ref} is the capacitance of the reference capacitor (0.47 μF), t is the sample thickness and A is the sample electrode area.

As a result, Figure 4.7B shows the *D-E* loops of the solvent cast PVDF under electric field strengths ranging from 100 MV·m^{-1} to 230 MV·m^{-1}, where hysteresis loops are narrow and a coercive field of 82 MV·m^{-1} is observed. On the other hand, in Figure 4.7C, the hysteresis loops of the precipitation printed then 80 °C hot pressed PVDF have stronger polarization, and a coercive field of 98 MV·m^{-1}. It should be noted that due to the remaining porosity (7% based on density measurement) of the 80 °C hot pressed PVDF, higher electric field than 180 MV·m^{-1} results in electrical breakdown of the PVDF sample. Therefore, the *D-E* loops of the precipitation printed then 80 °C hot pressed PVDF are not saturated, which means a saturated remnant polarization (P_R) value cannot be obtained. By comparing the *D-E* loops of the two types of PVDF samples under 180 MV·m^{-1} field strength (maximum before breakdown) in Figure 4.7D, it can be seen that the precipitation printed then 80 °C hot pressed PVDF has a higher measured P_R of 3.23 μC·cm^{-2} than the solvent cast PVDF (P_R = 0.44 μC·cm^{-2}), indicating a stronger ferroelectric performance that is attributed to the higher ferroelectric β phase content.

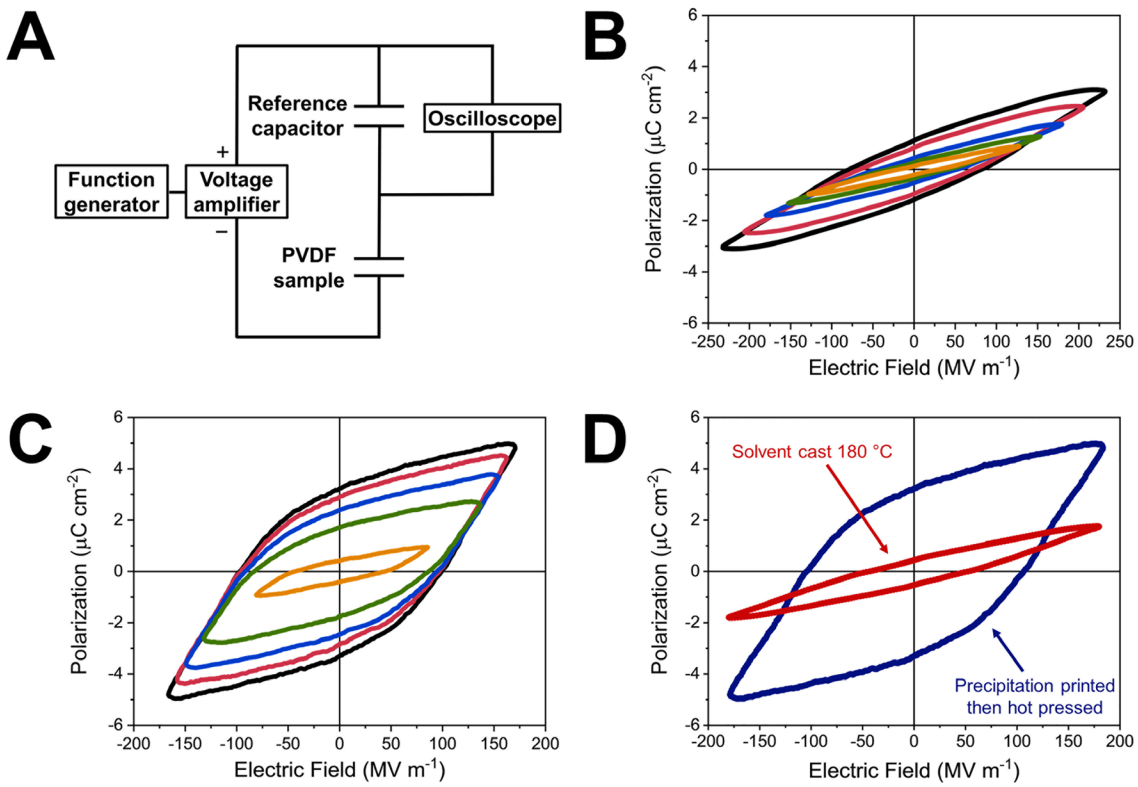

Figure 4.7. A) Sawyer-Tower circuit. B) *D-E* loops of solvent cast PVDF under various electric fields. C) *D-E* loops of precipitation printed then hot pressed PVDF under various electric fields. D) Comparison of *D-E* loops under the same electric field.

The dielectric constant, or relative permittivity of four types of PVDF samples in the frequency range from 20 Hz to 2 MHz was measured using a precision LCR meter (E4980A, Keysight Technologies), caliper and micrometer for capacitance and sample dimensions, respectively. The result in Figure 4.8 shows that the precipitation printed PVDF has a dielectric constant of only 3.55 at 1 kHz, which is 33.6% of the dielectric constant of solvent cast PVDF (10.58 at 1 kHz). This low dielectric constant is attributed to the low density of the precipitation printed PVDF (0.646±0.012 g·cm^{-3}), which has 64% porosity compared with fully dense PVDF. Using 80 °C hot pressing can increase the dielectric constant to 5.20 at 1 kHz, but the remaining porosity still limits the dielectric performance of the precipitation printed then hot pressed PVDF. Thus, a higher temperature hot pressing of 140 °C was applied to the precipitation printed PVDF to further soften the polymer in the densification process for better pore reduction. The resulting dielectric constant after 140 °C hot pressing reaches 9.48 at 1 kHz, which is almost 90% of the solvent cast PVDF. Therefore, it can be concluded that higher temperature hot pressing of the precipitation printed PVDF can lead to better dielectric constant, but the influence of pores on PVDF's dielectric constant cannot be eliminated completely by hot pressing.

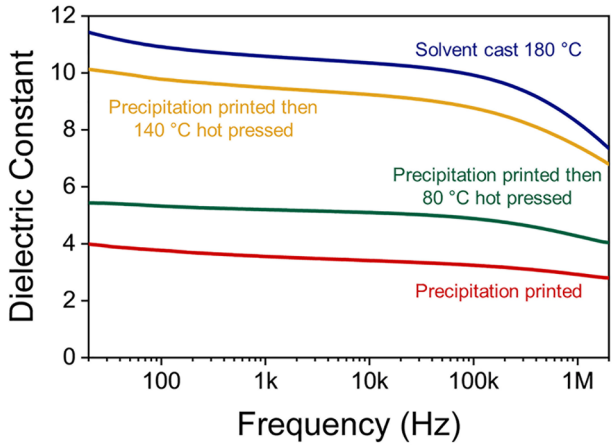

Figure 4.8. Dielectric constant of solvent cast PVDF, precipitation printed PVDF, and precipitation printed then hot pressed PVDF.

4.6 Electric poling

To obtain optimal piezoelectric response from the PVDF samples, electric poling was applied to PVDF samples prior to any piezoelectric testing. Although corona poling is reported to be a successful poling method for large films when trying to avoid sample shorting [247,248], precipitation printed PVDF samples have rough surfaces and porosity which make them vulnerable to corona current and small breakdown spots. Thus, direct contact poling was selected to be the poling method for precipitation printed PVDF. To increase the breakdown strength of the samples, printed PVDF samples were first soaked in an 80 °C oil bath for 1 h to fill the internal pores with oil. A high voltage (2–15 kV) was then applied across the thickness of the PVDF samples (100–200 μm) using two flat aluminum electrodes, forming a strong electric field of 20-100 $MV \cdot m^{-1}$ that remains below the breakdown strength of bulk PVDF (250–300 $MV \cdot m^{-1}$) [248]. The highest electric field before breakdown for the precipitation printed PVDF is 75 $MV \cdot m^{-1}$, for the printed then 80 °C pressed PVDF is 75 $MV \cdot m^{-1}$, and for the printed then 140 °C pressed PVDF is 100 $MV \cdot m^{-1}$. All PVDF samples were made to have a slightly larger area than the flat aluminum electrodes to avoid potential electric arcing around the edges of the sample. The PVDF samples were poled in 80 °C oil for 2 h and slowly cooled down to room temperature under the selected applied electric field. The poled samples were then washed with methanol to remove residual oil and dried under vacuum overnight. Once fully dry, the samples were sputter coated with thin gold electrodes on both sides for piezoelectric testing.

4.7 Piezoelectric properties

The piezoelectric charge coefficients (d_{33} and d_{31}) of precipitation printed PVDF were measured through direct piezoelectric effect. The longitudinal d_{33} coefficient was measured using a customized Berlincourt d_{33} meter [249,250] (Figure 4.9A) based on a piezoceramic stack actuator (PStVS 1000V VS45, Piezosystem Jena GmbH) and a piezoceramic force sensor (208C, PCB Piezotronics).The input excitation vibration was controlled by a function generator (33210A, Keysight Technologies), which fed a 10 Hz sinusoidal signal to the stack actuator. The dynamic force F applied on the sample was measured by the piezoceramic force sensor, while the induced charge Q was measured from the two semi-domed electrodes on each side of the sample, using a charge amplifier circuit (Figure 4.10) with a high pass cutoff frequency of 5.3 Hz. The d_{33} coefficient can be calculated as follows.

$$d_{33} = \frac{\text{longitudinal charge density}}{\text{longitudinal stress}} = \frac{Q}{F} \tag{4.9}$$

It should be noted that due to the dipole alignment direction of PVDF, the Q and F have a 180° phase difference, so the d_{33} values are negative. Figure 4.9B shows the measured d_{33} coefficient of four types of PVDF samples. Electric poling field strength has a significant influence on the d_{33} value, where the precipitation printed PVDF poled under a 75 $MV \cdot m^{-1}$ field has a d_{33} of -0.99 ± 0.10 $pC \cdot N^{-1}$, 8 times of the d_{33} of precipitation printed PVDF poled under a 20 $MV \cdot m^{-1}$ field. Nonetheless, the average d_{33} coefficient of printed and 75 $MV \cdot m^{-1}$ poled samples remains relatively low compared to that of stretched and poled PVDF sheets, since the precipitation printed PVDF only has a density of 0.646 $g \cdot cm^{-3}$ (64% porosity) [205]. Therefore, precipitation printed then hot pressed PVDF samples were also tested to evaluate the influence of porosity on the piezoelectric effect. The d_{33} coefficient of precipitation printed then 80 °C pressed PVDF after 75 $MV \cdot m^{-1}$ electric field poling is improved up to -6.42 ± 0.78 $pC \cdot N^{-1}$, a 550% increase relative to the directly printed PVDF poled under the same conditions. Using a higher temperature of 140 °C for hot pressing and a poling field of 100 $MV \cdot m^{-1}$ without breakdown, the d_{33} coefficient is finally improved to -18.09 ± 0.66 $pC \cdot N^{-1}$, which is comparable to biaxially stretched PVDF (−12 to −21 $pC \cdot N^{-1}$) [135,136] and only lower than uniaxially stretched PVDF (−30 $pC \cdot N^{-1}$) [135].

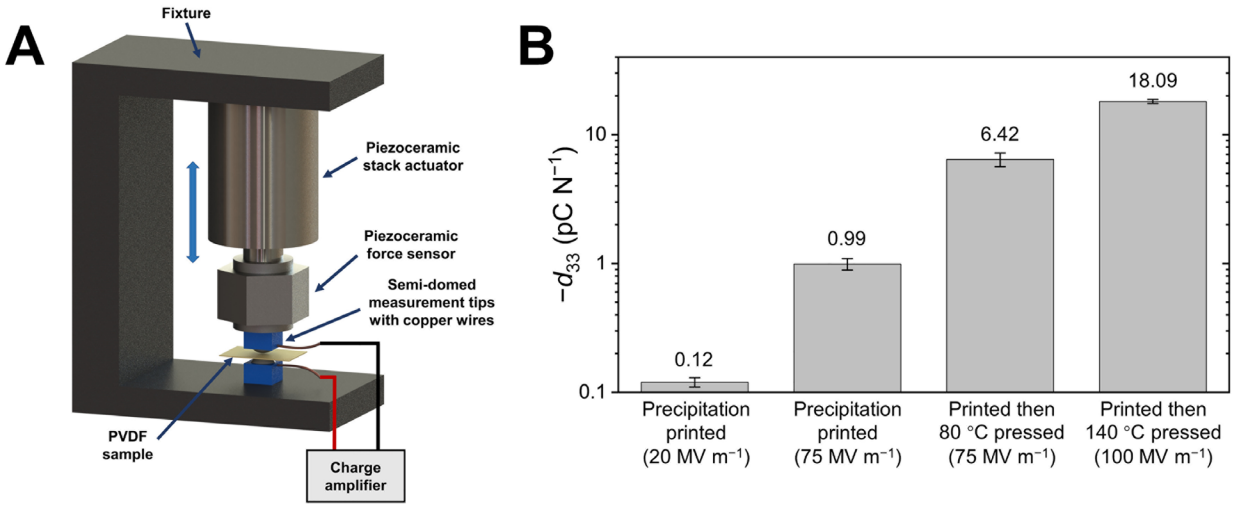

Figure 4.9. A) Customized d_{33} meter based on a piezoceramic stack actuator and a piezoceramic force sensor. B) Measured d_{33} values of four types of PVDF samples.

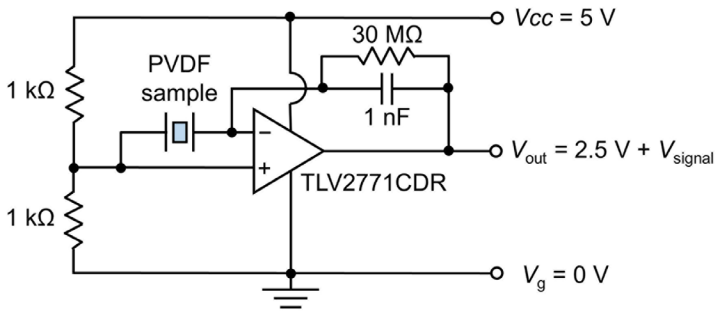

Figure 4.10. Charge amplifier circuit.

The transverse piezoelectric d_{31} coefficient was measured by using a dynamic mechanical analyzer (DMA, Q800, TA Instruments) in tension mode to precisely apply a 10 Hz uniaxial 0.5% sinusoidal strain to PVDF samples (25 mm×5 mm×0.1 mm) with gold electrodes sputtered on both sides (Figure 4.11A), through Equation 4.10,

$$d_{31} = \frac{\text{longitudinal charge density}}{\text{transverse stress}} = \frac{\frac{Q}{WL}}{\frac{F}{Wt}} = \frac{Qt}{FL} \tag{4.10}$$

where Q is the charge measured by the charge amplifier, F is the force measured by the DMA, t and L are the thickness and length of the sample electrode area, respectively. The measured d_{31} coefficients in Figure 4.11B also show a significant improvement in piezoelectric response when increasing the poling field from 20 MV·m^{-1} to 75 MV·m^{-1}. The measured d_{31} coefficient for precipitation printed PVDF samples poled under a 75 MV·m^{-1} field is 1.08±0.04 pC·N^{-1}, a 260% increase relative to the samples poled under a 20 MV·m^{-1} field (0.30±0.04 pC·N^{-1}). Like d_{33}, the

d_{31} coefficient can be further improved through hot pressing, as the reduced porosity after 80 °C pressing yields an approximately 100% improvement in d_{31} (1.95±0.21 pC·N^{-1}). An open-circuit voltage (measured by a Keysight Technologies B2980A electrometer) response plot highlighting the effect of hot pressing is shown in Figure 4.12. Using a higher temperature of 140 °C for hot pressing and a poling field of 100 MV·m^{-1}, the d_{31} coefficient is eventually improved to 8.69±1.60 pC·N^{-1}. In addition, the precipitation printing uses an in-plane (1-2 plane) 0°/90° alternating infill pattern, so transversely isotropic properties are expected for this plane. To investigate the isotropy of transverse piezoelectric charge coefficients, d_{31} and d_{32} coefficients were measured on printed then 140 °C pressed PVDF samples. As a result, in Table 4.2, no significant difference can be found between d_{31} and d_{32} (p=0.99), indicating a transversely isotropic piezoelectric behavior. Thess d_{31} and d_{32} values are also in the range of literature reported d_{31} and d_{32} values of biaxially stretched PVDF films (4 to 14 pC·N^{-1}) [135,136,251]. Another interesting discovery is that porous precipitation printed PVDF samples have higher d_{31} than d_{33} (in absolute value), implying more sensitive transverse piezoelectric response than longitudinal piezoelectric response due to the existence of pores. However, hot-pressed and densified PVDF samples behave more like conventional stretched PVDF films which have lower d_{31} than d_{33}.

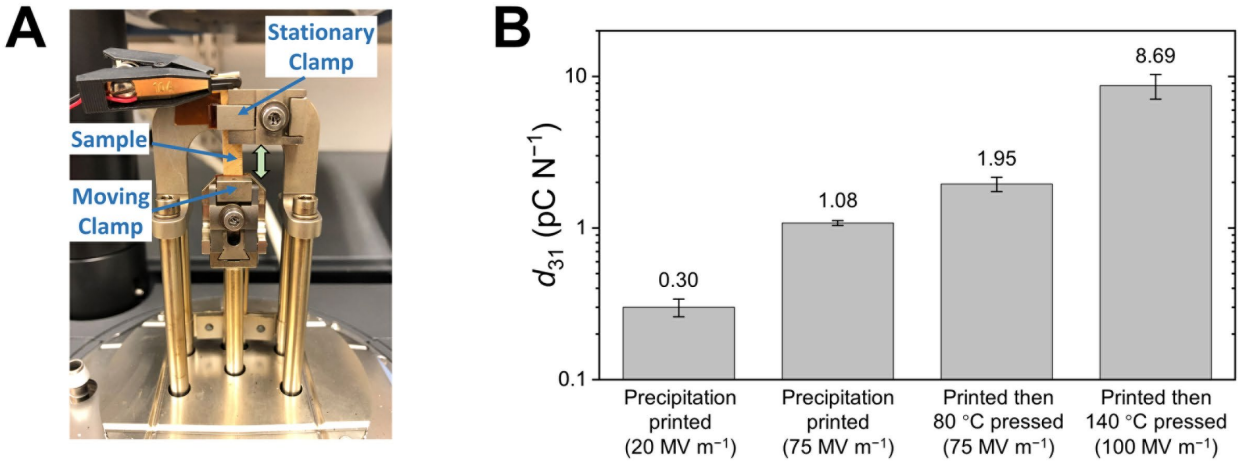

Figure 4.11. A) Customized d_{31} meter based on the tension mode dynamic mechanical analyzer. B) Measured d_{31} values of four types of PVDF samples.

Table 4.2. Measured d_{31} and d_{32} coefficients of the printed then 140 °C pressed PVDF.

	d_{31} (pC·N^{-1})	d_{32} (pC·N^{-1})
Printed then 140 °C pressed PVDF	8.69±1.60	8.68±2.22

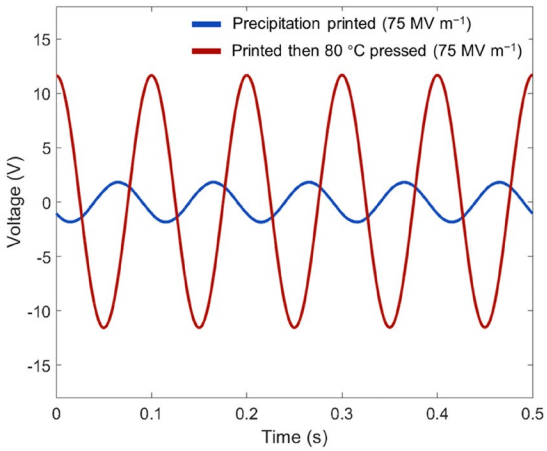

Figure 4.12. Open-circuit voltage plot of the precipitation printed PVDF and the printed then 80 °C pressed PVDF using the same poling conditions in d_{31} mode.

There are two main takeaways from this section based on the piezoelectric properties. First, precipitation printed PVDF after poling can achieve longitudinal and transverse piezoelectric charge coefficients at 1 $pC \cdot N^{-1}$ level, comparable or higher than other additively manufactured PVDF in the literature [142–144,148], while having much higher specific piezoelectric properties (per unit mass) and flexibility due to the high porosity. Since in Chapter 2 the capability of precipitation printing conductive PVDF nanocomposites on an existing neat PVDF structure was already demonstrated, by using dual material precipitation printing with a conductive electrode material in the future, 3D piezoelectric and porous PVDF devices with custom printed electrodes can be fabricated through precipitation printing and subsequent poling. Second, by hot pressing the precipitation printed PVDF, high piezoelectric performance 2D PVDF films with arbitrary shapes and scalable thickness can be produced without the need of stretching, which distorts the PVDF film shape.

4.8 Piezoelectric energy harvesting devices

To demonstrate the application of the proposed PVDF, two types of piezoelectric energy harvesters were fabricated and tested: a stretching mode (d_{31} mode) energy harvester and a compression mode (d_{33} mode) shoe insole energy harvester. A stretching mode energy harvester is a device that transforms waste mechanical energy from axial displacement into usable electrical energy and is often used in environments that have a significant amount of ambient vibration. Two 25 mm×5 mm×0.1 mm (final dimensions) rectangular bar-shape stretching mode energy harvesters, one being precipitation printed, and the other being printed then hot pressed (80 °C),

were poled with a 75 MV·m^{-1} electric field and then excited by 0.5% uniaxial tensile strain at varying frequencies using a DMA (Q800, TA Instruments), as shown in Figure 4.13A. The root mean square (RMS) voltage output of the energy harvesters loaded by a variable resistor ranging between 0–40 MΩ was measured by a Keysight Technologies B2980A electrometer, and the output power and power density of the energy harvesters follow the subsequent equations:

$$P = \frac{V_{RMS}^2}{R} \tag{4.11}$$

$$P_\rho = \frac{P}{At} \tag{4.12}$$

where P is the output power, P_ρ is power density, V_{RMS} is the measured RMS voltage, R is the load resistance, A and t are the area and thickness of the energy harvester, respectively.

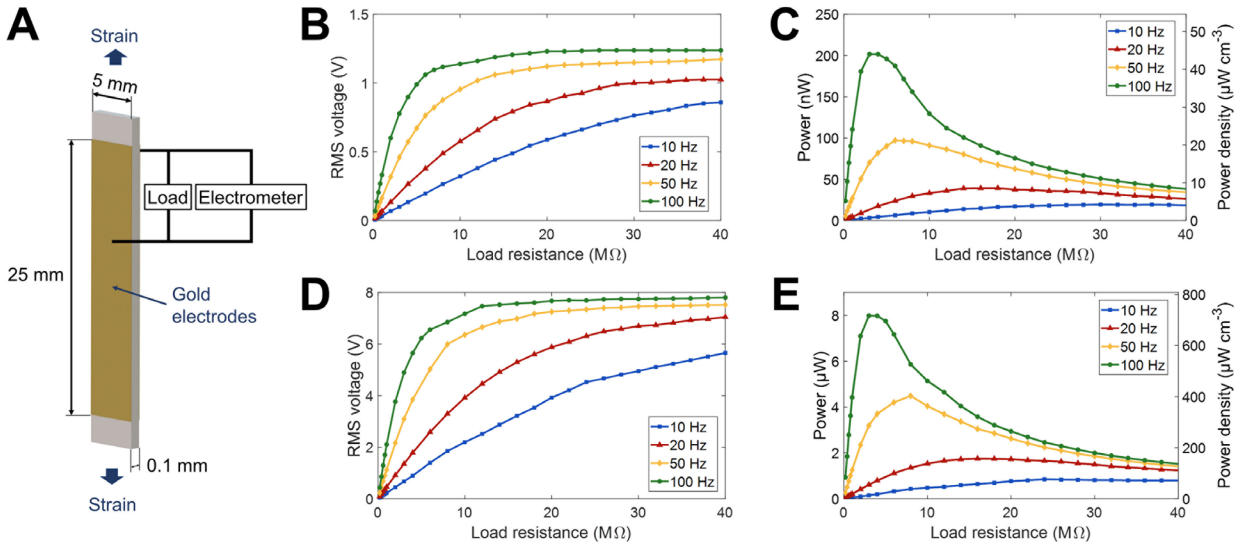

Figure 4.13. A) Stretching mode energy harvester. B–E) Precipitation printed stretching mode energy harvester with and without hot pressing loaded by variable resistance under different excitation frequency at 0.5% strain. B) Output RMS voltage without hot pressing. C) Power and power density without hot pressing. D) Output RMS voltage with hot pressing. E) Power and power density with hot pressing.

For the precipitation printed stretching mode energy harvester, in Figure 4.13B and C, as the excitation frequency increases, both the output voltage and power increase. The impedance of the sample decreases as the excitation frequency increases, resulting in the maximum output power occurring at a lower load resistance for higher excitation frequencies. The maximum output power and power density of the energy harvester under 100 Hz excitation (the highest excitation frequency that can be applied to the sample without breaking) at 0.5% strain are 202 nW and 44 μW·cm^{-3}, respectively. To further improve the energy harvesting performance, a stretching mode energy harvester based on printed then hot pressed PVDF was also tested, whose voltage and

power output are shown in Figure 4.13D and E. The maximum output power and power density of hot-pressed energy harvester are found to be 7.96 μW and 717 $\mu W \cdot cm^{-3}$, respectively, under 100 Hz excitation at 0.5% strain. Therefore, the stretching mode energy harvester after hot pressing displays a power density that is 16 times higher than that of the directly printed one, highlighting the importance of reducing internal porosity of precipitation printed PVDF through hot pressing to maximize energy harvesting performance.

A 3D printed heel insole energy harvester with dimensions of 70 mm×60 mm×6 mm was also fabricated to demonstrate the ability of a bulk piezoelectric device to collect waste mechanical energy in compression d_{33} mode (Figure 4.14A and B). The insole consists of three layers: a soft and porous precipitation printed top layer with curved edges to fit heels, a 0.25 mm thick precipitation printed then hot pressed (80 °C) middle layer acting as the piezoelectric energy harvester and a porous precipitation printed bottom layer providing structural support. The hot-pressed middle layer was poled in oil under a 75 $MV \cdot m^{-1}$ electric field. Once poled, the middle layer was sputtered with gold electrodes on both sides to which copper tapes were attached to measure the voltage output. All three layers were assembled by solvent welding using a PVDF solution and dried for 1 h under vacuum to obtain the final device. It was first tested under different compression force amplitudes and frequencies using a dynamic testing frame (E1000, Instron) to verify the piezoelectric performance of large-scale printed then hot pressed PVDF. As confirmed in Figure 4.14C, the open-circuit voltage response agrees with the d_{33} value measured in the previous section. The figure also shows that the open-circuit voltage increases slightly as the excitation frequency increases. The 2 Hz, 300 N amplitude excitation is used to simulate the force that an adult could apply on the heel insole, and it proves that the heel insole energy harvester would not saturate in this real case situation. The output RMS voltage, power and power density of the heel insole energy harvester are displayed in Figure 4.14D and E. To simulate the frequency of actual human steps, and due to the limitation of the stable load and frequency that could be generated by the testing instrument, only low frequencies (0.5 Hz, 2 Hz and 5 Hz) and a 100 N amplitude force were used for testing. The maximum power and power density occur under the highest frequency of 5 Hz, which are 345 nW and 1.2 $\mu W \cdot cm^{-3}$, respectively. It should be noted that the output power and power density would be higher if excited using a force amplitude of 300 N and at a similar frequency, since the energy harvester was not yet saturated (Figure 4.14C). Compared with other thin film piezoelectric shoe insole energy harvesters from literature,

precipitation printed full heel insole generates a comparable high voltage output (about 20–30 V) but lower power output, due to a much larger internal impedance caused by a larger thickness of our heel insole.

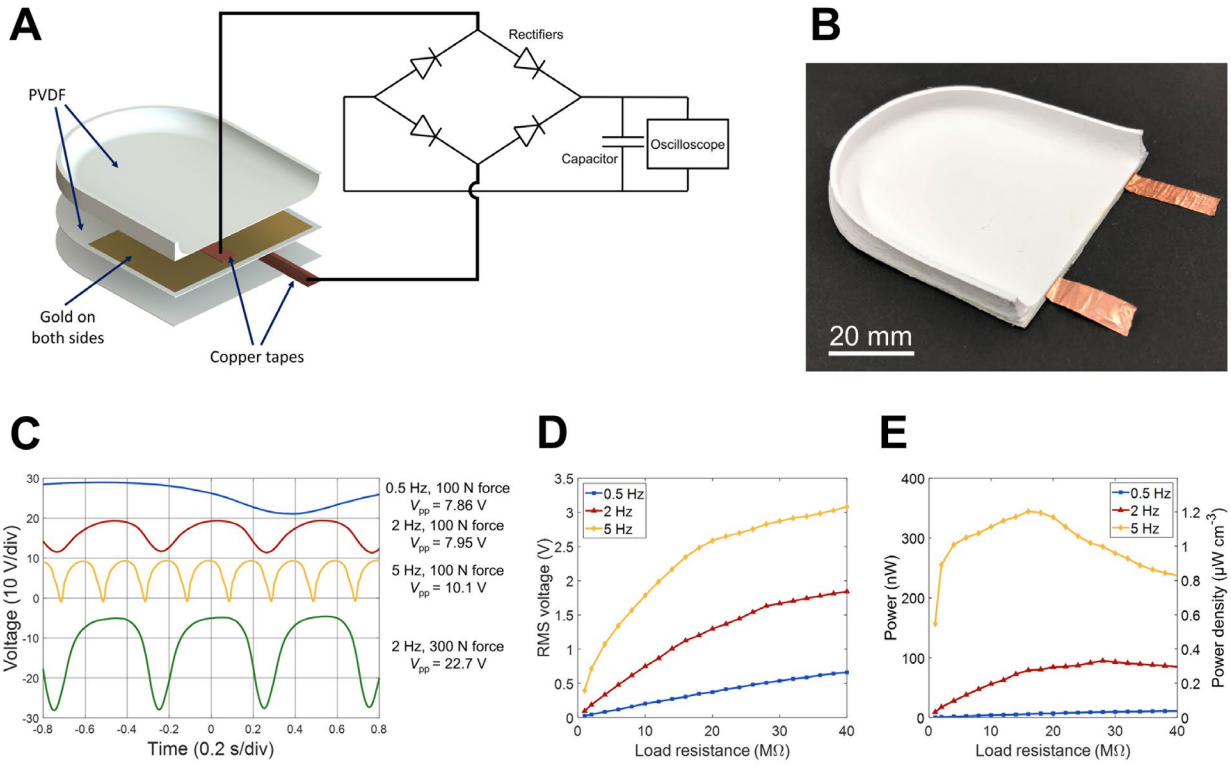

Figure 4.14. A) Schematic of the heel insole energy harvester with testing circuits. B) The fabricated heel insole energy harvester. C) Open-circuit voltage response of the heel insole energy harvester under different compression force amplitudes and frequencies. D–E) Output RMS voltage and power of the heel insole energy harvester under various loads.

After standard instrument testing, the energy harvesting performance of the heel insole under human walking was demonstrated. Figure 4.15A shows the open-circuit voltage response during 5 steps obtained using full wave rectifiers, where the peak voltage ranges from 17 V to 26 V due to natural variation in tread strengths. The heel insole energy harvester was then used to charge a 4.7 μF capacitor through a full wave rectifier. As seen in Figure 4.15B, after continuously stepping on the heel insole for 60 steps, the capacitor was charged to 1.7 V, equivalent to 8.0 μC in electric charge or 6.8 μJ of energy. When stepping on the heel insole for about 3 minutes, the capacitor could be charged up to 3.7 V (Figure 4.15C), thus storing 17.4 μC in electric charge or 32.2 μJ of energy. After charging of the capacitor stopped, the self-discharging rate of the energy harvesting system was about 1 $\mu C \cdot min^{-1}$, which ensures the energy storage efficiency. This demonstration highlights the piezoelectric energy harvesting performance of the printed heel insole as means to collect waste mechanical energy during daily walking and transform it into usable and

storable electrical energy. Therefore, precipitation printing provides a practical approach for fabricating bulk piezoelectric energy harvesters that exploit the d_{33} mode effect, which is typically difficult to achieve using thin films. In addition, simplicity and low cost of the fabrication processes are two other main advantages of the proposed heel insole energy harvester since it requires only four fabrication steps: PVDF precipitation printing, hot pressing, electric poling and assembly, compared with other devices using d_{31} mode effect that usually requires the fabrication and assembly of additional fixtures and substrates made of different materials [252,253]. For future work, precipitation printing enables the potential of dual material printing of both PVDF and conductive electrode material for conformal piezoelectric layers in complex structures, which can further improve the efficiency of energy harvesting.

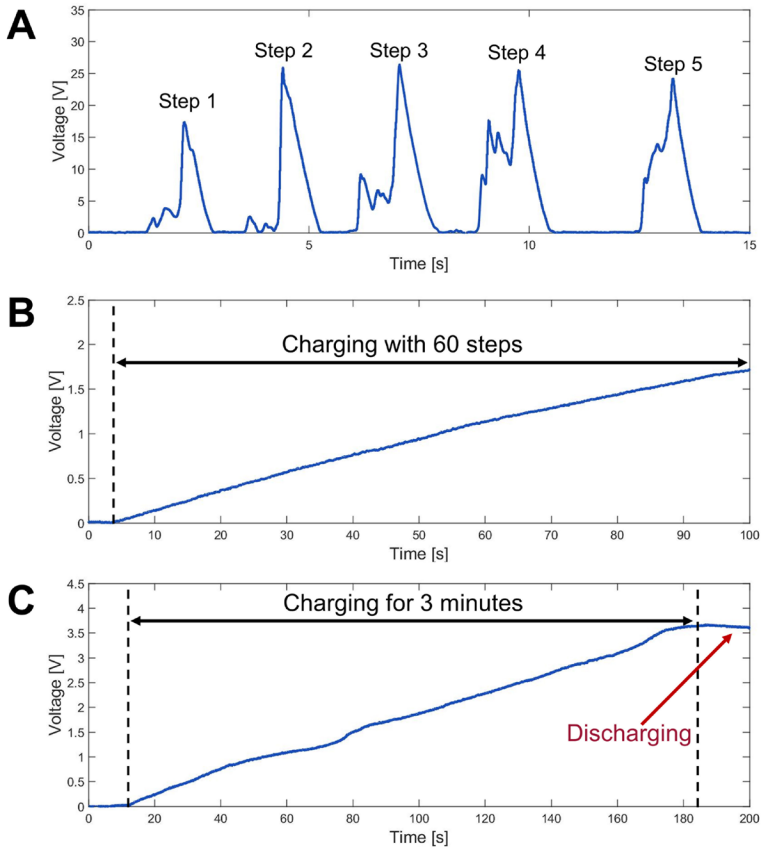

Figure 4.15. A) Open-circuit voltage time response of the heel insole energy harvester during 5 steps using rectifiers. B) Charging of a 4.7 µF capacitor to 1.7 V in 60 steps. (c) Charging a 4.7 µF capacitor to 3.7 V by stepping on the heel insole for 3 minutes.

4.9 Piezoelectric sensors embedded in 3D printed feathers

Piezoelectric PVDF can also act as stress and strain sensing materials, especially for dynamic changes and vibrations due to its ultrafast response time and large operating frequency

range. In a concurrent project about design and 3D printing artificial feathers with embedded aerodynamic sensing ability for future bio-inspired micro air vehicles (MAVs) and in vivo biomechanics study on birds, which is a collaboration with the University of Montana Field Research Station, we integrated precipitation printed then hot pressed PVDF into the artificial feather rachis for vibration sensing. Here, a brief summary of the design and fabrication of the 3D printed artificial feathers is provided first, while the main focus of this section is about the piezoelectric sensing on feather vibrations.

4.9.1 3D printed feather transducers with hierarchical vane structures

In this project, bio-inspired and 3D printed feather transducers were designed based on the Barbary dove (Streptopelia risoria) flight feathers. A dove feather typically consists of a stiff central shaft (rachis and calamus) and numerous branches (barbs) forming a relatively flat surface (vane) [254]. Even smaller branches (barbules) attached to the barbs have hooks to form an interlocking network between the adjacent barbs, which provides the feather structural integrity and also resists more deformation than a continuous membrane-type surface. Inspired by the dove flight feathers, artificial feathers of the same scale with hierarchical structures were designed and fabricated through two high-resolution 3D printing techniques for PVDF: electric field-assisted direct ink writing (DIW) [255] for the barbules networks and precipitation printing for the rachis and barbs (Figure 4.16). A superelastic nitinol (NiTi) wire was embedded in the printed rachis to match the stiffness of natural dove feathers. The self-sensing ability of the 3D printed feathers was realized by integrating a laser-printed strain gauge-type piezoresistive sensor (for static deformation measurement) and a precipitation printed then hot pressed piezoelectric PVDF sensor (for dynamic vibration measurement) into the rachis (Figure 4.17A). Although two types of sensors are used in the feather transducers, only the piezoelectric PVDF sensor's performance, which is relevant to this dissertation, will be studied in the following sections. In addition, the 3D printed feather transducers were based on two representative dove feathers, the 9th primary (P9) as one of the outer wingtip feathers and the 3rd secondary (S3) as one of the inner trailing edge feathers (Figure 4.17B), to study the functional difference between primary and secondary flight feathers.

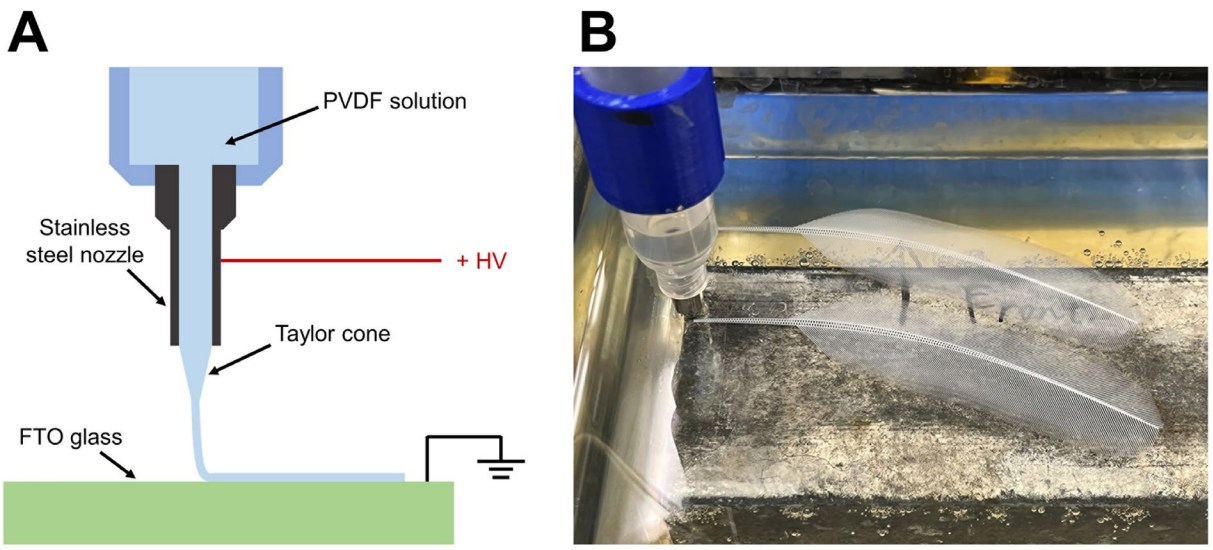

Figure 4.16. 3D printing processes for the fabrication of artificial feathers. A) Electric field-assisted DIW for barbules networks. B) Precipitation printing for barbs and rachis.

As a result, in Figure 4.17C, the 3D printed feather transducers (P9 transducer and S3 transducer) are presented alongside the corresponding natural dove feathers (P9 feather and S3 feather). The 3D printed feather transducers highly resemble the corresponding natural feathers in terms of size, shape and structure. Furthermore, the hierarchical structure of the 3D printed feather vane is compared to the natural feather vane by scanning electron microscope (SEM) imaging. In the case of a natrual feather vane in Figure 4.17D, branched and tapered barbs with a 50–100 μm width are interlocked by densely branched microscale barbules. The 3D printed feather vane in Figure 4.17E has branched but uniform width (200 μm) barbs, which are connected by grid-shape networks of barbules (10–20 μm width). The highly detailed barb structure acts as another example besides the demonstrations in Chapter 2 to highlight the printing resolution and precision of precipitation printed PVDF. Although the real-scale hierarchical structure of feather is achieved by 3D printing, the density of the barbules network is lower than the corresponding natural feathers due to the printing resolution limitation and feather zipping cannot be replicated due to the lack of barbule hooks [256,257]. However, like natural feathers, the 3D printed feather transducers in this project allow larger vane deformation than the membrane-type artificial feathers [258–261], which is attributed to the barbs-barbules network that allows shear deformation.

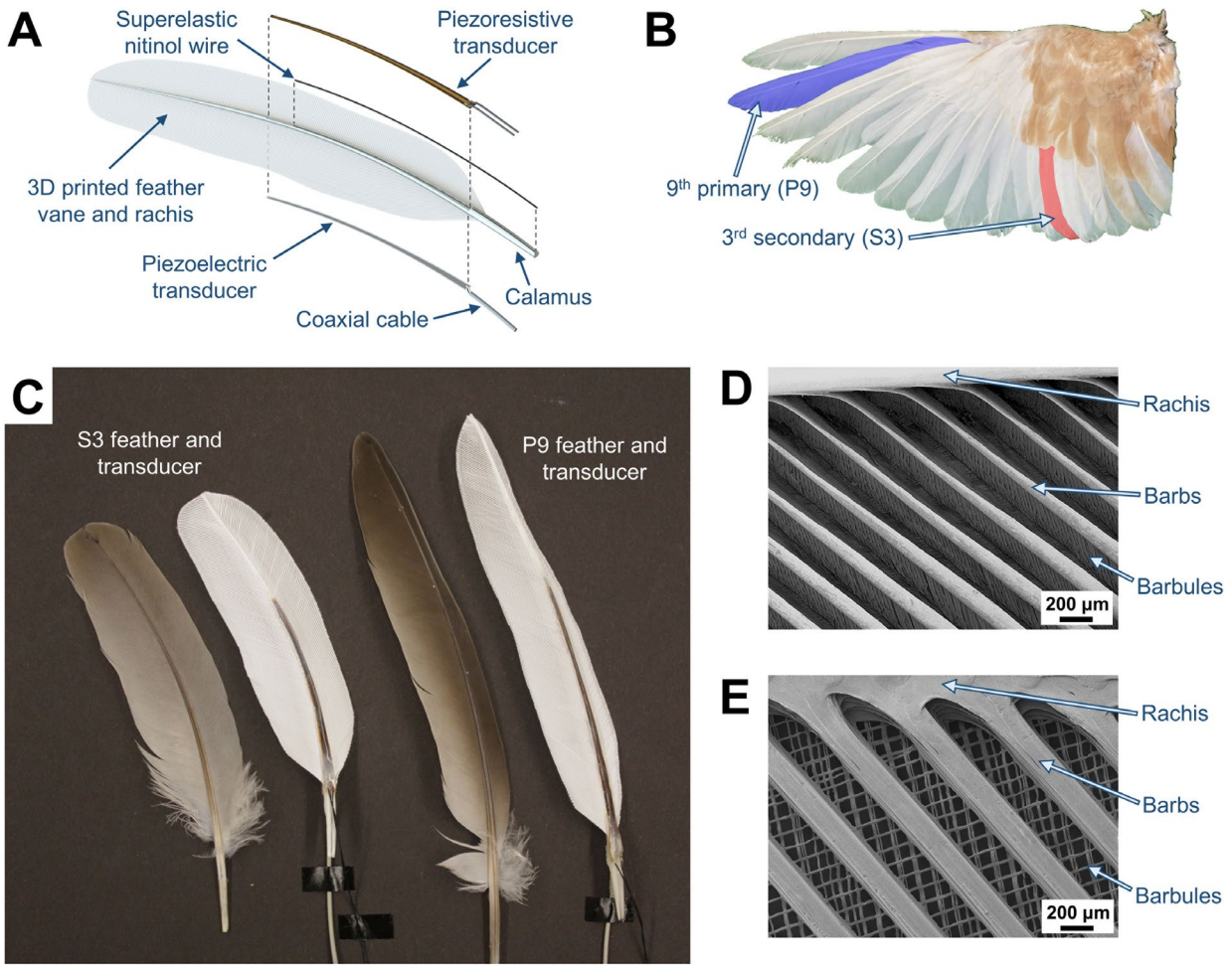

Figure 4.17. 3D printed artificial feather transducers. A) Components of a 3D printed feather transducer. B) Locations of the P9 and S3 feathers on a dove wing. C) Comparison of 3D printed feather transducers and natural feathers. D) SEM image of the natural feather vane structure with interlocking barbules between barbs. E) SEM image of the 3D printed feather vane structure with barbules network between barbs.

4.9.2 Dynamic characterization of feather transducers

The dynamic vibration sensing ability of the piezoelectric PVDF sensor in individual feather transducers was characterized by shaker vibration tests. In Figure 4.18A and E, individual feather transducers were clamped on an electrodynamic shaker (LDS V408, Brüel & Kjaer) with an attached base accelerometer (352C22, PCB Piezotronics). The feather vibration acceleration was measured by a laser vibrometer (LK-G5000, Keyence) in the acceleration mode, where the laser focus was 70 mm away from the clamped calamus for the P9 transducer and 50 mm for the S3 transducer. A customized voltage follower (Figure 4.19) was made for the high impedance piezoelectric signal conditioning. The piezoelectric voltage after signal conditioning was recorded by a data acquisition system (USB-4431, National Instruments) and high-pass filtered (1 Hz cutoff)

to remove the DC offset and became V_{piezo}. During vibration testing, sine wave sweeps from 5 Hz to 120 Hz with a duration of 1 min of the base excitation acceleration were applied to individual feather transducers, and the frequency response function (FRF) plots of the laser vibrometer measured acceleration and V_{piezo} with respect to the base acceleration for the P9 transducer are shown in Figure 4.18B and C. The V_{piezo} response shows the same resonance peak (62 Hz) that matches the external laser measurement, excellent signal coherence, sensitivity and no significant phase lag in a large frequency range. The slight mismatch between the FRFs is due to the different locations between the laser focus and the distributed piezoelectric sensor along the rachis. After frequency sweeps, acceleration amplitude sweeps at a constant frequency (62 Hz) were applied to the P9 transducer, and the amplitudes of V_{piezo} were compared to the vibration amplitude (measured as laser vibrometer acceleration). As a result, in Figure 4.18D, the amplitudes of V_{piezo} have linear relationships (R^2 = 0.999) with the laser acceleration amplitude, suggesting its dynamic sensing capability of the feather vibration amplitude. Figure 4.18F–H contain the dynamic characterization results of the S3 transducer following the same tests in Figure 4.18B–D. Similarly, the V_{piezo} response can accurately sense the two resonance frequencies of the S3 transducer in the 5–120 Hz rang, and the amplitude of V_{piezo} has a linear correlation with the vibration amplitude. Therefore, the piezoelectric PVDF sensor embedded in the 3D printed feather transducers is proved to provide abundant sensory information on the feather vibration frequency and amplitude.

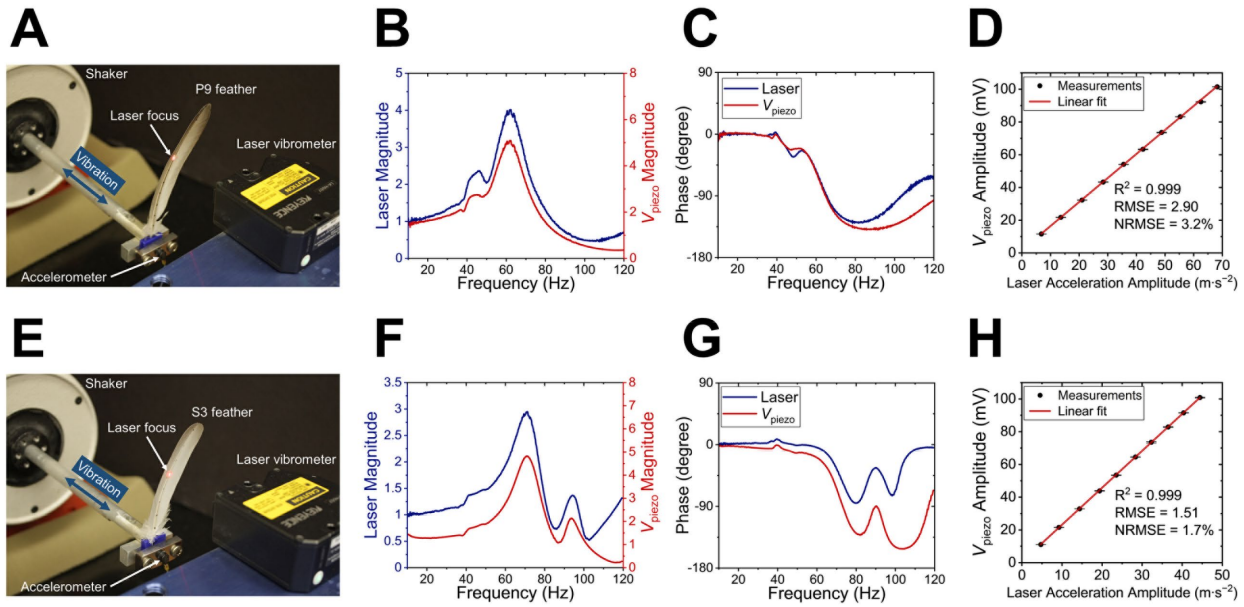

Figure 4.18. Dynamic characterization of feather transducers. A) Vibration test setup for the P9 feather and transducer. B–C) FRF magnitude and phase plots of the laser vibrometer and P9 transducer's V_{piezo} with respect to the based acceleration. D) Linear correction between the P9 transducer's V_{piezo} amplitude and base excitation amplitude. E–H) Dynamic characterization of the S3 transducer following the same tests in A–D.

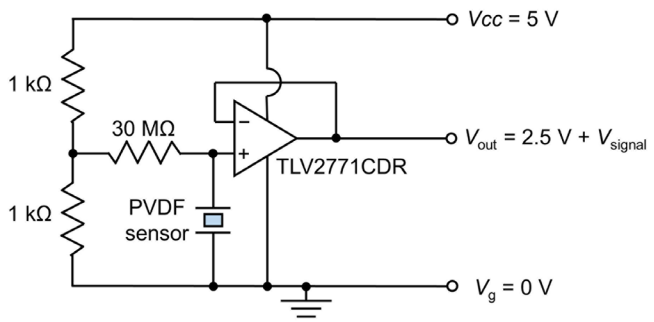

Figure 4.19. Voltage follower circuit for piezoelectric signal conditioning.

4.9.3 Individual feather transducer vibration sensing

After the shaker vibration tests that characterized the piezoelectric sensor performance, the individual 3D printed feather transducers were mounted in a wind tunnel with a 10 $m \cdot s^{-1}$ flow speed to investigate their ability of aerodynamic sensing. To simulate the P9 and S3 feather location and orientation on the dove wing during glide, the P9 transducer was tested with calamus perpendicular to the flow (Figure 4.20A), while the S3 transducer was tested with calamus parallel to the flow (Figure 4.20E). During angle of attack sweeps from −21.4° to 28.6°, the power of the piezoelectric signal was measured as P_{piezo}, which was then min-max normalized in the angle sweep range. As a result, in Figure 4.20B, the P_{piezo} of the P9 transducer has relatively low magnitudes when the angle of attack is from 0° to 7° (in the linear lift coefficient, C_L, range), and has high magnitudes from −20° to −10° and more than 20° where measured C_L deviates from the linear lift line, which correspond to the flow separation or vortex-induced vibration (VIV) at negative and positive angles [262], respectively. The vibration frequency can also be obtained by performing fast Fourier transform (FFT) on the V_{piezo}, and the lowest primary vibration frequencies for the P9 transducer at both −20° and 20° are around 50–60 Hz (Figure 4.20C and D), which are close to the first bending mode natural frequency of the P9 transducer. However, more higher frequency (above 100 Hz) vibration modes occur at 20° than −20°. For the S3 transducer, the vibration sensing result in Figure 4.20F shows only a main peak of P_{piezo} between 0° and 10° with a primary vibration frequency in 90–120 Hz range (Figure 4.20G), which is possibly the VIV of the feather transducer due to the interactions with the leading-edge shaft's wake vortices (Figure 4.20E) [263]. No stall-induced vibration can be observed in this case. It can be concluded that both the P9 and S3 transducers can sense the amplitude and frequency of flow separation or vortex-induced feather vibration through the piezoelectric signal, which can be used for potential stall detection.

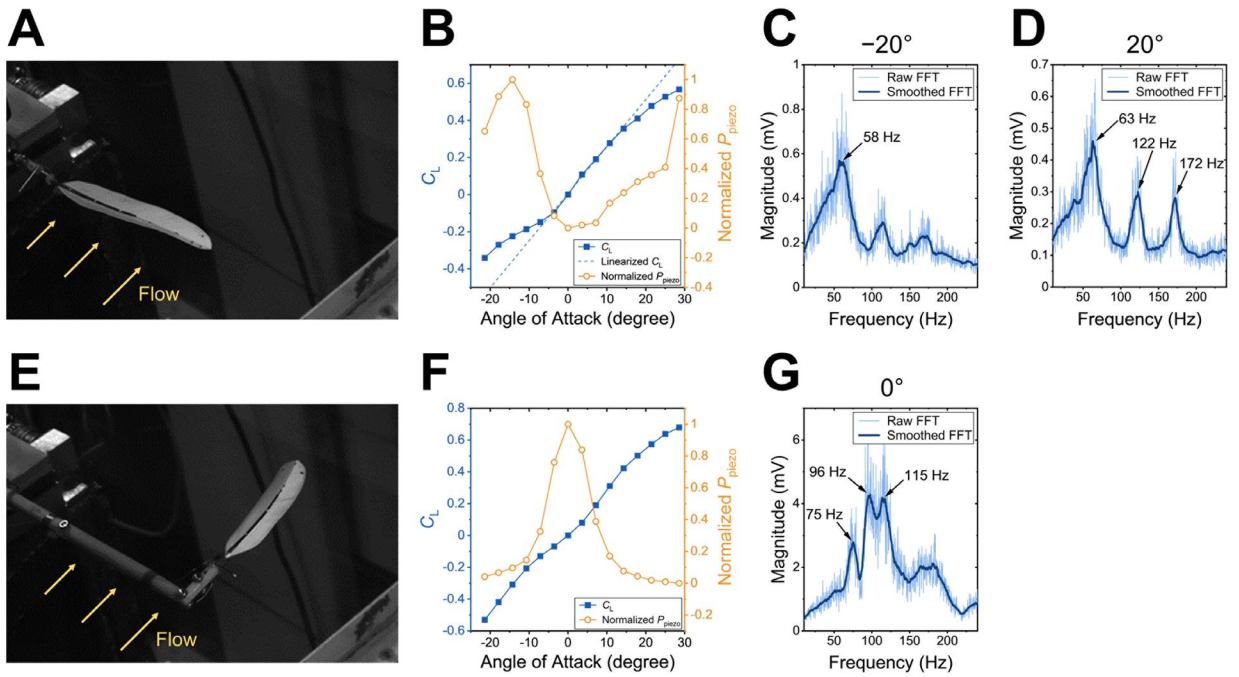

Figure 4.20. A) P9 transducer's orientation in the wind tunnel. B) Piezoelectric signal power measurements of the P9 transducer compared to its lift curve and linearized lift line. C–D) FFT spectra of the P9 transducer's piezoelectric signal at −20° and 20°. E) S3 transducer's orientation in the wind tunnel. F) Piezoelectric signal power measurements of the S3 transducer compared to its lift curve. G) FFT spectrum of the S3 transducer's piezoelectric signal at 0°.

4.9.4 Instrumented wing vibration sensing and gust detection

The P9 and S3 transducers were also instrumented onto a dried and spread dove left wing, to study their sensing ability of the whole wing aerodynamics and vibrations. Figure 4.21A shows the top view of the instrumented wing with wires connected to the transducers, and Figure 4.21B describes the wind tunnel test setup for the wing using a 10 $m \cdot s^{-1}$ flow speed and an angle of attack sweep from −25.0° to 71.4°. In Figure 4.21C, due to the strong stall effect, the wing C_L reaches a maximum at 25° and starts to decrease above 25°. The P9 transducer's piezoelectric signal can sense the flow separation-induced wing vibration at both below −10° and above 20° where the normalized P_{piezo} is high, and the peak P_{piezo} at 28° is a critical indicator of wing stall with about 3° error (Figure 4.21C). This error is due to the outmost location of the P9 and the lack of interaction with the wing, which results in a different stall angle of P9 transducer itself compared to the wing platform. In Figure 4.21D, the FFT spectra of the P9's V_{piezo} at both positive and negative angles of flow separation exhibit lower primary vibration frequency than the individual P9 transducer's vibration frequency in the wind tunnel, which can be explained by the more complicated interaction between adjacent feathers that produces lower frequency vibration modes. For the S3 transducer, since it is a trailing edge feather overlapped by the adjacent S2 and S4

feathers, strong interaction between feathers makes S3 share the main vibration features as the whole wing. In Figure 4.21E, two S3 transducer's P_{piezo} peaks occur at angles between the start of flow separation and stall (maximum C_L) for both positive and negative angles, which can be used as a stall warning sensor. FFT spectra of the S3's V_{piezo} at both positive and negative angles of flow separation show a clear major vibration frequency lower than the individual S3's vibration frequency (Figure 4.21F), which is possibly the vibration of the entire wing.

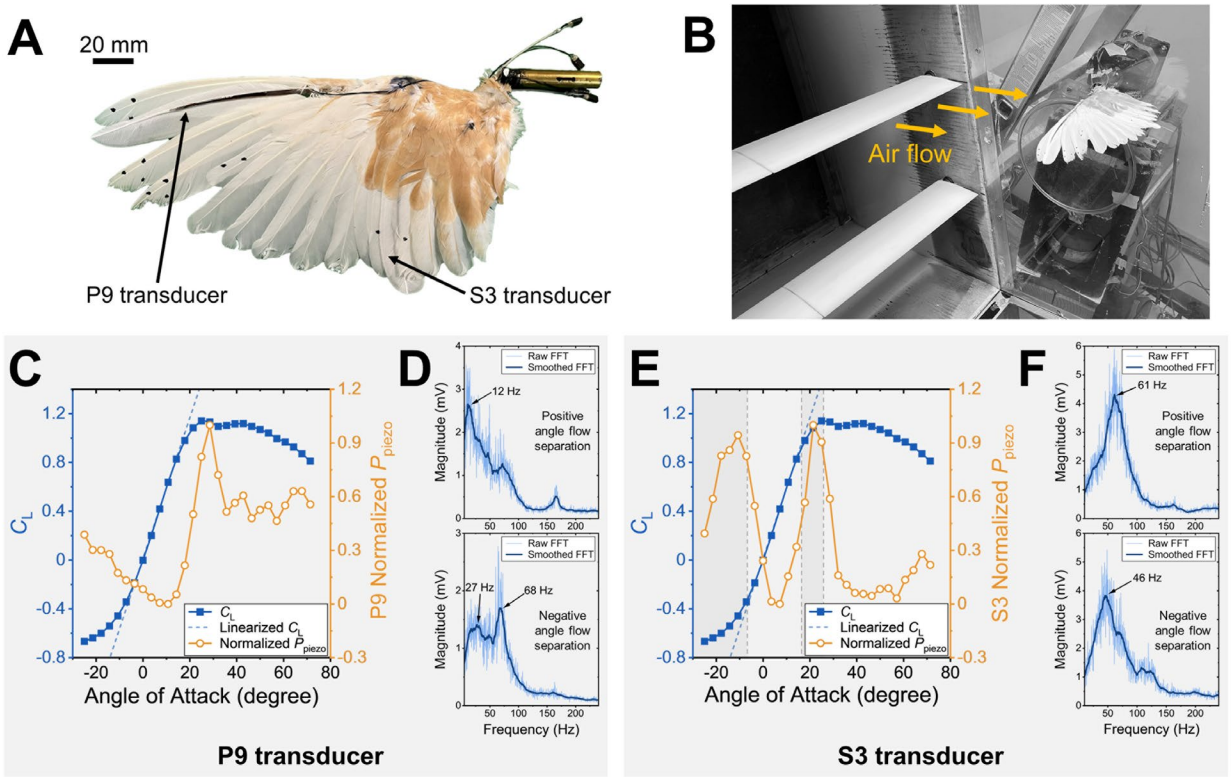

Figure 4.21. Feather transducers' sensing performance when instrumented on a spread dove wing. A) Top view of the instrumented left wing. B) Wind tunnel test setup for an instrumented wing. C) P9 piezoelectric signal power compared to the whole wing lift curve and linearized lift line. D) FFT spectra of the P9 piezoelectric signal at positive and negative angles when flow separation occurs. E) S3 piezoelectric signal power compared to the whole wing lift curve and linearized lift line. F) FFT spectra of the S3 piezoelectric signal at positive and negative angles when flow separation occurs.

The instrumented wing with two feather transducers can also sense environmental disturbances, such as upward gusts. Two vane gust generators in front of the testing wings with a 10° pitch angle change were used to simulate upward gusts (Figure 4.22A and B). Each gust cycle includes three steps of the vane gust generators: rapid pitching up, holding for 5 seconds, and rapid pitching down to the original position. The testing wing was kept at a 10° pitch angle with respect to the wind tunnel to simulate gliding flight. As a result, in Figure 4.22C, the C_L of the wing increases about 0.11 when under upward gusts, but the drag coefficient (C_D) remains nearly

unchanged. For vibration sensing, both raw piezoelectric voltage signals from the P9 and S3 transducers were post-processed using a band-pass filter ($V_{piezo,bp}$) to show vibration amplitudes in the primary vibration frequency range (5–30 Hz for P9 and 5–75 Hz for S3) based on the FFT spectra in Figure 4.21, and a moving average ($V_{piezo,avg}$) to show sudden and large deformations. In Figure 4.22D, the P9 $V_{piezo,avg}$ can detect the start and end time of each gust cycle, where the positive spikes indicate the upward flow direction change and negative spikes indicate the downward flow direction change. The P9 $V_{piezo,bp}$ amplitudes during normal glide and during gust cycles are also different, due to the gust induced P9 bending that increases wing tip vortices-induced vibration. In Figure 4.22E, the upward gusts have less influence on the vibration of the S3 transducer located on the inner portion of the wing. The lack of spikes in S3 $V_{piezo,avg}$ indicates that no significant S3 transducer deflection occurs when the upward gust hits the wing, and the lower S3 $V_{piezo,bp}$ amplitude during the gust cycles implies that the upward gust pushes secondary feathers together and reduces vibration. The average piezoelectric signal power P_{piezo} of P9 has a 460% increase under gusts, yet the average P_{piezo} of S3 has a 49% reduction under gusts (Figure 4.22F).

In conclusion, using piezoelectric PVDF as the dynamic sensing component in the 3D printed feather transducers can provide substantial sensory information on the feathered wing behavior, including the amplitude and frequency of the feather and wing vibration. Therefore, the 3D printed feather transducers with embedded aerodynamic sensing can be developed as a smart component in bio-inspired MAVs, which enables stall and gust detection for real-time adaptation in unsteady flows or dynamic flight conditions.

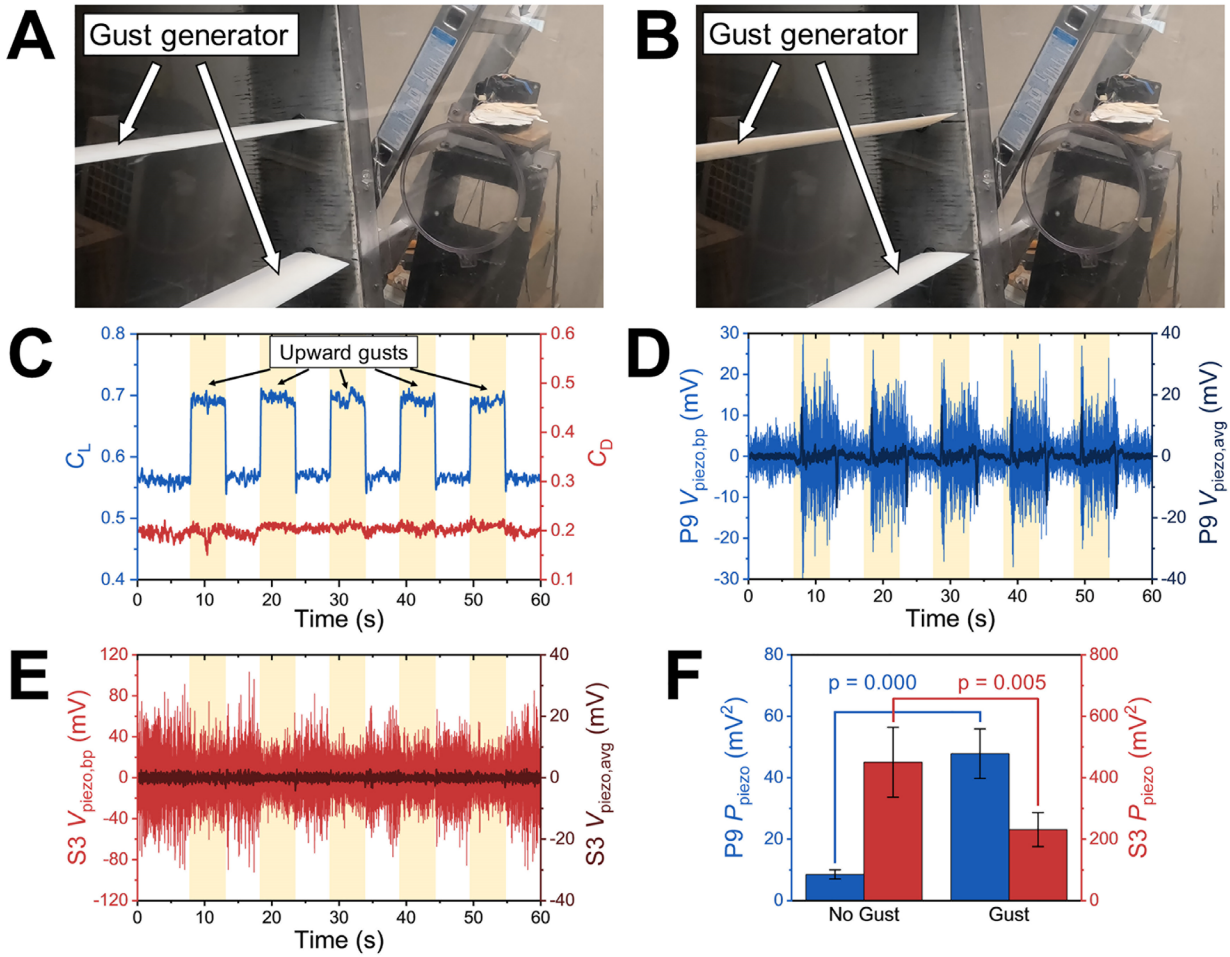

Figure 4.22. Response of the instrumented wing under simulated upward gusts. A) Normal glide condition. B) Upward gust condition. C) Change of C_L and C_D under five upward gust cycles. D) Change of P9 $V_{piezo,bp}$ and $V_{piezo,avg}$ under five upward gust cycles. E) Change of S3 $V_{piezo,bp}$ and $V_{piezo,avg}$ under five upward gust cycles. F) Comparison of the upward gust sensing ability of the P9 and S3 piezoelectric signal by using P_{piezo} (N=5 gusts).

4.10 Chapter summary

In this chapter, precipitation printing was shown to be an additive manufacturing process for producing high β phase PVDF, which is capable of fabricating bulk piezoelectric materials with complex geometries. It provides a simple and low-cost approach to enhance the piezoelectric β phase fraction in PVDF without the need for mechanical stretching, filler addition or chemical treatment. The β phase fraction of the precipitation printed PVDF from a DMF solution is reported to be more than 60% using FTIR analysis, which is more than 2 times increase relative to solvent cast PVDF films. The precipitation printed PVDF has stable β phase below 150 °C post-heating, which corresponds to the β phase onset melting temperature according to DSC analysis. Since the directly precipitation printed PVDF is highly porous, hot pressing at 80 °C and 140 °C were applied to densify the printed PVDF. FTIR, XRD and DSC characterization results indicate that hot

pressing can improve the total degree of crystallinity, while keeping the high β phase fraction. The measured *D-E* loops of the precipitation printed then hot pressed PVDF display a coercive field of 98 $MV \cdot m^{-1}$ and a maximum remnant polarization of 3.23 $\mu C \cdot cm^{-2}$ before sample breakdown, implying a strong ferroelectric behavior from the high β phase fraction. After electric poling, the porous precipitation printed PVDF exhibits a maximum piezoelectric d_{33} and d_{31} coefficients of $-0.99\ pC \cdot N^{-1}$ and $1.08\ pC \cdot N^{-1}$, respectively, and a dielectric constant of 3.55 at 1 kHz. After hot pressing and electric poling, the maximum piezoelectric d_{33} and d_{31} coefficients of PVDF are achieved to be $-18.09\ pC \cdot N^{-1}$ and $8.69\ pC \cdot N^{-1}$, respectively, by reducing the porosity and enhancing the dielectric constant to 9.48 at 1 kHz. Therefore, for future applications, precipitation printing can either be used to fabricate porous piezoelectric PVDF 3D structures with complex shapes and potentially customized electrodes by dual material printing, or be combined with hot pressing to produce PVDF 2D sheets of arbitrary geometries that have outstanding piezoelectric performance.

Precipitation printed PVDF was also demonstrated to fabricate piezoelectric energy harvesters and sensors. A stretching mode (d_{31} mode) energy harvester that was directly precipitation printed can generate a power density of up to 44 $\mu W \cdot cm^{-3}$, while a printed then hot pressed stretching mode energy harvester displays a power density up to 717 $\mu W \cdot cm^{-3}$. A full-scale wearable heel insole (d_{33} mode) energy harvester is shown to efficiently transform waste mechanical energy during daily walking into storable electrical energy, storing 32.2 μJ of energy into a capacitor after stepping on the heel insole for 3 minutes. Moreover, for sensing applications, precipitation printed then hot pressed PVDF was integrated into the rachis of the 3D printed artificial feathers to enable in situ aerodynamic sensing. The piezoelectric signal generated from the PVDF sensor can provide substantial sensory information on the entire wing behavior, including the amplitude and frequency of the feather and wing vibration, as well as stall and gust detection, when the wing is instrumented with the 3D printed feather transducers. In conclusion, precipitation printing is a promising additive manufacturing process to produce high β phase PVDF and piezoelectric devices with complex geometries.

Chapter 5 Precipitation Printing of Highly Stretchable Piezoelectric Sensors

5.1 Chapter introduction

With the recent development of soft robotics and wearable motion capture technology, strain/stress sensors used on soft actuators or human bodies that require a large strain sensing range (>50%) under dynamic loading conditions are in great demand. When under dynamic loading conditions, the strain/loading rates of the soft substrate can change and the pre-stretch strain of the quasi-static states may vary, which are challenging for existing stretchable piezoelectric sensors based on piezoceramic nanocomposites or smart pattern design of poly(vinylidene fluoride) (PVDF) films to produce reliable strain/stress measurements. To overcome these limitations, intrinsically stretchable piezoelectric polymer blends consisting of PVDF and a polar elastomer can be developed. In Chapter 5, polymer blends of PVDF and acrylonitrile butadiene rubber (NBR) are formed using precipitation printing, where a solution of both PVDF and unvulcanized NBR dissolved in *N,N*-dimethylformamide (DMF) is precipitated inside a water bath and solidified as a polymer blend that can be vulcanized by subsequent hot pressing [205,211]. As explained in Chapter 4, the PVDF-water interaction preferably orients the dipoles in the PVDF chain to form a TTT conformation (β phase), which also provides the piezoelectricity basis for the precipitation printed PVDF/NBR blends in this chapter. In addition, during precipitation printing, the rapid liquid-solid phase separation at room temperature can produce a unique blend morphology, where the PVDF phase and the NBR phase are highly mixed above micron level. The stretchability, dielectric properties and piezoelectric properties of the PVDF/NBR blends with different blend ratios are characterized, and the results show that a highly stretchable piezoelectric polymer blend with tailored macroscopically uniform properties can be developed. Next, the precipitation printed then hot pressed PVDF/NBR blends are used to fabricate piezoelectric sensors, and they exhibit excellent dynamic strain/stress sensing performance under large strains, without strain/loading rate and pre-stretch dependence. Therefore, the developed highly stretchable PVDF/NBR sensors can outperform existing stretchable piezoresistive and piezoelectric strain/stress sensors under dynamic loading conditions.

5.2 Fabrication of stretchable piezoelectric polymer blends

Four different weight ratios of the PVDF/NBR printing inks (20PVDF80NBR, 40PVDF60NBR, 60PVDF40NBR, 80PVDF20NBR, where the number in front of each polymer component is its weight percent out of total solid) along with neat PVDF (100PVDF) and neat NBR (100NBR) inks were obtained by dissolving the corresponding polymers and vulcanization agents in DMF to form 15 wt% solutions. Specifically, PVDF powder (Kynar 301F) was first dissolved in DMF (certified ACS, Fisher Chemical) to form a 15 wt% clear solution (100PVDF ink) via magnetic stirring and sonication (Branson M2800), while unvulcanized NBR (KNB 40M, Kumho Petrochemical) was also dissolved in DMF to form a 15 wt% uniform but opaque solution via sonication (sonic dismembrator model 500, Fisher Scientific). 1 wt% sulfur (Akrochem) and 1 wt% *N*-cyclohexyl-2-benzothioazole sulfenamide (Accelerator CBTS, Akrochem) based on the NBR solid weight were added into the NBR/DMF solution for further mixing to obtain 100NBR ink. For different ratios of PVDF/NBR blend inks, 100PVDF and 100NBR inks were mixed based on the corresponding weight ratios, followed by vortex mixing. The polymer inks were then precipitation printed in an ice/water bath on a glass substrate coated with a solvent cast 50PVDF50NBR film to produce 3D structures (about 0.2 to 1.5 mm thickness) of unvulcanized PVDF/NBR blends using the customized 3D printer for precipitation printing (Figure 5.1). The printing infill was set to be a 0°/90° alternating pattern to allow for transversely isotropic structures.

Besides all the studies of β phase promotion using precipitation printing in Chapter 4, the effect of water bath temperature during printing was further investigated here. Four different temperatures of the water bath were tested for precipitation printing of neat PVDF (100PVDF). It should be noted that the 0 °C bath was a mixture of ice and water. Lower than 0 °C salt (NaCl) water bath was also tested for precipitation printing, but the solvent exchange rate was too slow for continuous printing. Thus, bath temperature lower than 0 °C is not practical for this process considering printability. Figure 5.2 shows the Fourier-transform infrared spectroscopy (FTIR) spectra of 100PVDF printed in different temperature water baths. As the water temperature decreases, the α phase absorption peak at 763 cm^{-1} reduces intensity and the β phase peak at 1275 cm^{-1} increases intensity, meaning that printing in a lower temperature water bath promotes the β phase fraction, which agrees with literature results on phase inversion of PVDF membranes [130,132,264,265]. In the meantime, the other electroactive γ phase amount remains unchanged

regardless of the water bath temperature. As been shown in previous literature that β phase is preferably formed in the phase inversion process due to the hydrogen bonding between C–F groups in PVDF and O–H groups in water [245], a lower temperature slows down the solvent exchange rate, provides more time for PVDF-water interaction and extends the crystallization time of β phase. It should also be noted that the addition of NBR does not have significant influence on the PVDF phase composition according to our characterization results in the next section. Therefore, 0 °C ice/water mixture was selected as the printing bath for all neat PVDF and PVDF/NBR blends.

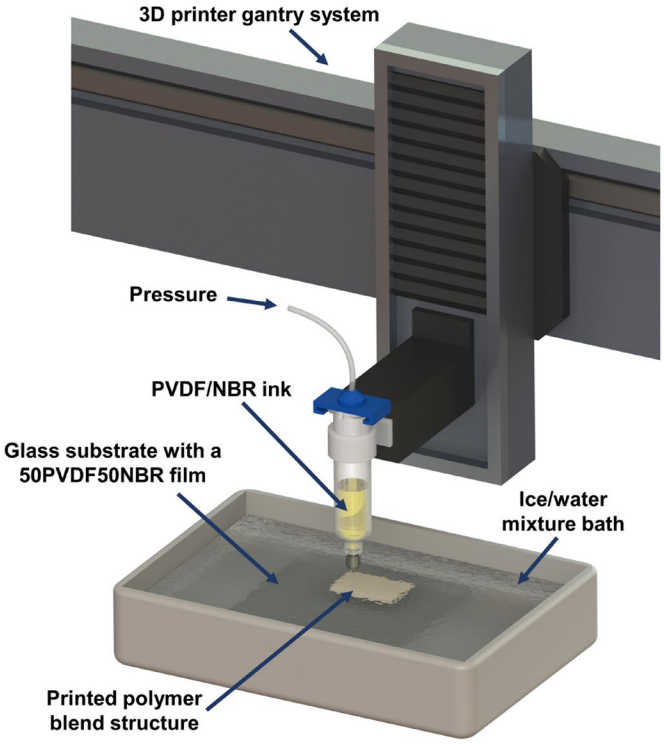

Figure 5.1. Precipitation printing of PVDF/NBR blends.

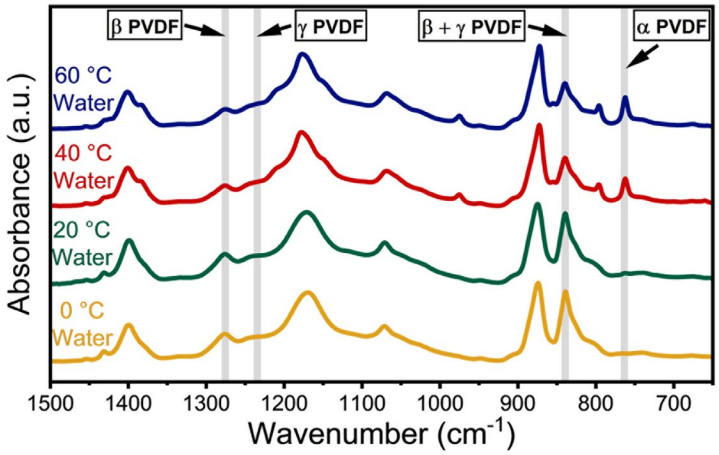

Figure 5.2. FTIR spectra of 100PVDF printed in water baths of different temperatures.

Table 5.1. Printing, hot pressing and electric poling parameters for PVDF/NBR blends.

	Nozzle diameter (μm)	Printing pressure (psi (kPa))	Printing speed ($mm \cdot s^{-1}$)	Hot pressing pressure (MPa)	Electric poling field ($MV \cdot m^{-1}$)
100PVDF	254	3.0 (20.7)	7	60	100
80PVDF20NBR	254	3.3 (22.8)	7	30	80
60PVDF40NBR	254	3.6 (24.8)	7	10	60
40PVDF60NBR	254	3.9 (26.9)	7	4.0	50
20PVDF80NBR	254	4.2 (29.0)	7	1.5	40
100NBR	254	4.5 (31.0)	7	0.5	N/A

After precipitation printing, unvulcanized PVDF/NBR blends were first dried under vacuum (25 in. -Hg) overnight and then hot-pressed using pressures in Table 5.1 at 140–150 °C, which is the vulcanization temperature of NBR using sulfur and a safe temperature range to preserve β phase PVDF according to the study in Chapter 4. To promote apparent piezoelectricity, the hot pressed and vulcanized PVDF/NBR blends were poled in an 80 °C oil bath under electric fields from 40 to 100 $MV \cdot m^{-1}$ (Table 5.1).

To prepare a stretchable electrode material compatible with the PVDF/NBR blends, a conductive nanocomposite paste was developed by first dissolving 0.87 g of unvulcanized NBR in 3.48 g of DMF via sonication. Then 8.08 g of tetrahydrofuran (THF, certified ACS, Fisher Chemical) was added to the solution and mixed again. Next, 0.13 g of multi-walled carbon nanotubes (MWCNTs, Cheap Tubes) were added into the solution and dispersed uniformly through sonication and magnetic stirring to form a conductive paste. Finally, 87 mg of trimethylolpropane tris(3-mercaptopropionate) (Sigma-Aldrich) and 17 mg of diphenyl(2,4,6-trimethylbenzoyl)phosphine oxide (Sigma-Aldrich) were also added to the paste for subsequent photocuring. The conductive paste could be applied to the surfaces of the poled PVDF/NBR blends and cured using an ultra-violet (UV) light to form electrodes for the stretchable piezoelectric sensors [266]. The whole fabrication process is illustrated in Figure 5.3.

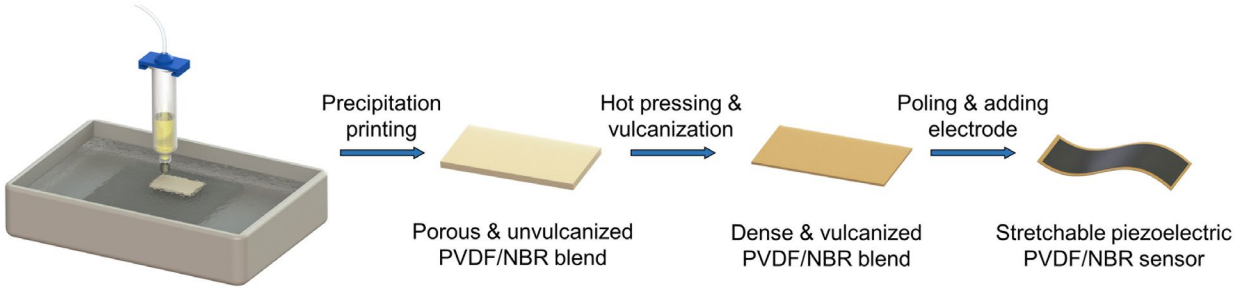

Figure 5.3. Fabrication steps of stretchable PVDF/NBR sensors.

5.3 Characterization of stretchable piezoelectric polymer blends

5.3.1 Fourier-transform infrared spectroscopy

The chemical structure of the precipitation printed and hot pressed PVDF/NBR blends were investigated through Fourier-transform infrared spectroscopy (FTIR) using a Nicolet iS50 spectrometer with a Smart iTR Attenuated Total Reflectance (ATR) accessory, and the resulting spectra of 6 different mixing ratio samples are shown in Figure 5.4. The intensity of C–H stretching absorption band increases as the NBR amount increases, which is attributed to the methylene group of the butadiene part (symmetrical stretching at 2850 cm^{-1} and asymmetrical stretching at 2920 cm^{-1}). Similar increasing trends can also be seen at 2237 cm^{-1} and 968 cm^{-1}, which are C≡N stretching of the acrylonitrile part and C–H wagging of the trans-1,4-structure of the butadiene part.

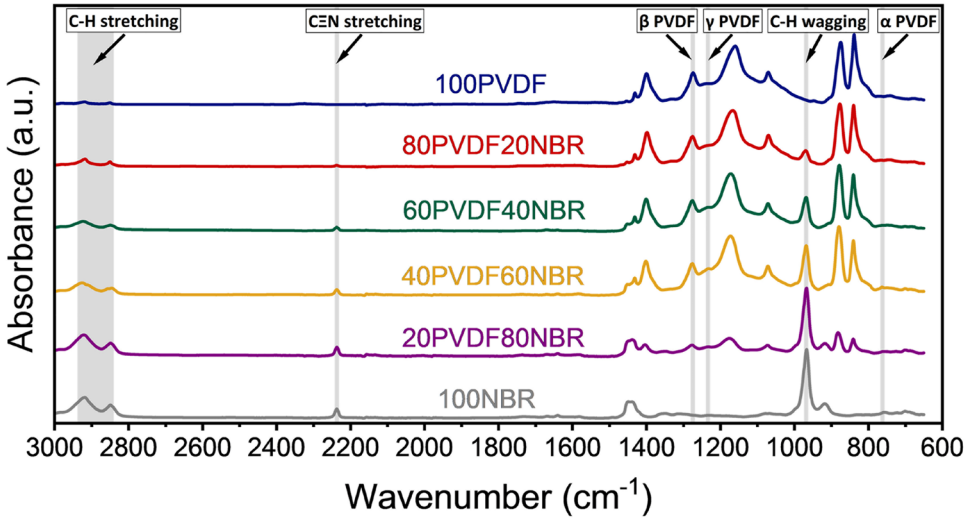

Figure 5.4. FTIR spectra of the PVDF/NBR blends.

The crystalline phases of PVDF can be determined by the characteristic peaks of α, β and γ phases. For all samples that contain PVDF, no clear α phase peak at 763 cm^{-1} can be seen, yet an intense β phase peak at 1275 cm^{-1} and a γ phase shoulder at 1234 cm^{-1} can be clearly observed. Quantitative phase fraction calculation was also performed following the same procedure described in Chapter 4. Table 5.2 shows that the β phase fraction in all PVDF/NBR blends are higher than neat PVDF, and the highest β phase fraction of 88.2% is observed in 60PVDF40NBR. When the NBR weight fraction exceeds 60 wt%, the β phase fraction drops due to the large amount of NBR during precipitation that limits the direct PVDF-water interaction to form hydrogen bonds. The phase fraction results confirm that the prepared PVDF/NBR blends have dominant polar β

phase and some extent of less polar γ phase in the crystalline region of PVDF, which provides the chemical structure basis of piezoelectricity.

Table 5.2. PVDF crystalline phase fractions in each PVDF/NBR blend.

	100PVDF	80PVDF20NBR	60PVDF40NBR	40PVDF60NBR	20PVDF80NBR
$F(\alpha)$	1.8%	1.9%	2.8%	6.2%	7.1%
$F(\beta)$	69.5%	83.2%	88.2%	80.0%	74.7%
$F(\gamma)$	28.7%	14.9%	9.0%	13.8%	18.2%

5.3.2 X-ray diffraction

The crystalline phases of PVDF/NBR blends can be further verified through X-ray diffraction (XRD), using a Rigaku Ultima IV X-ray diffractometer with CuKα radiation (λ = 0.154 nm). The XRD patterns in Figure 5.5 display that all samples with PVDF content exhibit a main β phase peak around 2θ from 20.7° to 20.8° (200/110) and a γ phase shoulder at 2θ = 18.5° (020), while showing no clear α phase peaks at 2θ = 17.6° (100) and 19.9° (021) [237,243,267]. As an amorphous polymer, 100NBR only shows an amorphous dome without any diffraction peak.

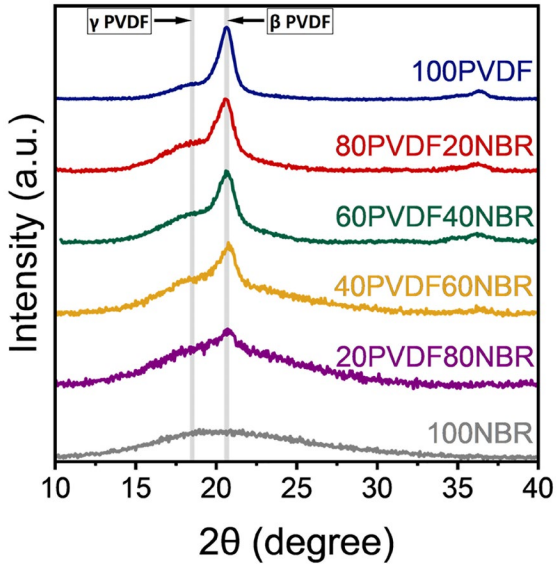

Figure 5.5. XRD patterns of the PVDF/NBR blends.

5.3.3 Differential scanning calorimetry

Differential scanning calorimetry (DSC) was applied to analyze the melting behavior of the semi-crystalline PVDF in PVDF/NBR blends using a differential scanning calorimeter (Q2000, TA Instruments) with a ramping rate of 5 °C·min^{-1}. In Figure 5.6A, all blends that contain PVDF show a broad β phase melting peak with onset of 150 °C and peak in 160–165 °C range, and a γ phase melting shoulder in 168–172 °C range. 100NBR is fully amorphous and displays no melting

peak in this temperature range. The degree of crystallinity (χ_c) of PVDF in each PVDF/NBR sample calculated based on the melting enthalpy following the procedure in Chapter 4 is listed in Table 5.3. It should be noted that these χ_c values are the fractions of crystalline phase out of the amount of PVDF, without considering the fully amorphous NBR phase. As a result, the χ_c of PVDF in these PVDF/NBR blends is found to increase as the NBR content increases, from 49.1% (100PVDF) to 57.2% (20PVDF80NBR).

The glass transition of amorphous PVDF and NBR can also be observed in the DSC curves (Figure 5.6B). The glass transition temperature (T_g) of the amorphous PVDF phase is around −41 °C, which is only visible in 100PVDF and 80PVDF20NBR samples (indicated in blue boxes) due to their high PVDF weight fraction and relatively lower χ_c. On the other hand, the T_g of NBR is around −21 °C, which can be seen in all samples that contain NBR (indicated in yellow boxes). Two distinct T_g values in a PVDF/NBR blend means the amorphous part of PVDF forms an immiscible polymer blend with NBR. Therefore, the PVDF/NBR blends in this work have three phases: crystalline PVDF (including α, β and γ), amorphous PVDF and amorphous NBR.

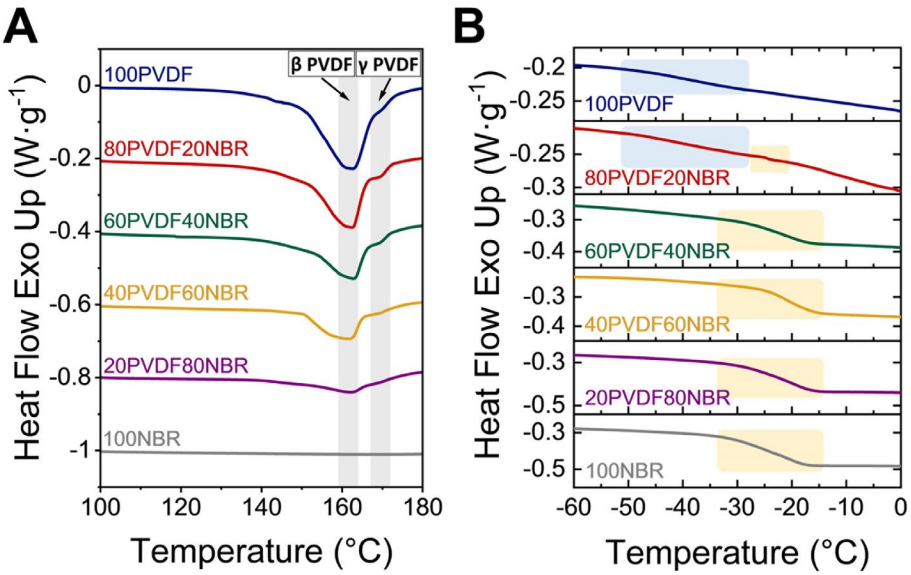

Figure 5.6. A) DSC curves showing PVDF melting in the PVDF/NBR blends. B) DSC curves showing glass transition in the PVDF/NBR blends (blue boxes: PVDF, yellow boxes: NBR).

Table 5.3. Degree of crystallinity (χ_c) of PVDF in the PVDF/NBR blends.

	Degree of crystallinity (χ_c)
100PVDF	49.1%
80PVDF20NBR	49.2%
60PVDF40NBR	52.7%
40PVDF60NBR	54.9%
20PVDF80NBR	57.2%

5.3.4 Energy-dispersive X-ray spectroscopy

To study the morphology of the PVDF/NBR blends, scanning electron microscopy (SEM) and energy-dispersive X-ray spectroscopy (EDS) using JEOL JSM-7800FLV were performed on the surfaces of PVDF/NBR films. Figure 5.7 displays the large area SEM images and EDS mappings of the chemical elements carbon (C) and fluorine (F), where distributed PVDF (F mapping) with overall uniformity in millimeter level is observed for all PVDF/NBR blends.

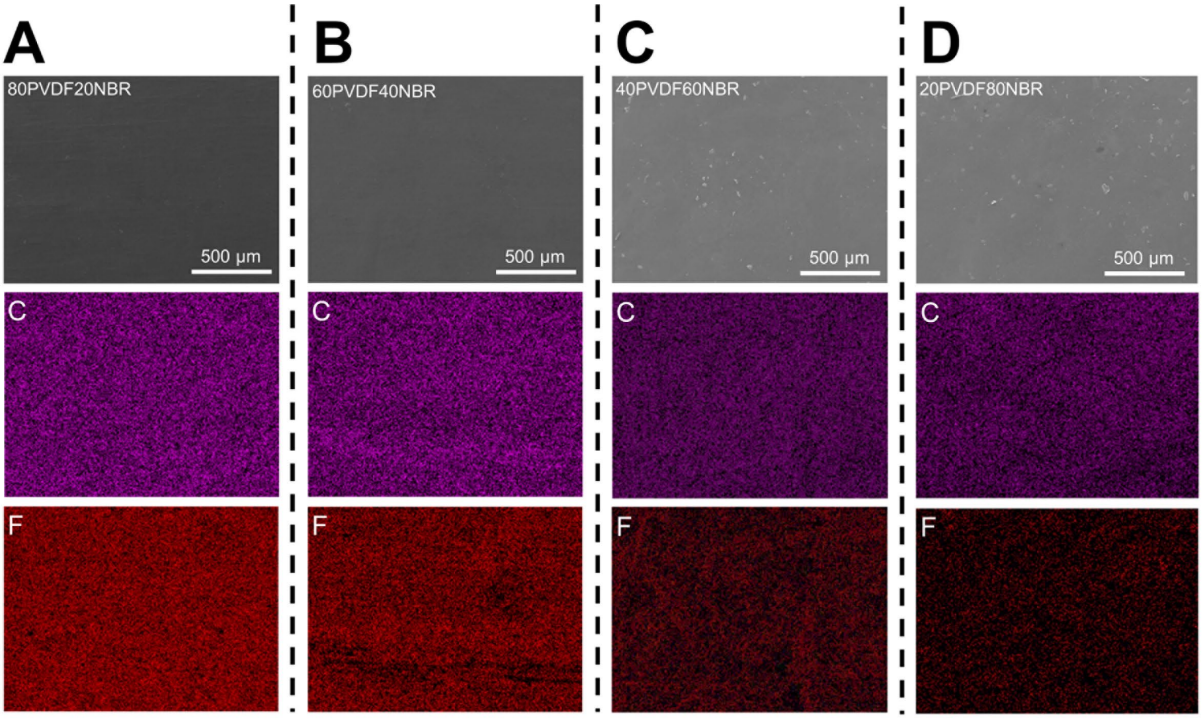

Figure 5.7. Large area SEM images and EDS element mappings (C and F) of the PVDF/NBR blends. A) 80PVDF20NBR. B) 60PVDF40NBR. C) 40PVDF60NBR. D) 20PVDF80NBR.

Higher magnification SEM images and EDS mappings in Figure 5.8A show a unique blend morphology of the surface of the PVDF/NBR blend (60PVDF40NBR as an example) formed by precipitation printing then hot pressing. Unlike the surface of the reference 60PVDF40NBR blend formed by solvent casting that has large NBR craters (diameters of 10–20 µm) in Figure 5.8B, the 60PVDF40NBR produced by precipitation printing then hot pressing in this work has a submicron level phase separation (Figure 5.8A) which remains stable after vulcanization. The mechanism of this polymer blend morphology formation is similar to widely studied phase inversion process to produce porous membranes, where the DMF has nearly instantaneous diffusion into water to facilitate solvent exchange while NBR and PVDF nucleate simultaneously without enough time and mobility for polymer-polymer diffusion [202]. The lack of polymer-polymer diffusion allows

the precipitation printed PVDF/NBR blend to keep a submicron level demixing of PVDF and NBR without NBR phase coarsening like solvent cast PVDF/NBR films. To have a better understanding of the blend morphology, the precipitation printed then hot pressed 60PVDF40NBR was also etched by hot DMF to remove the PVDF phase. The resulting surfaces in Figure 5.9 show that the remaining crosslinked NBR phase has a continuous and highly interlocked morphology with removed PVDF pores, but the average size of PVDF phase cannot be determined due to the swelling of NBR after DMF etching.

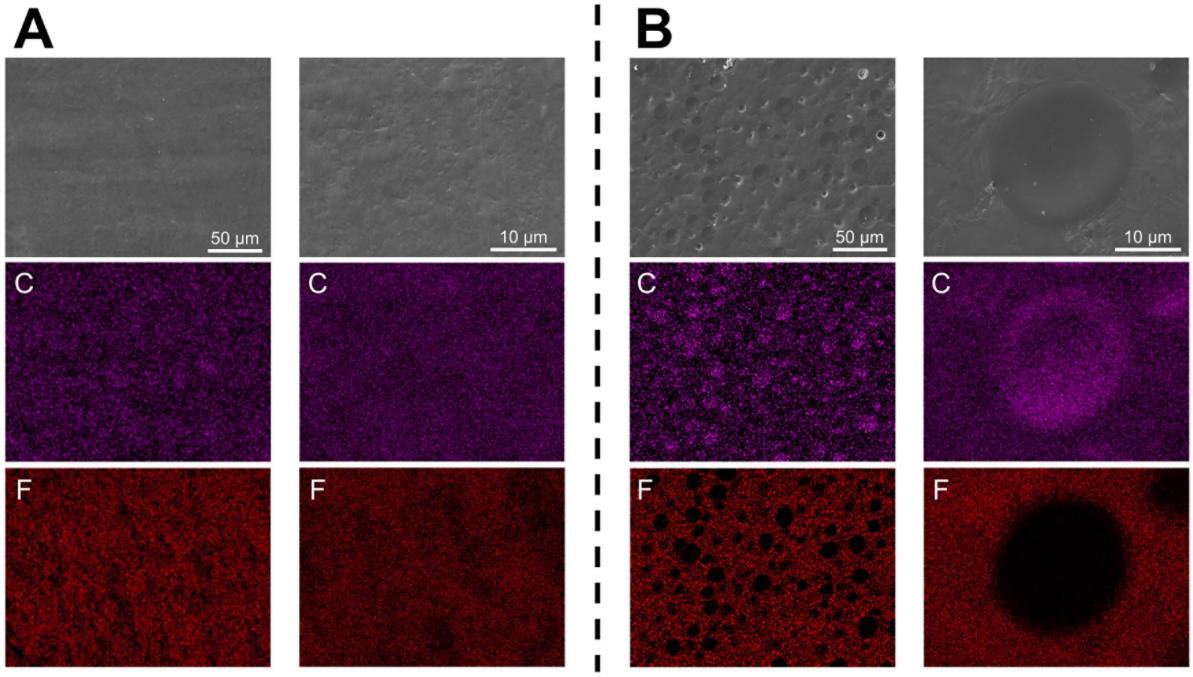

Figure 5.8. A) Surface SEM images and EDS mappings (C and F) of reference 60PVDF40NBR blend formed by solvent casting. B) Surface SEM images and EDS mappings of 60PVDF40NBR blend formed by precipitation printing then hot pressing.

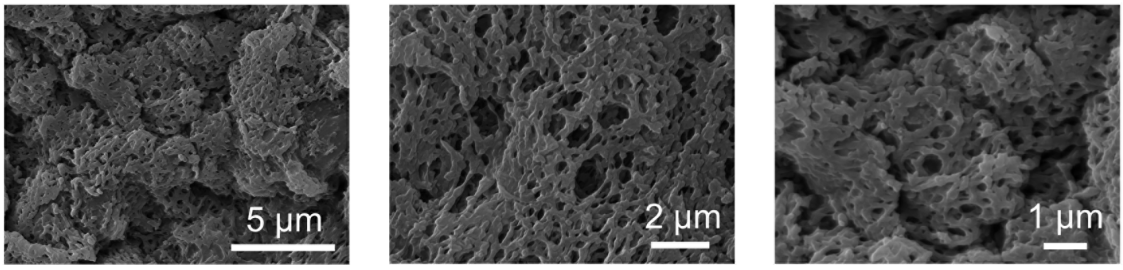

Figure 5.9. SEM images of hot DMF etched precipitation printed then hot pressed 60PVDF40NBR, where the remaining continuous phase is crosslinked NBR.

Figure 5.10 presents the SEM images and EDS mappings of PVDF/NBR blends with the other three blend ratios, and no clear phase separation (either C rich F lean or C lean F rich) can be observed above micron level. But the shadows of F mappings in Figure 5.10 do indicate that

the distribution of PVDF phase and NBR phase is slightly nonuniform due to the hot pressing and vulcanization process. This nonuniform phase distribution can also be seen in the EDS mappings and relative C and F element weight faction of different spots on the tensile fracture cross-sections of 20PVDF80NBR in Figure 5.11 and 40PVDF60NBR in Figure 5.12. For example, a large area EDS mapping of 20PVDF80NBR cross-section in Figure 5.11A shows that the relative weight fraction of F is 10.0%, but higher magnification EDS mappings have variations in the F relative weight fraction, especially in some spots that are relatively PVDF lean and NBR rich (Figure 5.11C). Similar phenomenon can be seen in 40PVDF60NBR cross-section EDS mappings, where the relative weight fraction of F has variations in different spots (Figure 5.12). The nonuniformity in the cross-section can be explained by the hot-pressing process during which the NBR phase has high mobility to fill pores and crosslink with itself. It should be noted that since only C rich F lean and C lean F rich regions are attributed to nonuniform phase distribution, all the dark spots in the EDS mappings in Figure 5.11 and Figure 5.12 coexist in both C and F mappings, meaning that they are just in the shadows with limited X-ray exposure during EDS measurements. Thus, spots with pure PVDF phase (C lean F rich) or pure NBR phase (C rich and no F) like the PVDF/NBR blends formed by solvent casting (Figure 5.8B) are not observed in precipitation printed then hot pressed PVDF/NBR blends, indicating the polymer blends in this work have a lower scale phase separation than the blends formed by solvent cast. Therefore, the precipitation printed then hot pressed PVDF/NBR can be considered as a single continuous elastomer phase above micron level, which is different from typical two-phase piezoelectric nanocomposites with phase sizes from several to tens of microns [184,186,268].

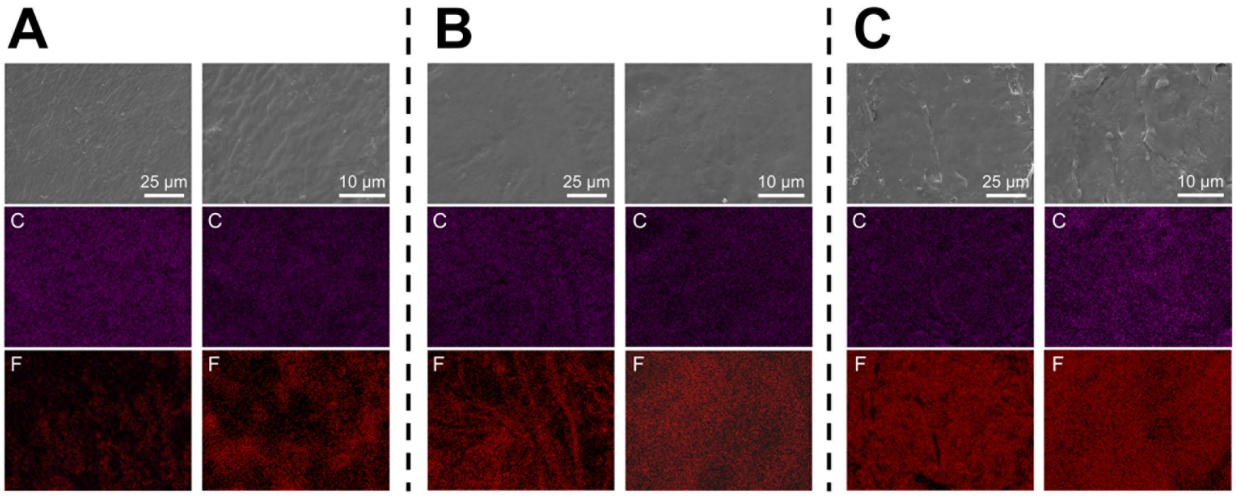

Figure 5.10. Surface SEM images and EDS mappings (C and F) of precipitation printed then hot pressed: A) 20 PVDF80NBR, B) 40PVDF60NBR, C) 80PVDF20NBR.

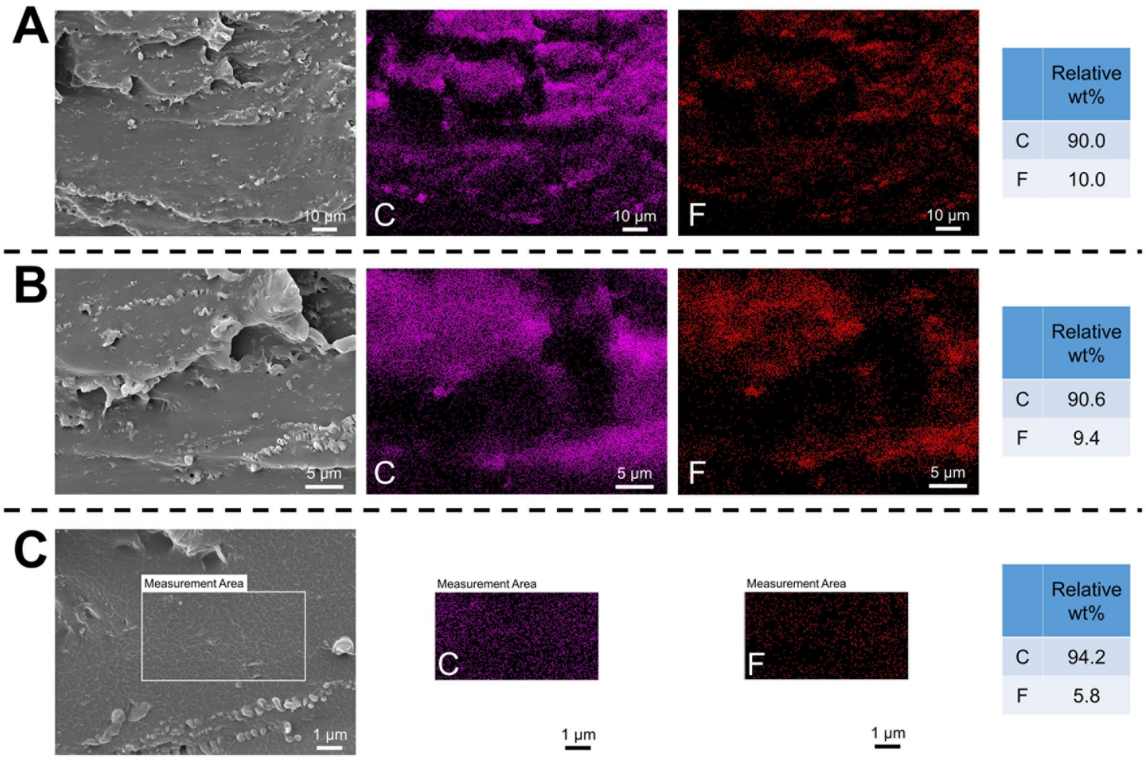

Figure 5.11. Tensile fracture cross-section SEM images and EDS mappings (C and F) of precipitation printed then hot pressed 20PVDF80NBR. Magnification: A) ×1000, B) ×3000, C) ×10000.

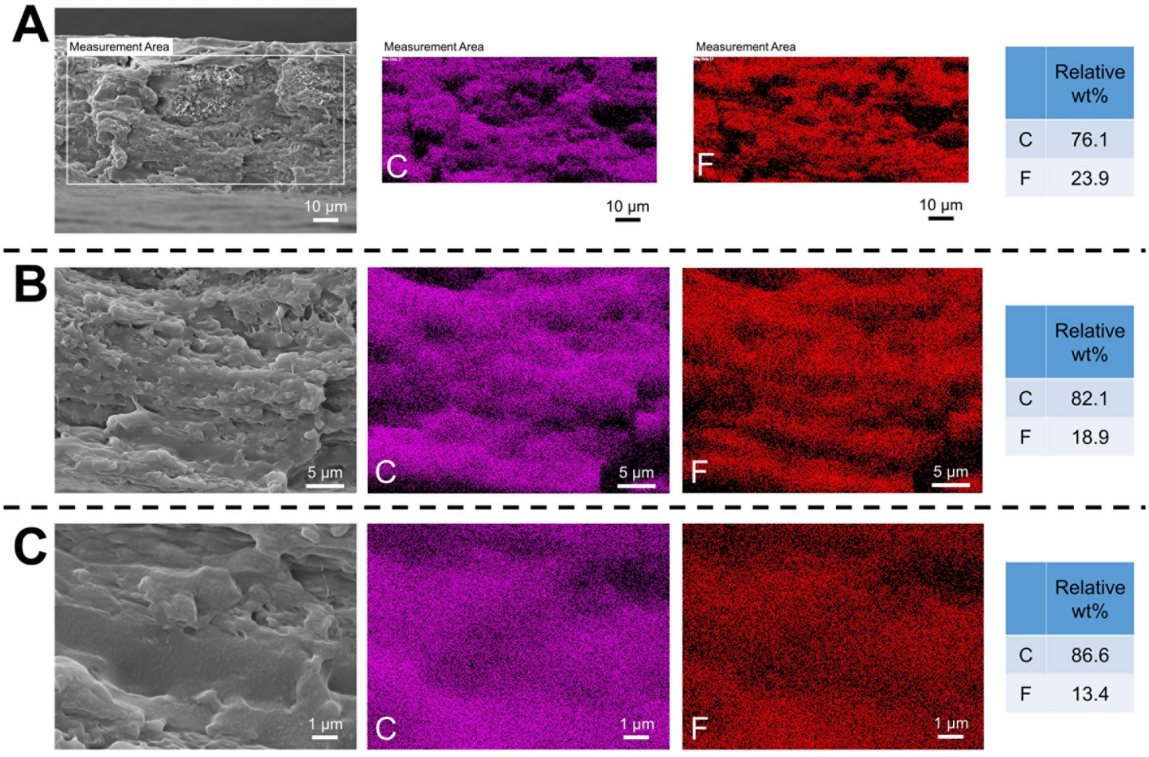

Figure 5.12. Tensile fracture cross-section SEM images and EDS mappings (C and F) of precipitation printed then hot pressed 40PVDF60NBR. Magnification: A) ×1000, B) ×3000, C) ×10000.

5.3.5 Mechanical properties

The mechanical properties of the PVDF/NBR blends were tested through tensile testing using a universal testing system (Model 5982, Instron) according to ASTM D638, where specimens were laser cut into the type V specimen shape for testing. The tensile test results in Figure 5.13A show that the Young's modulus drops significantly from 1045 MPa (100PVDF) to 16.2 MPa (20PVDF80NBR) as the NBR weight fraction increases, and the modulus at 100% elongation of 20PVDF80NBR is only 2.8 MPa. Similarly, in Figure 5.13B, the tensile strength of the blends decreases as the NBR weight fraction increases. However, the addition of NBR provides exceptional stretchability to the blend. The average elongation at break increases from 7% (100PVDF) to 544% (20PVDF80NBR), which is attributed to the high elongation (902%) of neat NBR. The stretchability of PVDF/NBR blend using 20PVDF80NBR as the example is demonstrated in Figure 5.13C. After quasi-static testing, cyclic loading tests were performed on a dynamic test instrument (E1000, Instron). Figure 5.13D shows the stress-strain curves of a 20PVDF80NBR sample under 100% strain cyclic loading with a 0.1 s^{-1} strain rate. After the first loading-unloading cycle, the 20PVDF80NBR sample has about 25% remaining strain, which mainly comes from its viscoelasticity and plastic deformation from the PVDF phase due to its low yield strain [205,269]. However, after the PVDF phase is plastically deformed, the following four consecutive cycles have almost identical stress-strain curves, lower hysteresis and lower peak stress compared to the first cycle. The remaining strain in these four cycles is only caused by the time-dependent viscoelasticity, which can be recovered if given enough settling time (about 5–10 s). Thus, preconditioning of the stretchable PVDF/NBR sensor before application by stretching through the operating strain range and then releasing is a simple and effective approach to improve repeatability and reduce hysteresis of this material. In the later Section 5.4, it will also be discussed that the viscoelastic hysteresis is strain rate dependent, which reduces as the strain rate increases. Therefore, to be used as a stretchable sensing material, high NBR content PVDF/NBR such as 20PVDF80NBR exhibits high elongation, consistent stress-strain curves under cyclic loading and low hysteresis under high strain rates, which is highly desirable for dynamic sensing conditions.

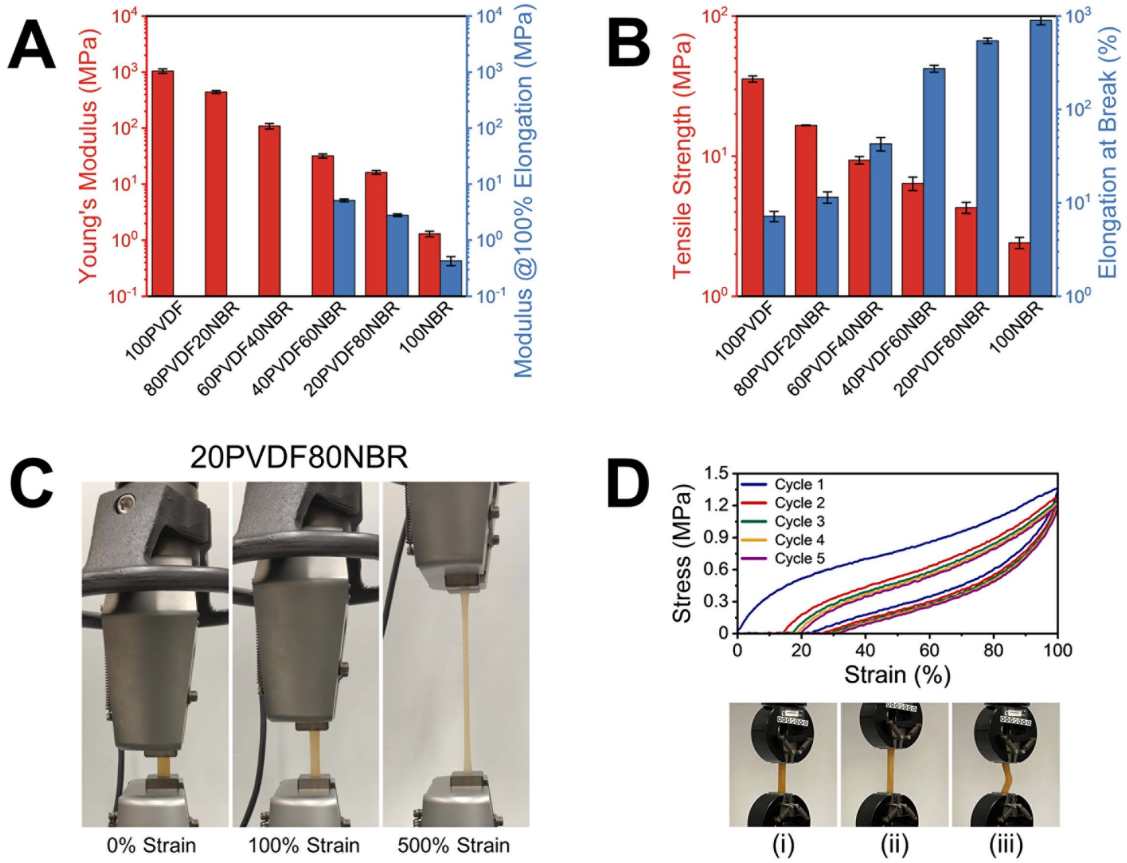

Figure 5.13. (A) Young's modulus and modulus at 100% elongation of the different blends. (B) Tensile strength and elongation at break of the different blends. (C) Stretchability of a 20PVDF80NBR sample. (D) Five consecutive loading-unloading cycles of a 20PVDF80NBR sample and the three stages of the first loading-unloading cycle: (i) initial state, (ii) peak strain state, (iii) unloaded state.

5.3.6 Dielectric and piezoelectric properties

The dielectric properties of the PVDF/NBR blends were measured in the frequency range from 20 Hz to 2 MHz, using a precision LCR meter (E4980A, Keysight Technologies). In Figure 5.14A, the dielectric constant of all PVDF/NBR blends drops as the frequency increases, while the drop above 100 kHz is more significant with higher NBR content. In addition, we noticed an abnormal phenomenon that the dielectric constant of the PVDF/NBR blend is higher than both neat PVDF and NBR at both low and high frequencies (Figure 5.14B). This phenomenon can be explained by the mechanism proposed in literature works of some other polymer blends, where the nanoscale mixing of two dipolar polymers can slightly increase the chain spacing and thus reduce the dipole reorientation barriers [270]. In Figure 5.14C, the loss tangent curves of the blends show an α relaxation that moves towards the lower frequency and has a higher peak value with an increasing amount of NBR [271]. The loss tangent on the low frequency end (Figure 5.14D) has a

dramatic increase as the NBR content increases, which can be explained by the Maxwell-Wagner polarization of heterogeneous materials. The high loss tangent of NBR attributes to the dielectric constant difference between the NBR and remaining sulfur or accelerator that induces interfacial charges [272]. The high loss tangent of PVDF/NBR blends with high NBR content at low frequencies can be one of the main drawbacks of the PVDF/NBR sensor for low frequency sensing since the dielectric energy loss will cause charge dissipation and measurement inaccuracy.

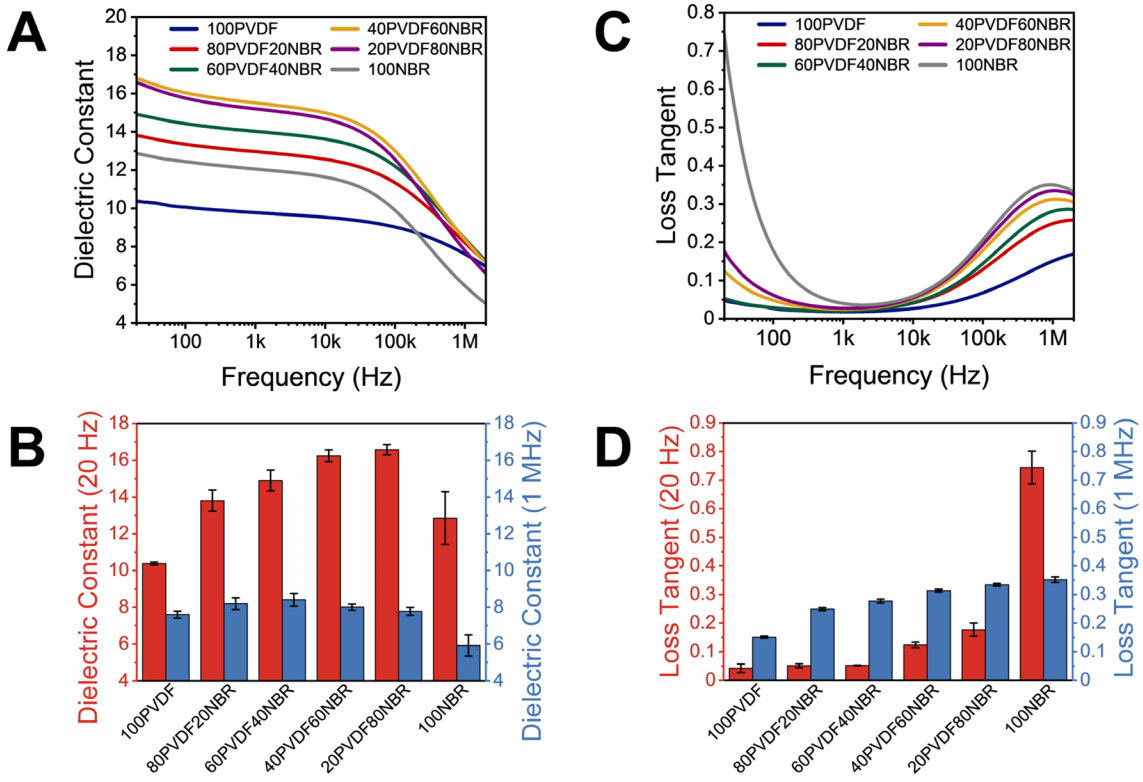

Figure 5.14. A) Dielectric constant of different blends with respect to frequency. B) Dielectric constant of different blends at 20 Hz and 1 MHz. C) Loss tangent of different blends with respect to frequency. D) Loss tangent of different blends 20 Hz and 1 MHz.

After electric poling of the PVDF/NBR blends using the electric field strength in Table 5.1, longitudinal and transverse piezoelectric properties of the blends were measured following the same procedure and setup described in Chapter 4. The piezoelectric voltage coefficients (g_{31}, g_{32} and g_{33}) are piezoelectric charge coefficients divided by the 3-direction permittivity. As explained in Chapter 4 that precipitation printed then hot pressed PVDF has transversely isotropic piezoelectric properties, the d_{31} and d_{32} coefficients of 100PVDF (printed in a 0 °C bath) are again confirmed to have no statistical difference ($p = 0.52$), unlike the transversely anisotropic stretched PVDF (Table 5.4). Thus, d_{31} and g_{31} of the PVDF/NBR blends are measured to represent the transverse piezoelectric properties. It should also be noted that by using a 0 °C printing bath,

100PVDF in this work has the best piezoelectric properties among all transversely isotropic PVDF samples in this dissertation, which reaches some of the best biaxially stretched PVDF films in the literature [136,251].

Table 5.4. Piezoelectric anisotropy of 100PVDF compared to stretched PVDF.

	d_{31} (pC·N^{-1})	d_{32} (pC·N^{-1})	d_{33} (pC·N^{-1})
100PVDF (printed in a 0 °C bath)	11.52±1.60	12.20±1.18	−23.01±1.58
Unidirectionally stretched PVDF	24.27±1.64	5.09±0.16	−30.14±1.61

For PVDF/NBR blends, in Figure 5.15A, both piezoelectric charge coefficients d_{31} and d_{33} decrease as the PVDF content reduces, yet the decrease in d_{33} is more significant than d_{31}. Similarly, after considering the permittivity of the blends, the piezoelectric voltage coefficient g_{33} in Figure 5.15B has a steeper drop than g_{31} as the PVDF weight fraction decreases, due to the anisotropy between the longitudinal (out-of-plane) and transverse (in-plane) modulus of the hot-pressed blends. In Figure 5.16, as the NBR weight fraction increases, the reduction in out-of-plane modulus is less than the reduction in in-plane modulus, which also results in higher out-of-plane modulus than in-plane modulus for blends having more than 40 wt% NBR. Densification of the porous precipitation printed PVDF/NBR in the out-of-plane direction by hot pressing contributes the most towards this trend in modulus, where the densification effectiveness by hot pressing improves as the soft NBR content increases. Therefore, it can be inferred that the anisotropic mechanical properties cause the different trends between the longitudinal and transverse piezoelectric properties. For low PVDF content blends such as 20PVDF80NBR, the transverse piezoelectric coefficients are higher than the longitudinal piezoelectric coefficients, indicating a more sensitive stretching mode sensing performance than the compression mode.

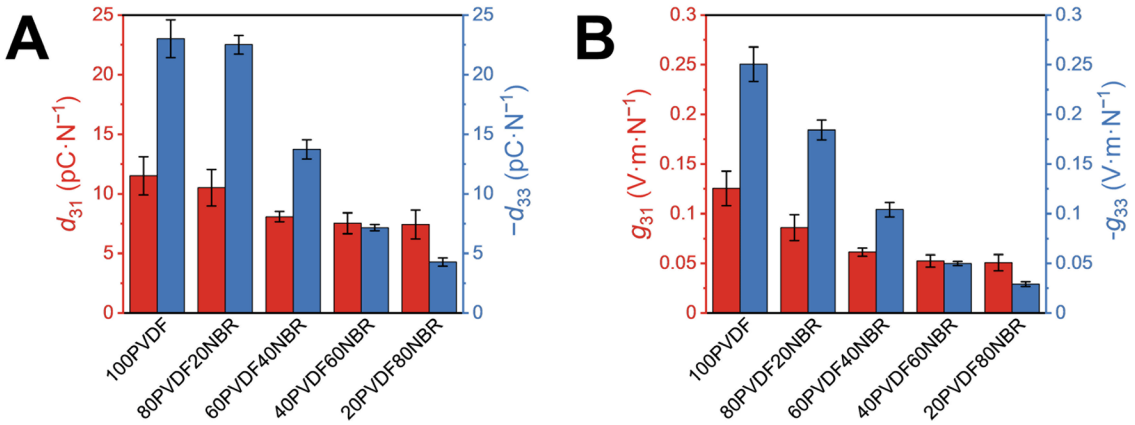

Figure 5.15. A) Piezoelectric charge coefficients of different blends. B) Piezoelectric voltage coefficients of different blends.

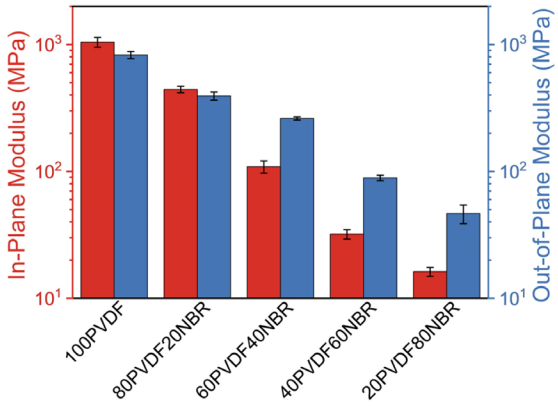

Figure 5.16. In-plane tensile modulus for d_{31} and out-of-plane compressive modulus for d_{33} of different polymer blends.

5.4 Performance of stretchable piezoelectric sensors

5.4.1 Stretchable conductive electrodes

The stretchability and electrical resistance of the MWCNTs/NBR conductive electrode was measured by coating and curing it on a 20PVDF80NBR sample surface for tensile test and was tested 4 times. The measured resistance change in Figure 5.17A shows that this conductive nanocomposite can be stretched to 100% strain for 4 times without permanent damage. As a piezoresistive material, MWCNTs/NBR itself has strain sensing ability. However, using this piezoresistive material as a sensor has some drawbacks that are explained as follows. First, the resistance change trend is nonlinear, which means a complicated function for curve fitting is required. Second, the uncertainty of the resistance change and gauge factor of the same sample based on 4 tests is high (Figure 5.17B), making the strain prediction inaccurate using resistance values. Third, most piezoresistive materials have temperature dependence of resistance, so does this MWCNTs/NBR nanocomposite. Figure 5.17C presents the temperature dependence of the resistance of MWCNTs/NBR (based on a 30 °C initial temperature), where the resistance drops 1% when the temperature increases to 40 °C and drops 5% when the temperature increases to 55 °C. The temperature coefficient of resistance is negative for the MWCNTs-based nanocomposites since quantum tunnelling of electrons is the main mechanism of electrical conductivity between MWCNTs [273]. Therefore, using MWCNTs/NBR as a strain sensor directly is inappropriate for applications that require high accuracy and repeatability. It is only used as an electrode material in this work for piezoelectric sensors. The Young's modulus of the MWCNTs/NBR nanocomposites

is measured to be 14.5 MPa, which matches the Young's modulus of high NBR content PVDF/NBR blends like 20PVDF80NBR and ensures low overall stiffness of the sensors.

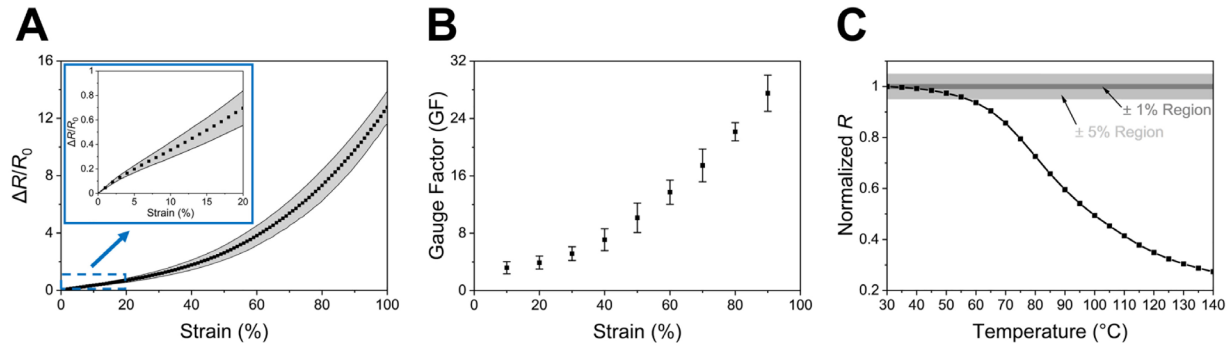

Figure 5.17. A) Normalized resistance change ($\Delta R/R_0$) of MWCNTs/NBR with respect to strain , where the gray band is the uncertainty band. B) Gauge factor with respect to strain. C) Normalized resistance (R) change of MWCNTs/NBR with respect to temperature.

5.4.2 Temperature dependence of piezoelectric outputs

The temperature dependence of the two piezoelectric outputs, charge (Q) and open-circuit voltage (V_{OC}) of the PVDF/NBR sensors was tested on a dynamic mechanical analyzer (DMA, Q800, TA Instruments) in tension mode to induce transverse piezoelectric effect. A 20PVDF80NBR sensor was used as an example. In Figure 5.18A, the measured Q of the 20PVDF80NBR first increases then decreases as the temperature increases from 30 °C in the DMA with constant strain amplitude, which is caused by the change in its dielectric constant. However, in Figure 5.18B, the measured V_{OC} shows a stable region near the initial temperature under controlled strain excitations. The V_{OC} drops 1% when the temperature increases to 52 °C and drops 5% when the temperature increases to 75 °C. This temperature-insensitive range of the V_{OC} is larger than that of the resistance of the MWCNTs/NBR nanocomposites in the previous Section 5.4.1. In contrast to the constant strain amplitude excitations, the Q and V_{OC} trends under constant stress amplitude excitations, which represent d_{31} and g_{31} trends, respectively, show a more significant temperature dependence. In Figure 5.18C and D, both Q and V_{OC} increase as the temperature rises until reaching about 90 °C, and then drop as the temperature further increases. The increasing stage can be mainly explained by the viscoelastic modulus reduction of the 20PVDF80NBR, and the decreasing stage attributes to the thermal depolarization of PVDF [134,274]. Thus, the V_{OC} of PVDF/NBR piezoelectric sensors is selected as the sensing signal which can provide temperature-insensitive strain measurements in a temperature range from 30 °C

to 75 °C. To predict the stress experienced by the PVDF/NBR sensor under varying temperatures using the V_{OC} measurement, an additional temperature measurement is still needed.

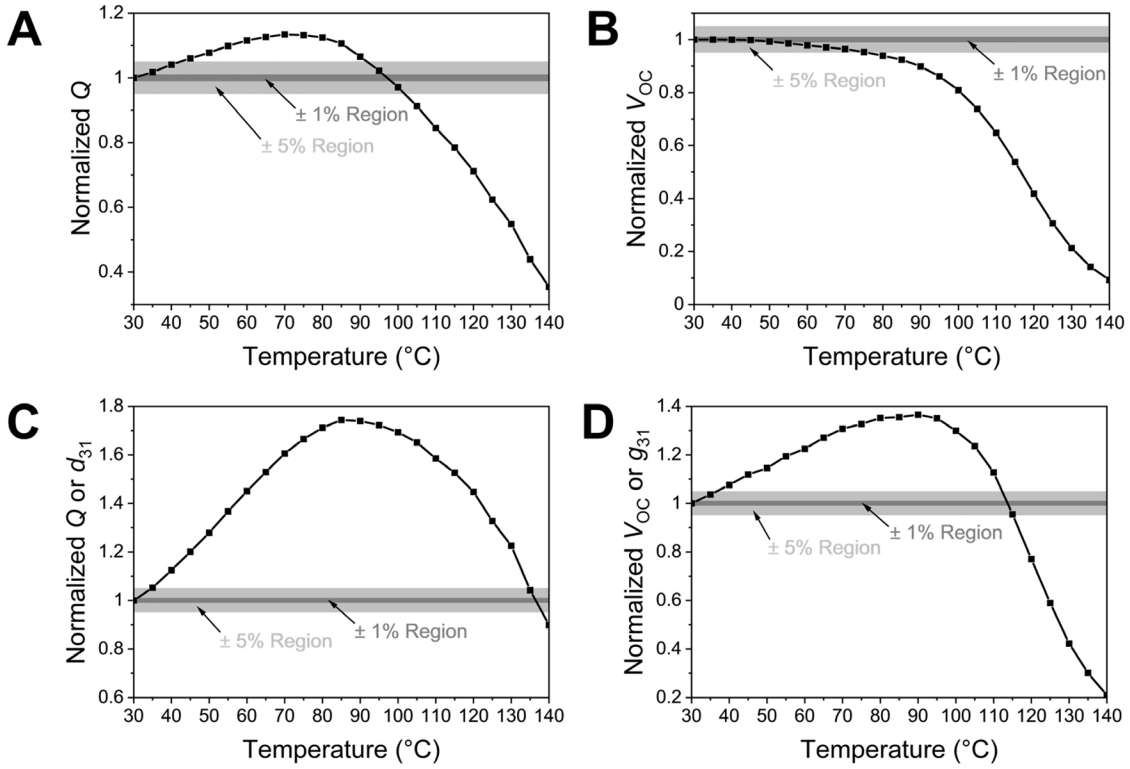

Figure 5.18. A) Normalized piezoelectric charge (Q) of 20PVDF80NBR under constant strain. B) Normalized piezoelectric open-circuit voltage (V_{OC}) of 20PVDF80NBR under constant strain. C) Normalized Q or d_{31} of 20PVDF80NBR under constant stress. D) Normalized V_{OC} or g_{31} of 20PVDF80NBR under constant stress. All normalizations are based on the quantities at 30 °C.

5.4.3 Stretching mode piezoelectric sensors

Stretching mode (g_{31} mode) piezoelectric sensors are used for elongation and bending curvature measurements in wearable sensors or soft actuator calibrations where the dynamic excitation is in the transverse direction, so the 20PVDF80NBR blend is chosen based on its high stretchability, low modulus and hysteresis. The stretching mode piezoelectric sensors were preconditioned (stretched then recovered) and tested using a dynamic test instrument (E1000, Instron), while the V_{OC} was measured using a high input impedance (> 1 GΩ) data acquisition system (Compact DAQ NI-9223, National Instruments). Figure 5.19 presents the characteristics of the stretching mode 20PVDF80NBR sensors including the working principle (Figure 5.19A). When subjected to a triangle wave strain excitation, the corresponding stress and voltage generation of a 20PVDF80NBR sensor are plotted in Figure 5.19B. Although the strain excitation is a linear triangle wave, the stress response is nonlinear due to viscoelasticity and hysteresis. The

generated voltage follows a similar trend to the stress. At the end of the cycle, the unrecovered strain causes buckling (Figure 5.13D) which explains the negative stress and voltage due to slight compression. If only observing the first half cycle and plotting the voltage against the stress and strain, the generated voltage is proportional to the stress but has a nonlinear relationship with the strain (Figure 5.19C). This study reveals that although exhibiting nonlinearity with hysteresis, 20PVDF80NBR has sufficient stress transfer efficiency between the phases even under high strains, because the piezoelectric voltage generated by the crystalline β phase PVDF is proportional to the apparent stress experienced by the entire polymer blend. However, the voltage-strain curve is nonlinear which is attributed to the nonlinear stress-strain curve of the polymer blend (Figure 5.13D).

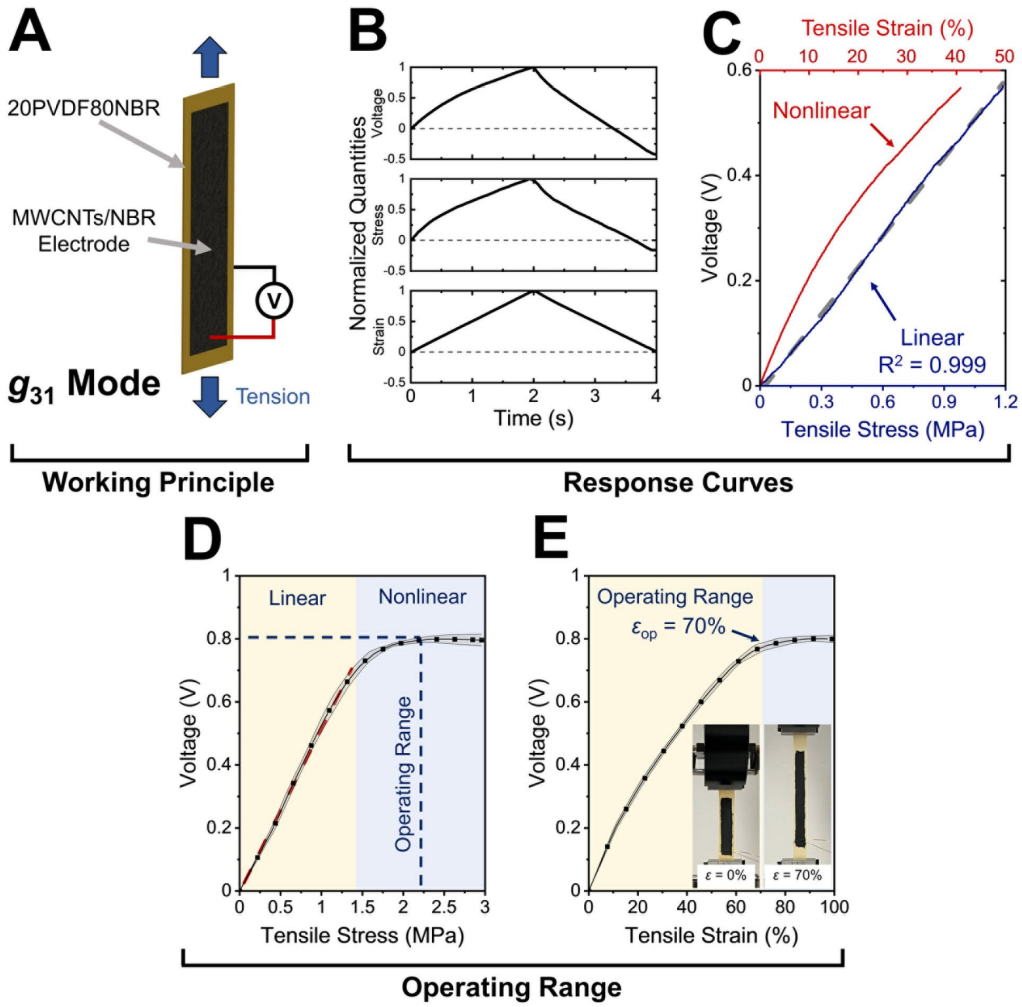

Figure 5.19. Characterization of the stretching mode 20PVDF80NBR sensors. A) Schematic of its working principle. B) Normalized voltage and stress response to a triangle strain excitation. C) Voltage-stress response with a linear fit and nonlinear voltage-strain response. D) Linear range and operating range of the voltage-stress curve with error bands. E) Operating range of the voltage-strain curve with error bands.

Next, the operating range of 20PVDF80NBR sensors was measured by repeatedly stretching a 20PVDF80NBR sensor to 100% strain. In Figure 5.19D, the 20PVDF80NBR sensor has a monotonic voltage-stress curve with an operating stress range up to 2.2 MPa, including a linear range up to 1.4 MPa. The voltage-strain curve is monotonic below 70% strain, indicating the maximum operating strain (ε_{op}) for strain sensing is 70% (Figure 5.19E). When the strain is above 70%, the generated voltage tends to saturate, which can be explained as an equilibrium between the voltage generation rate from the piezoelectric effect and the voltage draining rate based on the system time constant.

Furthermore, the frequency and strain rate dependence of the sensing behavior was investigated by using triangle wave excitations with various frequencies and amplitudes. Figure 5.20A shows the linear fitting slope of the voltage-stress (V-σ) response of a 20PVDF80NBR sensor under excitation frequencies from 0.25 to 4 Hz with a constant strain amplitude of 60%, which corresponds to strain rates ranging from 0.3 to 4.8 s^{-1}. The results show that the voltage-stress slope is frequency-independent and strain rate-independent according to one-way analysis of variance (ANOVA, $p = 0.945$). Similarly, the nonlinear voltage-strain response is also frequency and strain rate-insensitive for strains up to 60% (Figure 5.20B). Another test was performed on the same sensor with a fixed frequency of 0.5 Hz and various strain amplitudes, which corresponded to strain rates from 0.06 to 0.6 s^{-1}. In Figure 5.20C, all voltage-strain responses with different strain rates and strain amplitudes follow a consistent curve, confirming the strain rate independence of this sensor. However, all the frequency and strain rate independent strain/stress sensing properties are only based on the loading half cycle, while the unloading half cycle has more complicated sensing behavior due to the viscoelastic hysteresis combined with dielectric dissipation-based voltage draining. Therefore, hysteresis of the 20PVDF80NBR sensors are studied in Figure 5.20D–F. Due to the inaccurate load cell force measurement when the strain rate is high, stress measurements are kept under 2.4 s^{-1}, while voltage and strain measurements can reach 9.6 s^{-1}. For the mechanical hysteresis, in Figure 5.20D, the loading half cycle of the stress-strain curve keeps consistent under strain rate from 0.3–2.4 s^{-1}, but the hysteresis reduces as the strain rate increases. This result is supported by the strain rate-dependent deformation model of rubbers developed by Tomita et al., in which the hysteresis loss first increases and then decreases as the strain rate increases, depending on the stretch ratio (1+strain) [275]. When the stretch ratio is 1.6 in this case, the hysteresis loss reduces as the strain rate increases from 0.3 to 2.4 s^{-1}. This

agreement with Tomita's model can be explained by the submicron level phase separation of the 20PVDF80NBR, which does not have distinct phases and behaves like a homogeneous rubber. This confirms that the 20PVDF80NBR blend can be considered as a continuous elastomer phase above micron scale. For electro-mechanical hysteresis, the voltage-stress curves in Figure 5.20E show low hysteresis, no strain rate dependence and high linearity. Due to the piezoelectric voltage draining rate of the sensor system, at a low strain rate like 0.3 s^{-1}, the unloading half voltage-stress curve shows a slightly shifted slope and a slightly larger hysteresis. Figure 5.20F displays the voltage-strain curves under strain rate 0.3–9.6 s^{-1}. The voltage-strain curve of the loading half cycle is consistent under this large strain rate range, while the hysteresis decreases as the strain rate increases, like the trend of stress-strain hysteresis. For dynamic load conditions where strain rate or excitation frequency is high, the hysteresis of the piezoelectric 20PVDF80NBR blend is low due to its unique blend morphology, which overcomes the limitations of conventional two-phase sensing materials that usually have higher hysteresis at higher strain rate due to interfacial slipping and energy loss. To further reduce the hysteresis, higher sulfur content for NBR vulcanization can be used to increase the crosslink density and thus reduce the hysteresis loss.

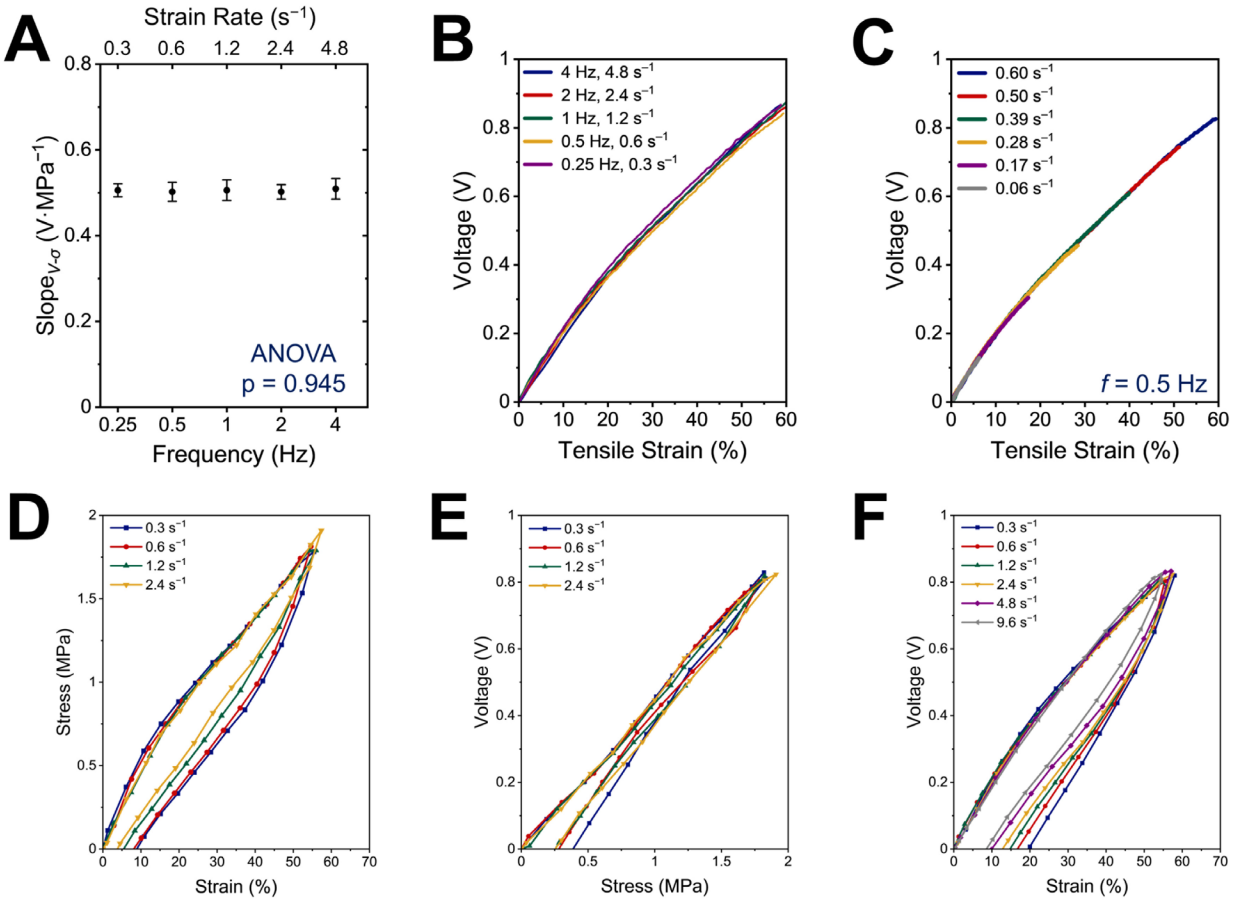

Figure 5.20. Frequency and strain rate dependence of the stretching mode 20PVDF80NBR sensors. A) Frequency-independent and strain rate-independent voltage-stress slopes. B) Frequency-independent and strain rate-independent voltage-strain curves up to 60% strain. C) Strain rate-independent voltage-strain curves with various strain amplitude excitations at 0.5 Hz. D) Strain rate-dependent stress-strain hysteresis. E) Strain rate-independent voltage-stress hysteresis. F) Strain rate-dependent voltage-strain hysteresis.

Moreover, the influence of pre-stretch strain on the dynamic sensing performance was investigated by applying a dynamic sinusoidal strain excitation (Figure 5.21A) on a pre-stretched 20PVDF80NBR sensor. In Figure 5.21B, the measured voltage-stress slopes do not have significant dependence on the pre-stretch strain below 60% according to ANOVA ($p = 0.939$), while the slope decreases as the pre-stretch strain exceeds 70%. On the other hand, the voltage-strain curves exhibit a consistent trend when the pre-stretch strain is below 50% (Figure 5.21C) but start to have a significant dependence on the pre-stretch strain when it is above 60%.

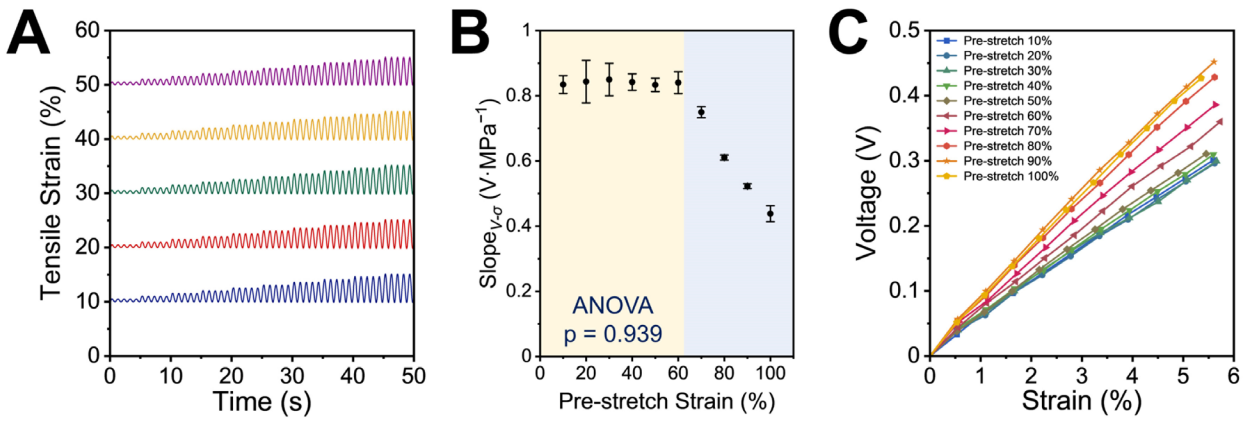

Figure 5.21. Pre-stretch strain dependence of the stretching mode 20PVDF80NBR sensors. A) Examples of the excitation dynamic strain for pre-stretch tests with pre-stretch strain 10% to 50%. B) Effect of pre-stretch strain on dynamic stress sensing. C) Effect of pre-stretch strain (10%–100%) on dynamic strain sensing.

The stretching mode 20PVDF80NBR sensor can also detect small changes in dynamic tensile stress and strain. Figure 5.22A shows the voltage and stress response to 1 Hz sine wave strain excitations with increasing amplitudes (0.15% to 1.1%). The stress response does not match with the strain excitation due to the hysteresis behavior of 20PVDF80NBR, but its amplitude aligns with the voltage response. It should be noted that the voltage for dynamic sensing is high pass filtered to remove the DC offset. Figure 5.22B presents the peak-to-peak voltage-stress and voltage-strain relationships based on Figure 5.22A data. The voltage-stress relationship is linear ($R^2 = 0.998$), and the voltage-strain relationship is nonlinear, similar to the triangle wave excitation case in Figure 5.19B. Thus, the stretching mode 20PVDF80NBR sensor has a high-resolution dynamic sensing capability for tensile stress and strain. In summary, the stretching mode 20PVDF80NBR can be used as both stretchable strain and stress sensors that only require calibrations prior to operation, which can provide simple and repeatable dynamic strain/stress measurements with a 70% operating strain range. It also allows for highly reliable strain/stress sensing up to 50% strain with advantages such as strain rate independence and negligible pre-stretch influence. These unique features make the stretching mode PVDF/NBR blend an outstanding strain sensing material with intrinsic stretchability compared to other existing works (Table 5.5), especially under dynamic loading conditions. To further improve stretchability and operating strain range, smart pattern design can be applied to PVDF/NBR blend as the base material to fabricate ultra-stretchable piezoelectric sensors in the future.

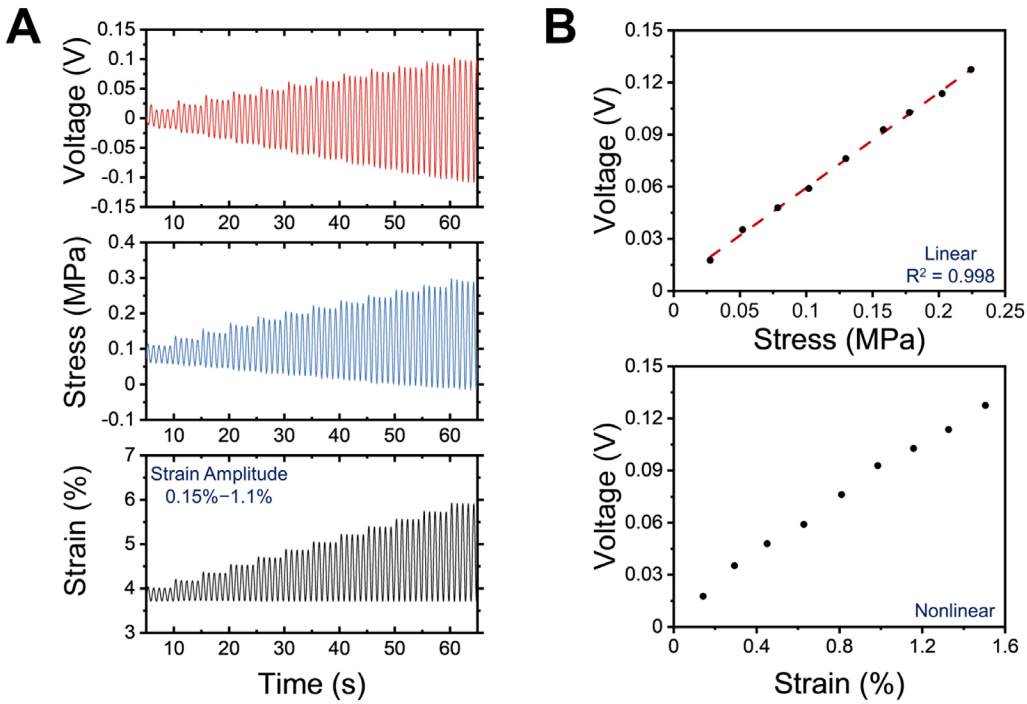

Figure 5.22. High-resolution dynamic sensing of a stretching mode 20PVDF80NBR sensor. A) Voltage and stress response to sine wave strain excitations with increasing amplitudes (0.15% to 1.1%). B) Linear voltage-stress relationship and nonlinear voltage-strain relationship of this dynamic sensing test.

Table 5.5. Comparison of the stretching mode piezoelectric PVDF/NBR sensor in this work with other stretchable piezoelectric sensors.

Category	Type	Material	Stretchability	Maximum sensing strain	Strain rate dependence	Reference
Pattern design	Kirigami	PVDF film and PDMS	/	30%	Yes	[181]
	Kirigami	PVDF film and PET film	320%	/	Yes	[180]
	Serpentine structure	PVDF film and UV film	/	35%	/	[179]
	Wavy structure	PVDF microfibers and VHB film	> 350%	/	Yes	[176]
	Wavy structure	PVDF nanofibers and PDMS	110%	100%	Yes	[177]
Material design	Nanocomposite	PZT/silicone	> 200%	50%	Yes	[186]
	Nanocomposite	PZT/PDMS	254%	/	/	[187]
	Nanocomposite	PMN-PT/ MWCNTs/ silicone	> 200%	/	Yes	[184]
	Nanocomposite	$BaTiO_3$/PDMS	/	/	Yes	[268]
	Sandwich composite	PVDF-TrFE nanofibers/PDMS	>30%	/	/	[189]
	Polymer blend	PVDF/NBR	544%	70%	No	This work

5.4.4 Compression mode piezoelectric sensors

Compression mode sensors are used for tactile sensing, pressure and normal force measurements, where the dynamic excitations are in the longitudinal direction. Considering the balance between transverse stretchability and longitudinal piezoelectric sensitivity (g_{33}), both 40PVDF60NBR and 20PVDF80NBR were tested as compression mode sensors in this work, yet 40PVDF60NBR was preferred for better sensitivity with moderate stretchability (274%). The characteristics of the 40PVDF60NBR compression mode sensors are presented in Figure 5.23, including the working principle (Figure 5.23A). It should be noted that during all compression tests, the two compression plates were never released from the sensor surfaces and a small compressive preload was always applied to the sensor to avoid any triboelectric effect. When a 40PVDF60NBR sensor was subjected to an increasing compressive load, the voltage-stress response was linear and the voltage-strain relationship was nonlinear (Figure 5.23B), which is attributed to the nonlinear compressive stress-strain behavior. Moreover, for large-amplitude compressive stress sensing, a 40PVDF60NBR sensor was excited by triangular compressions with increasing amplitude, and the voltage generation aligned with the stress input after high pass (0.1 Hz cutoff) filtering off the low-frequency drift due to the dielectric dissipation induced voltage draining (Figure 5.23C). By plotting peak voltages with respect to peak stresses (Figure 5.23D), the voltage is again proportional to the stress in the compression mode, with a linear range up to about 4.8 MPa compressive stress (corresponding compressive strain 16%). In addition, the resolution of its dynamic sensing ability was demonstrated through measuring the voltage output under small amplitude sinusoidal compressive excitations (Figure 5.23E), which can be as low as 0.01 MPa. The various voltage amplitudes and stress amplitudes in this test are plotted in Figure 5.23F**,** and they can be well fitted by a linear function ($R^2 = 0.998$). Furthermore, the frequency and loading rate dependence of the compression mode 40PVDF60NBR was investigated by applying triangular compressive loads with different frequencies but a constant load amplitude. When under 0.25 to 4 Hz triangular compressive wave excitations, which correspond to loading rates from 0.07 to 1.12 $kN \cdot s^{-1}$, the slopes of the linear voltage-stress relationships show no significant dependence on the excitation frequency or loading rate according to one-way ANOVA ($p = 0.782$, Figure 5.23G). On the other hand, although the voltage-strain curves are nonlinear, they consistently follow the same trend regardless of frequency or loading rate (Figure 5.23H). Finally, the effect of transverse direction pre-stretch strain on longitudinal sensing performance

was investigated by stretching a 40PVDF60NBR sensor to target strains and measuring the longitudinal piezoelectric responses simultaneously. From Figure 5.23I, it can be seen that the slope of voltage-stress relationships is almost identical when the pre-stretch strain is below 40% (ANOVA $p = 0.584$), which allows for reliable compression stress/force sensing even on stretched substrates.

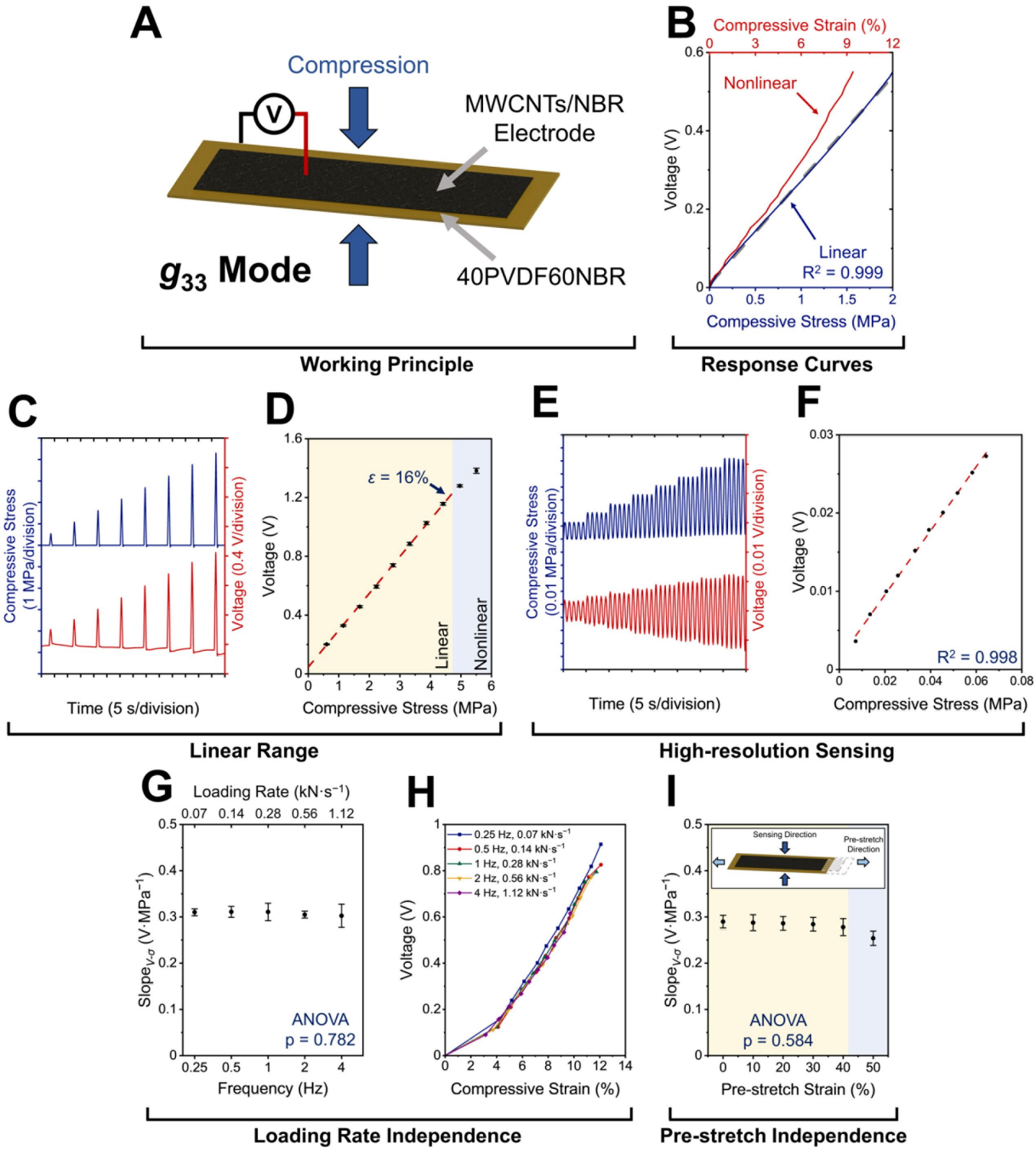

Figure 5.23. Characterization of the compression mode 40PVDF60NBR sensors. (A) Schematic of its working principle. (B) Voltage response with respect to stress and strain. (C) Voltage response to triangular compressive stresses with increasing amplitudes. (D) Linear range of the voltage-stress curves. (E) Voltage response to small

amplitude sinusoidal compressive stresses. (F) Linear voltage-stress relationship for small amplitudes. (G) Frequency and loading rate-independent voltage-stress slopes. (H) Frequency and loading rate-independent nonlinear voltage-strain curves. (I) Effect of transverse direction pre-stretch strain on longitudinal stress sensing.

The compression mode 20PVDF80NBR sensors presented in Figure 5.24 is a lower sensitivity but higher stretchability alternative to the 40PVDF60NBR sensor. When a 20PVDF80NBR sensor was subjected to an increasing compressive load, the voltage-stress response was linear and the voltage-strain relationship was nonlinear (Figure 5.24B), due to the changing compressive modulus at different strains. For large-amplitude compressive stress sensing, a 20PVDF80NBR sensor was excited by triangular compressions with increasing amplitude, and the voltage generation aligned with the stress input after high pass filtering with a cutoff frequency of 0.1 Hz (Figure 5.24C). By plotting peak voltages with respect to peak stresses (Figure 5.24D), the voltage is proportional to the stress in the compression mode, with a linear range up to about 2.2 MPa compressive stress (corresponding compressive strain 11%). The resolution of its dynamic sensing ability was demonstrated through measuring the voltage output under small amplitude sinusoidal compressive excitations in Figure 5.24E, which can be as low as 0.05 MPa. The various voltage amplitudes and stress amplitudes in this test are plotted in Figure 5.24F**,** and they have a linear correlation ($R^2 = 0.998$). The frequency and loading rate dependence of the compression mode 20PVDF80NBR was also investigated. When under 0.25 to 4 Hz triangular compressive wave excitations, which correspond to loading rates from 24 to 392 $N \cdot s^{-1}$, the slopes of the linear voltage-stress relationships show no significant dependence on the excitation frequency or loading rate according to ANOVA ($p = 0.961$, Figure 5.24G). Although the voltage-strain curves are nonlinear, they consistently follow the same trend regardless of frequency or loading rate (Figure 5.24H). The effect of transverse direction pre-stretch strain on longitudinal sensing performance of a 20PVDF80NBR sensor was finally studied. In Figure 5.24I, the slopes of voltage-stress relationships are almost identical when the pre-stretch strain is below 70% (ANOVA $p = 0.993$), implying a reliable compression stress/force sensing even on highly stretched substrates.

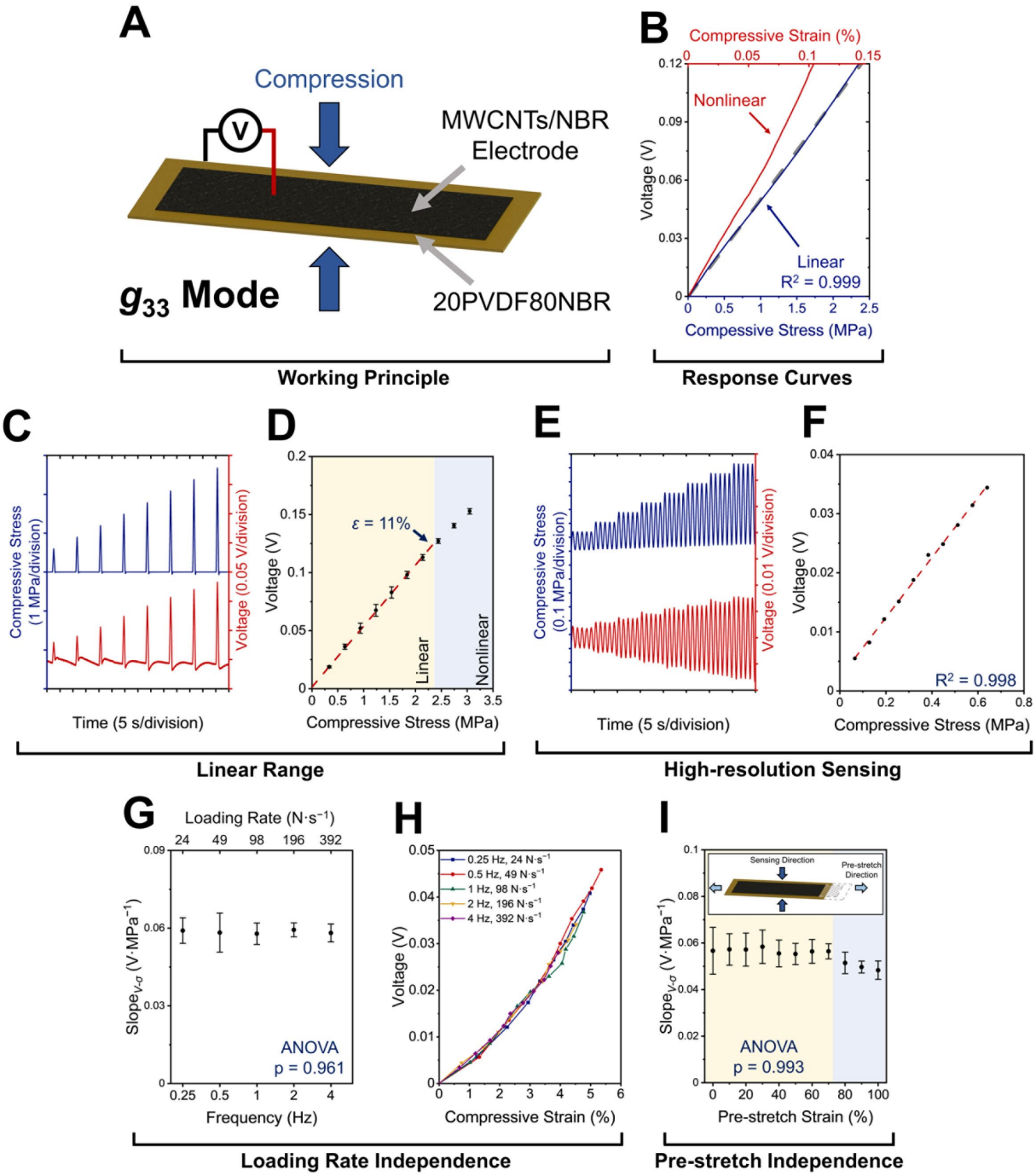

Figure 5.24. Characterization of the compression mode 20PVDF80NBR sensors. (A) Schematic of its working principle. (B) Voltage response with respect to stress and strain. (C) Voltage response to triangular compressive stresses with increasing amplitudes. (D) Linear range of the voltage-stress curves. (E) Voltage response to small amplitude sinusoidal compressive stresses. (F) Linear voltage-stress relationship for small amplitudes. (G) Frequency and loading rate-independent voltage-stress slopes. (H) Frequency and loading rate-independent nonlinear voltage-strain curves. (I) Effect of transverse direction pre-stretch strain on longitudinal stress sensing.

To conclude, when used as a stress/force sensor in the compression mode, with only a voltage-stress slope calibration prior to operation, 40PVDF60NBR or 20PVDF80NBR sensors can

measure dynamic stress or force based on the piezoelectric voltage output with high resolution and repeatability, which is also loading rate and pre-stretch insensitive. However, for low loading rate cases, the calibrated results are only accurate in the loading cycle, while the unloading cycle have voltage drifting issue due to the nature of piezoelectricity, dielectric charge dissipation and viscoelastic hysteresis. Therefore, the stretchable PVDF/NBR sensors are better suited to highly dynamic loading conditions.

5.5 Verification of stretchable piezoelectric sensors

To be used as reliable and accurate strain/stress sensors for various applications, PVDF/NBR sensors were bonded to multiple substrates to verify their sensing performance. The strain measurement accuracy of stretching mode 20PVDF80NBR sensors on three different materials was verified through digital image correlation (DIC). In Figure 5.25A, a 20PVDFNBR sensor was bonded to a soft silicone rubber (Mold Star 30, Smooth-On, Shore 30A hardness) by a silicone adhesive (Clear Silicone, Loctite) and tested uniaxially, and the voltage output was recorded to predict the tensile strain according to the previously calibrated voltage-strain curve for this sensor in Section 5.4.3. The local strain under the sensor covered area measured by DIC agreed with the strain prediction using the voltage measurement, indicating a reliable local strain prediction after bonding to a substrate. However, the far-field strain of the soft silicone measured by the tensile test frame was always higher than the sensor local strain, which was caused by the stiffness mismatch between the neat soft silicone and the soft silicone bonded to a sensor. When a sensor was bonded to a stiffer silicone rubber substrate (RTV664, Momentive, Shore 62A hardness), not only the local strain but also the far-field strain matched the strain prediction based on voltage reading due to the lower sensor modulus than the substrate (Figure 5.25B). A 20PVDF80NBR sensor was also attached to a less stretchable but porous polyester fabric, and the strain prediction was verified by both the local and far-field strain measurements (Figure 5.25C). Thus, stretching mode 20PVDF80NBR sensors can accurately measure local strain of any substrates after bonding, without affecting the substrate strain distribution if substrates have comparable or higher modulus than the sensor and adhesive. For ultra-soft substrates, sensors made of higher NBR content blends (*e.g.,* 10PVDF90NBR) can be fabricated and bonded with softer silicone adhesives.

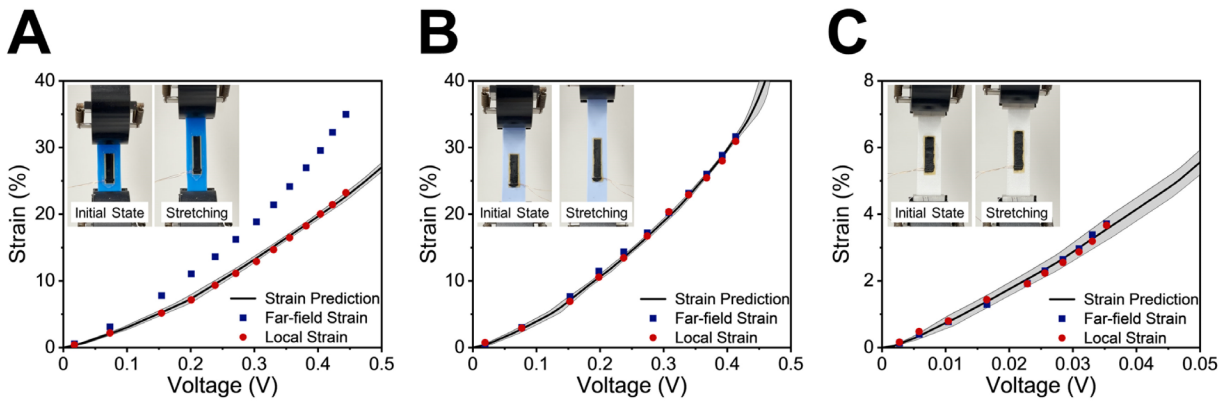

Figure 5.25. Strain verification of stretching mode 20PVDF80NBR sensors when bonded to: (A) Shore 30A silicone rubber, (B) Shore 62A silicone rubber, (C) polyester fabric.

The stress or force measurement accuracy of the compression mode 40PVDF60NBR and 20PVDF80NBR sensors embedded in soft structures was verified based on a commercial piezoceramic force sensor (208C, PCB Piezotronics, Figure 5.26A). It should be noted that only force is directly measurable because of unknown contact area. When applying external forces to a 40PVDF60NBR sensor in a silicone structure on top of a fixed piezoceramic force sensor (Figure 5.26B), the force predicted by the 40PVDF60NBR sensor, and the same force measured by the piezoceramic force sensor are shown in Figure 5.26C. The force prediction and reference measurement are in close agreement with each other, while some slight distinctions still exist due to the contact surface alignment error and discharging time constant difference between the two sensors. Similarly, the force measurement verification of a compression mode 20PVDF80NBR sensor is presented in Figure 5.26D. Due to its lower sensitivity, the noise level of the force prediction from the 20PVDF80NBR sensor is higher than the 40PVDF60NBR sensor. In general, the verification results confirm that these two modes of PVDF/NBR sensors can be used on soft structures for reliable strain and force measurements.

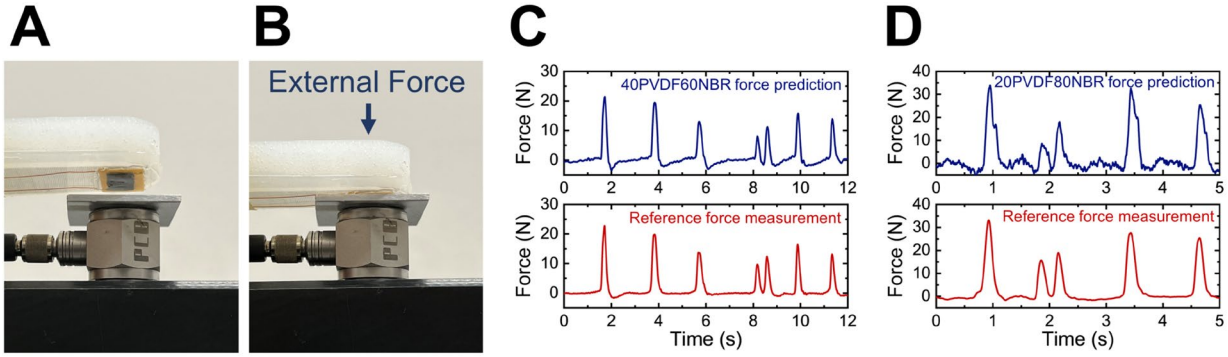

Figure 5.26. A) Force verification of a compression mode 40PVDF60NBR or 20PVDF80NBR sensor embedded in the tip of a silicone structure. B) During testing, an external force was exerted on the silicone structure and transferred

to the piezoceramic force sensor. C) Force verification result of the 40PVDF60NBR sensor. D) Force verification result of the 20PVDF80NBR sensor.

5.6 Application of stretchable piezoelectric sensors

The application of stretchable PVDF/NBR piezoelectric sensors was demonstrated by the strain and contact force sensing on a pneumatic soft actuator (Figure 5.27A). A pneumatic soft actuator made of silicone rubber (Dragon Skin 20, Smooth-On, Shore 20A hardness) was fabricated through a molding process using 3D printed molds (using an UltiMaker 3 printer) with channeled design. A layer of polyester fabric was embedded in the bottom layer of the soft actuator as stiffener to improve the bending actuation. After the soft actuator fabrication, a calibrated 20PVDF80NBR stretching mode sensor was bonded to the top surface as the inflation sensor and a calibrated 40PVDF60NBR compression mode sensor was bonded to the tip area of the bottom surface using a silicone adhesive (Clear Silicone, Loctite) as the contact sensor. The sensor surfaces were covered by additional silicone (Dragon Skin 20) to protect electrodes. The two voltage signals, V_i and V_c, from the inflation and contact sensors, respectively, were measured by the same high input impedance data acquisition system (Compact DAQ NI-9223, National Instruments). The measured voltages were all high pass filtered (0.1 Hz cutoff) to remove the baseline drift, and then converted to top surface inflation strain and bottom tip contact force based on the calibration curves. The pneumatic soft actuator was driven by a small constant flow rate air pump with a solenoid valve.

Figure 5.27B shows a free actuation case without any external load, where the actuator was inflated and deflated twice with different inflating time. The inflation sensor had active strain measurements when it was stretched during the inflation process, and its strain measurements tracked the two different bending curvatures. On the other hand, the contact sensor on the less stretchable bottom surface showed negligible force change during the inflating and deflating cycles, which was caused by the voltage generation from unavoidable bottom surface stretching in the transverse direction and undesirable wire vibration induced high-impedance piezoelectric voltage change. Figure 5.27C shows a loaded actuation case, where the actuator was inflated, blocked by a cylindrical obstacle, and deflated. In this case, the inflation sensor picked up a change in strain as the inflating process began, and then had a reduction in strain rate after the actuator touched the obstacle. Though having a similar inflating time, the peak strain in the loaded actuation case was lower than the second inflating cycle in the free actuation case, indicating a decreased

bending curvature due to the blockage. The tip contact sensor started showing significant force reading after the actuator touched the obstacle, and the force exerted on the contact sensor went up as the inflating process continued. It should be noted that at the time of deflation, the actuator was suddenly released from the obstacle, causing a strong voltage spike in the contact sensor measurement due to the triboelectric effect. This resulted in a meaningless force prediction from the contact sensor right after it was detached from the obstacle. To solve this problem, methods to separate the triboelectric contribution such as flexible shielding coatings need to be developed [276].

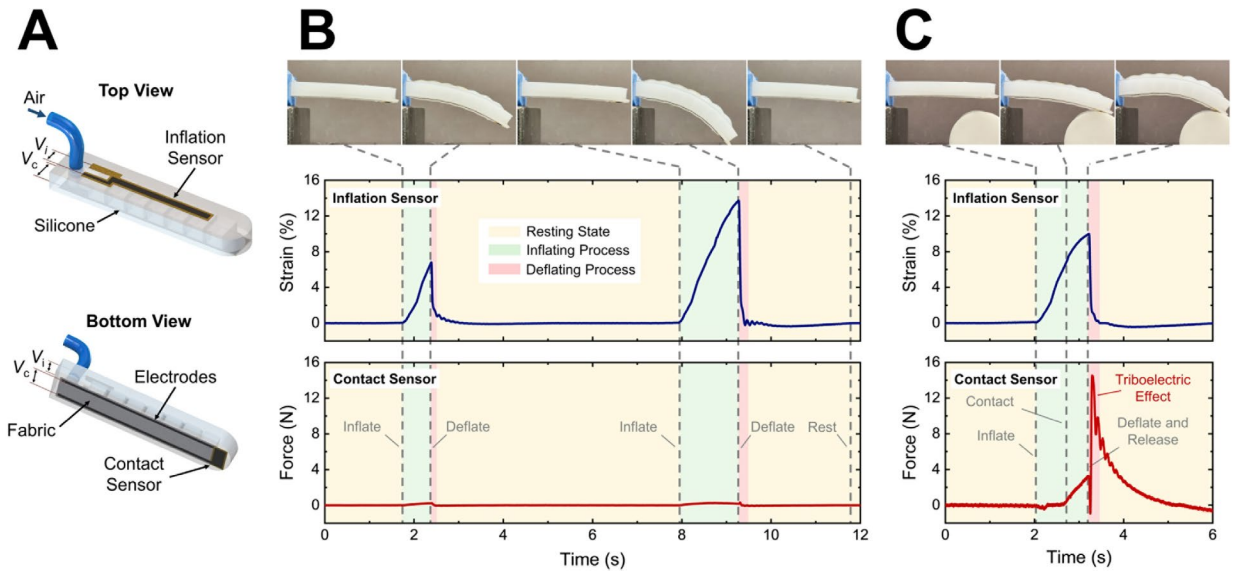

Figure 5.27. A) Schematics of a pneumatic soft actuator with a PVDF/NBR inflation sensor and a PVDF/NBR contact sensor. B) Sensing demonstration in a free actuation case without any external load. C) Sensing demonstration in a loaded actuation case.

To further demonstrate the force sensing capability of stretchable compression mode PVDF/NBR sensors, a 40PVDF60NBR sensor bonded to a Shore 62A silicone (RTV664, Momentive) was tested with and without transverse pre-stretch strains. A compressed air source with a constant pressure was used as the longitudinal force excitation to the sensor, which had no direct contact with the sensor surface to avoid triboelectric effect. In Figure 5.28, at the moment when the compressed air was turned on, a sudden spike of force (~ 4 N) was measured by the sensor due to the impulse, followed by a stabilized force of 2 N with slow decay due to the constant air pressure. When the compressed air was turned off, a sudden drop in force reading followed by slow decay due to the sensor dielectric dissipation and high pass filtering effect was observed. Comparing the force measurements in both unstretched and pre-stretched (33% strain) cases, the peak impulse force and the stabilized force are consistent, confirming a reliable force measurement

from the sensor regardless of the pre-stretch strain. The main difference between the two cases is the signal decay rate, which is caused by the change of the system time constant based on the sensor capacitance and resistance after stretching. In general, the stretchable PVDF/NBR sensors demonstrate promising dynamic strain and stress (force) sensing capabilities for soft structures, while additional methods to remove triboelectric contribution such as flexible shielding [276] and using flexible electronics [277,278] to enable in-situ signal conditioning are needed for future practical operations.

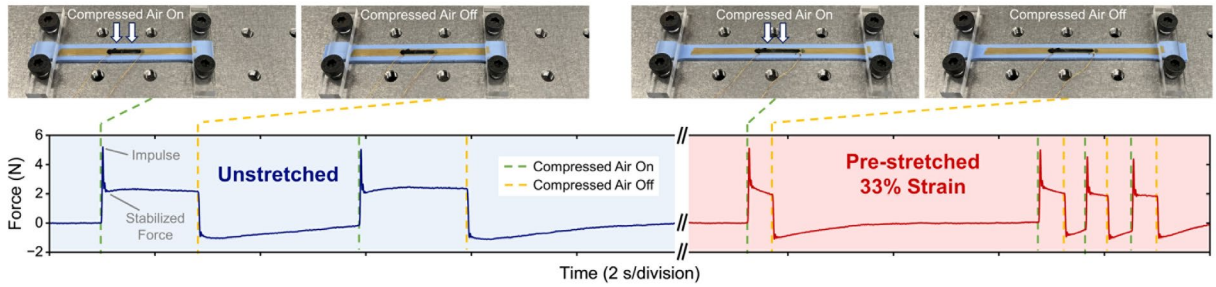

Figure 5.28. Compression mode 40PVDF60NBR sensor force sensing demonstration in unstretched and pre-stretched (33% strain) cases.

5.7 Chapter summary

In this chapter, a novel stretchable piezoelectric PVDF/NBR polymer blend was produced through precipitation printing then hot pressing for vulcanization. By using a 0 °C ice/water bath for precipitation printing of the PVDF/NBR blends, high PVDF crystallinity with dominant β phase was observed in all blend ratios, which provides the chemical structure basis for piezoelectricity. In addition, unlike thermal induced phase separation (TIPS) processes such as solvent casting for polymer blend formation, the polymer blends formed by precipitation printing is based on non-solvent induced phase separation (NIPS) at a low temperature, which leads to a unique submicron level phase separation regarding to the blend morphology. The resulting PVDF/NBR blends can be considered as a continuous elastomer phase above micron scale, which behaves like rubber and is different from typical two-phase piezoelectric nanocomposites. Tensile testing results show that PVDF/NBR blends are highly stretchable with an elongation at break of 274% for 40PVDF60NBR and 544% for 20PVDF80NBR.

After electric poling and adding stretchable MWCNTs/NBR electrodes, the PVDF/NBR blends exhibit outstanding piezoelectric properties, which can be used as both stretchable dynamic strain (stretching mode) and stress (compression mode) sensors. The stretching mode 20PVDF80NBR sensors have an operating sensing range up to 70% strain, which is strain rate-

independent in the range from 0.06 to 4.8 s^{-1} and insensitive to pre-stretch up to 50% strain. The compression mode 40PVDF60NBR sensors have a linear voltage-stress relationship below 4.8 MPa stress, with loading rate independence in the range from 0.07 to 1.12 $kN \cdot s^{-1}$ and transverse pre-stretch independence up to 40% strain. Similarly, the lower sensitivity but more stretchable compression mode 20PVDF80NBR sensors have a linear voltage-stress relationship below 2.2 MPa stress, with loading rate independence in the range from 24 to 392 $N \cdot s^{-1}$ and transverse pre-stretch independence up to 70% strain. Hysteresis study implies that the PVDF/NBR sensors have lower hysteresis loss at higher frequencies and faster loading rates, making them highly suited to dynamic conditions. Based on these advantages, the two demonstrations of the pneumatic soft actuator with two sensors and the sensor on a pre-stretched soft substrate show the potential application of PVDF/NBR sensors for reliable and accurate sensing of stretchable structures under dynamic loading conditions, which can be used for wearable sensing devices, soft actuator calibration and soft robot control. Therefore, this chapter offers a new approach to fabricate intrinsically stretchable piezoelectric polymer blends by using precipitation printing, and the resulting polymer blends can provide excellent piezoelectric sensing performance relying on their unique blend morphology. Future research on combing this intrinsically stretchable piezoelectric polymer blend with smart pattern design, like kirigami designs and wavy shapes, can lead to the development of ultra-stretchable sensing materials.

Chapter 6 Conclusions

Additive manufacturing (AM) of polymers have become a crucial part of the industrial manufacturing process due to its advantages in fabricating complex structures and cost efficiency in low-volume productions. Multiple AM processes for polymers are commercially available, such as material extrusion, powder bed fusion, vat photopolymerization and material jetting, but they have been mostly applied to general-purpose and some engineering thermoplastics, as well as photocurable liquid resins. High-performance engineering polymers, which have outstanding heat resistance and can be continuously used under elevated temperatures, usually require only low-volume production that is suitable for AM. However, challenges arising from the huge thermal gradient, thermal stress and heating rate in the material extrusion and powder bed fusion processes limit the mechanical properties of the high-performance polymers produced by AM. On the other hand, multifunctional polymers like piezoelectric polymers become lightweight and flexible substitutions for inorganic materials in the electronic industry to produce capacitors and sensors. AM can potentially allow fabricating piezoelectric polymers in complex geometries, but the piezoelectric phase transformation in common piezoelectric polymers such as poly(vinylidene fluoride) (PVDF) makes thermal energy-based AM processes unsuitable for this application. The purpose of the research in this dissertation is to address the challenges in using thermal energy-based AM processes to produce high-performance polymers and piezoelectric PVDF, which leads to the development of precipitation printing. Precipitation printing utilizes solvent power to dissolve or disperse polymers and relies on the non-solvent induced phase separation (NIPS) for polymer solidification, without the need for polymer melting or solvent thermal evaporation induced solidification. By controlling the solvent/non-solvent pairs and printing parameters, precipitation printing also allows for porosity, microstructure and mechanical property tailoring of the printed parts. In this dissertation, precipitation printing has been successfully applied to polysulfone (PSU), para-aramid and piezoelectric PVDF, which provides a new concept and a solution to fill a gap in additive manufacturing of high-performance and piezoelectric structures.

6.1 Summary of results

The concept of precipitation printing was introduced in Chapter 2. A target polymer was first dissolved or dispersed in a proper solvent to form a homogeneous printing solution or colloid. Then the printing solution was selectively dispensed on top of a printing substrate which was immersed in a non-solvent bath, and the printing paths were controlled by a gantry system. During the printing process, mutual diffusion between the solvent and non-solvent caused polymer solidification based on NIPS, and the interlayer bonding was based on solvent welding. The printed wet structures were removed from the bath and dried in an oven to evaporate the excessive solvent and non-solvent until a dry structure was obtained. Since the NIPS process has been shown in the literature studies on the microstructure tailoring of porous membranes, the effect of solvent/non-solvent pairs, the effect of printing solution concentration and the effect of non-solvent bath temperature on the microstructure and porosity of precipitation printed parts were investigated. As a result, when a weaker and higher viscosity non-solvent was used, spinodal decomposition could be avoided and a denser microstructure could be produced. When a stronger and lower viscosity non-solvent was selected, rapid spinodal decomposition led to a highly porous microstructure. A higher printing solution concentration could result in higher final density, and a higher non-solvent bath temperature could reduce the dimensional contraction after drying. Precipitation printing was also demonstrated on various polymers, including poly(methyl methacrylate) (PMMA), PVDF, multiwalled carbon nanotubes/PVDF nanocomposites, and thermosetting acrylonitrile butadiene rubber (NBR).

After the fundamental studies of the concept, mechanism and microstructure tailoring of the precipitation printing process, precipitation printing was applied to high-performance polymers in Chapter 3. The first example was based on PSU, which is an amorphous thermoplastic with a glass transition temperature (T_g) of about 185 °C. By using cast solution phase inversion time study, wet spinning and solvent welding performance test in a non-solvent bath, two ternary systems were selected for dense PSU and porous PSU precipitation printing. The printed dense PSU exhibited excellent mechanical properties (2.47 GPa Young's modulus and 70.6 MPa tensile strength) in both in-plane and layer stacking directions, which outperform the commercially available PSU produced by material extrusion especially in the layer stacking direction. On the other hand, the printed porous PSU had only 34% density relative to the original PSU pellets, and their mechanical properties were highly anisotropic due to the fast precipitation rate and weak

interlayer bonding. Both printed dense and porous PSU had a T_g around 200 °C and a decomposition temperature (T_d) of about 500 °C in nitrogen, indicating the high thermal stability of the raw material was preserved after printing. The second example was para-aramid, also known as its trade name Kevlar®. To date, Kevlar® has been used as fibers, fabrics or in composites for structural or ballistic applications, which could not be processed through existing AM processes. In the second half of Chapter 3, AM of all-aramid 3D structures was achieved for the first time through simultaneous precipitation printing and protonation of aramid nanofiber (ANF) colloid (printing ink). The ANF printing ink was prepared through a deprotonation and dissolution process of Kevlar® fabric using a potassium hydroxide (KOH)/dimethyl sulfoxide (DMSO)/water system. By precipitation printing the ANF printing ink in a propylene glycol (PG) bath, wet ANF structures could be obtained, which were further washed and dried to induce ANF self-assembly and form all-aramid structures. Although dimensional contraction of more than 50% was observed during the self-assembly process, the contraction ratio was predictable and could provide guidance for producing dry structures with expected dimensions by designing larger wet ANF structures. The printed all-aramid material had unprecedented mechanical and thermal properties including a Young's modulus of 7.2 GPa, a tensile strength of 146 MPa and a service temperature more than 400 °C, which outperforms all existing unfilled high-performance polymers produced by AM.

As for PVDF, NIPS process of PVDF solution in water coagulation bath has already been proved as an effective approach to promote it β phase in porous membranes [132,245]. In Chapter 4, the phase composition of the precipitation printed PVDF using the PVDF/*N,N*-dimethylformamide (DMF)/water system was characterized. According to Fourier-transform infrared spectroscopy (FTIR), X-ray diffraction (XRD) and differential scanning calorimetry (DSC) analysis, precipitation printed PVDF showed dominant β phase with a small portion of γ phase, distinct from the solvent cast (at 180 °C) PVDF film that was mostly α phase. The mechanism for β phase formation during precipitation printing was explained by the hydrogen bonding between PVDF and water, which promotes the all-trans conformation at the PVDF solution and water interface. The β phase PVDF could be preserved after hot pressing at both 80 °C and 140 °C, and the density and dielectric constant of PVDF could also be mostly recovered after hot pressing. After electric poling, precipitation printed porous PVDF had highest d_{33} and d_{31} of −0.99 pC·N^{-1} and 1.08 pC·N^{-1}, respectively, while precipitation printed then hot pressed PVDF had highest d_{33} and d_{31} of −18.09 pC·N^{-1} and 8.69 pC·N^{-1}, respectively. The precipitation printed

PVDF was finally demonstrated as stretching and compression mode piezoelectric energy harvesters, and also strain sensors for vibration sensing in 3D printed artificial feathers.

Based on the dominant β phase PVDF formed by precipitation printing in Chapter 4, precipitation printing was then applied to fabricate stretchable PVDF/NBR polymer blends as piezoelectric sensors. By dissolving PVDF and unvulcanized NBR together in DMF and precipitation printing the mixture in a water bath, porous PVDF/NBR blends were produced could be subsequently hot pressed to induced densification and vulcanization. PVDF phase characterization results showed that β phase was still dominant in all PVDF/NBR blends. Moreover, a unique polymer blend morphology of submicron level phase separation was discovered in precipitation printed then hot pressed PVDF/NBR blends, distinct from the blend morphology of solvent cast PVDF/NBR blends. In the case of 20PVDF80NBR (20 wt% PVDF and 80 wt% NBR), its Young's modulus was only 16.2 MPa and its elongation at break was up to 544%, indicating its high stretchability. After electric poling and adding a stretchable electrode material, 20PVDF80NBR was demonstrated as stretching mode piezoelectric strain sensors that have an operating range up to 70% strain with strain rate and pre-stretch strain independent dynamic sensing performance. In addition, 40PVDF60NBR and 20PVDF80NBR were also demonstrated as compression mode piezoelectric force sensors that have loading rate and pre-stretch strain independent sensing performance. Therefore, precipitation printed then hot pressed PVDF/NBR was shown to be a promising intrinsically stretchable piezoelectric material for strain and stress sensing.

6.2 Contributions

The main contribution of this dissertation is the development of precipitation printing as a novel polymer AM process, which provides a new concept and a solution to fill a gap in AM of high-performance and multifunctional polymers. By using solvent power to dissolve polymers and using NIPS mechanism for polymer solidification, precipitation printing can avoid the challenges arising from the thermal energy-based AM processes such as material extrusion and powder bed fusion. Therefore, precipitation printing can provide a new solution for AM of specialty polymers with high thermal and mechanical properties, and allow for unique microstructure and porosity tailoring of the printed parts towards different applications.

The investigation of the mechanisms and process control of precipitation printing in this dissertation can provide a comprehensive guide for future researchers when using precipitation printing for diverse materials. Specifically, the polymer solidification mechanism in precipitation printing is based on NIPS of the polymer/solvent/non-solvent ternary system, which can be illustrated using ternary phase diagrams. The interlayer bonding mechanism in precipitation printing is based on solvent welding, but the competition between solvent welding to the previous layer and solvent diffusion into the non-solvent also needs to be considered in precipitation printing. The study of the effects of solvent/non-solvent pairs, printing solution concentration and non-solvent bath temperature on microstructure and porosity tailoring presents a general guideline for ternary system and printing parameter selection to produce either dense or porous desired microstructure. More importantly, this dissertation shows that cast solution phase inversion study, wet spinning and solvent welding performance test in a non-solvent bath should be carried out as preliminary studies to select the optimal ternary system and printing parameters prior to the precipitation printing of a new material. By following this systematic selection process, precipitation printing can be applied to more diverse materials in the future.

As for the application in AM of high-performance polymers, precipitation printing provides two significant technological advancements. First, as shown in the PSU case, by selecting a slow precipitation rate ternary system with high boiling point solvent and non-solvent, high-performance thermoplastic parts fabricated by precipitation printing can have outstanding mechanical properties comparable to the raw material properties, exceeding the quality of printed parts produced by material extrusion. Second, precipitation printing opens a new research area of AM of ultrahigh-performance polymers like aramid that have never been processed through neither conventional injection molding nor AM processes to form 3D structures before. This dissertation is the first demonstration of using a novel AM process to produce all-aramid 3D structures, which also exhibit unprecedented mechanical and thermal properties. Thus, precipitation printing can become a promising tool to explore and extend the limit of ultrahigh-performance polymeric 3D structures.

In addition, precipitation printing provides a brand-new approach to fabricate piezoelectric β phase PVDF through AM. Unlike existing AM processes for PVDF β phase promotion using in situ electric poling during material extrusion or solvent cast 3D printing that still produce substantial amount of α phase PVDF, precipitation printing allows the production of β phase

dominant PVDF with a portion of γ phase and negligible amount of α phase. Thus, after adding electrodes and electric poling, precipitation printed high β phase but porous PVDF 3D structures can be used to fabricate piezoelectric sensors with complex 3D shapes, which is challenging for all other existing fabrication processes. Moreover, after hot pressing and electric poling, 2D PVDF films with designed planar shapes have outstanding transversely isotropic piezoelectric properties comparable to the biaxially stretched PVDF films in the literature [135,136,251], but do not require a stretching process that changes the film geometry. In a similar manner, stretchable PVDF/NBR piezoelectric polymer blend produced by precipitation printing also showcases a novel category of intrinsically stretchable piezoelectric material. The mechanism of precipitation printing allows the formation of a highly mixed PVDF/NBR blend morphology with submicron level phase separation, which is ideal for highly stretchable piezoelectric sensors to improve stress-transfer efficiency between the elastomer phase and piezoelectric phase. Therefore, precipitation printing paves the way for producing multidimensional piezoelectric PVDF-based devices in a scalable and material efficient approach.

In summary, precipitation printing offers a new concept in AM research and industrial manufacturing process to produce structural parts made of high-performance polymers and functional devices made of piezoelectric polymers, which can be beneficial for aerospace, automotive, electronics and biomedical industries.

6.3 Recommendation for future work

The concept and fundamental features of precipitation printing, as well as its application in several representative high-performance and piezoelectric polymers were proposed, studied, and demonstrated in this dissertation. Since the research on the topic of precipitation printing is still at a preliminary stage, substantial future research topics can be related to or based on this dissertation. In this section, the recommendation for future work is divided into three main categories: process characterization, process improvements and application in diverse materials.

6.3.1 Process characterization

More characterization of the precipitation printing process and the printed material properties should be studied in the future to have a deeper understanding of this process. For example, as shown in Chapter 2 that precipitation printing enables microstructure and porosity tailoring of the printed parts, the shape, orientation and size of the pores can be studied. The

correlation between the printing parameters and the pore size need to be further characterized for different materials, which can be a guide to produce microporous 3D structures with tailored pore distribution for desired anisotropic properties. On the other hand, to understand the limit of precipitation printing in fabricating complex geometries, the ability of printing overhang structures without support using different solvent/non-solvent pairs and printing parameters can be studied. Moreover, the effect of solvent contamination in the non-solvent, or the effect of using a recycled non-solvent on the microstructure and mechanical properties of the printed parts can be investigated to determine the recyclability of the non-solvent with the goal of reducing material cost.

6.3.2 Process improvements

Currently, the precipitation printing setup in this dissertation is limited to one single material printing at a time, with only one nozzle size for a fixed printing resolution throughout the printing process. Multi-material precipitation printing is one of the future improvements that can be made by modifying the printer setup to accommodate for dual or multiple syringes independently controlled by pressure controllers, similar to the dual-head material extrusion 3D printers [279,280]. By developing a precipitation printer with multiple dispensing syringes, either multi-material printing or single-material printing with different nozzle sizes can be achieved to produce more complex 3D structures. One specific application of multi-material precipitation printing is to fabricate piezoelectric PVDF devices with conductive electrode materials in a single process. A metal nanowires/PVDF nanocomposite material can be developed as an electrode material for precipitation printing, which can bond to the piezoelectric PVDF layer by solvent welding. The incorporation of dual-material printing in PVDF devices can allow the design of 3D piezoelectric sensors with customized electrode patterns, such as curved sensing surface and multi-dimensional stress sensing components. Thus, 3D piezoelectric sensors or sensor arrays can be efficiently fabricated in two steps: precipitation printing and subsequent electric poling using the printed electrodes.

In addition, the studies of precipitation printing in this dissertation are all based on polar non-solvents. In the future, nonpolar non-solvents like oils can be attempted to fabricate nonpolar or low polarity polymers such as polypropylene (PP) and polystyrene (PS) through precipitation printing. Moreover, by using a nonpolar non-solvent bath, electric field can be applied between

the nozzle and the printing substrate, to develop an electric field-assisted precipitation printing setup. This proposed process can potentially enable in situ electric poling of a piezoceramic filled nanocomposite material during precipitation printing. The use of a nonpolar non-solvent bath can also allow for a higher dielectric breakdown strength between the nozzle and the printing substrate than the existing material extrusion process with in-situ electric poling which is operated in air. This electric field-assisted precipitation printing provides a new concept of one-step fabrication of piezoelectric nanocomposites in the future.

6.3.3 Application in diverse materials

The research of precipitation printing is still at an early stage, and only several types of engineering and piezoelectric polymers are demonstrated in this dissertation. In the future, precipitation printing of other high-performance polymers such as polyamide imide (PAI) and polyetherimide (PEI), nonpolar polymers such as PP and PS, and other elastomers can be tested and characterized. Furthermore, multifunctional nanocomposites like conductive nanocomposites using a polymer matrix can be developed for precipitation printing of multifunctional devices.

Another future application of precipitation printing is in AM of metals and ceramics using highly loaded metal or ceramic particles dispersed in a polymer solution. By precipitation printing the highly loaded printing ink in a non-solvent bath, the solidified polymer can act as a binder for the metal or ceramic particles and provide structure stability for the printed parts. After the printing process is completed, the printed green part can be heat treated in a high-temperature furnace to remove the polymer binder and sinter the metal or ceramic particles together, similar to the post-processing methods used in the extrusion-based metal or ceramic AM processes reported in the literature [64,67]. Therefore, precipitation printing has the potential to be expanded to diverse materials, including polymers, polymer nanocomposites, polymer blends, metals, ceramics and hybrid materials.

Bibliography

[1] I. Gibson, D. Rosen, B. Stucker, Additive Manufacturing Technologies: 3D Printing, Rapid Prototyping, and Direct Digital Manufacturing, 2nd ed., Springer-Verlag, New York, 2015. https://doi.org/10.1007/978-1-4939-2113-3.

[2] D. Bourell, J.P. Kruth, M. Leu, G. Levy, D. Rosen, A.M. Beese, A. Clare, Materials for additive manufacturing, CIRP Annals 66 (2017) 659–681. https://doi.org/10.1016/j.cirp.2017.05.009.

[3] S.C. Ligon, R. Liska, J. Stampfl, M. Gurr, R. Mülhaupt, Polymers for 3D Printing and Customized Additive Manufacturing, Chem. Rev. 117 (2017) 10212–10290. https://doi.org/10.1021/acs.chemrev.7b00074.

[4] J.C. Vasco, Chapter 16 - Additive manufacturing for the automotive industry, in: J. Pou, A. Riveiro, J.P. Davim (Eds.), Additive Manufacturing, Elsevier, 2021: pp. 505–530. https://doi.org/10.1016/B978-0-12-818411-0.00010-0.

[5] M. Salmi, Additive Manufacturing Processes in Medical Applications, Materials 14 (2021) 191. https://doi.org/10.3390/ma14010191.

[6] C. Scott, Wohlers Report 2023 Unveils Continued Double-Digit Growth, Wohlers Associates (2023). https://wohlersassociates.com/news/wohlers-report-2023-unveils-continued-double-digit-growth/ (accessed December 7, 2023).

[7] S.-Z. Guo, F. Gosselin, N. Guerin, A.-M. Lanouette, M.-C. Heuzey, D. Therriault, Solvent-Cast Three-Dimensional Printing of Multifunctional Microsystems, Small 9 (2013) 4118–4122. https://doi.org/10.1002/smll.201300975.

[8] Z. Miao, J. Seo, M.A. Hickner, Solvent-cast 3D printing of polysulfone and polyaniline composites, Polymer 152 (2018) 18–24. https://doi.org/10.1016/j.polymer.2018.05.055.

[9] J.A. Lewis, Direct Ink Writing of 3D Functional Materials, Advanced Functional Materials 16 (2006) 2193–2204. https://doi.org/10.1002/adfm.200600434.

[10] F. Kim, S.E. Yang, H. Ju, S. Choo, J. Lee, G. Kim, S. Jung, S. Kim, C. Cha, K.T. Kim, S. Ahn, H.G. Chae, J.S. Son, Direct ink writing of three-dimensional thermoelectric microarchitectures, Nat Electron 4 (2021) 579–587. https://doi.org/10.1038/s41928-021-00622-9.

[11] G.R. Guillen, Y. Pan, M. Li, E.M.V. Hoek, Preparation and Characterization of Membranes Formed by Nonsolvent Induced Phase Separation: A Review, Ind. Eng. Chem. Res. 50 (2011) 3798–3817. https://doi.org/10.1021/ie101928r.

[12] C. Kahrs, T. Gühlstorf, J. Schwellenbach, Influences of different preparation variables on polymeric membrane formation via nonsolvent induced phase separation, Journal of Applied Polymer Science 137 (2020) 48852. https://doi.org/10.1002/app.48852.

[13] G.D. Goh, Y.L. Yap, H.K.J. Tan, S.L. Sing, G.L. Goh, W.Y. Yeong, Process–Structure–Properties in Polymer Additive Manufacturing via Material Extrusion: A Review, Critical Reviews in Solid State and Materials Sciences 45 (2020) 113–133. https://doi.org/10.1080/10408436.2018.1549977.

[14] B.N. Turner, S.A. Gold, A review of melt extrusion additive manufacturing processes: II. Materials, dimensional accuracy, and surface roughness, Rapid Prototyping Journal 21 (2015) 250–261. https://doi.org/10.1108/RPJ-02-2013-0017.
[15] R.B. Kristiawan, F. Imaduddin, D. Ariawan, Ubaidillah, Z. Arifin, A review on the fused deposition modeling (FDM) 3D printing: Filament processing, materials, and printing parameters, Open Engineering 11 (2021) 639–649. https://doi.org/10.1515/eng-2021-0063.
[16] W. Zhong, F. Li, Z. Zhang, L. Song, Z. Li, Short fiber reinforced composites for fused deposition modeling, Materials Science and Engineering: A 301 (2001) 125–130. https://doi.org/10.1016/S0921-5093(00)01810-4.
[17] F. Ning, W. Cong, J. Qiu, J. Wei, S. Wang, Additive manufacturing of carbon fiber reinforced thermoplastic composites using fused deposition modeling, Composites Part B: Engineering 80 (2015) 369–378. https://doi.org/10.1016/j.compositesb.2015.06.013.
[18] A.N. Dickson, J.N. Barry, K.A. McDonnell, D.P. Dowling, Fabrication of continuous carbon, glass and Kevlar fibre reinforced polymer composites using additive manufacturing, Additive Manufacturing 16 (2017) 146–152. https://doi.org/10.1016/j.addma.2017.06.004.
[19] V. Tambrallimath, R. Keshavamurthy, S. D, P.G. Koppad, G.S.P. Kumar, Thermal behavior of PC-ABS based graphene filled polymer nanocomposite synthesized by FDM process, Composites Communications 15 (2019) 129–134. https://doi.org/10.1016/j.coco.2019.07.009.
[20] M. Nikzad, S.H. Masood, I. Sbarski, Thermo-mechanical properties of a highly filled polymeric composites for Fused Deposition Modeling, Materials & Design 32 (2011) 3448–3456. https://doi.org/10.1016/j.matdes.2011.01.056.
[21] K.M. Rahman, T. Letcher, R. Reese, Mechanical Properties of Additively Manufactured PEEK Components Using Fused Filament Fabrication, in: American Society of Mechanical Engineers Digital Collection, 2016. https://doi.org/10.1115/IMECE2015-52209.
[22] K.C. Chuang, J.E. Grady, R.D. Draper, E.-S.E. Shin, C. Patterson, T.D. Santelle, Additive Manufacturing and Characterization of Ultem Polymers and Composites, in: Dallas, TX, 2015. https://ntrs.nasa.gov/citations/20160001352 (accessed February 23, 2023).
[23] E.R. Fitzharris, I. Watt, D.W. Rosen, M.L. Shofner, Interlayer bonding improvement of material extrusion parts with polyphenylene sulfide using the Taguchi method, Additive Manufacturing 24 (2018) 287–297. https://doi.org/10.1016/j.addma.2018.10.003.
[24] S. Kaur, D.P. Singh, Effect of annealing temperature on dielectric behavior of PVDF thick films, AIP Conference Proceedings 1832 (2017) 120003. https://doi.org/10.1063/1.4980688.
[25] K. Singh, Experimental study to prevent the warping of 3D models in fused deposition modeling, Int J Plast Technol 22 (2018) 177–184. https://doi.org/10.1007/s12588-018-9206-y.
[26] J. Han, J. Tong, X. Tian, L. Xia, D. Ma, Thermal Simulation and Warping Deformation Experimental Study of PEEK in Material Extrusion, Macromolecular Theory and Simulations 30 (2021) 2000055. https://doi.org/10.1002/mats.202000055.
[27] M.S. Alsoufi, A.E. Elsayed, Warping Deformation of Desktop 3D Printed Parts Manufactured by Open Source Fused Deposition Modeling (FDM) System, Int J Mech & Mechatro Eng 17 (2017) 11.
[28] S. Ahn, M. Montero, D. Odell, S. Roundy, P.K. Wright, Anisotropic material properties of fused deposition modeling ABS, Rapid Prototyping Journal 8 (2002) 248–257. https://doi.org/10.1108/13552540210441166.

[29] N.S. Hmeidat, R.C. Pack, S.J. Talley, R.B. Moore, B.G. Compton, Mechanical anisotropy in polymer composites produced by material extrusion additive manufacturing, Additive Manufacturing 34 (2020) 101385. https://doi.org/10.1016/j.addma.2020.101385.
[30] S.J. Park, S.J. Park, Y. Son, I.H. Ahn, Reducing anisotropy of a part fabricated by material extrusion via warm isostatic pressure (WIP) process, Additive Manufacturing 55 (2022) 102841. https://doi.org/10.1016/j.addma.2022.102841.
[31] C. Duty, J. Failla, S. Kim, T. Smith, J. Lindahl, V. Kunc, Z-Pinning approach for 3D printing mechanically isotropic materials, Additive Manufacturing 27 (2019) 175–184. https://doi.org/10.1016/j.addma.2019.03.007.
[32] P. Kim, T. Smith, J. Failla, J. Lindahl, V. Kunc, C. Duty, Parametric Analysis on Vertical Pins for Strengthening Extrusion-Based Printed Parts, in: Long Beach, CA, 2018: p. 1269. https://www.osti.gov/biblio/1474874 (accessed December 12, 2023).
[33] I. Gibson, D. Rosen, B. Stucker, Vat Photopolymerization Processes, in: I. Gibson, D. Rosen, B. Stucker (Eds.), Additive Manufacturing Technologies: 3D Printing, Rapid Prototyping, and Direct Digital Manufacturing, Springer, New York, NY, 2015: pp. 63–106. https://doi.org/10.1007/978-1-4939-2113-3_4.
[34] F. Zhang, L. Zhu, Z. Li, S. Wang, J. Shi, W. Tang, N. Li, J. Yang, The recent development of vat photopolymerization: A review, Additive Manufacturing 48 (2021) 102423. https://doi.org/10.1016/j.addma.2021.102423.
[35] J. Zhang, Q. Hu, S. Wang, J. Tao, M. Gou, Digital Light Processing Based Three-dimensional Printing for Medical Applications, International Journal of Bioprinting 6 (2019) 242. https://doi.org/10.18063/ijb.v6i1.242.
[36] Z. Zhao, X. Tian, X. Song, Engineering materials with light: recent progress in digital light processing based 3D printing, Journal of Materials Chemistry C 8 (2020) 13896–13917. https://doi.org/10.1039/D0TC03548C.
[37] J.R. Tumbleston, D. Shirvanyants, N. Ermoshkin, R. Janusziewicz, A.R. Johnson, D. Kelly, K. Chen, R. Pinschmidt, J.P. Rolland, A. Ermoshkin, E.T. Samulski, J.M. DeSimone, Continuous liquid interface production of 3D objects, Science 347 (2015) 1349–1352. https://doi.org/10.1126/science.aaa2397.
[38] R. Janusziewicz, J.R. Tumbleston, A.L. Quintanilla, S.J. Mecham, J.M. DeSimone, Layerless fabrication with continuous liquid interface production, Proceedings of the National Academy of Sciences 113 (2016) 11703–11708. https://doi.org/10.1073/pnas.1605271113.
[39] X. Zhang, X.N. Jiang, C. Sun, Micro-stereolithography of polymeric and ceramic microstructures, Sensors and Actuators A: Physical 77 (1999) 149–156. https://doi.org/10.1016/S0924-4247(99)00189-2.
[40] Q. Ge, Z. Li, Z. Wang, K. Kowsari, W. Zhang, X. He, J. Zhou, N.X. Fang, Projection micro stereolithography based 3D printing and its applications, Int. J. Extrem. Manuf. 2 (2020) 022004. https://doi.org/10.1088/2631-7990/ab8d9a.
[41] K.-S. Lee, D.-Y. Yang, S.H. Park, R.H. Kim, Recent developments in the use of two-photon polymerization in precise 2D and 3D microfabrications, Polymers for Advanced Technologies 17 (2006) 72–82. https://doi.org/10.1002/pat.664.
[42] X. Zhou, Y. Hou, J. Lin, A review on the processing accuracy of two-photon polymerization, AIP Advances 5 (2015) 030701. https://doi.org/10.1063/1.4916886.

[43] D.L. Naik, R. Kiran, On anisotropy, strain rate and size effects in vat photopolymerization based specimens, Additive Manufacturing 23 (2018) 181–196. https://doi.org/10.1016/j.addma.2018.08.021.
[44] J.V. Crivello, E. Reichmanis, Photopolymer Materials and Processes for Advanced Technologies, Chem. Mater. 26 (2014) 533–548. https://doi.org/10.1021/cm402262g.
[45] X. Xu, A. Awad, P. Robles-Martinez, S. Gaisford, A. Goyanes, A.W. Basit, Vat photopolymerization 3D printing for advanced drug delivery and medical device applications, Journal of Controlled Release 329 (2021) 743–757. https://doi.org/10.1016/j.jconrel.2020.10.008.
[46] W. Zhao, Z. Wang, J. Zhang, X. Wang, Y. Xu, N. Ding, Z. Peng, Vat Photopolymerization 3D Printing of Advanced Soft Sensors and Actuators: From Architecture to Function, Advanced Materials Technologies 6 (2021) 2001218. https://doi.org/10.1002/admt.202001218.
[47] M. Sireesha, J. Lee, A.S.K. Kiran, V. Jagadeesh Babu, B.B. T. Kee, S. Ramakrishna, A review on additive manufacturing and its way into the oil and gas industry, RSC Advances 8 (2018) 22460–22468. https://doi.org/10.1039/C8RA03194K.
[48] A. Elkaseer, K.J. Chen, J.C. Janhsen, O. Refle, V. Hagenmeyer, S.G. Scholz, Material jetting for advanced applications: A state-of-the-art review, gaps and future directions, Additive Manufacturing 60 (2022) 103270. https://doi.org/10.1016/j.addma.2022.103270.
[49] O. Gülcan, K. Günaydın, A. Tamer, The State of the Art of Material Jetting—A Critical Review, Polymers 13 (2021) 2829. https://doi.org/10.3390/polym13162829.
[50] M. Sugavaneswaran, G. Arumaikkannu, Analytical and experimental investigation on elastic modulus of reinforced additive manufactured structure, Materials & Design (1980-2015) 66 (2015) 29–36. https://doi.org/10.1016/j.matdes.2014.10.029.
[51] Y.L. Yap, W.Y. Yeong, Shape recovery effect of 3D printed polymeric honeycomb, Virtual and Physical Prototyping 10 (2015) 91–99. https://doi.org/10.1080/17452759.2015.1060350.
[52] M.J. Mirzaali, M.E. Edens, A.H. de la Nava, S. Janbaz, P. Vena, E.L. Doubrovski, A.A. Zadpoor, Length-scale dependency of biomimetic hard-soft composites, Sci Rep 8 (2018) 12052. https://doi.org/10.1038/s41598-018-30012-9.
[53] A. Mostafaei, A.M. Elliott, J.E. Barnes, F. Li, W. Tan, C.L. Cramer, P. Nandwana, M. Chmielus, Binder jet 3D printing—Process parameters, materials, properties, modeling, and challenges, Progress in Materials Science 119 (2021) 100707. https://doi.org/10.1016/j.pmatsci.2020.100707.
[54] M. Ziaee, N.B. Crane, Binder jetting: A review of process, materials, and methods, Additive Manufacturing 28 (2019) 781–801. https://doi.org/10.1016/j.addma.2019.05.031.
[55] C. Polzin, S. Spath, H. Seitz, Characterization and evaluation of a PMMA-based 3D printing process, Rapid Prototyping Journal 19 (2013) 37–43. https://doi.org/10.1108/13552541311292718.
[56] S.J. Park, H.G. Ju, S.J. Park, S. Hong, Y. Son, I.H. Ahn, New possibilities in polymer binder jetting additive manufacturing via infiltration and warm isostatic pressing, Materials & Design 231 (2023) 112045. https://doi.org/10.1016/j.matdes.2023.112045.
[57] S. Riechmann, O. Wunnicke, A. Kwade, The Effect of Binder Loading on the Pore Size of 3D Printed PMMA, Materials 14 (2021) 1190. https://doi.org/10.3390/ma14051190.

[58] A. Yegyan Kumar, Y. Bai, A. Eklund, C.B. Williams, The effects of Hot Isostatic Pressing on parts fabricated by binder jetting additive manufacturing, Additive Manufacturing 24 (2018) 115–124. https://doi.org/10.1016/j.addma.2018.09.021.
[59] T. Dahmen, N.G. Henriksen, K.V. Dahl, A. Lapina, D.B. Pedersen, J.H. Hattel, T.L. Christiansen, M.A.J. Somers, Densification, microstructure, and mechanical properties of heat-treated MAR-M247 fabricated by Binder Jetting, Additive Manufacturing 39 (2021) 101912. https://doi.org/10.1016/j.addma.2021.101912.
[60] S. Sun, M. Brandt, M. Easton, 2 - Powder bed fusion processes: An overview, in: M. Brandt (Ed.), Laser Additive Manufacturing, Woodhead Publishing, 2017: pp. 55–77. https://doi.org/10.1016/B978-0-08-100433-3.00002-6.
[61] R. Singh, A. Gupta, O. Tripathi, S. Srivastava, B. Singh, A. Awasthi, S.K. Rajput, P. Sonia, P. Singhal, K.K. Saxena, Powder bed fusion process in additive manufacturing: An overview, Materials Today: Proceedings 26 (2020) 3058–3070. https://doi.org/10.1016/j.matpr.2020.02.635.
[62] A.T. Sutton, C.S. Kriewall, M.C. Leu, J.W. Newkirk, Powder characterisation techniques and effects of powder characteristics on part properties in powder-bed fusion processes, Virtual and Physical Prototyping 12 (2017) 3–29. https://doi.org/10.1080/17452759.2016.1250605.
[63] W.E. King, A.T. Anderson, R.M. Ferencz, N.E. Hodge, C. Kamath, S.A. Khairallah, A.M. Rubenchik, Laser powder bed fusion additive manufacturing of metals; physics, computational, and materials challenges, Applied Physics Reviews 2 (2015) 041304. https://doi.org/10.1063/1.4937809.
[64] J. Dong, Y. Li, P. Lin, M.A. Leeflang, S. van Asperen, K. Yu, N. Tümer, B. Norder, A.A. Zadpoor, J. Zhou, Solvent-cast 3D printing of magnesium scaffolds, Acta Biomaterialia 114 (2020) 497–514. https://doi.org/10.1016/j.actbio.2020.08.002.
[65] S. Bodkhe, G. Turcot, F.P. Gosselin, D. Therriault, One-Step Solvent Evaporation-Assisted 3D Printing of Piezoelectric PVDF Nanocomposite Structures, ACS Appl. Mater. Interfaces 9 (2017) 20833–20842. https://doi.org/10.1021/acsami.7b04095.
[66] J.W. Tolbert, D.E. Hammerstone, N. Yuchimiuk, J.E. Seppala, L.W. Chow, Solvent-Cast 3D Printing of Biodegradable Polymer Scaffolds, Macromolecular Materials and Engineering 306 (2021) 2100442. https://doi.org/10.1002/mame.202100442.
[67] C. Xu, A. Bouchemit, G. L'Espérance, L.L. Lebel, D. Therriault, Solvent-cast based metal 3D printing and secondary metallic infiltration, Journal of Materials Chemistry C 5 (2017) 10448–10455. https://doi.org/10.1039/C7TC02884A.
[68] J. Cesarano, S. Grieco, Robocasting: A New Technique for the Freeform Fabrication of Near-Net-Shape Ceramics, Materials Technology 12 (1997) 98–100. https://doi.org/10.1080/10667857.1997.11752736.
[69] M. a. S.R. Saadi, A. Maguire, N.T. Pottackal, M.S.H. Thakur, M.Md. Ikram, A.J. Hart, P.M. Ajayan, M.M. Rahman, Direct Ink Writing: A 3D Printing Technology for Diverse Materials, Advanced Materials 34 (2022) 2108855. https://doi.org/10.1002/adma.202108855.
[70] A. M'Barki, L. Bocquet, A. Stevenson, Linking Rheology and Printability for Dense and Strong Ceramics by Direct Ink Writing, Sci Rep 7 (2017). https://doi.org/10.1038/s41598-017-06115-0.
[71] S. Tagliaferri, A. Panagiotopoulos, C. Mattevi, Direct ink writing of energy materials, Materials Advances 2 (2021) 540–563. https://doi.org/10.1039/D0MA00753F.

[72] A. Maguire, N. Pottackal, M.A.S.R. Saadi, M.M. Rahman, P.M. Ajayan, Additive manufacturing of polymer-based structures by extrusion technologies, Oxford Open Materials Science 1 (2021) itaa004. https://doi.org/10.1093/oxfmat/itaa004.
[73] L. Wei, J. Li, S. Zhang, B. Li, Y. Liu, F. Wang, S. Dong, Fabrication of SiOC ceramic with cellular structure via UV-Assisted direct ink writing, Ceramics International 46 (2020) 3637–3643. https://doi.org/10.1016/j.ceramint.2019.10.083.
[74] K. Chen, X. Kuang, V. Li, G. Kang, H. Jerry Qi, Fabrication of tough epoxy with shape memory effects by UV-assisted direct-ink write printing, Soft Matter 14 (2018) 1879–1886. https://doi.org/10.1039/C7SM02362F.
[75] M. Invernizzi, G. Natale, M. Levi, S. Turri, G. Griffini, UV-Assisted 3D Printing of Glass and Carbon Fiber-Reinforced Dual-Cure Polymer Composites, Materials 9 (2016) 583. https://doi.org/10.3390/ma9070583.
[76] L.L. Lebel, B. Aissa, M.A.E. Khakani, D. Therriault, Ultraviolet-Assisted Direct-Write Fabrication of Carbon Nanotube/Polymer Nanocomposite Microcoils, Advanced Materials 22 (2010) 592–596. https://doi.org/10.1002/adma.200902192.
[77] T. Wu, P. Jiang, X. Zhang, Y. Guo, Z. Ji, X. Jia, X. Wang, F. Zhou, W. Liu, Additively manufacturing high-performance bismaleimide architectures with ultraviolet-assisted direct ink writing, Materials & Design 180 (2019) 107947. https://doi.org/10.1016/j.matdes.2019.107947.
[78] R. Tu, H.A. Sodano, Additive manufacturing of high-performance vinyl ester resin via direct ink writing with UV-thermal dual curing, Additive Manufacturing 46 (2021) 102180. https://doi.org/10.1016/j.addma.2021.102180.
[79] A. Sarmah, S.K. Desai, A.G. Crowley, G.C. Zolton, G.B. Tezel, E.M. Harkin, T.Q. Tran, K. Arole, M.J. Green, Additive manufacturing of nanotube-loaded thermosets via direct ink writing and radio-frequency heating and curing, Carbon 200 (2022) 307–316. https://doi.org/10.1016/j.carbon.2022.08.063.
[80] J.E. Aw, X. Zhang, A.Z. Nelson, L.M. Dean, M. Yourdkhani, R.H. Ewoldt, P.H. Geubelle, N.R. Sottos, Self-Regulative Direct Ink Writing of Frontally Polymerizing Thermoset Polymers, Advanced Materials Technologies 7 (2022) 2200230. https://doi.org/10.1002/admt.202200230.
[81] Y. Guo, Y. Liu, J. Liu, J. Zhao, H. Zhang, Z. Zhang, Shape memory epoxy composites with high mechanical performance manufactured by multi-material direct ink writing, Composites Part A: Applied Science and Manufacturing 135 (2020) 105903. https://doi.org/10.1016/j.compositesa.2020.105903.
[82] L. del-Mazo-Barbara, M.-P. Ginebra, Rheological characterisation of ceramic inks for 3D direct ink writing: A review, Journal of the European Ceramic Society 41 (2021) 18–33. https://doi.org/10.1016/j.jeurceramsoc.2021.08.031.
[83] A. Schwab, R. Levato, M. D'Este, S. Piluso, D. Eglin, J. Malda, Printability and Shape Fidelity of Bioinks in 3D Bioprinting, Chem. Rev. 120 (2020) 11028–11055. https://doi.org/10.1021/acs.chemrev.0c00084.
[84] V. Mittal, High Performance Polymers: An Overview, in: High Performance Polymers and Engineering Plastics, John Wiley & Sons, Ltd, 2011: pp. 1–20. https://doi.org/10.1002/9781118171950.ch1.
[85] C.W. Weyhrich, T.E. Long, Additive manufacturing of high-performance engineering polymers: present and future, Polymer International 71 (2022) 532–536. https://doi.org/10.1002/pi.6343.

[86] M.J. El-Hibri, S.A. Weinberg, Polysulfones, in: Encyclopedia of Polymer Science and Technology, John Wiley & Sons, Ltd, 2001. https://doi.org/10.1002/0471440264.pst291.
[87] R.O. Johnson, H.S. Burlhis, Polyetherimide: A new high-performance thermoplastic resin, Journal of Polymer Science: Polymer Symposia 70 (1983) 129–143. https://doi.org/10.1002/polc.5070700111.
[88] S. Diaham, M.-L. Locatelli, Dielectric properties of polyamide-imide, J. Phys. D: Appl. Phys. 46 (2013) 185302. https://doi.org/10.1088/0022-3727/46/18/185302.
[89] W. Ye, G. Lin, W. Wu, P. Geng, X. Hu, Z. Gao, J. Zhao, Separated 3D printing of continuous carbon fiber reinforced thermoplastic polyimide, Composites Part A: Applied Science and Manufacturing 121 (2019) 457–464. https://doi.org/10.1016/j.compositesa.2019.04.002.
[90] M.Y. Keating, High glass transitions of high-performance thermoplastics, Thermochimica Acta 319 (1998) 201–212. https://doi.org/10.1016/S0040-6031(98)00419-5.
[91] A.S. Rahate, K.R. Nemade, S.A. Waghuley, Polyphenylene sulfide (PPS): state of the art and applications, Reviews in Chemical Engineering 29 (2013) 471–489. https://doi.org/10.1515/revce-2012-0021.
[92] P. Chen, H. Wang, J. Su, Y. Tian, S. Wen, B. Su, C. Yang, B. Chen, K. Zhou, C. Yan, Y. Shi, Recent Advances on High-Performance Polyaryletherketone Materials for Additive Manufacturing, Advanced Materials 34 (2022) 2200750. https://doi.org/10.1002/adma.202200750.
[93] J.R. Brown, B.C. Ennis, Thermal Analysis of Nomex® and Kevlar® Fibers, Textile Research Journal 47 (1977) 62–66. https://doi.org/10.1177/004051757704700113.
[94] T. Yamashita, H. Tomitaka, T. Kudo, K. Horie, I. Mita, Degradation of sulfur-containing aromatic polymers: Photodegradation of polyethersulfone and polysulfone, Polymer Degradation and Stability 39 (1993) 47–54. https://doi.org/10.1016/0141-3910(93)90124-2.
[95] W. Wu, Z. Li, G. Lin, J. Ma, Z. Gao, H. Qu, F. Zhang, Additive manufacturing of continuous BF-reinforced PES composite material and mechanical and wear properties evaluation, J Mater Sci 57 (2022) 12903–12915. https://doi.org/10.1007/s10853-022-07425-z.
[96] N. Mys, R. Van de Sande, A. Verberckmoes, L. Cardon, Processing of polysulfone to free flowing powder for part manufacturing through selective laser sintering, AIP Conference Proceedings 1779 (2016) 100002. https://doi.org/10.1063/1.4965570.
[97] C.A. Chatham, T.E. Long, C.B. Williams, Powder bed fusion of poly(phenylene sulfide) at bed temperatures significantly below melting, Additive Manufacturing 28 (2019) 506–516. https://doi.org/10.1016/j.addma.2019.05.025.
[98] A. Das, C.A. Chatham, J.J. Fallon, C.E. Zawaski, E.L. Gilmer, C.B. Williams, M.J. Bortner, Current understanding and challenges in high temperature additive manufacturing of engineering thermoplastic polymers, Additive Manufacturing 34 (2020) 101218. https://doi.org/10.1016/j.addma.2020.101218.
[99] C. Yang, X. Tian, D. Li, Y. Cao, F. Zhao, C. Shi, Influence of thermal processing conditions in 3D printing on the crystallinity and mechanical properties of PEEK material, Journal of Materials Processing Technology 248 (2017) 1–7. https://doi.org/10.1016/j.jmatprotec.2017.04.027.
[100] J.-W. Tseng, C.-Y. Liu, Y.-K. Yen, J. Belkner, T. Bremicker, B.H. Liu, T.-J. Sun, A.-B. Wang, Screw extrusion-based additive manufacturing of PEEK, Materials & Design 140 (2018) 209–221. https://doi.org/10.1016/j.matdes.2017.11.032.

[101] S. Berretta, Y. Wang, R. Davies, O.R. Ghita, Polymer viscosity, particle coalescence and mechanical performance in high-temperature laser sintering, J Mater Sci 51 (2016) 4778–4794. https://doi.org/10.1007/s10853-016-9761-6.
[102] N. Yi, R. Davies, A. Chaplin, O. Ghita, Novel backbone modified polyetheretherketone (PEEK) grades for powder bed fusion with enhanced elongation at break, Additive Manufacturing 55 (2022) 102857. https://doi.org/10.1016/j.addma.2022.102857.
[103] J.M. Gardner, G. Sauti, J.-W. Kim, R.J. Cano, R.A. Wincheski, C.J. Stelter, B.W. Grimsley, D.C. Working, E.J. Siochi, 3-D printing of multifunctional carbon nanotube yarn reinforced components, Additive Manufacturing 12 (2016) 38–44. https://doi.org/10.1016/j.addma.2016.06.008.
[104] K.I. Byberg, A.W. Gebisa, H.G. Lemu, Mechanical properties of ULTEM 9085 material processed by fused deposition modeling, Polymer Testing 72 (2018) 335–347. https://doi.org/10.1016/j.polymertesting.2018.10.040.
[105] H. Wu, M. Sulkis, J. Driver, A. Saade-Castillo, A. Thompson, J.H. Koo, Multi-functional ULTEM^{TM}1010 composite filaments for additive manufacturing using Fused Filament Fabrication (FFF), Additive Manufacturing 24 (2018) 298–306. https://doi.org/10.1016/j.addma.2018.10.014.
[106] W. Ye, W. Wu, X. Hu, G. Lin, J. Guo, H. Qu, J. Zhao, 3D printing of carbon nanotubes reinforced thermoplastic polyimide composites with controllable mechanical and electrical performance, Composites Science and Technology 182 (2019) 107671. https://doi.org/10.1016/j.compscitech.2019.05.028.
[107] M. Hegde, V. Meenakshisundaram, N. Chartrain, S. Sekhar, D. Tafti, C.B. Williams, T.E. Long, 3D Printing All-Aromatic Polyimides using Mask-Projection Stereolithography: Processing the Nonprocessable, Advanced Materials 29 (2017) 1701240. https://doi.org/10.1002/adma.201701240.
[108] Y. Guo, J. Xu, C. Yan, Y. Chen, X. Zhang, X. Jia, Y. Liu, X. Wang, F. Zhou, Direct Ink Writing of High Performance Architectured Polyimides with Low Dimensional Shrinkage, Advanced Engineering Materials 21 (2019) 1801314. https://doi.org/10.1002/adem.201801314.
[109] C. Wang, S. Ma, D. Li, J. Zhao, H. Zhou, D. Wang, D. Zhou, T. Gan, D. Wang, C. Liu, C. Qu, C. Chen, 3D Printing of Lightweight Polyimide Honeycombs with the High Specific Strength and Temperature Resistance, ACS Appl. Mater. Interfaces 13 (2021) 15690–15700. https://doi.org/10.1021/acsami.1c01992.
[110] L. Chen, H. Liu, H. Qi, J. Chen, High-electromechanical performance for high-power piezoelectric applications: Fundamental, progress, and perspective, Progress in Materials Science 127 (2022) 100944. https://doi.org/10.1016/j.pmatsci.2022.100944.
[111] M. Smith, S. Kar-Narayan, Piezoelectric polymers: theory, challenges and opportunities, International Materials Reviews 67 (2022) 65–88. https://doi.org/10.1080/09506608.2021.1915935.
[112] E. Fukada, Piezoelectricity as a fundamental property of wood, Wood Science and Technology 2 (1968) 299–307. https://doi.org/10.1007/BF00350276.
[113] E. Fukada, I. Yasuda, Piezoelectric Effects in Collagen, Jpn. J. Appl. Phys. 3 (1964) 117. https://doi.org/10.1143/JJAP.3.117.
[114] S. Anwar, D. Pinkal, W. Zajaczkowski, P. von Tiedemann, H. Sharifi Dehsari, M. Kumar, T. Lenz, U. Kemmer-Jonas, W. Pisula, M. Wagner, R. Graf, H. Frey, K. Asadi, Solution-

processed transparent ferroelectric nylon thin films, Science Advances 5 (2019) eaav3489. https://doi.org/10.1126/sciadv.aav3489.
[115] Y. Takase, J.W. Lee, J.I. Scheinbeim, B.A. Newman, High-temperature characteristics of nylon-11 and nylon-7 piezoelectrics, Macromolecules 24 (1991) 6644–6652. https://doi.org/10.1021/ma00025a014.
[116] S.L. Wu, J.I. Scheinbeim, B.A. Newman, Ferroelectricity and piezoelectricity of nylon 11 films with different draw ratios, Journal of Polymer Science Part B: Polymer Physics 37 (1999) 2737–2746. https://doi.org/10.1002/(SICI)1099-0488(19991001)37:19<2737::AID-POLB3>3.0.CO;2-O.
[117] H. Kawai, The Piezoelectricity of Poly (vinylidene Fluoride), Jpn. J. Appl. Phys. 8 (1969) 975. https://doi.org/10.1143/JJAP.8.975.
[118] A. Vinogradov, F. Holloway, Electro-mechanical properties of the piezoelectric polymer PVDF, Ferroelectrics 226 (1999) 169–181. https://doi.org/10.1080/00150199908230298.
[119] P. Ueberschlag, PVDF piezoelectric polymer, Sensor Review 21 (2001) 118–126. https://doi.org/10.1108/02602280110388315.
[120] E. Giannetti, Semi-crystalline fluorinated polymers, Polymer International 50 (2001) 10–26. https://doi.org/10.1002/1097-0126(200101)50:1<10::AID-PI614>3.0.CO;2-W.
[121] A.J. Lovinger, Ferroelectric Polymers, Science 220 (1983) 1115–1121. https://doi.org/10.1126/science.220.4602.1115.
[122] G.T. Davis, J.E. McKinney, M.G. Broadhurst, S.C. Roth, Electric-field-induced phase changes in poly(vinylidene fluoride), Journal of Applied Physics 49 (1978) 4998–5002. https://doi.org/10.1063/1.324446.
[123] A.J. Lovinger, Annealing of poly(vinylidene fluoride) and formation of a fifth phase, Macromolecules 15 (1982) 40–44. https://doi.org/10.1021/ma00229a008.
[124] A. Salimi, A.A. Yousefi, Analysis Method: FTIR studies of β-phase crystal formation in stretched PVDF films, Polymer Testing 22 (2003) 699–704. https://doi.org/10.1016/S0142-9418(03)00003-5.
[125] R. Gregorio, M. Cestari, Effect of crystallization temperature on the crystalline phase content and morphology of poly(vinylidene fluoride), Journal of Polymer Science Part B: Polymer Physics 32 (1994) 859–870. https://doi.org/10.1002/polb.1994.090320509.
[126] K. Matsushige, K. Nagata, S. Imada, T. Takemura, The II-I crystal transformation of poly(vinylidene fluoride) under tensile and compressional stresses, Polymer 21 (1980) 1391–1397. https://doi.org/10.1016/0032-3861(80)90138-X.
[127] R.P. Vijayakumar, D.V. Khakhar, A. Misra, Studies on α to β phase transformations in mechanically deformed PVDF films, Journal of Applied Polymer Science 117 (2010) 3491–3497. https://doi.org/10.1002/app.32218.
[128] Y. Ye, Y. Jiang, Z. Wu, H. Zeng, Phase Transitions of Poly(vinylidene Fluoride) Under Electric Fields, Integrated Ferroelectrics 80 (2006) 245–251. https://doi.org/10.1080/10584580600659423.
[129] S. Satapathy, S. Pawar, P.K. Gupta, K.B.R. Varma, Effect of annealing on phase transition in poly(vinylidene fluoride) films prepared using polar solvent, Bull Mater Sci 34 (2011) 727. https://doi.org/10.1007/s12034-011-0187-0.
[130] M. Fortunato, D. Cavallini, G. De Bellis, F. Marra, A. Tamburrano, F. Sarto, M.S. Sarto, Phase Inversion in PVDF Films with Enhanced Piezoresponse Through Spin-Coating and Quenching, Polymers 11 (2019) 1096. https://doi.org/10.3390/polym11071096.

[131] V. Khurana, R.R. Kisannagar, S.S. Domala, D. Gupta, In Situ Polarized Ultrathin PVDF Film-Based Flexible Piezoelectric Nanogenerators, ACS Appl. Electron. Mater. 2 (2020) 3409–3417. https://doi.org/10.1021/acsaelm.0c00667.
[132] N. Soin, D. Boyer, K. Prashanthi, S. Sharma, A.A. Narasimulu, J. Luo, T.H. Shah, E. Siores, T. Thundat, Exclusive self-aligned β-phase PVDF films with abnormal piezoelectric coefficient prepared via phase inversion, Chem. Commun. 51 (2015) 8257–8260. https://doi.org/10.1039/C5CC01688F.
[133] M. Tao, F. Liu, B. Ma, L. Xue, Effect of solvent power on PVDF membrane polymorphism during phase inversion, Desalination 316 (2013) 137–145. https://doi.org/10.1016/j.desal.2013.02.005.
[134] J.D. Sherman, J. Elloian, J. Jadwiszczak, K.L. Shepard, On the Temperature Dependence of the Piezoelectric Response of Prepoled Poly(vinylidene fluoride) Films, ACS Appl. Polym. Mater. 2 (2020) 5110–5120. https://doi.org/10.1021/acsapm.0c00902.
[135] R.G. Kepler, R.A. Anderson, Piezoelectricity and pyroelectricity in polyvinylidene fluoride, Journal of Applied Physics 49 (1978) 4490–4494. https://doi.org/10.1063/1.325454.
[136] Y. Huang, G. Rui, Q. Li, E. Allahyarov, R. Li, M. Fukuto, G.-J. Zhong, J.-Z. Xu, Z.-M. Li, P.L. Taylor, L. Zhu, Enhanced piezoelectricity from highly polarizable oriented amorphous fractions in biaxially oriented poly(vinylidene fluoride) with pure β crystals, Nat Commun 12 (2021) 675. https://doi.org/10.1038/s41467-020-20662-7.
[137] J.F. Legrand, Structure and ferroelectric properties of P(VDF-TrFE) copolymers, Ferroelectrics 91 (1989) 303–317. https://doi.org/10.1080/00150198908015747.
[138] Y. Liu, H. Aziguli, B. Zhang, W. Xu, W. Lu, J. Bernholc, Q. Wang, Ferroelectric polymers exhibiting behaviour reminiscent of a morphotropic phase boundary, Nature 562 (2018) 96–100. https://doi.org/10.1038/s41586-018-0550-z.
[139] H. Xu, Z.-Y. Cheng, D. Olson, T. Mai, Q.M. Zhang, G. Kavarnos, Ferroelectric and electromechanical properties of poly(vinylidene-fluoride–trifluoroethylene–chlorotrifluoroethylene) terpolymer, Applied Physics Letters 78 (2001) 2360–2362. https://doi.org/10.1063/1.1358847.
[140] Z. Han, Y. Liu, X. Chen, W. Xu, Q. Wang, Enhanced Piezoelectricity in Poly(vinylidene fluoride-co-trifluoroethylene-co-chlorotrifluoroethylene) Random Terpolymers with Mixed Ferroelectric Phases, Macromolecules 55 (2022) 2703–2713. https://doi.org/10.1021/acs.macromol.1c02302.
[141] C. Lee, J.A. Tarbutton, Electric poling-assisted additive manufacturing process for PVDF polymer-based piezoelectric device applications, Smart Mater. Struct. 23 (2014) 095044. https://doi.org/10.1088/0964-1726/23/9/095044.
[142] D.A. Porter, T.V.T. Hoang, T.A. Berfield, Effects of in-situ poling and process parameters on fused filament fabrication printed PVDF sheet mechanical and electrical properties, Additive Manufacturing 13 (2017) 81–92. https://doi.org/10.1016/j.addma.2016.11.005.
[143] H. Kim, F. Torres, Y. Wu, D. Villagran, Y. Lin, T.-L. Tseng, Integrated 3D printing and corona poling process of PVDF piezoelectric films for pressure sensor application, Smart Mater. Struct. 26 (2017) 085027. https://doi.org/10.1088/1361-665X/aa738e.
[144] J. Fan, N. Deneke, S. Xu, B. Newell, J. Garcia, C. Davis, W. Wu, R.M. Voyles, R.A. Nawrocki, Electric poling-assisted additive manufacturing technique for piezoelectric active poly(vinylidene fluoride) films: Towards fully three-dimensional printed functional materials, Additive Manufacturing 60 (2022) 103248. https://doi.org/10.1016/j.addma.2022.103248.

[145] S. Bodkhe, P.S.M. Rajesh, F.P. Gosselin, D. Therriault, Simultaneous 3D Printing and Poling of PVDF and Its Nanocomposites, ACS Appl. Energy Mater. 1 (2018) 2474–2482. https://doi.org/10.1021/acsaem.7b00337.
[146] R. Han, L. Zheng, G. Li, G. Chen, S. Ma, S. Cai, Y. Li, Self-Poled Poly(vinylidene fluoride)/MXene Piezoelectric Energy Harvester with Boosted Power Generation Ability and the Roles of Crystalline Orientation and Polarized Interfaces, ACS Appl. Mater. Interfaces 13 (2021) 46738–46748. https://doi.org/10.1021/acsami.1c14007.
[147] Y. Xue, T. Yang, Y. Zheng, E. Wang, H. Wang, L. Zhu, Z. Du, X. Hou, K.-C. Chou, The mechanism of a PVDF/CsPbBr3 perovskite composite fiber as a self-polarization piezoelectric nanogenerator with ultra-high output voltage, J. Mater. Chem. A 10 (2022) 21893–21904. https://doi.org/10.1039/D2TA03559F.
[148] H. Pei, Y. Xie, Y. Xiong, Q. Lv, Y. Chen, A novel polarization-free 3D printing strategy for fabrication of poly (Vinylidene fluoride) based nanocomposite piezoelectric energy harvester, Composites Part B: Engineering 225 (2021) 109312. https://doi.org/10.1016/j.compositesb.2021.109312.
[149] X. Liu, Y. Shang, J. Zhang, C. Zhang, Ionic Liquid-Assisted 3D Printing of Self-Polarized β-PVDF for Flexible Piezoelectric Energy Harvesting, ACS Appl. Mater. Interfaces 13 (2021) 14334–14341. https://doi.org/10.1021/acsami.1c03226.
[150] R.I. Haque, R. Vié, M. Germainy, L. Valbin, P. Benaben, X. Boddaert, Inkjet printing of high molecular weight PVDF-TrFE for flexible electronics, Flex. Print. Electron. 1 (2015) 015001. https://doi.org/10.1088/2058-8585/1/1/015001.
[151] A. Spanou, C. Persson, S. Johansson, Fully 3D-printed PVDF-TrFE based piezoelectric devices with PVDF-TrFE-rGO composites as electrodes, Micro and Nano Engineering 19 (2023) 100190. https://doi.org/10.1016/j.mne.2023.100190.
[152] N.A. Shepelin, V.C. Lussini, P.J. Fox, G.W. Dicinoski, A.M. Glushenkov, J.G. Shapter, A.V. Ellis, 3D printing of poly(vinylidene fluoride-trifluoroethylene): a poling-free technique to manufacture flexible and transparent piezoelectric generators, MRS Communications 9 (2019) 159–164. https://doi.org/10.1557/mrc.2019.19.
[153] Z. Zhou, H. Tang, H.A. Sodano, Scalable Synthesis of Morphotropic Phase Boundary Lead Zirconium Titanate Nanowires for Energy Harvesting, Advanced Materials 26 (2014) 7547–7554. https://doi.org/10.1002/adma.201403286.
[154] H.Y. Choi, Y.G. Jeong, Microstructures and piezoelectric performance of eco-friendly composite films based on nanocellulose and barium titanate nanoparticle, Composites Part B: Engineering 168 (2019) 58–65. https://doi.org/10.1016/j.compositesb.2018.12.072.
[155] A. Choudhury, Dielectric and piezoelectric properties of polyetherimide/BaTiO3 nanocomposites, Materials Chemistry and Physics 121 (2010) 280–285. https://doi.org/10.1016/j.matchemphys.2010.01.035.
[156] M.H. Malakooti, F. Julé, H.A. Sodano, Printed Nanocomposite Energy Harvesters with Controlled Alignment of Barium Titanate Nanowires, ACS Appl. Mater. Interfaces 10 (2018) 38359–38367. https://doi.org/10.1021/acsami.8b13643.
[157] D.Y. Hyeon, G.-J. Lee, S.-H. Lee, J.-J. Park, S. Kim, M.-K. Lee, K.-I. Park, High-temperature workable flexible piezoelectric energy harvester comprising thermally stable (K,Na)NbO3-based ceramic and polyimide composites, Composites Part B: Engineering 234 (2022) 109671. https://doi.org/10.1016/j.compositesb.2022.109671.

[158] M. Gao, L. Li, W. Li, H. Zhou, Y. Song, Direct Writing of Patterned, Lead-Free Nanowire Aligned Flexible Piezoelectric Device, Advanced Science 3 (2016) 1600120. https://doi.org/10.1002/advs.201600120.
[159] C. Li, W. Luo, X. Liu, D. Xu, K. He, PMN-PT/PVDF Nanocomposite for High Output Nanogenerator Applications, Nanomaterials 6 (2016) 67. https://doi.org/10.3390/nano6040067.
[160] U. Yaqoob, R.M. Habibur, M. Sheeraz, H.C. Kim, Realization of self-poled, high performance, flexible piezoelectric energy harvester by employing PDMS-rGO as sandwich layer between P(VDF-TrFE)-PMN-PT composite sheets, Composites Part B: Engineering 159 (2019) 259–268. https://doi.org/10.1016/j.compositesb.2018.09.102.
[161] S. Xu, Y. Yeh, G. Poirier, M.C. McAlpine, R.A. Register, N. Yao, Flexible Piezoelectric PMN–PT Nanowire-Based Nanocomposite and Device, Nano Lett. 13 (2013) 2393–2398. https://doi.org/10.1021/nl400169t.
[162] R. Tu, B. Zhang, H.A. Sodano, Lead titanate nanowires/polyamide-imide piezoelectric nanocomposites for high-temperature energy harvesting, Nano Energy 97 (2022) 107175. https://doi.org/10.1016/j.nanoen.2022.107175.
[163] C. Chen, X. Wang, Y. Wang, D. Yang, F. Yao, W. Zhang, B. Wang, G.A. Sewvandi, D. Yang, D. Hu, Additive Manufacturing of Piezoelectric Materials, Advanced Functional Materials 30 (2020) 2005141. https://doi.org/10.1002/adfm.202005141.
[164] P. Singh, L.S. Smith, M. Bezdecny, M. Cheverton, J.A. Brewer, V. Venkataramani, Additive manufacturing of PZT-5H piezoceramic for ultrasound transducers, in: 2011 IEEE International Ultrasonics Symposium, 2011: pp. 1111–1114. https://doi.org/10.1109/ULTSYM.2011.0273.
[165] S.M. Gaytan, M.A. Cadena, H. Karim, D. Delfin, Y. Lin, D. Espalin, E. MacDonald, R.B. Wicker, Fabrication of barium titanate by binder jetting additive manufacturing technology, Ceramics International 41 (2015) 6610–6619. https://doi.org/10.1016/j.ceramint.2015.01.108.
[166] F. Castles, D. Isakov, A. Lui, Q. Lei, C.E.J. Dancer, Y. Wang, J.M. Janurudin, S.C. Speller, C.R.M. Grovenor, P.S. Grant, Microwave dielectric characterisation of 3D-printed BaTiO3/ABS polymer composites, Sci Rep 6 (2016) 22714. https://doi.org/10.1038/srep22714.
[167] R. Tao, J. Shi, F. Granier, M. Moeini, A. Akbarzadeh, D. Therriault, Multi-material fused filament fabrication of flexible 3D piezoelectric nanocomposite lattices for pressure sensing and energy harvesting applications, Applied Materials Today 29 (2022) 101596. https://doi.org/10.1016/j.apmt.2022.101596.
[168] A. Renteria, V.H. Balcorta, C. Marquez, A.A. Rodriguez, I. Renteria-Marquez, J. Regis, B. Wilburn, S. Patterson, D. Espalin, T.-L. (Bill) Tseng, Y. Lin, Direct ink write multi-material printing of PDMS-BTO composites with MWCNT electrodes for flexible force sensors, Flex. Print. Electron. 7 (2022) 015001. https://doi.org/10.1088/2058-8585/ac442e.
[169] D. Yao, H. Cui, R. Hensleigh, P. Smith, S. Alford, D. Bernero, S. Bush, K. Mann, H.F. Wu, M. Chin-Nieh, G. Youmans, X. (Rayne) Zheng, Achieving the Upper Bound of Piezoelectric Response in Tunable, Wearable 3D Printed Nanocomposites, Advanced Functional Materials 29 (2019) 1903866. https://doi.org/10.1002/adfm.201903866.
[170] K. Kim, W. Zhu, X. Qu, C. Aaronson, W.R. McCall, S. Chen, D.J. Sirbuly, 3D Optical Printing of Piezoelectric Nanoparticle–Polymer Composite Materials, ACS Nano 8 (2014) 9799–9806. https://doi.org/10.1021/nn503268f.

[171] X. Wang, Z. Liu, T. Zhang, Flexible Sensing Electronics for Wearable/Attachable Health Monitoring, Small 13 (2017) 1602790. https://doi.org/10.1002/smll.201602790.
[172] M. Amjadi, K.-U. Kyung, I. Park, M. Sitti, Stretchable, Skin-Mountable, and Wearable Strain Sensors and Their Potential Applications: A Review, Advanced Functional Materials 26 (2016) 1678–1698. https://doi.org/10.1002/adfm.201504755.
[173] Y. Mengüç, Y.-L. Park, E. Martinez-Villalpando, P. Aubin, M. Zisook, L. Stirling, R.J. Wood, C.J. Walsh, Soft wearable motion sensing suit for lower limb biomechanics measurements, in: 2013 IEEE International Conference on Robotics and Automation, 2013: pp. 5309–5316. https://doi.org/10.1109/ICRA.2013.6631337.
[174] N. Lu, D.-H. Kim, Flexible and Stretchable Electronics Paving the Way for Soft Robotics, Soft Robotics 1 (2014) 53–62. https://doi.org/10.1089/soro.2013.0005.
[175] D.-H. Kim, J. Song, W.M. Choi, H.-S. Kim, R.-H. Kim, Z. Liu, Y.Y. Huang, K.-C. Hwang, Y. Zhang, J.A. Rogers, Materials and noncoplanar mesh designs for integrated circuits with linear elastic responses to extreme mechanical deformations, Proceedings of the National Academy of Sciences 105 (2008) 18675–18680. https://doi.org/10.1073/pnas.0807476105.
[176] Y. Yuan, Y. Dai, M. Xu, Z. Wang, Z. Chen, Highly Stretchable Piezoelectric Strain Sensor With Dual Wavy Structures of PVDF Microfibers, in: 2020 IEEE 4th Information Technology, Networking, Electronic and Automation Control Conference (ITNEC), 2020: pp. 2418–2422. https://doi.org/10.1109/ITNEC48623.2020.9085027.
[177] Y. Duan, Y. Huang, Z. Yin, N. Bu, W. Dong, Non-wrinkled, highly stretchable piezoelectric devices by electrohydrodynamic direct-writing, Nanoscale 6 (2014) 3289–3295. https://doi.org/10.1039/C3NR06007A.
[178] S. Xu, Y. Zhang, J. Cho, J. Lee, X. Huang, L. Jia, J.A. Fan, Y. Su, J. Su, H. Zhang, H. Cheng, B. Lu, C. Yu, C. Chuang, T. Kim, T. Song, K. Shigeta, S. Kang, C. Dagdeviren, I. Petrov, P.V. Braun, Y. Huang, U. Paik, J.A. Rogers, Stretchable batteries with self-similar serpentine interconnects and integrated wireless recharging systems, Nat Commun 4 (2013) 1543. https://doi.org/10.1038/ncomms2553.
[179] Z. Ji, M. Zhang, Highly sensitive and stretchable piezoelectric strain sensor enabled wearable devices for real-time monitoring of respiratory and heartbeat simultaneously, Nanotechnology and Precision Engineering 5 (2022) 013002. https://doi.org/10.1063/10.0009365.
[180] Y.-G. Kim, J.-H. Song, S. Hong, S.-H. Ahn, Piezoelectric strain sensor with high sensitivity and high stretchability based on kirigami design cutting, Npj Flex Electron 6 (2022) 1–8. https://doi.org/10.1038/s41528-022-00186-4.
[181] R. Sun, S.C. Carreira, Y. Chen, C. Xiang, L. Xu, B. Zhang, M. Chen, I. Farrow, F. Scarpa, J. Rossiter, Stretchable Piezoelectric Sensing Systems for Self-Powered and Wireless Health Monitoring, Advanced Materials Technologies 4 (2019) 1900100. https://doi.org/10.1002/admt.201900100.
[182] C. Dagdeviren, P. Joe, O.L. Tuzman, K.-I. Park, K.J. Lee, Y. Shi, Y. Huang, J.A. Rogers, Recent progress in flexible and stretchable piezoelectric devices for mechanical energy harvesting, sensing and actuation, Extreme Mechanics Letters 9 (2016) 269–281. https://doi.org/10.1016/j.eml.2016.05.015.
[183] H. Zhou, Y. Zhang, Y. Qiu, H. Wu, W. Qin, Y. Liao, Q. Yu, H. Cheng, Stretchable piezoelectric energy harvesters and self-powered sensors for wearable and implantable devices, Biosensors and Bioelectronics 168 (2020) 112569. https://doi.org/10.1016/j.bios.2020.112569.

[184] C.K. Jeong, J. Lee, S. Han, J. Ryu, G.-T. Hwang, D.Y. Park, J.H. Park, S.S. Lee, M. Byun, S.H. Ko, K.J. Lee, A Hyper-Stretchable Elastic-Composite Energy Harvester, Advanced Materials 27 (2015) 2866–2875. https://doi.org/10.1002/adma.201500367.
[185] W. Wu, S. Bai, M. Yuan, Y. Qin, Z.L. Wang, T. Jing, Lead Zirconate Titanate Nanowire Textile Nanogenerator for Wearable Energy-Harvesting and Self-Powered Devices, ACS Nano 6 (2012) 6231–6235. https://doi.org/10.1021/nn3016585.
[186] X. Chou, J. Zhu, S. Qian, X. Niu, J. Qian, X. Hou, J. Mu, W. Geng, J. Cho, J. He, C. Xue, All-in-one filler-elastomer-based high-performance stretchable piezoelectric nanogenerator for kinetic energy harvesting and self-powered motion monitoring, Nano Energy 53 (2018) 550–558. https://doi.org/10.1016/j.nanoen.2018.09.006.
[187] J.E.Q. Quinsaat, T. de Wild, F.A. Nüesch, D. Damjanovic, R. Krämer, G. Schürch, D. Häfliger, F. Clemens, T. Sebastian, M. Dascalu, D.M. Opris, Stretchable piezoelectric elastic composites for sensors and energy generators, Composites Part B: Engineering 198 (2020) 108211. https://doi.org/10.1016/j.compositesb.2020.108211.
[188] Z. He, F. Rault, M. Lewandowski, E. Mohsenzadeh, F. Salaün, Electrospun PVDF Nanofibers for Piezoelectric Applications: A Review of the Influence of Electrospinning Parameters on the β Phase and Crystallinity Enhancement, Polymers 13 (2021) 174. https://doi.org/10.3390/polym13020174.
[189] S.-H. Park, H.B. Lee, S.M. Yeon, J. Park, N.K. Lee, Flexible and Stretchable Piezoelectric Sensor with Thickness-Tunable Configuration of Electrospun Nanofiber Mat and Elastomeric Substrates, ACS Appl. Mater. Interfaces 8 (2016) 24773–24781. https://doi.org/10.1021/acsami.6b07833.
[190] S. Siddiqui, D.-I. Kim, E. Roh, L.T. Duy, T.Q. Trung, M.T. Nguyen, N.-E. Lee, A durable and stable piezoelectric nanogenerator with nanocomposite nanofibers embedded in an elastomer under high loading for a self-powered sensor system, Nano Energy 30 (2016) 434–442. https://doi.org/10.1016/j.nanoen.2016.10.034.
[191] I. s. Elashmawi, N. a. Hakeem, Effect of PMMA addition on characterization and morphology of PVDF, Polymer Engineering & Science 48 (2008) 895–901. https://doi.org/10.1002/pen.21032.
[192] S.J. Kang, Y.J. Park, I. Bae, K.J. Kim, H.-C. Kim, S. Bauer, E.L. Thomas, C. Park, Printable Ferroelectric PVDF/PMMA Blend Films with Ultralow Roughness for Low Voltage Non-Volatile Polymer Memory, Advanced Functional Materials 19 (2009) 2812–2818. https://doi.org/10.1002/adfm.200900589.
[193] J.R. Leppe-Nerey, M.E. Nicho, F.Z. Sierra-Espinosa, F. Hernández-Guzmán, M. Fuentes-Pérez, Experimental study of piezoelectric polymeric film as energy harvester, Materials Science and Engineering: B 272 (2021) 115366. https://doi.org/10.1016/j.mseb.2021.115366.
[194] D. Valadorou, A.N. Papathanassiou, E. Kolonelou, E. Sakellis, Boosting the electro-mechanical coupling of piezoelectric polyvinyl alcohol–polyvinylidene fluoride blends by dispersing nano-graphene platelets, J. Phys. D: Appl. Phys. 55 (2022) 295501. https://doi.org/10.1088/1361-6463/ac629d.
[195] N. Shehata, R. Nair, R. Boualayan, I. Kandas, A. Masrani, E. Elnabawy, N. Omran, M. Gamal, A.H. Hassanin, Stretchable nanofibers of polyvinylidenefluoride (PVDF)/thermoplastic polyurethane (TPU) nanocomposite to support piezoelectric response via mechanical elasticity, Sci Rep 12 (2022) 8335. https://doi.org/10.1038/s41598-022-11465-5.

[196] H. Kim, L.C.D. Manriquez, M.T. Islam, L.A. Chavez, J.E. Regis, M.A. Ahsan, J.C. Noveron, T.-L.B. Tseng, Y. Lin, 3D printing of polyvinylidene fluoride/photopolymer resin blends for piezoelectric pressure sensing application using the stereolithography technique, MRS Communications 9 (2019) 1115–1123. https://doi.org/10.1557/mrc.2019.109.
[197] C. Xu, Y. Wang, Y. Chen, Highly toughened poly(vinylidene fluoride)/nitrile butadiene rubber blends prepared via peroxide-induced dynamic vulcanization, Polymer Testing 33 (2014) 179–186. https://doi.org/10.1016/j.polymertesting.2013.11.012.
[198] X. Jiang, C. Xu, Y. Wang, Y. Chen, Polyvinylidene Fluoride/Acrylonitrile Butadiene Rubber Blends Prepared Via Dynamic Vulcanization, Journal of Macromolecular Science, Part B 54 (2015) 58–70. https://doi.org/10.1080/00222348.2014.984577.
[199] C.M. Hansen, The Universality of the Solubility Parameter, Product R&D 8 (1969) 2–11. https://doi.org/10.1021/i360029a002.
[200] C.M. Hansen, Hansen Solubility Parameters: A User's Handbook, Second Edition, 2nd ed., CRC Press, Boca Raton, 2007. https://doi.org/10.1201/9781420006834.
[201] C. Bărdacă Urducea, A.C. Nechifor, I.A. Dimulescu, O. Oprea, G. Nechifor, E.E. Totu, I. Isildak, P.C. Albu, S.G. Bungău, Control of Nanostructured Polysulfone Membrane Preparation by Phase Inversion Method, Nanomaterials 10 (2020) 2349. https://doi.org/10.3390/nano10122349.
[202] R. m. Boom, H. w. w. Rolevink, Th. van den Boomgaard, C. a. Smolders, Microscopic structures in phase inversion membranes: The use of polymer blends for membrane formation by immersion precipitation, Makromolekulare Chemie. Macromolecular Symposia 69 (1993) 133–140. https://doi.org/10.1002/masy.19930690114.
[203] M.J. Troughton, ed., Chapter 16 - Solvent Welding, in: Handbook of Plastics Joining (Second Edition), William Andrew Publishing, Boston, 2009: pp. 139–143. https://doi.org/10.1016/B978-0-8155-1581-4.50018-4.
[204] D. Cormier, J. Taylor, A process for solvent welded rapid prototype tooling, Robotics and Computer-Integrated Manufacturing 17 (2001) 151–157. https://doi.org/10.1016/S0736-5845(00)00049-1.
[205] R. Tu, E. Sprague, H.A. Sodano, Precipitation printing towards diverse materials, mechanical tailoring and functional devices, Additive Manufacturing 35 (2020) 101358. https://doi.org/10.1016/j.addma.2020.101358.
[206] Z. Miao, J. Seo, M.A. Hickner, Solvent-cast 3D printing of polysulfone and polyaniline composites, Polymer 152 (2018) 18–24. https://doi.org/10.1016/j.polymer.2018.05.055.
[207] P. Fang, K. Liu, R. Shao, Y. Li, W. Ji, C. Yang, Phase inversion simulation of polymer PVDF membrane based on a fluid model, Advances in Mechanical Engineering 14 (2022) 16878132221095918. https://doi.org/10.1177/16878132221095918.
[208] L. Yilmaz, A.J. McHugh, Analysis of nonsolvent–solvent–polymer phase diagrams and their relevance to membrane formation modeling, Journal of Applied Polymer Science 31 (1986) 997–1018. https://doi.org/10.1002/app.1986.070310404.
[209] V.K. Stokes, Joining methods for plastics and plastic composites: An overview, Polymer Engineering & Science 29 (1989) 1310–1324. https://doi.org/10.1002/pen.760291903.
[210] C.Y. Yue, Influence of the Bonding Solvent on the Structure and Strength of Solvent Welded Joints, The Journal of Adhesion 20 (1986) 99–116. https://doi.org/10.1080/00218468608074941.

[211] R. Tu, H.A. Sodano, Highly Stretchable Printed Poly(vinylidene fluoride) Sensors through the Formation of a Continuous Elastomer Phase, ACS Appl. Mater. Interfaces 15 (2023) 22320–22331. https://doi.org/10.1021/acsami.3c01168.
[212] R. Karyappa, A. Ohno, M. Hashimoto, Immersion precipitation 3D printing (*ip* 3DP), Mater. Horiz. 6 (2019) 1834–1844. https://doi.org/10.1039/C9MH00730J.
[213] M.A. Cullinan, M.L. Culpepper, Carbon nanotubes as piezoresistive microelectromechanical sensors: Theory and experiment, Phys. Rev. B 82 (2010) 115428. https://doi.org/10.1103/PhysRevB.82.115428.
[214] S.-Y. Cheng, J.-M. Tseng, S.-Y. Lin, J.P. Gupta, C.-M. Shu, Runaway reaction on tert-butyl peroxybenzoate by DSC tests, J Therm Anal Calorim 93 (2008) 121–126. https://doi.org/10.1007/s10973-007-8831-z.
[215] P. Radovanovic, S.W. Thiel, S.-T. Hwang, Formation of asymmetric polysulfone membranes by immersion precipitation. Part I. Modelling mass transport during gelation, Journal of Membrane Science 65 (1992) 213–229. https://doi.org/10.1016/0376-7388(92)87024-R.
[216] K.-J. Baik, J.-Y. Kim, J.-S. Lee, S.-C. Kim, H.-K. Lee, Morphology of Membranes Formed from Polysulfone/Polyethersulfone/N-methyl-2-pyrrolidone/Water System by Immersion Precipitation, Macromolecular Research 9 (2001) 285–291.
[217] S.S. Madaeni, A. Rahimpour, Effect of type of solvent and non-solvents on morphology and performance of polysulfone and polyethersulfone ultrafiltration membranes for milk concentration, Polymers for Advanced Technologies 16 (2005) 717–724. https://doi.org/10.1002/pat.647.
[218] C.A. Smolders, A.J. Reuvers, R.M. Boom, I.M. Wienk, Microstructures in phase-inversion membranes. Part 1. Formation of macrovoids, Journal of Membrane Science 73 (1992) 259–275. https://doi.org/10.1016/0376-7388(92)80134-6.
[219] M.A. Frommer, R.M. Messalem, Mechanism of Membrane Formation. VI. Convective Flows and Large Void Formation during Membrane Precipitation, Product R&D 12 (1973) 328–333. https://doi.org/10.1021/i360048a015.
[220] R.J. Ray, W.B. Krantz, R.L. Sani, Linear stability theory model for finger formation in asymmetric membranes, Journal of Membrane Science 23 (1985) 155–182. https://doi.org/10.1016/S0376-7388(00)82216-4.
[221] L.K. Wang, J.P. Chen, Y.-T. Hung, N.K. Shammas, eds., Membrane and Desalination Technologies, Humana Press, Totowa, NJ, 2011. https://doi.org/10.1007/978-1-59745-278-6.
[222] N.H. Wright Ahmad Fauzi Ismail, Chris, ed., Membrane Fabrication, CRC Press, Boca Raton, 2015. https://doi.org/10.1201/b18149.
[223] X. Wang, L. Zhang, D. Sun, Q. An, H. Chen, Effect of coagulation bath temperature on formation mechanism of poly(vinylidene fluoride) membrane, Journal of Applied Polymer Science 110 (2008) 1656–1663. https://doi.org/10.1002/app.28169.
[224] M. Romay, N. Diban, A. Urtiaga, Thermodynamic Modeling and Validation of the Temperature Influence in Ternary Phase Polymer Systems, Polymers 13 (2021) 678. https://doi.org/10.3390/polym13050678.
[225] H.-J. Chen, Q.-Y. Bai, M.-C. Liu, G. Wu, Y.-Z. Wang, Ultrafast, cost-effective and scaled-up recycling of aramid products into aramid nanofibers: mechanism, upcycling, closed-loop recycling, Green Chemistry 23 (2021) 7646–7658. https://doi.org/10.1039/D1GC01805A.

[226] B. Yang, L. Wang, M. Zhang, J. Luo, X. Ding, Timesaving, High-Efficiency Approaches To Fabricate Aramid Nanofibers, ACS Nano 13 (2019) 7886–7897. https://doi.org/10.1021/acsnano.9b02258.
[227] M. Yang, K. Cao, L. Sui, Y. Qi, J. Zhu, A. Waas, E.M. Arruda, J. Kieffer, M.D. Thouless, N.A. Kotov, Dispersions of Aramid Nanofibers: A New Nanoscale Building Block, ACS Nano 5 (2011) 6945–6954. https://doi.org/10.1021/nn2014003.
[228] J. Floor, B. van Deursen, E. Tempelman, Tensile strength of 3D printed materials: Review and reassessment of test parameters:, Materials Testing 60 (2018) 679–686. https://doi.org/10.3139/120.111203.
[229] B. Podsiadły, A. Skalski, W. Rozpiórski, M. Słoma, Are We Able to Print Components as Strong as Injection Molded?—Comparing the Properties of 3D Printed and Injection Molded Components Made from ABS Thermoplastic, Applied Sciences 11 (2021) 6946. https://doi.org/10.3390/app11156946.
[230] T. Yap, N. Heathman, T. Phillips, J. Beaman, M. Tehrani, Additive Manufacturing of Polyaryletherketone (PAEK) polymers and their composites, Composites Part B: Engineering 266 (2023) 111019. https://doi.org/10.1016/j.compositesb.2023.111019.
[231] H.C. Kim, H.A. Sodano, Ultra-High Toughness Fibers Using Controlled Disorder of Assembled Aramid Nanofibers, Advanced Functional Materials 33 (2023) 2208661. https://doi.org/10.1002/adfm.202208661.
[232] Q. Cheng, Y. Liu, J. Lyu, Q. Lu, X. Zhang, W. Song, 3D printing-directed auxetic Kevlar aerogel architectures with multiple functionalization options, Journal of Materials Chemistry A 8 (2020) 14243–14253. https://doi.org/10.1039/D0TA02590A.
[233] G. Han, B. Zhou, Z. Li, Y. Feng, C. Liu, C. Shen, Ultrafine aramid nanofibers prepared by high-efficiency wet ball-milling-assisted deprotonation for high-performance nanopaper, Mater. Horiz. (2023). https://doi.org/10.1039/D3MH00600J.
[234] P. Xia, H. Li, Y. Wang, J. Wang, Processing aramid nanofiber/modified graphene oxide hydrogel into ultrastrong nanocomposite film, Applied Surface Science 545 (2021) 149004. https://doi.org/10.1016/j.apsusc.2021.149004.
[235] R. Tu, H.C. Kim, H.A. Sodano, Additive Manufacturing of High-Temperature Thermoplastic Polysulfone with Tailored Microstructure via Precipitation Printing, ACS Appl. Mater. Interfaces 15 (2023) 45270–45280. https://doi.org/10.1021/acsami.3c09048.
[236] R. Tu, E. Sprague, H.A. Sodano, Precipitation-Printed High-β Phase Poly(vinylidene fluoride) for Energy Harvesting, ACS Appl. Mater. Interfaces 12 (2020) 58072–58081. https://doi.org/10.1021/acsami.0c16207.
[237] X. Cai, T. Lei, D. Sun, L. Lin, A critical analysis of the α, β and γ phases in poly(vinylidene fluoride) using FTIR, RSC Advances 7 (2017) 15382–15389. https://doi.org/10.1039/C7RA01267E.
[238] Ye. Bormashenko, R. Pogreb, O. Stanevsky, Ed. Bormashenko, Vibrational spectrum of PVDF and its interpretation, Polymer Testing 23 (2004) 791–796. https://doi.org/10.1016/j.polymertesting.2004.04.001.
[239] M. Benz, W.B. Euler, Determination of the crystalline phases of poly(vinylidene fluoride) under different preparation conditions using differential scanning calorimetry and infrared spectroscopy, Journal of Applied Polymer Science 89 (2003) 1093–1100. https://doi.org/10.1002/app.12267.

[240] M. Benz, W.B. Euler, O.J. Gregory, The Role of Solution Phase Water on the Deposition of Thin Films of Poly(vinylidene fluoride), Macromolecules 35 (2002) 2682–2688. https://doi.org/10.1021/ma011744f.
[241] K.S. Seshadri, R.N. Jones, The shapes and intensities of infrared absorption bands—A review, Spectrochimica Acta 19 (1963) 1013–1085. https://doi.org/10.1016/0371-1951(63)80187-3.
[242] J.T. Reilly, J.M. Walsh, M.L. Greenfield, M.D. Donohue, Analysis of FT-IR spectroscopic data: The Voigt profile, Spectrochimica Acta Part A: Molecular Spectroscopy 48 (1992) 1459–1479. https://doi.org/10.1016/0584-8539(92)80154-O.
[243] D.M. Esterly, B.J. Love, Phase transformation to β-poly(vinylidene fluoride) by milling, Journal of Polymer Science Part B: Polymer Physics 42 (2004) 91–97. https://doi.org/10.1002/polb.10613.
[244] K. Nakagawa, Y. Ishida, Annealing effects in poly(vinylidene fluoride) as revealed by specific volume measurements, differential scanning calorimetry, and electron microscopy, Journal of Polymer Science: Polymer Physics Edition 11 (1973) 2153–2171. https://doi.org/10.1002/pol.1973.180111107.
[245] S. Chen, X. Li, K. Yao, F.E.H. Tay, A. Kumar, K. Zeng, Self-polarized ferroelectric PVDF homopolymer ultra-thin films derived from Langmuir–Blodgett deposition, Polymer 53 (2012) 1404–1408. https://doi.org/10.1016/j.polymer.2012.01.058.
[246] M. Zhang, A.-Q. Zhang, B.-K. Zhu, C.-H. Du, Y.-Y. Xu, Polymorphism in porous poly(vinylidene fluoride) membranes formed via immersion precipitation process, Journal of Membrane Science 319 (2008) 169–175. https://doi.org/10.1016/j.memsci.2008.03.029.
[247] D. Waller, A. Safari, Corona poling of PZT ceramics and flexible piezoelectric composites, Ferroelectrics 87 (1988) 189–195. https://doi.org/10.1080/00150198808201381.
[248] C.F. Groner, M.N. Hirsh, Comparison of poling techniques for inducing piezoelectric behavior in PVF2, in: 1985 5th International Symposium on Electrets (ISE 5), 1985: pp. 912–917. https://doi.org/10.1109/ISE.1985.7341594.
[249] D. Berlincourt, H. Jaffe, L.R. Shiozawa, Electroelastic Properties of the Sulfides, Selenides, and Tellurides of Zinc and Cadmium, Phys. Rev. 129 (1963) 1009–1017. https://doi.org/10.1103/PhysRev.129.1009.
[250] W.P. Mason, Physical Acoustics: Principles and Methods, Academic Press, New York, 2013.
[251] G.M. Sessler, A. Berraissoul, Tensile and bending piezoelectricity of single-film PVDF monomorphs and bimorphs, IEEE Transactions on Electrical Insulation 24 (1989) 249–254. https://doi.org/10.1109/14.90283.
[252] J. Zhao, Z. You, A Shoe-Embedded Piezoelectric Energy Harvester for Wearable Sensors, Sensors (Basel, Switzerland) 14 (2014) 12497–12510. https://doi.org/10.3390/s140712497.
[253] K. Fan, Z. Liu, H. Liu, L. Wang, Y. Zhu, B. Yu, Scavenging energy from human walking through a shoe-mounted piezoelectric harvester, Appl. Phys. Lett. 110 (2017) 143902. https://doi.org/10.1063/1.4979832.
[254] T.N. Sullivan, A. Pissarenko, S.A. Herrera, D. Kisailus, V.A. Lubarda, M.A. Meyers, A lightweight, biological structure with tailored stiffness: The feather vane, Acta Biomaterialia 41 (2016) 27–39. https://doi.org/10.1016/j.actbio.2016.05.022.
[255] J. Plog, Y. Jiang, Y. Pan, A.L. Yarin, Electrostatically-assisted direct ink writing for additive manufacturing, Additive Manufacturing 39 (2021) 101644. https://doi.org/10.1016/j.addma.2020.101644.

[256] F. Zhang, L. Jiang, S. Wang, Repairable cascaded slide-lock system endows bird feathers with tear-resistance and superdurability, Proceedings of the National Academy of Sciences 115 (2018) 10046–10051. https://doi.org/10.1073/pnas.1808293115.
[257] J.-S. Zhao, J. Zhang, Y. Zhao, Z. Zhang, P. Godefroit, Shaking the wings and preening feathers with the beak help a bird to recover its ruffled feather vane, Materials & Design 187 (2020) 108410. https://doi.org/10.1016/j.matdes.2019.108410.
[258] M. Di Luca, S. Mintchev, G. Heitz, F. Noca, D. Floreano, Bioinspired morphing wings for extended flight envelope and roll control of small drones, Interface Focus 7 (2017) 20160092. https://doi.org/10.1098/rsfs.2016.0092.
[259] D.T. Grant, M. Abdulrahim, R. Lind, Flight Dynamics of a Morphing Aircraft Utilizing Independent Multiple-Joint Wing Sweep, International Journal of Micro Air Vehicles 2 (2010) 91–106. https://doi.org/10.1260/1756-8293.2.2.91.
[260] Z. Hui, Y. Zhang, G. Chen, Aerodynamic performance investigation on a morphing unmanned aerial vehicle with bio-inspired discrete wing structures, Aerospace Science and Technology 95 (2019) 105419. https://doi.org/10.1016/j.ast.2019.105419.
[261] E. Ajanic, M. Feroskhan, S. Mintchev, F. Noca, D. Floreano, Bioinspired wing and tail morphing extends drone flight capabilities, Science Robotics 5 (2020). https://doi.org/10.1126/scirobotics.abc2897.
[262] F.M. Besem, J.D. Kamrass, J.P. Thomas, D. Tang, R.E. Kielb, Vortex-Induced Vibration and Frequency Lock-In of an Airfoil at High Angles of Attack, Journal of Fluids Engineering 138 (2015). https://doi.org/10.1115/1.4031134.
[263] J.F. Derakhshandeh, M.M. Alam, A review of bluff body wakes, Ocean Engineering 182 (2019) 475–488. https://doi.org/10.1016/j.oceaneng.2019.04.093.
[264] X. Wang, L. Zhang, D. Sun, Q. An, H. Chen, Formation mechanism and crystallization of poly(vinylidene fluoride) membrane via immersion precipitation method, Desalination 236 (2009) 170–178. https://doi.org/10.1016/j.desal.2007.10.064.
[265] L.-P. Cheng, Effect of Temperature on the Formation of Microporous PVDF Membranes by Precipitation from 1-Octanol/DMF/PVDF and Water/DMF/PVDF Systems, Macromolecules 32 (1999) 6668–6674. https://doi.org/10.1021/ma990418l.
[266] C. Decker, T.N.T. Viet, Photocrosslinking of functionalized rubbers, 8. The thiol-polybutadiene system, Macromolecular Chemistry and Physics 200 (1999) 1965–1974. https://doi.org/10.1002/(SICI)1521-3935(19990801)200:8<1965::AID-MACP1965>3.0.CO;2-W.
[267] T. Lei, X. Cai, X. Wang, L. Yu, X. Hu, G. Zheng, W. Lv, L. Wang, D. Wu, D. Sun, L. Lin, Spectroscopic evidence for a high fraction of ferroelectric phase induced in electrospun polyvinylidene fluoride fibers, RSC Adv. 3 (2013) 24952–24958. https://doi.org/10.1039/C3RA42622J.
[268] K.-I. Park, S. Bin Bae, S. Ho Yang, H. Ik Lee, K. Lee, S. Jun Lee, Lead-free BaTiO 3 nanowires-based flexible nanocomposite generator, Nanoscale 6 (2014) 8962–8968. https://doi.org/10.1039/C4NR02246G.
[269] L. Laiarinandrasana, J. Besson, M. Lafarge, G. Hochstetter, Temperature dependent mechanical behaviour of PVDF: Experiments and numerical modelling, International Journal of Plasticity 25 (2009) 1301–1324. https://doi.org/10.1016/j.ijplas.2008.09.008.
[270] Y. Thakur, B. Zhang, R. Dong, W. Lu, C. Iacob, J. Runt, J. Bernholc, Q.M. Zhang, Generating high dielectric constant blends from lower dielectric constant dipolar polymers

using nanostructure engineering, Nano Energy 32 (2017) 73–79. https://doi.org/10.1016/j.nanoen.2016.12.021.
[271] P. Janik, M. Paluch, J. Ziolo, W. Sulkowski, L. Nikiel, Low-frequency dielectric relaxation in rubber, Phys. Rev. E 64 (2001) 042502. https://doi.org/10.1103/PhysRevE.64.042502.
[272] S.L. Abd-El-Messieh, A.F. Younan, Dielectric relaxation and mechanical properties of natural and chloroprene rubber with some nitroaniline additives, Journal of Applied Polymer Science 62 (1996) 805–812. https://doi.org/10.1002/(SICI)1097-4628(19961031)62:5<805::AID-APP13>3.0.CO;2-R.
[273] S. Gong, Z. H. Zhu, Z. Li, Electron tunnelling and hopping effects on the temperature coefficient of resistance of carbon nanotube/polymer nanocomposites, Physical Chemistry Chemical Physics 19 (2017) 5113–5120. https://doi.org/10.1039/C6CP08115K.
[274] J. Hafner, M. Teuschel, M. Schneider, U. Schmid, Origin of the strong temperature effect on the piezoelectric response of the ferroelectric (co-)polymer P(VDF70-TrFE30), Polymer 170 (2019) 1–6. https://doi.org/10.1016/j.polymer.2019.02.064.
[275] Y. Tomita, K. Azuma, M. Naito, Computational evaluation of strain-rate-dependent deformation behavior of rubber and carbon-black-filled rubber under monotonic and cyclic straining, International Journal of Mechanical Sciences 50 (2008) 856–868. https://doi.org/10.1016/j.ijmecsci.2007.09.010.
[276] C. Chen, S. Zhao, C. Pan, Y. Zi, F. Wang, C. Yang, Z.L. Wang, A method for quantitatively separating the piezoelectric component from the as-received “Piezoelectric” signal, Nat Commun 13 (2022) 1391. https://doi.org/10.1038/s41467-022-29087-w.
[277] W. Gao, H. Ota, D. Kiriya, K. Takei, A. Javey, Flexible Electronics toward Wearable Sensing, Acc. Chem. Res. 52 (2019) 523–533. https://doi.org/10.1021/acs.accounts.8b00500.
[278] P. Wang, M. Hu, H. Wang, Z. Chen, Y. Feng, J. Wang, W. Ling, Y. Huang, The Evolution of Flexible Electronics: From Nature, Beyond Nature, and To Nature, Advanced Science 7 (2020) 2001116. https://doi.org/10.1002/advs.202001116.
[279] G. McGrady, K. Walsh, Dual Extrusion FDM Printer for Flexible and Rigid Polymers, in: American Society of Mechanical Engineers Digital Collection, 2021. https://doi.org/10.1115/MSEC2020-8377.
[280] H. Kim, E. Park, S. Kim, B. Park, N. Kim, S. Lee, Experimental Study on Mechanical Properties of Single- and Dual-material 3D Printed Products, Procedia Manufacturing 10 (2017) 887–897. https://doi.org/10.1016/j.promfg.2017.07.076.